Investigating the evolution of surface water on Mars through spectroscopy of secondary minerals

Thesis by

Ellen Kathleen Leask

In Partial Fulfillment of the Requirements for the degree of
Doctor of Philosophy

Caltech

CALIFORNIA INSTITUTE OF TECHNOLOGY
Pasadena, California

2020
Defended 9 January 2020

Ellen Kathleen Leask
ORCID: 0000-0002-3220-4003

ACKNOWLEDGEMENTS

I would like to thank Bethany Ehlmann for her support, encouragement, understanding, and thoroughness of edits over the course of the degree, as well as the invaluable introductions to the Mars community. Thanks also to the members of my thesis committee—especially George Rossman for his enthusiasm about any mineral question over the years. None of this work would have been possible without the help of the GPS office staff, who keep everything running—especially Julie Lee, Ulrika Terrones, and Loreta Young.

For help with any and all geospatial problems, I would like to thank Jay Dickson, who taught me bash scripting, gdal, GMT, ISIS, enabled the production of digital elevation models from stereo pairs, and many other things over the last few years. I would also like to acknowledge the support of the Ehlmann lab group as it has evolved over the years, especially Abby Fraeman for help with imaging spectroscopy in my first year, and Rebecca Greenberger for help, advice, cat photos, and tea and ice cream breaks.

For day-to-day sanity, I have really appreciated the welcoming atmosphere of the planetary science grad students, and the daily lunch train to have a chance to socialize and reset during the day. Thanks especially to officemates over the years for their support, wonderful conversations, and tolerating bad puns—and thanks in particular to Michael Wong, who took the time to teach me some basic elements of graphic design for posters and presentations which have been extremely helpful.

Many of my close friends here at Caltech have also been part of the Caltech Occidental Concert Band—having a weekly musical outlet has been wonderful, as are the friends through band. I'd especially like to thank Dan Johnson, Nelson Yanes, and Rebecca Glaudell for their friendship, kindness, and support. Friends from other life stages have also been very important—especially Alisha Deshpande, who made LA feel like home instantly. I'd also like to thank my family for their support and encouragement—especially my sister Anne Leask, without whom I would not have written the GRE, applied to grad school, stayed in the program, or remained (mostly) sane. There are no words to express how much your practical and emotional support has meant to me over the ups and downs of the last few years.

ABSTRACT

Despite its current arid climate, Mars' surface preserves a wide variety of morphologies and minerals that point to a water-rich past. However, the mechanisms and timing of this environmental change are not yet well understood. In this dissertation, we explore a variety of water-related minerals through visible-shortwave infrared (VSWIR) reflectance spectroscopy to better understand the environmental conditions at the time of their formation, and trace the evolution of surface water on Mars over time. We also demonstrate the capabilities of VSWIR spectroscopy at laboratory and field scales in a Mars analogue environment (Samail Ophiolite, Oman)—an emerging technique for use on future landed missions that enables us to differentiate between spectrally-similar minerals and spot rare minerals that help to constrain environmental conditions and better understand the geologic context of samples. On Mars, we use orbital datasets (predominantly CRISM, the Compact Reconnaissance Imaging Spectrometer for Mars) to investigate secondary minerals in the southern highlands of Mars, focusing on perchlorate, chloride, and sulphate minerals. We identify a previously unknown artifact in the CRISM dataset, which mimics perchlorate absorptions; previous orbital perchlorate detections (including those associated with recurring slope lineae) are not robust when data are reprocessed, suggesting that there may not be orbitally-detectable reservoirs of perchlorate on Mars, which would enable liquid brines to exist at the surface today. A detailed investigation of chloride deposits across the southern highlands of Mars points to an episodic surface-runoff water source rather than upwelling groundwater, a process which continued to create chloride deposits into the Amazonian era. Where chloride and sulphate deposits are in close proximity (Terra Sirenum, Mars), they do not appear to be genetically related as they often are on Earth; instead, they point to chemically distinct groundwater vs. surface water reservoirs in Terra Sirenum through the Hesperian and into the Amazonian. Together, these studies indicate that briny and/or acidic volumes of water at the surface capable of creating mineral deposits continued to exist—at least episodically—on Mars into the Amazonian, rather than ceasing much earlier in Mars' history.

PUBLISHED CONTENT AND CONTRIBUTIONS

Leask, E. K. and B. L. Ehlmann (2016). "Identifying and quantifying mineral abundance through VSWIR microimaging spectroscopy: A comparison to XRD and SEM." 8th Workshop on Hyperspectral Image and Signal Processing: Evolution in Remote Sensing (WHISPERS). IEEE.

E.K.L. participated in the conception of the project, prepared and measured samples using a hyperspectral imaging system and a scanning electron microscope, converted linear unmixing code to IDL, prepared the data and figures, and participated in writing the manuscript.

--*Adapted for the contents in Chapter 2*

Leask, E., et al. (2018). "Challenges in the search for perchlorate and other hydrated minerals with 2.1-µm absorptions on Mars." Geophysical Research Letters 45(22): 12,180-112,189, doi: 10.1029/2018GL080077.

E.K.L. participated in the conception of the project, analyzed spectral data, prepared figures, and participated in writing the manuscript.

--*Adapted for the contents in Chapter 4*

TABLE OF CONTENTS

LIST OF ILLUSTRATIONS

***Chapter 2**: Identifying and Quantifying Mineral Abundance through VSWIR Microimaging Spectroscopy: A Comparison to XRD and SEM*

***Chapter 3:** Understanding carbonate formation, serpentinization and crust formation with micro/meso-scale infrared imaging spectroscopy in a Mars analogue system, Samail Ophiolite, Oman*

***Chapter 4**: Challenges in the search for perchlorate and other hydrated minerals with 2.1-μm absorptions on Mars*

***Chapter 5**: Evidence for deposition of chloride on Mars from small-volume surface water events into the Late Hesperian-Early Amazonian*

Chapter 6*: A history of alteration in Terra Sirenum, Mars: evidence for chemically distinct waters forming sulphates vs chlorides into the Amazonian*

LIST OF TABLES

Number *Page*

Chapter 3

Chapter 5

Chapter 6

LIST OF ACRONYMS

CRISM: Compact Reconnaissance Imaging Spectrometer for Mars

CTX: ConTeXt Camera

DEM: Digital Elevation Models

EDS: Energy Dispersive Spectroscopy

HiRISE: High Resolution Imaging Science Experiment

I/F: Radiance/Flux

MOLA: Mars Orbiting Laser Altimeter

MRO: Mars Reconnaissance Orbiter

OMEGA: Observatoire pour la Minéralogie, l’Eau, les Glaces, et l’Activité

PCA: Principal Components Analysis

RMS: Root Mean Square

RSL: Recurring Slope Lineae

SEM: Scanning Electron Microscopy

THEMIS: Thermal Emission Imaging System

UCIS: Ultra Compact Imaging Spectrometer

VSWIR: Visible-Shortwave Infrared (~0.4-2.5µm)

VNIR: Visible-Near Infrared (~0.4-1.0µm)

XRD: X-ray Diffraction

Chapter 1

INTRODUCTION

1.1 Mars' geologic history

Mars is our closest planetary neighbor, and shares many similarities with Earth—both have active atmospheres that help shape the surface, volcanoes, ice caps, and seasonal cycles. However, while Earth's crust is changed and recycled through plate tectonics and active hydrological cycles, much of Mars' surface has remained largely unchanged over the past 3-4 billion years (Tanaka et al., 2014). Thus, Mars' surface can help us understand an era of our solar system's history that has been largely lost on Earth. Furthermore, like Earth, Mars has experienced massive global climate shifts, evolving into an arid climate from a once-wet environment capable of carving deep valleys into the surface.

Technological advances since the advent of the telescope in the early 1600s have allowed us to observe Mars in ever-increasing detail, with the first maps of albedo features produced in the 1830s by Mädler and Beer. The Mariner 4 flyby of Mars in 1964 marked a step change in our ability to observe and understand the processes that have shaped the surface of Mars; data returned from Mariner 9 (1971) were the first to show extensive fluvial networks and outflow channels (e.g. Masursky et al., 1977; Baker, 1974). Subsequent orbital missions have improved image resolution (down to ~25cm/pixel), and provided many more datasets of chemical information (gamma ray and neutron spectrometry), elevation information (laser altimetry and stereo image pairs), and mineralogical information, through visible-shortwave infrared and thermal infrared spectroscopy.

From these combined datasets, we have begun to compile a global history of Mars. Using crater counting, high-resolution imagery, and reflectance spectroscopy, a few hypotheses have emerged to explain the systematic changes we observe. The oldest preserved terrain (Noachian; 4.1-3.6 Ga (Hartmann & Neukum, 2001)) shows evidence of fluvial dissection, drainage networks, and sedimentary basins (Carr, 1995; Cabrol & Grin, 1999; Mangold et al., 2004; Hynek et al., 2010). But was this era Earth-like in climate, with warm temperatures and high water/rock ratios? Or was it only sometimes warm enough for surface flow, but mostly cold and icy? Extensive clay minerals are found throughout Noachian terrain, perhaps correlated with the availability of surface water in Mars' early history (Bibring et al., 2006; Murchie et al., 2009). The Hesperian era (3.6-~3.1 Ga) is marked by large volcanic units and outflow channels (e.g. Werner, 2009; Squyres, 1984; Fassett & Head, 2008); these have been hypothesized to mark a step change in Mars' evolution, perhaps associated with a shift to more sulphate-rich mineralogy (Bibring et al., 2006). In the most recent era (Amazonian; ~3.1 Ga-present), Mars has been thought to be arid, with water locked away in ices, aeolian processes sculpting the surface (Arvidson et al., 1979; Golombek et al., 2014), and mineralogical changes dominated by iron oxides (Bibring et al., 2006). However, recent work (e.g. Martin et al., 2017) has indicated that alteration processes (e.g. sulphate precipitation) may have continued well into the Amazonian. In this work, we explore some of these hypotheses to further develop our understanding of how surface waters on Mars have evolved through time.

With these advances in our understanding of Mars' history come further questions—fundamentally, how and why did Mars change over time? What caused a robust atmosphere necessary to sustain surface hydrology to disappear (e.g. Pollack et al., 1987)? Where did that atmosphere go? And when was the last surface water present on Mars? In this thesis, we address parts of these fundamental questions by exploring secondary minerals found on Mars' surface through visible-shortwave infrared imaging spectroscopy. We investigate how carbonate spectra—a key phase to understand Mars' past atmosphere and/or neutral to alkaline (potentially habitable) waters—may be masked in carbonate/serpentine Mars analogue systems on Earth, and how future missions could use evolving techniques to find these phases *in situ*. On Mars, we investigate perchlorate and chloride mineral detections, as these soluble minerals can depress the freezing point of water, allowing it to stay liquid at colder temperatures, and are the last minerals to form from an evaporating, briny water body. And in Terra Sirenum, an ancient region southwest of Tharsis with a rich diversity of alteration mineralogy, we explore the relationship of these minerals to one another through time. We use these local and regional trends in alteration mineralogy to better understand the timing and evolution of surface waters on Mars.

1.2 Chapter Summaries

In the first section of this thesis, we investigate a Mars analogue environment on Earth (the Samail Ophiolite, Oman) using visible-shortwave infrared imaging spectrometers in the laboratory (Chapter 2) and field (Chapter 3). The Samail Ophiolite is a heavily serpentinized fragment of Earth's oceanic crust/mantle sequence that is exposed at the surface in an arid, relatively vegetation-free environment, and so is an analogue for carbonate-serpentine systems observed in orbital spectroscopic data on Mars (Ehlmann et al., 2010; Michalski et al., 2010; Amador et al., 2018). In Chapter 2, we use a prototype microimaging reflectance spectrometer to identify minerals, quantify their abundances, and assess textural relationships at a sub-millimeter scale. We evaluate the performance of this technique relative to traditional geochemical techniques, including quantitative x-ray diffraction (XRD) analysis, and energy-dispersive spectroscopy (EDS) on a scanning electron microscope (SEM). We are able to identify spatially coherent rare phases that may be below XRD detection limits, as well as partially altered mineral phases (pyroxenes). At this small scale, abundance estimates derived from linear unmixing are typically within ~10% of abundance estimates from XRD and EDS analysis.

In Chapter 3, we demonstrate how a similar instrument can operate in the field. We discriminate between carbonate mineral endmembers and serpentine in outcrop, which have overlapping major absorptions and can be difficult to disentangle in orbital datasets. Spectral endmembers on the ground are compared with airborne HyMap data of the region. We note that abundance estimates from linear mixtures depend strongly on the endmember choice, especially the overall reflectance and grain size of endmembers chosen. We detect rare phases in outcrop, such as remnant pyroxenes, and small veins and clasts of key alteration minerals such as prehnite and epidote, which help establish the pressure and temperature conditions of alteration. This capability would be very useful for future landed missions, to fully explore and characterize the diversity in a site.

In chapters 4-6, we focus on results from CRISM orbital spectroscopic data of Mars. In Chapter 4, we set out to use machine learning to find more pixels similar to those identified as perchlorate in Ojha et al. (2015) and Massé et al. (2010). Instead, we found a previously unidentified systematic artifact in CRISM data, which mimics the spectral properties of perchlorate. We find this artifact in > 90% of images examined (although typically in <0.05% of pixels in a given image). A filtering step in the data processing pipeline, between radiance and I/F versions of the data, convolves narrow artifacts (“spikes”) with real atmospheric absorptions in these wavelength regions to create spurious absorption-like features, predominantly at 1.9 and 2.1 µm (on the wings of atmospheric carbon dioxide absorptions). Previously-reported orbital perchlorate detections—such as those associated with recurring slope lineae (Ojha et al., 2015), used as evidence for episodic liquid water present at the surface of Mars today—appear to be a result of this systematic artifact.

In Chapter 5, we explore the environmental settings of previously-detected chloride deposits (Osterloo et al., 2010) across the southern highlands of Mars. Here, we aim to better understand when chlorides were deposited (where they are dateable through crater counting), and assess the potential water and ion sources for their formation. We look at all available high resolution imagery, building digital elevation models wherever stereo image pairs are available. All targeted CRISM images intersecting chloride deposits are analyzed, looking for accessory minerals including clays, sulphates, and carbonates. Earlier studies which investigated subsets of CRISM images covering chloride deposits (El Maarry et al, 2013; Ruesch et al., 2012) found that chlorides did not occur with sulphates, as one might expect in a sequence of evaporites (e.g. Eugster and Hardie, 1978). Looking at all available data, we confirm that sulphates do not accompany chloride detections. Furthermore, while chloride deposits are found in local topographic lows, they are not in flat, playa-like settings, instead ranging in elevation over tens of meters, and typically at asymmetric elevations within basins—present at higher elevations on the side of basin with chloride-filled inlet channels. We interpret the chloride deposits as likely sourced from surface water runoff, consistent with their presence at a wide range of elevations and within channels. While almost all chlorides are found within Noachian terrain, a small number are clearly in channels carved into volcanic terrain (dated at 3.4-2.3 Ga). We infer from this that the processes creating chloride deposits persisted into the Amazonian, at least in some locations on Mars; this is a significant shift from previous works, which have placed the chloride deposits in the Noachian due to their association with ancient terrains (e.g. Hill and Christiansen, 2019), or prior to the onset of Hesperian sulphates and volcanism (e.g. Ruesch et al., 2012). A possible surface water source could be small amounts of meltwater and/or deliquescence, while chloride anions could be derived from the surface layer of dust/soil, perhaps brought to the surface by capillary action in clay rich soils prevalent in Noachian terrain.

In Chapter 6, we focus on Terra Sirenum, a region southwest of the Tharsis volcanic province on Mars. Here, a wide range of secondary minerals have been identified within close proximity—clays, sulphates, carbonates, and chlorides. In this chapter, we incorporate high resolution imagery and elevation models to understand the relationship between alteration minerals, and infer their likely fluid and/or ion sources. We use a machine learning algorithm to look for further, small mineral detections that may have been overlooked using traditional spectral processing techniques, verifying possible detections by hand to ensure they are not a result of the instrument artifacts. Using this technique, we find a number of new acid sulphate detections, whose major cations (Al (III) vs Fe (II)) match the dominant clay mineralogy of each location. Unlike chlorides, which are found throughout the intercrater plains, sulphates are almost exclusively found in basins; we interpret them as most likely derived from an upwelling groundwater source, possibly volcanic given the inferred sulphurous, acidic composition of the water, and the presence of units consistent with basaltic resurfacing. Dating these volcanic capping units, we find that they get younger (3.5-1.4 Ga) from west to east (towards Tharsis), consistent with the global findings of Werner (2009). These age ranges overlap with chloride deposit formation (see Chapter 5), although even in Terra Sirenum, adjacent chlorides and sulphates appear unrelated, separated by a capping unit or several hundred meters of elevation difference. If chlorides and sulphates are formed episodically (and independently) throughout the Hesperian and into the Amazonian, this points to disconnected surface and groundwater reservoirs, perhaps separated by a permafrost layer. Occasional climate changes (seasonal, obliquity) could cause limited melting of surface ice, creating a local water source for high-elevation chloride deposits, while episodes of volcanism could provide both a heat and water source for upwelling sulphurous, acidic waters.

1.3 References

Amador, E. S., et al. (2018). "A search for minerals associated with serpentinization across Mars using CRISM spectral data." Icarus 311: 113-134.

Arvidson, R., et al. (1979). "Differential aeolian redistribution rates on Mars." Nature 278(5704): 533.

Baker, V. R. and D. J. Milton (1974). "Erosion by catastrophic floods on Mars and Earth." Icarus 23(1): 27-41.

Bibring, J.-P., et al. (2006). "Global mineralogical and aqueous Mars history derived from OMEGA/Mars Express data." Science 312(5772): 400-404.

Carr, M. H. (1995). "The martian drainage system and the origin of valley networks and fretted channels." Journal of Geophysical Research: Planets 100(E4): 7479-7507.

Ehlmann, B., et al. (2010). "Geologic setting of serpentine deposits on Mars." Geophysical research letters 37(6).

El-Maarry, M. R., et al. (2013). "Analysis of polygonal cracking patterns in chloride-bearing terrains on Mars: Indicators of ancient playa settings." Journal of Geophysical Research: Planets 118(11): 2263-2278.

Eugster, H. P. and L. A. Hardie (1978). Saline lakes. Lakes, Springer: 237-293.

Fassett, C. I. and J. W. Head III (2008). "Valley network-fed, open-basin lakes on Mars: Distribution and implications for Noachian surface and subsurface hydrology." Icarus 198(1): 37-56.

Golombek, M., et al. (2014). "Small crater modification on Meridiani Planum and implications for erosion rates and climate change on Mars." Journal of Geophysical Research: Planets 119(12): 2522-2547.

Hartmann, W. K. and G. Neukum (2001). Cratering chronology and the evolution of Mars. Chronology and evolution of Mars, Springer: 165-194.

Hill, J. and P. Christensen (2019). "New Constraints on the Formation Ages of the Chloride-Bearing Deposits in the martian Southern Hemisphere." LPI Contributions 2089.

Hynek, B. M., et al. (2010). "Updated global map of martian valley networks and implications for climate and hydrologic processes." Journal of Geophysical Research: Planets 115(E9).

Mangold, N., et al. (2004). "Evidence for precipitation on Mars from dendritic valleys in the Valles Marineris area." Science 305(5680): 78-81.

Massé, M., et al. (2010). "Martian polar and circum-polar sulfate-bearing deposits: Sublimation tills derived from the North Polar Cap." Icarus 209(2): 434-451.

Masursky, H., et al. (1977). "Classification and time of formation of martian channels based on Viking data." Journal of Geophysical Research 82(28): 4016-4038.

Michalski, J. R. and P. B. Niles (2010). "Deep crustal carbonate rocks exposed by meteor impact on Mars." Nature Geoscience 3(11): 751-755.

Murchie, S. L., et al. (2009). "A synthesis of martian aqueous mineralogy after 1 Mars year of observations from the Mars Reconnaissance Orbiter." Journal of Geophysical Research: Planets 114(E2).

Ojha, L., et al. (2015). "Spectral evidence for hydrated salts in recurring slope lineae on Mars." Nature Geoscience 8(11): 829.

Osterloo, M. M., et al. (2010). "Geologic context of proposed chloride-bearing materials on Mars." Journal of Geophysical Research: Planets 115(E10).

Pollack, J. B., et al. (1987). "The case for a wet, warm climate on early Mars." Icarus 71(2): 203-224.

Ruesch, O., et al. (2012). "Compositional investigation of the proposed chloride-bearing materials on Mars using near-infrared orbital data from OMEGA/MEx." Journal of Geophysical Research: Planets 117(E11).

Squyres, S. W. (1984). "The history of water on Mars." Annual Review of Earth and Planetary Sciences 12(1): 83-106.

Tanaka, K. L., et al. (2014). "Geologic map of Mars." United States Geological Survey Sci. Invest. (Map, scale 1: 20,000,000).

Werner, S. C. (2009). "The global martian volcanic evolutionary history." Icarus 201(1): 44-68.

Chapter 2

IDENTIFYING AND QUANTIFYING MINERAL ABUNDANCE THROUGH VSWIR MICROIMAGING SPECTROSCOPY: A COMPARISON TO XRD AND SEM

Ellen K. Leask[1] and Bethany L. Ehlmann[1, 2]

[1]Division of Geological & Planetary Sciences, California Institute of Technology, Pasadena, CA 91125

[2]Jet Propulsion Laboratory, California Institute of Technology, Pasadena, CA, 91109

Leask, E. K. and B. L. Ehlmann (2016). "Identifying and quantifying mineral abundance through VSWIR microimaging spectroscopy: A comparison to XRD and SEM." 8th Workshop on Hyperspectral Image and Signal Processing: Evolution in Remote Sensing (WHISPERS). IEEE.

Abstract

Visible-shortwave infrared microimaging reflectance spectroscopy is a new technique to identify minerals, quantify abundances, and assess textural relationships at sub-millimeter scale without destructive sample preparation. Here, we used a prototype instrument to image serpentinized igneous rocks and carbonate-rich travertine deposits to evaluate performance, relative to traditional techniques: XRD (mineralogical analysis of bulk powders with no texture preservation) and SEM/EDS (analysis of phases and textures using chemical data from polished thin sections). VSWIR microimaging spectroscopy is ideal for identifying spatially coherent rare phases, below XRD detection limits. The progress of alteration can also be inferred from spectral parameters and may correspond to phases that are amorphous in XRD. However, VSWIR microimaging spectroscopy can sometimes be challenging with analyses of very dark materials (reflectance <0.05) and mineral mixtures occurring at a spatial scales multiple factors below the pixel size. Abundances derived from linear unmixing typically agree with those from XRD and EDS within ~10%.

1 Introduction

Visible to shortwave infrared (VSWIR) reflectance spectroscopy has been used for large-scale compositional mapping on Earth, Mars, and other planets at scales of tens of meters to km per pixel (e.g., Green et al., 1998; Bibring et al., 2005; Murchie et al., 2007; DeSanctis et al., 2013). The prototype Ultra-Compact Imaging Spectrometer (UCIS; Van Gorp et al., 2014), implemented for this work in microscopic mode, allows direct comparison with remote sensing data and identification of minerals and textures at microscale. VSWIR microimaging spectroscopy is a new geosciences technique for performing mineralogic analysis, which is non-destructive, preserves petrographic relationships, and requires minimal sample preparation (Greenberger et al., 2015). Because each mineral has a different set of conditions under which it is stable, identifying multiple minerals while preserving textural context allows for tighter constraints on geochemical conditions at the time of formation. It is not currently feasible to make and study thin sections on rocks in situ on planetary surfaces; VSWIR microimaging spectroscopy provides an alternative method to obtain a similar level of petrographic information.

Samples from the Samail Ophiolite (Oman) are used as an analogue for martian carbonate and serpentine deposits (e.g. Ehlmann and Mustard, 2012) to evaluate the ability of VSWIR microimaging spectroscopy to identify minerals present, distinguish carbonates of different chemistries from minerals with absorptions at similar wavelength positions, and to quantify mineral abundances. This work is part of a larger project to establish methods of identifying and quantifying carbonate content at multiple spatial scales using reflectance spectroscopy. Here, we compare microimaging spectroscopy results to current standard geosciences techniques for mineralogy and petrology: powder XRD for bulk mineralogy and SEM/EDS for texture and phase chemistry.

2 Methods

2.1. Data Collection

Fifteen cut rock samples from the Samail Ophiolite (Oman), representing a suite of textures and compositions, were measured with UCIS over the wavelength range 0.5-2.5 µm, with 10 nm spectral resolution, and a pixel footprint of 81x81 µm (e.g., Fig. 1). Each sample takes ~3 minutes to image. Two or more subsamples of each rock were sent to two external laboratories (ActLabs, K-T Geoservices) for x-ray diffraction (XRD) analyses of powdered samples for mineral identification and quantitative abundance estimates. Two samples were polished, imaged with UCIS, then carbon coated, and imaged on a scanning electron microscope (SEM). Energy-dispersive spectroscopy (EDS) maps were obtained over the area of the sample, providing elemental abundance data for direct comparison with UCIS data.

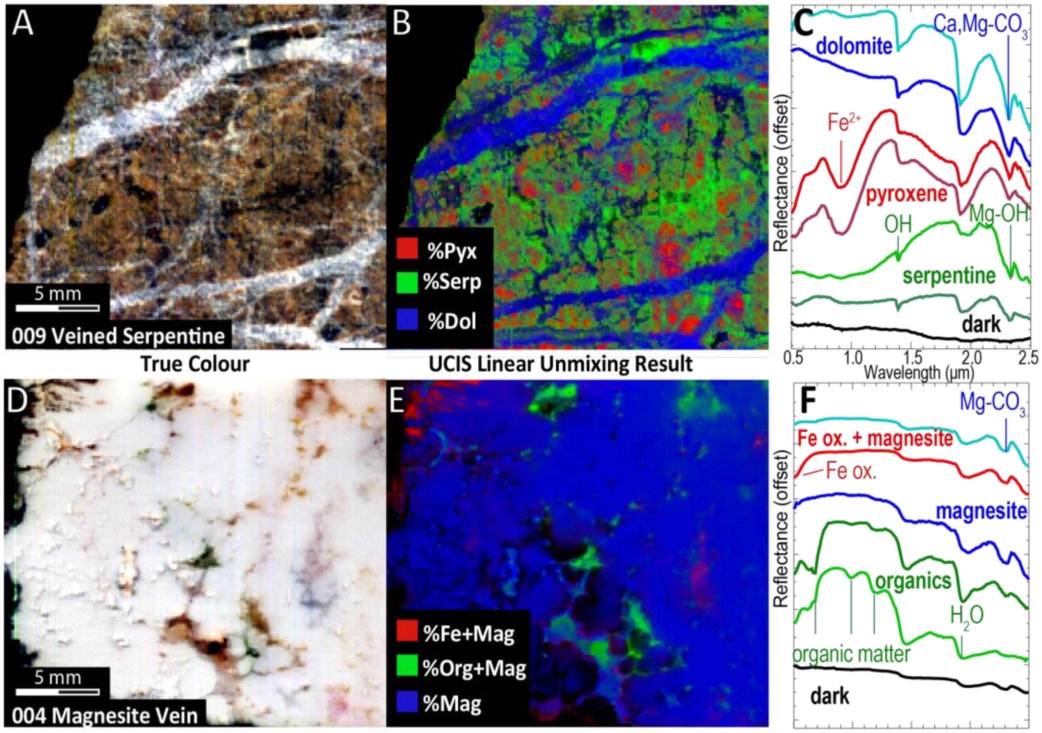

Fig.2-1. Linear unmixing examples. A-C: Veined serpentinite sample. Unmixing results (B) highlight veins and remnant pyroxene (endmember spectra shown in C). D-F: Magnesite vein sample, with organic matter (green) in porous areas.

2.2. Endmember Selection

Principal component analyses (PCA) using built-in algorithms in ENVI were run on each image. The first ~20 principal components were investigated through ENVI's n-dimensional visualizer; potential endmembers were selected based on the vertices of the point cloud. A parsimonious set of endmembers was determined for each sample, based on the potential endmembers and expert user analysis. Regions of interest (~15 pixels) were drawn for each endmember, taking the mean spectrum for the region. Automated endmember selection algorithms (K-means, ISODATA) were tested, but failed to identify minerals of interest (strongly biased to overall reflectance and not sensitive to subtle differences in shape or band position).

2.3. Linear Unmixing

At this spatial scale, many pixels consist of a single mineral phase. As a first-order approximation, we use linear spectral unmixing to estimate the abundance of phases, assuming most mixed spectra result from areal 'checkerboard' mixtures, where endmember spectra combine linearly, proportional to their areal abundance within a pixel. Best-fit abundance estimates are obtained using a fully constrained (sum to 1), non-negative linear least squares algorithm (Heylen et al., 2011). If initial output images were noisy and did not follow observable textures in the rock, endmembers were re-chosen until the output was coherent. Endmember selection was refined until average RMS errors were under 0.05. Nonlinear algorithms were not considered in this study, as particle size is not consistent and optical constants are not available for natural samples.

2.4. EDS Comparison

UCIS images were co-registered with EDS elemental abundance maps for two samples. Single-pixel endmembers corresponding to the same physical locations were used to unmix both the elemental abundance and spectral data independently via the same algorithm. Mineral phases were also mapped via absorption band depth and band centre parameters in VSWIR data, and element ratios and abundances in EDS data, allowing direct spatial correlation of elemental and spectral data on a pixel-by-pixel basis.

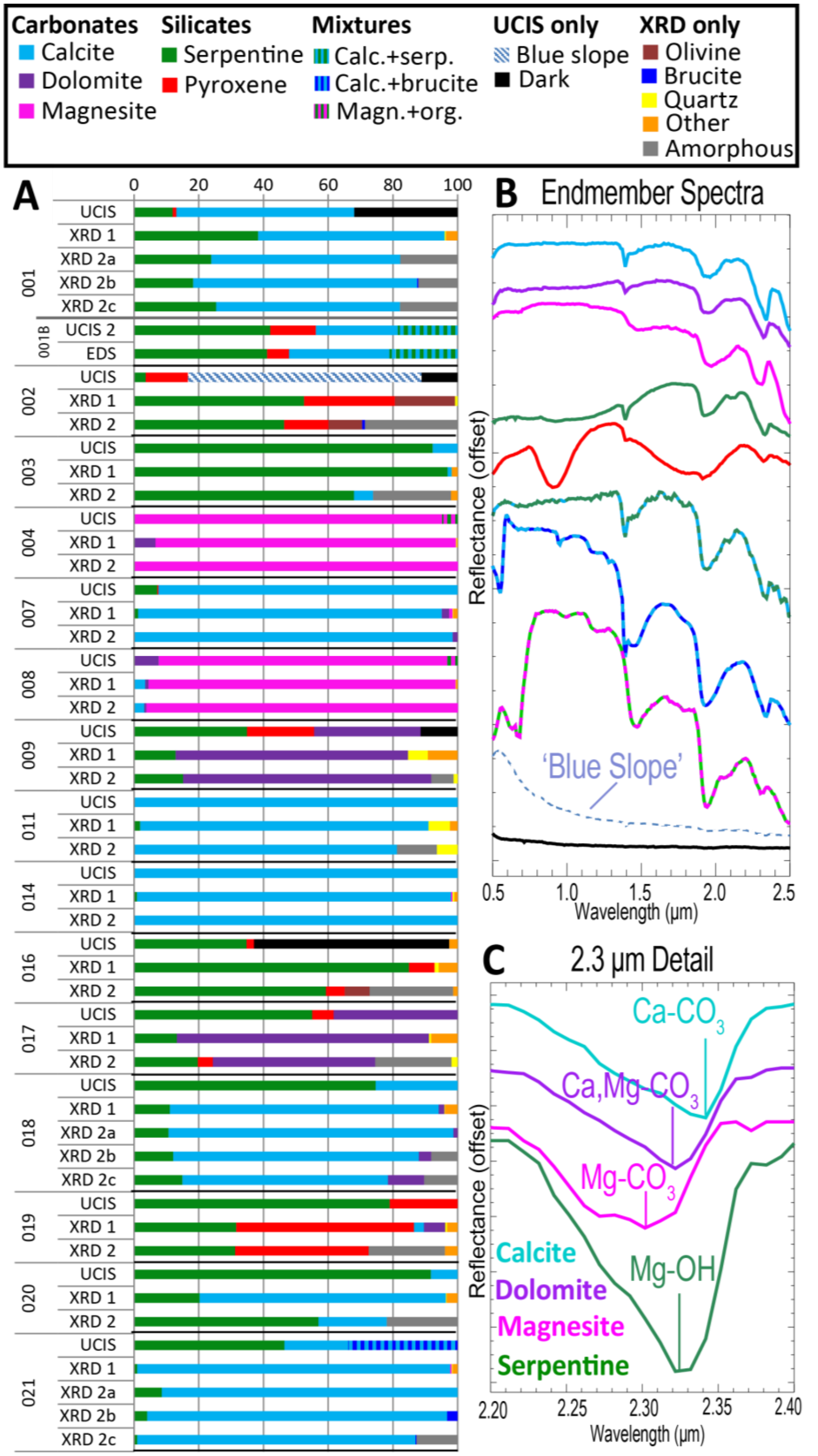

Fig. 2-2. Comparison of linear unmixing results (UCIS) and XRD abundance estimates (A). B: Examples of endmember spectra used in unmixing. C: Zoom showing subtle differences in the 2.3µm absorption between carbonates and serpentine.

3 Results

3.1. Mineral Identification

In 13 of 15 samples, UCIS identifies all the same major (>5% abundance) mineral phases as XRD analysis (Fig. 2). Exceptions are a very dark sample (002), where UCIS did not detect 10-19% olivine, and brighter sample (011), where UCIS did not identify ~6% quartz found by XRD. Notably, UCIS data reliably differentiated between carbonate minerals (calcite, dolomite, and magnesite) and serpentine with very similar overall spectra, based on the exact position of the 2.3μm absorption (Fig. 2C; Gaffey, 1987; Clark, 1999). Specific carbonate minerals can be clearly distinguished when each phase extends over several pixels. Sub-pixel mixtures of carbonate phases (such as dolomite and calcite in the pore spaces of a magnesite vein sample (004, 008), seen with SEM) cannot always be uniquely distinguished. Phases that are present only within fine-grained mixtures may sometimes be identified if they possess distinctive (if subtle) absorptions; for instance, brucite in sample 021 was identified by a hydroxyl absorption at 1.4 μm, in addition to a slight 2.48μm absorption and sharp 0.95 μm band. In magnesite vein samples 004 and 008, absorption features consistent with organic matter are also noted—a sharp ‘red edge’ at ~0.8 μm, and minor absorptions in the 1-2 μm range associated with C-H, N-H, and C-O bonds (Fig. 1F; ASD, 2013).

3.2. Mineral Quantification

Images from the linear unmixing highlight expected petrologic textures for rocks of this type: the ‘dolomite’ endmember occurs in veins, while the ‘pyroxene’ endmember is concentrated in the centres of clasts (Fig. 1B). The algorithm works even for discriminating spectrally similar endmembers; for example, sample 004 has 6 different magnesite-type endmembers, including stripes of magnesite with a reddish (ferric) coating and organic-rich magnesite within porosity (Fig.1E).

For most samples, abundance estimates between UCIS and XRD are the same within 10-15% (median total difference per sample); scatter between multiple XRD analyses of different subsamples of the same rock is 5-10%. (The two darkest samples, 002 and 016, were not included in this, as less than half the sample can be reliably classified with VSWIR as implemented here, discussed further below). Given the heterogeneous nature of many of the samples, including individual clasts comprising a large portions of some samples (e.g., 001, 018, 021), natural variance in abundance is expected. Furthermore, XRD abundances are reported in wt. %, while UCIS are areal %. UCIS data consistently show higher pyroxene and serpentine in samples with a high amorphous component and/or heavy veining (003, 017, 018, 019, 020, 021), but this may be a true difference in sensitivity of the techniques to incipient alteration, as discussed below.

Direct comparison of areal abundances from EDS and UCIS is possible for sample 001 (Fig. 3C, D). Here, determinations are very similar (EDS (UCIS)): 41 (42) % serpentine, 31 (25) % calcite, 21 (18) % mixed carbonate and serpentine, and 7 (14) % pyroxene.

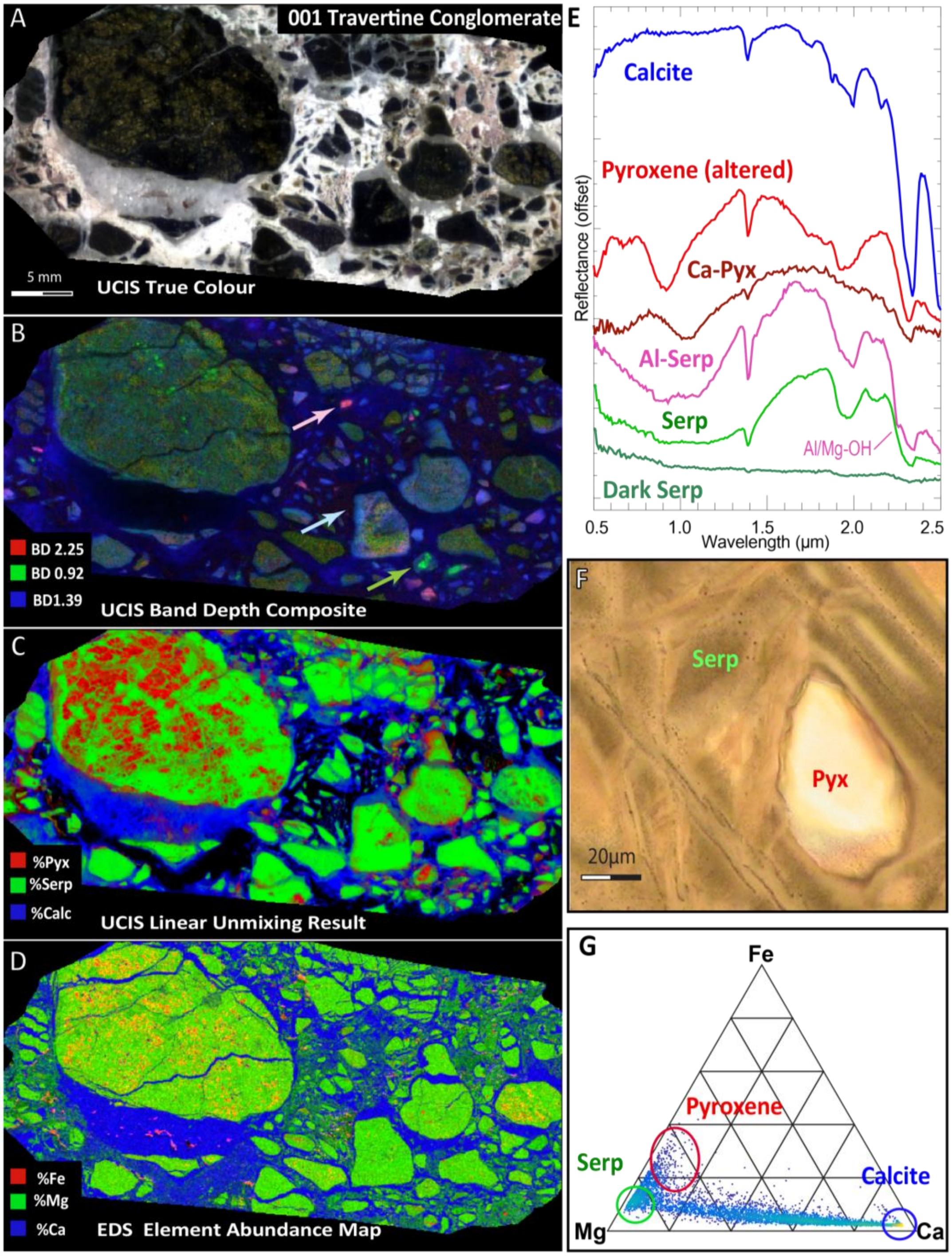

Fig. 2-3. UCIS and EDS for a travertine conglomerate sample. RGB composite of key band depths (B) highlights rare clasts and textures. Unmixing results in C (using endmember spectra (E)) closely correspond to elemental abundances from EDS (D). F) Thin section photomicrograph showing micro-opaques associated with pyroxene alteration. G) Ternary plot of EDS data showing serpentine, pyroxene, and calcite endmembers with a clear mixing line between serpentine and calcite, with endmembers used in (D).

4 Discussion

Overall, this study demonstrates that VSWIR microimaging spectroscopy provides bulk mineralogy estimates of comparable accuracy to XRD for most of this set of samples, and provides mineralogical and textural information comparable to SEM/EDS. Below, we highlight some of the key challenges as well as the key advantages of this new technique vs. existing geological methods for mineralogy.

4.1 Microimaging Spectroscopy Challenges

4.1.1 Dark Minerals and ‘Blue Slope’ Spectra

There are at least two related processes responsible for the difficulty in identifying minerals in dark (<0.05 reflectance) samples: (1) dark phases absorbing most of the photons, leading to little reflected light back to the detector, and (2) internal scattering caused by extremely fine-grained opaque minerals. Issue (1) can be addressed simply by increased acquisition times to average many spectra and optimization of instrument design to improve SNR (this particular instrument configuration, which utilizes a not-full performance detector spare leftover from a flight project, was not optimized). Issue (2) is harder to address—the presence of <2μm opaques within brighter minerals (Fig. 3F) may cause Rayleigh or Mie type scattering at SWIR wavelengths, creating a ‘blue slope’ that dominates the spectral signature for that pixel.

4.1.2 Minerals without strong VSWIR absorptions

Quartz and other minerals such as feldspars do not have strong VSWIR absorptions, and so they are not expected to be detected with this technique. However, it is sometimes possible to infer their presence by identifying their alteration products—here, we searched unsuccessfully for an absorption at 2.2 μm associated with hydrated silica (Lauger and Florke, 1974).

4.1.3 Grain Size and Mixed Phases

Four samples (001, 004, 008, and 021) include a mixed-mineral endmember. Mixed mineral endmembers were chosen when either spectral properties of the mixed phase were significantly different from either endmember or where no pure second endmember pixels could be found (e.g. calcite with brucite, magnesite with organics). Fine grained minerals are not expected to combine linearly. Using a mixed endmember in linear spectral unmixing is a way to estimate how much of the mixed phase is present, but we cannot quantify how much each contributes to the mixture. Additionally, linear mixture modelling is controlled by the overall albedo of the phase in question, a parameter controlled by grain size as well as composition. We chose to implement a simple algorithm (endmember selection and linear unmixing) as a fast way to apply VSWIR microspectroscopy. It is clear that as VSWIR microimaging spectroscopy develops as a mineralogic tool, more sophisticated algorithms will be developed and implemented, including nonlinear mixture modelling (e.g. Hapke, 1981). Furthermore, there is a need for further tests with samples (e.g. siltstones and mudstones) where grains are mostly below the spatial resolution of the instrument. Instrument design and algorithms can then be optimized for rock samples of multiple grain sizes, including for performance within a few factors of the diffraction limit (~10 µm/pixel for VSWIR).

4.2 Microimaging Spectroscopy Advantages

4.2.1 Rare and Amorphous Phases

UCIS identifies spatially coherent rare phases below the detection limit of powder XRD. Distinctive 0.9-µm pyroxene absorptions (Fig 1C, 2B, 3E; Cloutis and Gaffey, 1991) are seen in samples 001, 007, and 009, though pyroxene is not detected by XRD. Petrographic analysis of thin sections confirms the presence of pyroxene. Pixels with pure pyroxene are rare; most show different degrees of partial alteration to serpentine (sharp 1.4- and 2.3-µm absorptions; Fig. 1C, 1F). This may be included in the 'amorphous' fraction of XRD results; hence with UCIS, we can get a clearer picture of the bulk mineral composition in such samples and the processes driving alteration by the ability to simultaneously detect the primary mineral and secondary product. Several clasts in conglomerate sample 001 were identified as Al-bearing serpentine or chlorite due to a small 2.25-µm absorption (caused by Al/Mg-OH vibrational overtones (Bishop et al., 2008); Fig.3B, E). EDS elemental mapping confirms that these clasts contain much more Al than other clasts.

4.2.2 Textural Interpretation

A key advantage of VSWIR microimaging spectroscopy vs. XRD is its ability to obtain mineralogical information with petrographic context, allowing process interpretation. For example, environmental history can be seen in travertine conglomerate sample 001: (1) most pyroxene is altered to serpentine in a typical ultramafic mesh-like alteration texture (green in Fig. 3B; red in Figs. 3C,D); (2) large-grained calcite veins form (dark blue, Fig. 3C,D), possibly associated with 1.4µm (OH) alteration in adjacent serpentine (light blue, Fig.3B); (3) clasts are broken up and rounded through a sediment transport process; (4) clasts are cemented in a fine-grained calcite/serpentine matrix. EDS also retains spatial relationships, but requires a high degree of sample preparation, which is expensive and time consuming (~7 hours vs ~3 mins), and is insensitive to ~isochemical alteration (elemental abundances of serpentine and pyroxene are very similar (Figs. 3C vs. D, 3G)).

5 Conclusions

VSWIR microimaging spectroscopy combined with linear spectral unmixing provides estimates of quantitative mineral abundance consistent with abundance estimates from XRD (weight %) and EDS (area %). The UCIS prototype instrument demonstrates the ability to identify all VSWIR-active phases and differentiate between carbonate minerals and other minerals like serpentines with major absorptions in the same wavelength region (~10 nm difference in band position), though further instrument and algorithm optimization is needed to deal with <0.05 albedo phases and fine-grained mixtures at sub-pixel scale. UCIS is especially well-suited to identify spatially coherent rare phases that would be missed by traditional techniques, such as XRD, and is an effective, rapid method to survey a set of samples with minimal preparation.

Acknowledgements

Thanks to A. Fraeman, C. Sanders, and B. Van Gorp for assistance with sample data acquisition and to the entire JPL UCIS team. This work was partially supported by a NASA Mars Fundamental Research Program grant (#NNX12AB42G) to B.L.E., a JPL-RTD/PDF to B.L.E. and D. Blaney, and a private grant to Caltech from the Rose Hills Foundation.

2.6 References

ASD Inc. (2013). "Near-IR Absorption Bands." Retrieved 02-07-16, from http://cdn2.hubspot.net/hub/45853/file-244381196-pdf/docs/near-ir_absorption_bands_chart.pdf?t=1454607097572.

Bibring, J.-P., et al. (2005). "Mars surface diversity as revealed by the OMEGA/Mars Express observations." Science 307(5715): 1576-1581.

Bishop, J., et al. (2008). "Reflectance and emission spectroscopy study of four groups of phyllosilicates: Smectites, kaolinite-serpentines, chlorites and micas." Clay Minerals 43(1): 35-54.

Clark, R. N. (1999). "Spectroscopy of rocks and minerals, and principles of spectroscopy." Manual of remote sensing 3: 3-58.

Cloutis, E. A. and M. J. Gaffey (1991). "Pyroxene spectroscopy revisited: Spectral-compositional correlations and relationship to geothermometry." Journal of Geophysical Research: Planets 96(E5): 22809-22826.

DeSanctis, M. C., et al. (2013). "Vesta's mineralogical composition as revealed by the visible and infrared spectrometer on Dawn." Meteoritics & Planetary Science 48(11): 2166-2184.

Ehlmann, B. L. and J. F. Mustard (2012). "An in-situ record of major environmental transitions on early Mars at Northeast Syrtis Major." Geophysical research letters 39(11).

Gaffey, S. J. (1987). "Spectral reflectance of carbonate minerals in the visible and near infrared (0.35–2.55 μm): Anhydrous carbonate minerals." Journal of Geophysical Research: Solid Earth (1978–2012) 92(B2): 1429-1440.

Green, R. O., et al. (1998). "Imaging spectroscopy and the airborne visible/infrared imaging spectrometer (AVIRIS)." Remote Sensing of Environment 65(3): 227-248.

Greenberger, R. N., et al. (2015). "Imaging spectroscopy of geological samples and outcrops: Novel insights from microns to meters." GSA Today 25(12).

Hapke, B. (1981). "Bidirectional reflectance spectroscopy: 1. Theory." Journal of Geophysical Research: Solid Earth 86(B4): 3039-3054.

Heylen, R., et al. (2011). "Fully constrained least squares spectral unmixing by simplex projection." Geoscience and Remote Sensing, IEEE Transactions on 49(11): 4112-4122.

Lauger, K. and O. Florke (1974). "Near infrared absorption spectra (4,000-9,000 cm-1) of opals and the role of ‘water’in these SiO 2· nH 2 O minerals." Fortschr. Miner 52: 17-51.

Murchie, S., et al. (2007). "Compact reconnaissance imaging spectrometer for Mars (CRISM) on Mars reconnaissance orbiter (MRO)." Journal of Geophysical Research: Planets (1991–2012) 112(E5).

Van Gorp, B., et al. (2014). "Ultra-compact imaging spectrometer for remote, in situ, and microscopic planetary mineralogy." Journal of Applied Remote Sensing 8(1): 084988-084988.

Chapter 3

UNDERSTANDING CARBONATE FORMATION, SERPENTINIZATION AND CRUST FORMATION WITH MICRO/MESO-SCALE INFRARED IMAGING SPECTROSCOPY IN A MARS ANALOGUE SYSTEM, SAMAIL OPHIOLITE, OMAN

Ellen K. Leask[1], Bethany L. Ehlmann[1, 2], Rebecca N. Greenberger[1], Patrick Pinet[3]

[1]Division of Geological & Planetary Sciences, California Institute of Technology, Pasadena, CA 91125

[2]Jet Propulsion Laboratory, California Institute of Technology, Pasadena, CA, 91109

[3]Toulouse University, Observatoire Midi-Pyrénées, Centre National de la Recherche Scientifique, UMR 5562 14 av. E. Belin, 31400 Toulouse, France

Abstract

High-resolution imaging spectroscopy maps composition remotely in spatial context, and meso- and micro-scale instruments have been proposed for planetary missions. Prior work shows the technique can detect and localize rare phases, distinguish mineral solid solutions and Fe (II)/Fe (III), and track subtle compositional changes, facilitating geologic interpretation. Here, we demonstrate the capabilities of a visible-shortwave infrared imaging spectrometer in a Mars analogue environment: the Samail Ophiolite, Oman. At outcrop and hand sample scales, we discriminate between spectrally similar carbonate and serpentine phases, as well as carbonate solid solutions. We demonstrate how mineral detection is scale-dependent, showing that a serpentinite outcrop with ~40 area% carbonate in fine veins (1mm-5cm) can look like pure serpentine from a distance, while at another location, airborne data of an outcrop of >48 area% carbonate and 18 area% serpentine looks like pure carbonate. Detections of partially altered remnant pyroxenes and localized epidote and prehnite also facilitate understanding of protolith composition, as well as the temperatures and pressures of multiple generations of faulting and alteration. Cross-cutting veins of different compositions (calcite, dolomite, magnesite, serpentine, and chlorite) trace pathways and time-ordering of alteration, indicating different generations and changing fluid composition. In natural magnesite veins, minor amounts of ferrous iron appear similar to olivine's strong 1-µm absorption, though XRD shows that no olivine is present. We differentiate between photosynthetic materials (e.g. bacterial mats vs vegetation) with the visible/near-infrared parts of the spectrum, but require the shortwave infrared to identify most organic materials and distinguish most mineral phases.

Plain Language Summary

Imaging spectroscopy from airplanes or satellites using visible to shortwave infrared wavelengths of light is a type of remote sensing that helps us to map different rock types on Earth and other planetary bodies. With this technique, each pixel in an image has a corresponding spectrum in hundreds of wavelength channels that contains absorptions that serve as fingerprints that is diagnostic of specific material compositions. Here, we demonstrate how the same technique can be used at much smaller scales, in the field and in the lab, and how it could be useful on future rover missions. We took an imaging spectrometer to the Samail Ophiolite (Oman), which has many of the same water-formed minerals as we find at some locales on Mars. We can differentiate between minerals that look similar from a distance, spot rare minerals in a scene, and use the spatial context of mineral detections to understand the time order of events affecting a rock. Sometimes they are small pieces left intact after fluids have changed

most of the rock, and sometimes they can help us understand the pressure, temperature, and/or chemical environment that the rock used to be in. These rare minerals could then be sampled or studied more intensively to better understand the whole system. We see that in a natural setting, a serpentine-rich rock can have as much as 40% carbonate and still look like serpentine from a distance—but in a different place, carbonate can mask at least 18% serpentine, and so having on-the-ground information at multiple spatial scales is helpful for interpreting remote sensing datasets. We find that some carbonates can have features that look like olivine, despite no olivine being present. The same instrument can also be used to find biological materials, and can differentiate between fresh and dried organic material, as well as vegetation and bacterial mats. These capabilities may be of interest to field biologists.

1 Introduction

Reflectance imaging spectroscopy in the visible-shortwave infrared (VSWIR) wavelength range is a powerful remote sensing technique that has allowed us to map compositional changes on a variety of planetary bodies, including Earth, Mars, Ceres, Pluto, and many others (Swayze et al., 1992; Bibring et al., 2005; Murchie et al., 2009; DeSanctis et al., 2015; Stern et al., 2015). Imaging spectrometers are also now available for field use on Earth on unpiloted aerial vehicles (UAVs), tripod-based imaging systems, and mounted racks for laboratory scanning of samples. Planetary instruments have also been matured and have been proposed for landed missions at meso- and micro-scales (e.g., Van Gorp et al., 2014; Blaney et al., 2016; Ehlmann et al., 2016; Green et al., 2015).

The mineralogy with spatial context would be valuable for a landed mission. A handful of sites on Mars with both carbonate and serpentine have been identified (Ehlmann et al., 2010; Michalski et al., 2010), including those in the vicinity of the Mars-2020 landing site at Jezero crater with its potential extended mission toward NE Syrtis. These carbonate-serpentine sites are of particular interest, because such carbonate/serpentine systems on Earth host chemosynthetic life, producing abiotic hydrogen and methane gases (e.g. Schulte et al., 2006; Rempfert et al., 2017). Furthermore, serpentinization of ultramafic rocks can lock away carbon dioxide in carbonate minerals, removing it from the atmospheric/hydrologic reservoirs (Kelemen and Matter, 2008). On Mars, this has been proposed as a possible mechanism for its evolution from a robust surface hydrologic system (as evidenced by extensive fluvial systems, e.g. Pieri, 1980; Carr, 1995; Hynek et al., 2011) to the arid planet we see today (e.g. Pollack et al., 1987; Edwards and Ehlmann, 2015).

Here, we perform meso- and micro-scale field- and lab-based imaging spectroscopy of a Mars analogue site (Samail Ophiolite, Oman), to explore the spectral diversity in context within natural carbonate/serpentine settings, and demonstrate the capabilities of such an instrument for targeting, sampling, and interpreting biological and geological environments. The large Samail ophiolite exposes serpentinized and carbonated ultramafic rocks at the Earth's surface in a desert environment, with limited surface vegetation to obscure the underlying lithology, making it a Mars analogue environment suited to investigation with imaging spectroscopy. We integrate data from 3 scales (airborne survey (Roy et al., 2009), outcrop imaging, and hand samples) to demonstrate how the micro- and meso-scale imaging can help us better interpret the larger scale mapping data by identifying endmember minerals, remnant protolith, textural relationships between minerals indicative of process and/or timing, as well as the quantification of minerals at different scales.

2 Methods

2.1 Field site geologic setting

The Samail Ophiolite (Oman) is one of the largest and best preserved ophiolites on Earth. It is a fragment of Cretaceous oceanic lithosphere (~100 Ma; Tilton et al., 1981) that was obducted ~70 Ma (Searle and Cox, 1999). The ophiolite ranges from mafic to ultramafic in composition, with sections identified as harzburgites, dunites, wehrlites, and gabbros (e.g. Amri et al. 1996; Roy et al., 2009). Ultramafic portions of the ophiolite have been heavily serpentinized (e.g. Barnes et al., 1978); these serpentinized zones are typically found with associated carbonate, either in veins, or in travertine deposits at the surface. These springs are often hyperalkaline, with pH of 10-12 (e.g. Neal and Stanger, 1984). Here, we investigate a range of sites within the ophiolite: two serpentinite sites with extensive veining (Al Qaryatayn and Wadi Dimah), one of which has remnant orthopyroxene and the other clinopyroxene, as well as a listvenite site (complete carbonation of the ultramafic protolith, discussed below), and a travertine/serpentine site. Three of these sites are within HyMap coverage (Fig. 2).

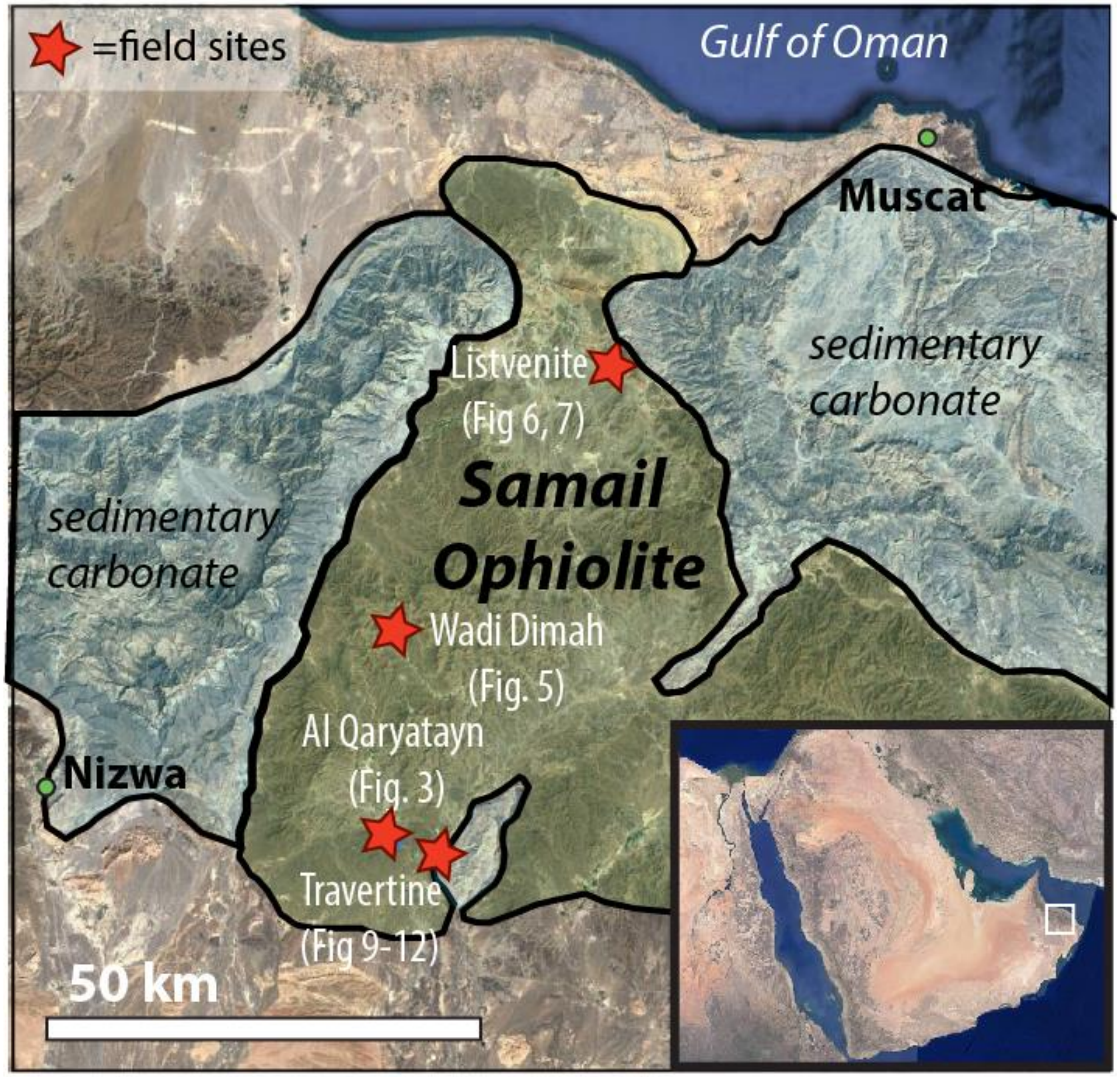

Fig. 3-1. Field locations within Samail Ophiolite, Oman. The Al Qaryatayn site (Fig 3) is a typical serpentinite with carbonate veins at many scales, while the Wadi Dimah site (Fig 5) contains a mixture of altered mafic and ultramafic rocks. The listvenite site (Fig 6, 7) at the northern edge of the ophiolite reflects complete carbonation of the rock, while at the travertine site (Figs, 9-12) at the southern edge of the ophiolite; hyperalkaline springs are actively precipitating carbonate on top of veined serpentinite.

2.2 Headwall Imaging Spectrometer

The pushbroom imaging spectrometer used for this work was custom built by Headwall Photonics, Inc. for Caltech, and combines data from two sensors to cover a nominal spectral range from ~0.4-2.6 μm, with a signal-to-noise ratio with laboratory illumination above 100 in all channels. The VNIR sensor (visible-near infrared) covers 0.4-1 μm with 5 nm spectral resolution, while the SWIR sensor (shortwave-infrared) covers the ~1-2.6-µm region with 6 nm spectral resolution (see Greenberger et al., 2016 for further detail). At a standoff of 20m, the instantaneous field of view (IFOV) is 0.6 cm in VNIR and 1.7 cm in SWIR. The spectrometer is mounted on a rotating stage on a tripod in the field, or above a linear sample stage in the laboratory, and takes ~30 seconds to ~3 minutes to acquire a single image. The VNIR and SWIR arrays gather data simultaneously. Data are calibrated to Spectralon panels of known reflectance that are placed in the scene. Panels of 5%, 20%, and 99% were utilized in our fieldwork. (Note that a planetary mission would use an onboard calibration target on the craft.) For this work, we downsample the spatial resolution of the VNIR sensor to match the lower spatial resolution SWIR array, and co-register the two images, matching the VNIR to the SWIR spectrum at 0.969 µm. Hand samples were cut to provide a flat surface for imaging in the laboratory (see Leask et al., 2016), but no other preparation was involved.

2.2.1 Field calibration & atmospheric caveats

Field data were calibrated to reflectance by dark current subtraction and a standard flat-field correction (measured in an integrating sphere) to account for non-uniform instrument response. We used an empirical method for atmospheric correction: first dark-object subtraction (Chavez et al., 1988) to remove the additive haze component, followed by multiplicative correction scaled to the 99% reflectance Spectralon panel in each scene. Other atmospheric correction algorithms (e.g. FLAASH©; Cooley et al., 2002), designed for airborne and orbital datasets, did not markedly differ from the basic empirical approach. In our data, the atmospheric path length in a single image could range from ~1m to >500m (mountains in the distance), with many of the atmospheric bands completely saturated, making modelling difficult. In figures below, atmospheric oxygen and water absorptions are made partially transparent (~0.76 µm, ~1.15 µm, and broad bands at ~1.4 and ~1.9 µm). Furthermore, the longest wavelengths of the SWIR were not always reliable in the field dataset, likely due to decreasing detector sensitivity at long wavelength and the low signal at this part of the spectral range due to absorptions by atmospheric water beyond 2.5 µm. Data presented here are therefore only to 2.45 or 2.50 µm, rather than the nominal 2.6 µm limit of the sensor.

2.2.2 Spectral parameters

A series of parameters were developed to discriminate between minerals based on their major absorptions, exact band centres of those absorptions, slopes/ratios where only part of the absorption was covered, and combinations thereof (after Pelkey et al.2007; Viviano-Beck et al., 2014; Greenberger et al., 2016). These features reflect electronic transitions or molecular vibrations that are characteristic of specific minerals, atmospheric gases, water, or biological materials. We mask out scene locations with an averaged SWIR reflectance <0.05 (generally shadowed regions), as well as clouds and sky. In figures where we focus on mineralogy, we also mask out biological materials (primarily small bushes). Table 1 lists relevant minerals and their chemical formulae. Specific features used to parametrize each additional mineral are discussed with the appropriate sites below. Mineral maps shown in figures below were developed using combinations of parameters (listed in Table 2). For a given mineral, we combine parameters capturing the diagnostic absorptions not masked by atmospheric bands (for example, serpentine has a 2.12-µm absorption in addition to a deep 2.32-µm absorption. In cases where our parameters may capture spectrally similar minerals, we also explicitly exclude pixels with additional absorptions—for instance, epidote and chlorite both have absorptions at 2.25 and 2.34 µm, but epidote has an additional diagnostic absorption at 1.56 µm. Carbonates are identified based on the similar depth of 2.3- and 2.5-µm absorptions (partially characterized by a “peak” at ~2.4 µm, given the poor data quality at 2.5 µm), and the exact position of these absorptions to distinguish between carbonate minerals. Serpentines are differentiated from carbonates by their 2.12-µm absorption and asymmetry in the large 2.32-µm and shallow 2.5-µm absorptions.

	Formulae	**Diagnostic Absorptions**	**(References)**
Carbonates			
Calcite	$CaCO_3$	(2.17), 2.33-2.34, 2.53-2.54	Gaffey, 1985; Gaffey, 1986
Dolomite	$CaMg(CO_3)_2$	2.315-2.325, 2.51-2.52	Gaffey, 1985; Gaffey, 1986
Magnesite	$MgCO_3$	2.30-2.31, 2.50	Gaffey, 1985
Siderite	$Fe^{2+}CO_3$	1.1, 2.32-2.33, 2.53	Gaffey, 1985
Igneous minerals			
Olivine (forsterite, fayalite)	$(Mg, Fe^{2+})SiO_4$	~1.05	Sunshine & Pieters, 1998
Orthopyroxene (enstatite, ferrosilite)	$(Mg, Fe^{2+})_2Si_2O_6$	~0.9, ~1.9	Cloutis & Gaffey, 1991
Clinopyroxene (e.g. augite, diopside)	$\sim Ca(Fe^{2+}, Mg)\ Si_2O_6$	~1.05, ~2.3	Cloutis & Gaffey, 1991
Plagioclase (e.g. anorthite)	$CaAl_2Si_2O_8$	(no strong features)	
Secondary silicate minerals			
Serpentine	$(Fe^{2+}, Mg)_3Si_2O_5(OH)_4$	2.12, 2.32-2.34, 2.5	Bishop et al., 2008
Chlorite (clinochlore, chamosite)	$(Mg, Fe^{2+})_5Al(AlSi_3O_{10})(OH)_8$	2.25, 2.33-2.35	Bishop et al., 2008
Prehnite	$Ca_2Al_2Si_3O_{10}(OH)_2$	1.48, 2.23+2.29, 2.34	
Epidote	$\{Ca_2\}\{Al_2Fe^{3+}\}Si_2O_7(SiO_4)O(OH)$	1.56, 2.25, 2.34	
Mica (Cr-muscovite/ fuchsite)	$K(Al,Cr)_3Si_3O_{10}(OH)_2$	1.4, 2.20-2.25, 2.30-2.35	Bishop et al., 2008 (*other micas)
Kaolinite	$Al_2(Si_2O_5)(OH)_4$	2.17+2.21	Bishop et al., 2008
Quartz	SiO_2	(none)	

Table 3-1. Relevant minerals and their chemical formulae

Parameter	Formula	Notes
R1000	R1000	Reflectance/dark
R1070/R1650	R1070/R1650	Water
R1500	R1500	Reflectance/dark
BD1130_atmos	1-R1.130/Continuum(1.065 to 1.170)	Atmosphere
BD1200_org	1-R1.200/Continuum(1.090 to 1.245)	Organics
BD1455_broad_water	1-R1.455/Continuum(1.405 to 1.550)	OH
R1457/R1481	R1457/R1481	Prehnite
BD1475_prehnite	1-R1.475/Continuum(1.455 to 1.510)	Prehnite OH
R1500/R1000	R1500/R1000	Fe-slope (e.g. pyroxene, olivine, serpentine)
R1500/R2400	R1500/R2400	Pyroxene shape (also has many false positives)
BD1565_epidote	1-R1.565/Continuum(1.490 to 1.655)	Epidote
R1750/R2120	R1750/R2120	Dry vegetation
BD2120	1-R2.116/Continuum(2.065 to 2.185)	Boxy 2.1-ish absorption in serpentine
BD2120_2	1-R2.110/Continuum(2.080 to 2.160)	Boxy 2.1-ish absorption in serpentine
R2165/R2110	R2165/R2110	Serpentine, organics
BD2180_kln	1-R2.18/Continuum(2.1 to 2.24)	Part of kaolinite doublet
BD2200_broad	1-R2.20/Continuum(2.15 to 2.30)	Si-OH, (illite/muscovite)
BD2200kln	1-R2.21/Continuum(2.1 to 2.24)	Part of kaolinite doublet
Kaolinite_slope	(R2.232+r2.238)/(R2.202+R2.208)	Positive slope at long end of kaolinite doublet to distinguish from Si-OH or other overlapping features
BD2230	1-R2.230/Continuum(2.15 to 2.27)	Si-OH; prehnite
BD2250	1-R2.25/Continuum(2.18 to 2.265)	AlFe-OH or Si-OH; chlorite
BD2255	1-R2.255/Continuum(2.10 to 2.43)	Epidote
BD2300_2	1-R2.302/Continuum(2.248 to 2.368)	Magnesite
BD2300_carb	1-R2.30/Continuum(2.16 to 2.34)	2.3 micron feature in Mg-carbonates
BD2320	1-R2.318/Continuum(2.120 to 2.37)	Dolomite, serpentine
BD2320_2	1-R2.322/Continuum(2.29 to 2.358)	Dolomite, serpentine
BD2320_narrow	1-R2.32/Continuum(2.28 to 2.35)	Dolomite (narrower)
BD2330	1-R2.33/Continuum(2.180 to 2.39)	Calcite
BD2330_2	1-R2.330/Continuum(2.116 to 2.38)	Calcite
BD2330_narrow	1-R2.33/Continuum(2.28 to 2.35)	Calcite
BD2340	1-R2.34/Continuum(2.18 to 2.39)	C-O combination in carbonates; wavelengths optimized for calcite; prehnite; epidote
BD2350	1-R2.350/Continuum(2.160 to 2.385)	Chlorite
BD2360	1-R2.358/Continuum(2.29 to 2.40)	Illite/muscovite
BD2390	1-R2.386/Continuum(2.35 to 2.42)	Talc
D2500	1-R2.47/R2.40	Drop in carbonates at 2.5
NDVI	(R0.85-R0.65)/(R0.85+R0.65)	Chlorophyll

Table 3-2. Spectral parameters, formulae, and reason for parameter

2.2.3 Carbonate quantification estimates

The best solutions for abundance estimation are via linear unmixing (e.g., Mustard & Pieters, 1989; Lapotre et al., 2017), but for 1-15+ GB scenes, deployment of such algorithms is computationally prohibitive. We initially tried a linear unmixing code based on Heylen et al. (2011), but found that it did not reliably discriminate well between serpentine and different carbonates. Primarily, best-fit solutions were dictated to match the brightnesses of given endmembers, and the brightness of the region of interest in the field could vary greatly due to changing viewing angles across an outcrop and shadows. Consequently, we use the simple areal percentage (number of pixels) of carbonate, as captured by parameters in discrete veins (see discussion of spatial scale of mixing below).

2.3 HyMap data

Airborne hyperspectral data for this region were acquired in December 2002, using a HyMap instrument (Pinet et al., 2003; Roy et al., 2009; see Fig. 2). HyMap collects data between 0.45-2.48 µm, with a spectral resolution of 15-20 nm (Cocks et al., 1998); data have been atmospherically corrected with a radiative transfer model (Gao et al., 1999), and geometrically corrected using a digital elevation model (for further detail, see Clenet et al., 2013). Field locations in this study were chosen for particularly strong carbonate and serpentine spectral signatures in the HyMap dataset.

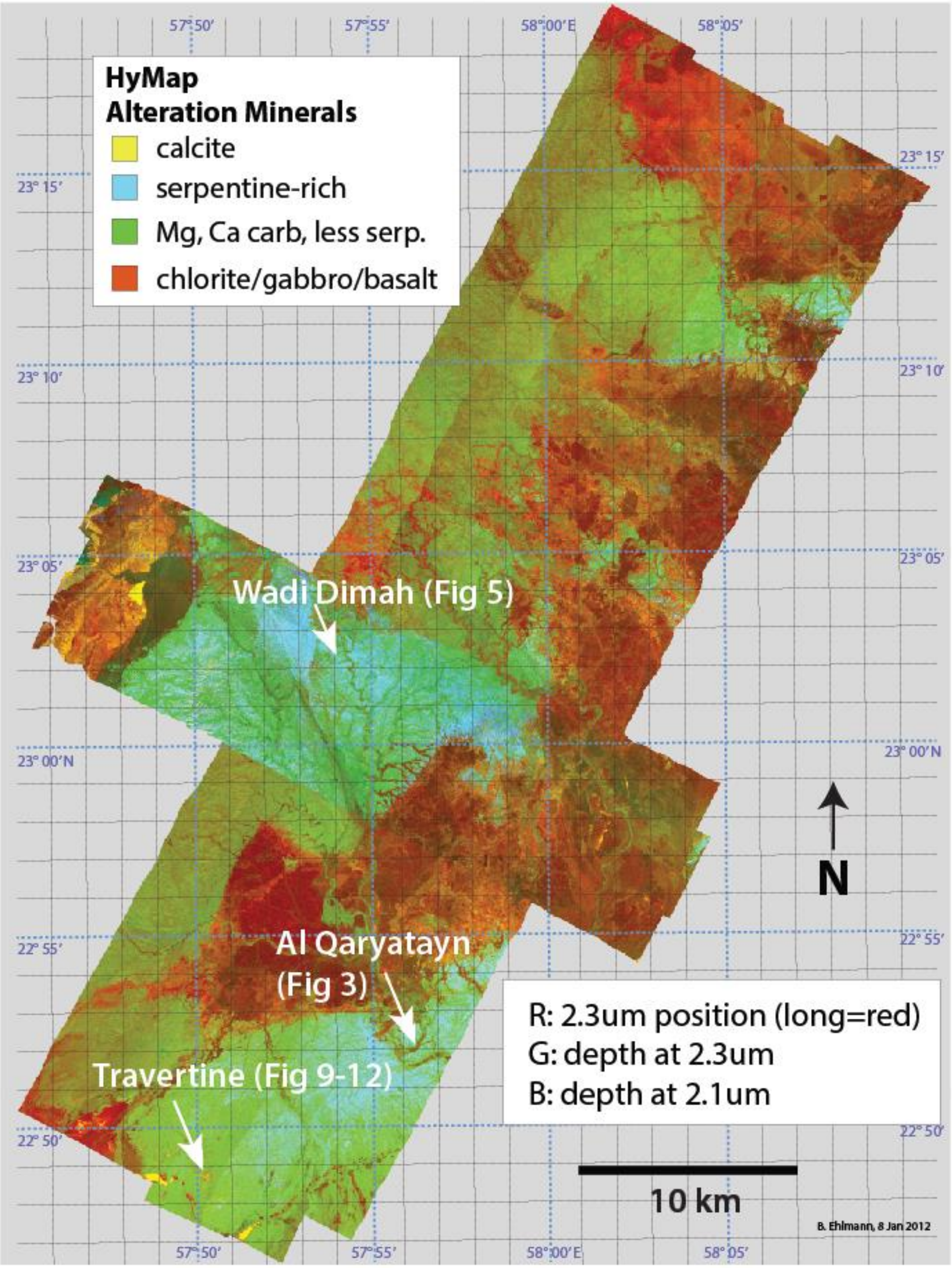

Fig 3-2. HyMap stretch highlighting compositional variability (after Ehlmann, 2012). Carbonate springs show up as bright yellow, while the strongest serpentine signatures show up as blue. Reds are consistent with chlorite/gabbro/basalt compositions.

2.4 X-ray diffraction

X-ray diffraction (XRD) patterns were measured on a PANalytical X'Pert Pro instrument at the California Institute of Technology, which has a Cu K-alpha radiation source. Here, we analyzed a 2ϴ range from 20-60°, using a current of 40 mA, voltage of 45 kV, and time step of 80s.

2.5 Spectral libraries

VSWIR reference spectra shown are from the United States Geological Survey's Spectral Library (version 7; Kokaly et al., 2017) or from Brown University's Reflectance Experiment Laboratory (RELAB) database, resampled to the same spectral wavelengths as our dataset. Reference XRD patterns were downloaded from RRUFF (Bindi et al., 2015).

3 Results from Field Imaging Spectroscopy

From all the sites imaged in the field, we focus on presenting four sites that encompass four different geologic settings within the ophiolite and thus the types of geological and biological investigations enabled by imaging spectroscopy (Fig. 1). The Al Qaryatayn site is a typical ultramafic serpentinite site, with carbonate veins and many scales (Fig. 3), while Wadi Dimah contains both mafic and ultramafic altered rocks (Fig. 5). The listvenite site (Fig. 6, E), at the northern edge of the ophiolite, is heavily metasomatized as part of the basal sequence of the ophiolite (e.g. Falk and Kelemen, 2015). At the opposite edge of the ophiolite, we imaged a hyperalkaline travertine spring (Fig. 9-12), where fresh calcite is precipitating on top of veined serpentinite.

3.1 Al Qaryatayn (22.870 N, 57.939 E; Fig. 3)

This site is an example of a heavily veined serpentinite, in an outcrop exposed above a dry valley. At a distance of ~30 m, the spectral signatures are dominated by serpentine (Fig. 3a, b), with a weak 2.12-µm absorption, strong 2.33-µm absorption, and downturn towards a smaller 2.5-µm absorption (these absorptions are due to Mg-OH bonds; Bishop et al., 2008). However, when we image the same outcrop at a distance of ~2.5 m (Fig. 3c, d), clear carbonate veins ~1-5cm thick are distinguished by their bright white colour, presence of a 2.3-µm absorption, and lack of 2.12-µm serpentine absorption. Unfortunately, the data quality of the 2.4-2.6 µm wavelength range here is poor, so we cannot measure the expected band centre at ~2.5 µm. Instead, we look at the width and position of the "peak" between the 2.3- and 2.5-µm absorptions, and the slope between 2.38-2.45 µm. Here, we see the band centres of the carbonate absorptions shift from ~2.315-2.320 µm (consistent with dolomite; Gaffey, 1986) to ~2.330-2.340 µm, consistent with calcite. At this scale, a minimum of ~22% (58,539/ 266,817) of the pixels in the image are classified as carbonate veins. While these veins appear to be dominantly carbonate, it is possible that they may also be mixtures with a small amount of serpentine within the veins.

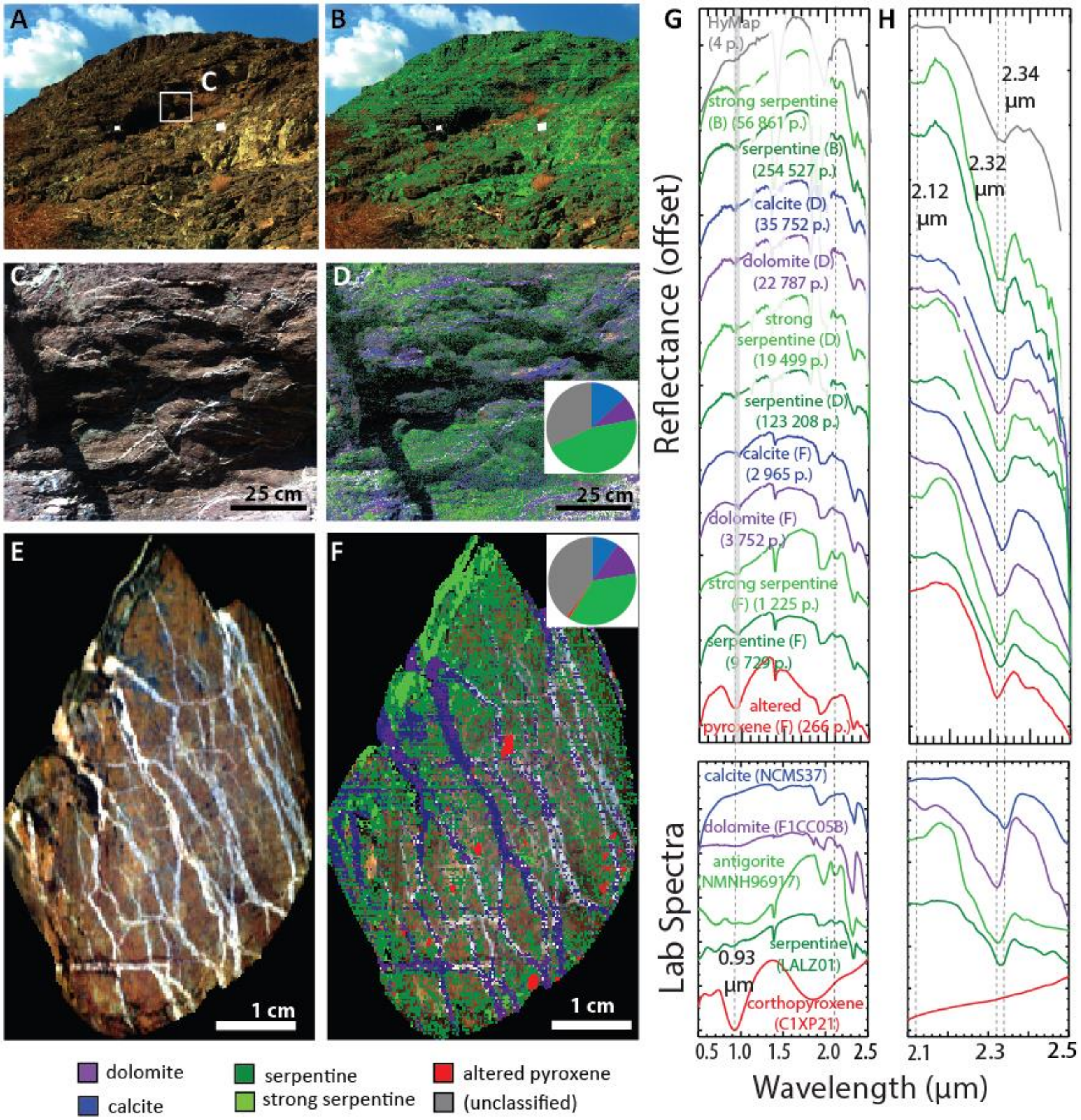

Fig 3-3. Al Qaryatayn field site, serpentinite with carbonate veins at multiple scales (22.870 N, 57.939 E). (a, b) Outcrop overview taken from a distance of ~ 20-40 m. White squares are 30x 30 cm Spectralon© panels; reddish brown blobs excluded from the parameter map are bushes. Green colours in (b) map pixels classified as serpentine. (c, d) Close-up image of the veined serpentinite. At this scale, veins are mapped as a mixture of calcite and dolomite, and account for ~ 22% of the pixels in the scene. (e, f) Hand sample of typical matrix from this site shows further mm-scale carbonate veining (again, both calcite and dolomite, accounting for a further ~ 22% of the rock), a cross-cutting coarse serpentine vein, and small, partially altered, remnant orthopyroxenes. (g, h) Spectra corresponding to the parameter maps in panels (b, d, f). Grey line at 0.97 µm shows the detector join, while atmospheric bands are transparent in field data. Detail from the key 2.1-2.5 µm region is shown in (h).

In the laboratory, we cut open a typical example of the matrix from this site, and imaged it at ~250 µm/pixel (Fig. 3e, f) scale. Fine, mm-scale carbonate veins are readily visible, accounting for at least a further ~22 area% (6,717/30,010) of the rock. If we assume this example is typical of the whole outcrop, this means that an outcrop that appears to be entirely serpentine from a distance actually contains ~40% carbonate veins (22% plus a further 22% of the remaining ~78% matrix) at multiple scales. In Fig. 4, we use serpentine and calcite spectral endmembers from this sample to investigate linear mixtures. Here, we note that the diagnostic 2.12-µm serpentine absorption disappears at ~70% calcite/30% serpentine; this is also where the 2.5-µm carbonate absorption is defined.

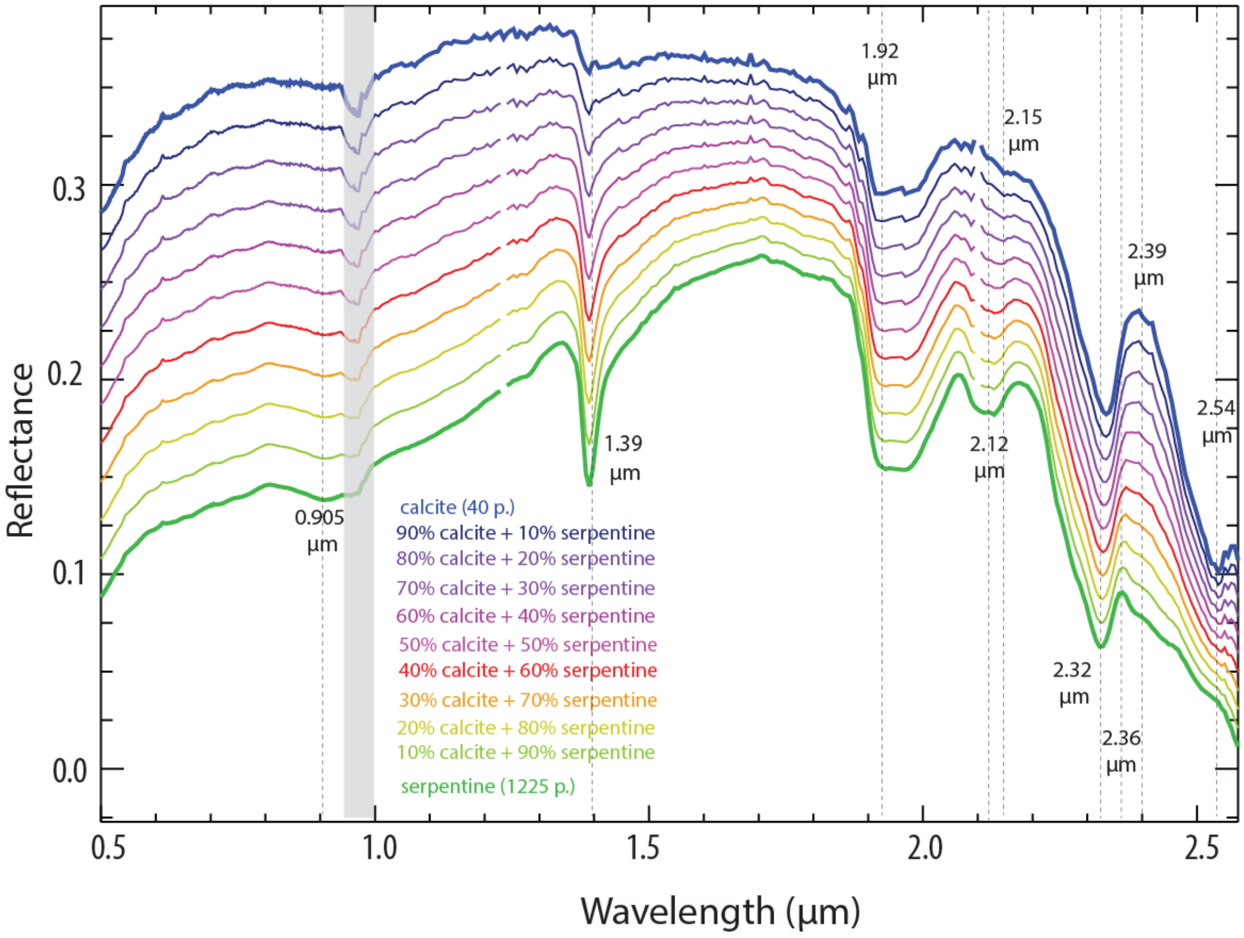

Fig 3-4. Linear mixture between serpentine and calcite (spectra from Al Qaryatayn hand sample imaged in the laboratory (Fig 3-3 e, f)). Diagnostic serpentine absorption at 2.12 µm disappears at about 70% calcite/30% serpentine; here, the longer-wavelength uptick defining the 2.54 µm calcite absorption also becomes clear. The "peak" at ~ 2.4 µm (between 2.3 and 2.5 µm absorptions) takes on a broader, carbonate-like shape at ~ 50% serpentine/calcite.

We also observe several interesting petrographic textures at the lab scale, including small zones of partially altered orthopyroxene. Pyroxenes have broad electronic absorptions (due to Fe^{2+}) at ~1 and 2 µm (e.g. Hunt and Salisbury, 1970). The exact position of these absorptions changes with pyroxene composition, with orthopyroxene bands usually centred ~0.9 and 1.9 µm and clinopyroxenes centred ~1.05 and 2.35 µm (e.g. Cloutis and Gaffey, 1991).

A large vein of coarse crystalline serpentine cross-cuts several smaller carbonate veins at the top left edge of the sample (Fig. 3f), indicating that the rock underwent a later stage of veining after the initial formation of carbonate veins, and that the fluids in this later stage were significantly more enriched in silica (or perhaps contained less CO_2). Furthermore, we see distinct zones of calcite and dolomite within the same carbonate veins. We interpret this to mean that the fluid composition changed over the course of carbonate vein formation. Dolomite tends to be found near the centre of larger calcite veins, where we would expect the last fluid to flow.

3.2 Wadi Dimah (23.044 N, 57.900 E; Fig. 5)

This site is a veined serpentinite outcrop at the bottom of a dry valley (Fig. 5). Nearby, we see a small exposure of layered pyroxene/plagioclase cumulates, indicating a more calcium- and aluminum-rich protolith in this region. Averaged, the spectrum of the whole outcrop looks like serpentine, but with the imaging spectrometer, we can track veins, fractures, and alteration of a variety of compositions. Whitish veins in Fig. 5a are mostly dolomite (purple in Fig. 5b), but may sometimes also contain serpentine, or be surrounded by strong serpentine signals (green in Fig. 5b, d). Weak serpentine-related absorptions are present throughout the outcrop, with the strongest associated with veins. Serpentine absorptions of intermediate strength are found in the clasts surrounding the outcrop, rather than in the outcrop itself.

We also see a number of minerals present over small spatial extents at this site, including clinopyroxene, chlorite, epidote, and prehnite (see Table 1 for mineral formulae). Clinopyroxene is identified by its absorption at ~1.03 µm and broad 2-µm absorption, and is present in small areas within the outcrop, and in a number of clasts. As in the Al Qaryatayn site (Fig. 3), being able to find and sample/measure small amounts of unaltered rock is a very useful capability to understand the history of alteration, and perhaps probe deeper crustal conditions with igneous minerals. In Fig. 5b, d, we see chlorite in veins and along fracture planes, identified by the presence of a 2.25-µm Al/Fe^{3+} (or Mg)-OH combination band, in addition to a stronger Fe^{2+}-OH combination band at 2.35 µm (Bishop et al., 2008); a 1.39-µm OH band is hidden by atmospheric water. Epidote is also concentrated in specific areas, but not confined to veins or fracture planes—however, it is at a nexus of intense serpentine, dolomite, and chlorite veins, and so may reflect enhanced alteration in that location. Epidote is spectrally similar to chlorite, with a minor absorption at 2.25 µm and larger absorption at ~2.34 µm, but has an additional diagnostic feature at 1.56

µm. Prehnite is found in clasts (Fig. 5d); where in the rock, it closely follows banded plagioclase/pyroxene layers, indicating that the alteration was very local (note that banded pyroxene/plagioclase layers are not continuous, but are exposed in discontinuous patches in the outcrop). Prehnite is identified by its sharp 1.48 µm absorption, paired small absorptions at 2.23 and 2.29 µm, and larger 2.34-µm absorption.

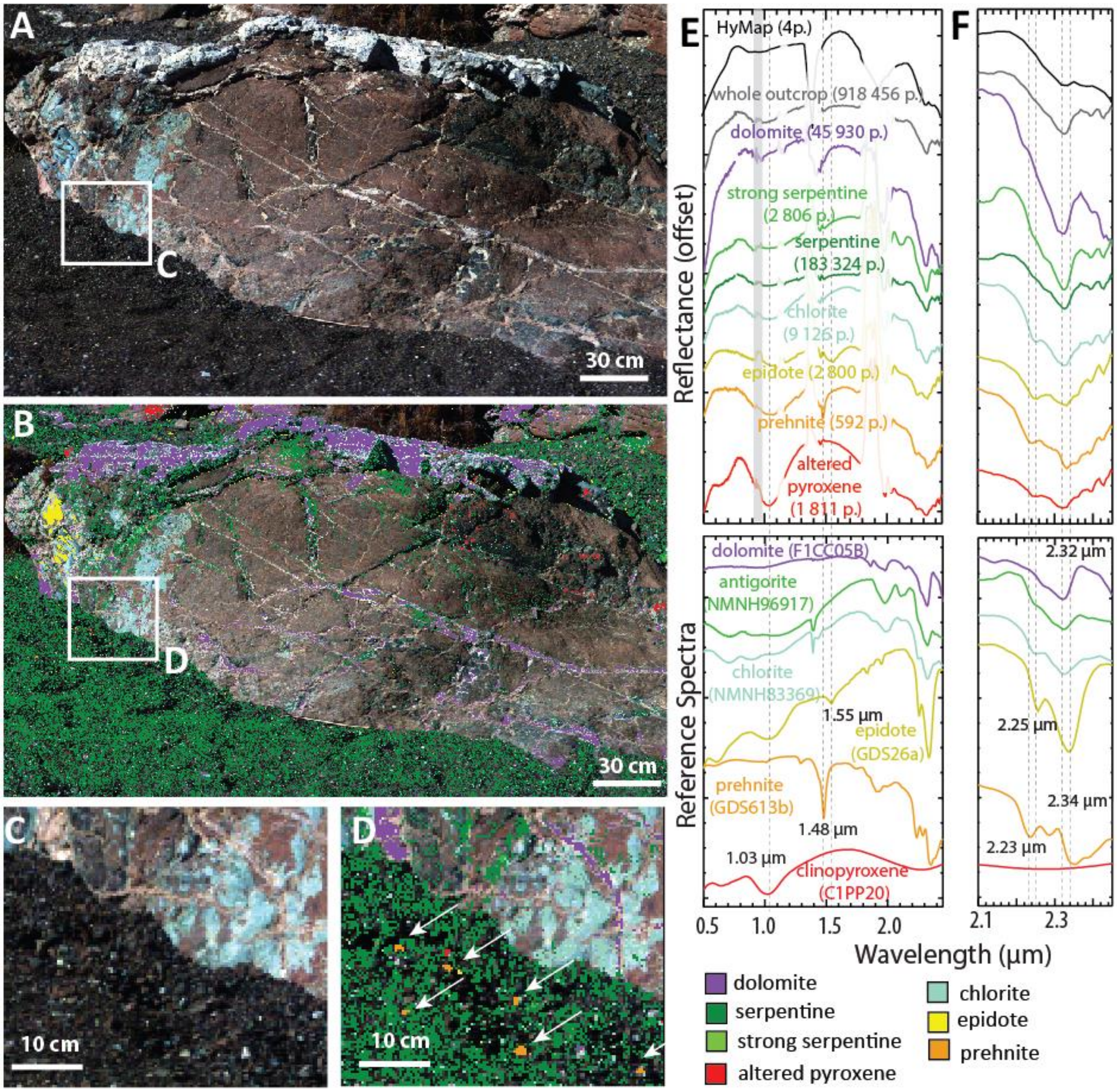

Fig 3-5. Wadi Dimah field site, showing typical carbonate/serpentine mineralization in addition to a number of low-grade metamorphic, Al-enriched minerals (23.044 N, 57.900 E). (a, b) Outcrop of serpentinite with dolomite (purple) and serpentine (green) veins. The gravel around the outcrop displays a stronger serpentine signal than the outcrop itself (grey in E, F). Chlorite (aquamarine) is present in a fracture plane and some veins, while epidote (yellow) appears to be in the rock matrix, between several large veins of different compositions. Pyroxene (red) is present in clasts and in small amounts in the matrix of the serpentinite, as remnants of the protolith. Prehnite (orange) is also present in small clasts (white arrows, D). (E, F) Spectra corresponding to coloured regions in B, D. Grey line at 0.97 µm shows the detector join, while atmospheric bands are transparent in field data. Detail from the key 2.1-2.45 µm region is shown in (h).

Chlorite, epidote, and prehnite are all minerals indicative of low grade metamorphism (prehnite-pumpellyite facies), and associated with moderate temperatures ~250-400°C and pressures 2-8 kbar (Liou et al., 1983; Frey and Robinson, 2009). Prehnite in particular is only stable within that temperature range, and so is a very useful indicator mineral for past pressure/temperature history. Furthermore, ratios of ferric iron/aluminum in epidote and prehnite vary with formation temperature, and so may be used to pin down a narrow temperature range for alteration fluids (Liou et al., 1983).

In addition to the metamorphic history, these minerals tell us about the composition of the protolith—chlorite, prehnite, and epidote are all aluminum-bearing, with prehnite and epidote requiring calcium as well. These will only form where these elements are present, telling us that this was not initially an ultramafic rock, but likely was more mafic (and therefore aluminous) in composition.

3.3 Listvenite (23.369 N, 58.185 E; Fig. 6, 7)

The listvenite field site is an exposed, smoothed outcrop within a dry wash (Fig. 6), immediately downstream from higher-grade metamorphic sole of the ophiolite. This image was taken at a distance of ~2m. Listvenite (with many alternative spellings) is the end result of carbonation of a peridotite, where all Mg resides in carbonate minerals (magnesite +/- dolomite) and Si is quartz (+/- Cr-muscovite, commonly called fuchsite) (Halls & Zhao, 1995; Falk and Kelemen, 2015). On Earth, magnesite is rarely the dominant carbonate mineral, with the exception of these altered ultramafic environments. On Mars, where we see carbonate in orbital data (~20m/pixel (Murchie et al., 2007); Ehlmann et al., 2008; Niles et al., 2013 and others), the band centres are often consistent with magnesite instead of the longer wavelengths of dolomite, calcite, and siderite. Of the sites we visited with an imaging spectrometer, this was the only site where the dominant mineral signature (averaged over the whole rock; Fig. 6g, h) was magnesite, identified by absorptions centred at 2.305 and 2.50 µm (Gaffey, 1985). Here, we see predominantly magnesite throughout the rock matrix, with veins of dolomite, and veins of magnesite with a very strong ~1-µm absorption (Fig. 6c, d). Despite the wide, deep 1-µm absorption, common in minerals with ferrous iron, the 2.3- and 2.5-µm band positions are consistent with magnesite rather than siderite (Fig. 6g, h). Gaffey et al. (1986) noted that even small amounts of iron (0.5-3.5 wt% FeO) may cause large 1-µm features in carbonates.

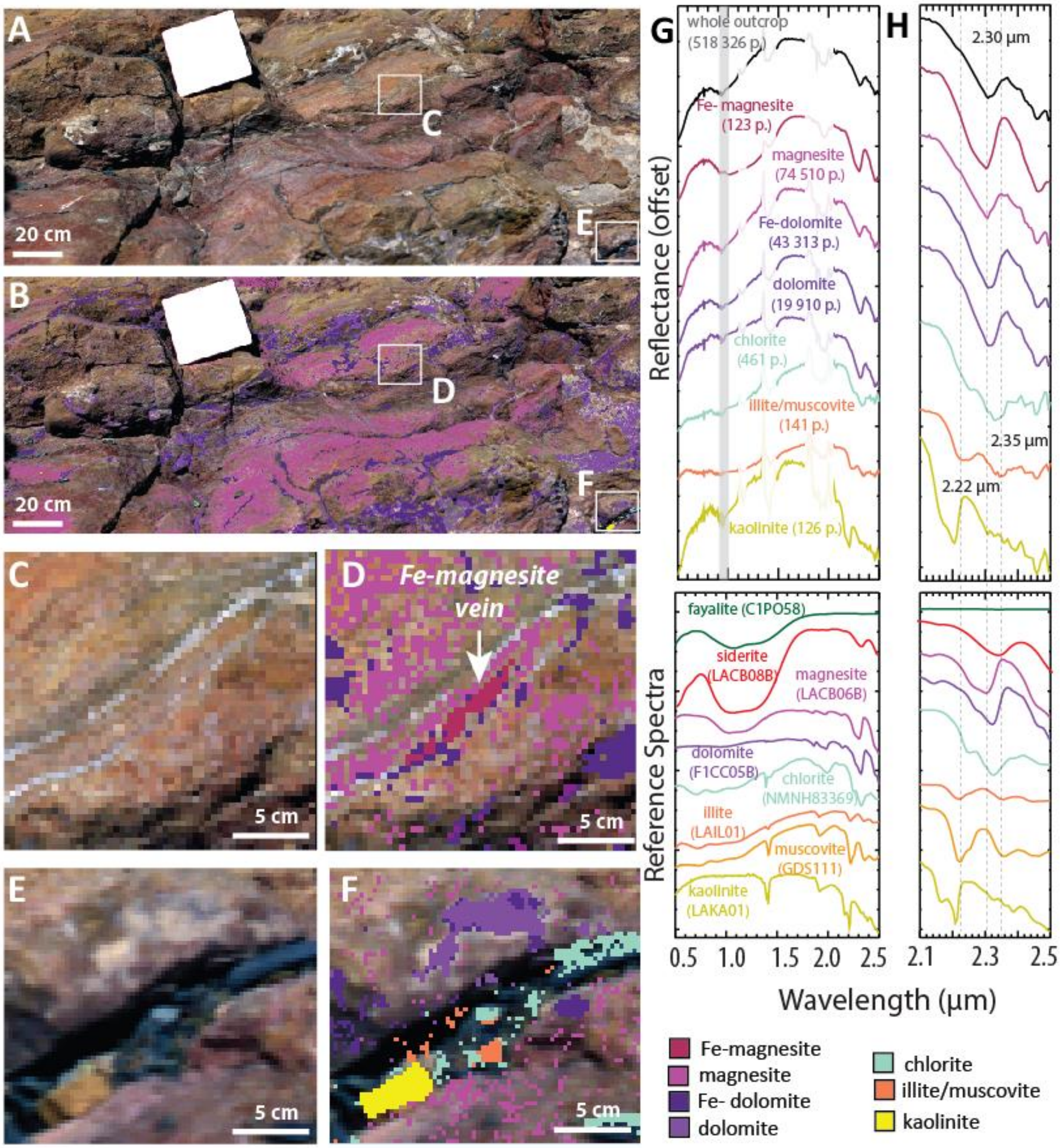

Fig 3-6 (a) Listvenite field site, located within a dry wash (23.369 N, 58.185 E). Outcrop is veined, reddish, and smooth; whitish parts are later caliche-type cement. White square is a Spectralon© panel, 30x 30 cm. (b) Most of this outcrop appears to be magnesite (magenta) , with veins of magnesite with a large 1 µm absorption (likely dues to trace amounts of ferrous iron; see panels C, D for detail), and some dolomite veins (dark purple), which have a minor 1 µm feature. Caliche deposits (light purple) are also dolomite, and lack any trace of the 1 µm absorption. (c, d) Close-up of a vein of magnesite with deep, olivine-like 1 µm absorption feature. Vein is between 2 white parallel veins, likely quartz (which is spectrally neutral in this range). (E, F) Close-up of clasts in bottom right of image. Clasts are identified by their absorptions between 2.1-2.5 µm; they are kaolinite (yellow), mica (illite or muscovite; coral), and chlorite (aquamarine).

At smaller spatial scales (Fig. 6e, f), we see small, discrete clasts of kaolinite, chlorite, and muscovite. Kaolinite is identified by its characteristic asymmetric 2.17-2.21 µm absorption (Al-Al-OH combination band; Bishop et al., 2008), while muscovite has similarly-sized absorptions at 2.22 and 2.35 µm. Spectrally, we cannot readily differentiate between muscovite and illite (a clay-like mica); however, these minerals have very different habits and luster, so are readily differentiated in the field or with a microimager. These more aluminous clasts have been transported downstream from the fault zone, and allow us to explore the mineral diversity of the watershed without having to access it directly—analogous to the Jezero crater landing site for Mars 2020 with transported sedimentary material within a basin. A VSWIR imaging spectrometer can readily detect rare clasts amongst all the cobbles, allowing targeted sampling of the available mineral diversity.

3.3.1 Listvenite hand sample (Fig. 7)

A cobble from this site (Fig. 7) shows the textures of magnesite with intergrown, light-green muscovite, an opaque phase, and a vein of magnesite with a very strong 1-µm absorption, similar to olivine (e.g. Sunshine and Pieters, 1998; see below). Given previous work in the area, we interpret the light-green muscovite as Cr-muscovite (fuchsite), while the opaques are likely relict Cr-spinel or Fe-oxides (Falk & Kelemen, 2015). We were not able to find any spectral library matches for fuchsite, which has a distinctive 0.62 µm absorption which contributes to its colour. However, it has the 1.41- and 2.22-µm absorptions expected, and a small 2.35-µm absorption.

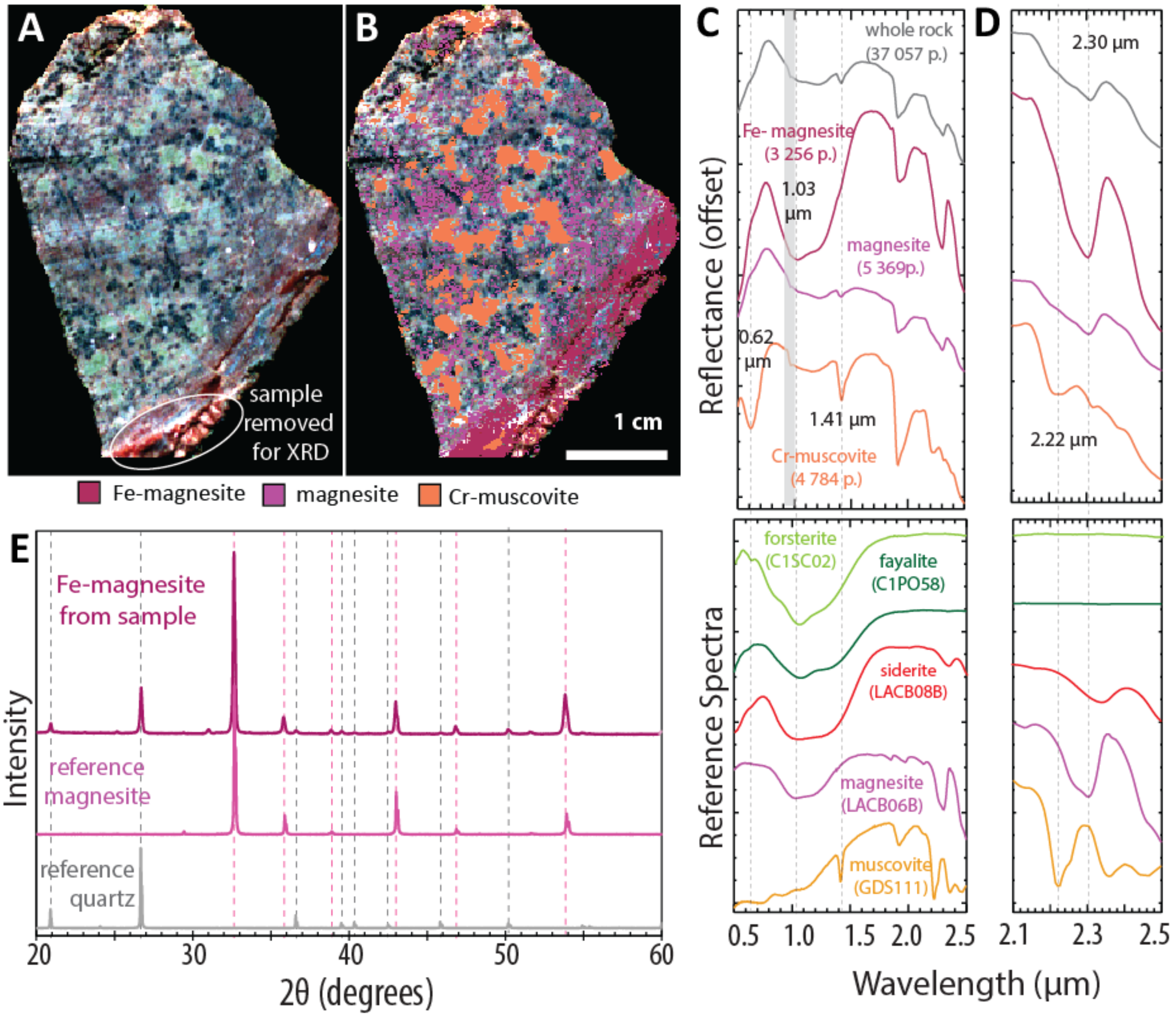

Fig 3-7. (a, b) Listvenite hand sample. Matrix is mixture of magnesite (magenta), Cr-muscovite/fuchsite (light green in visible; coral in parameter stretch), and opaques (like Cr or Fe oxides). We were unable to find reference spectra for Cr-muscovite/fuchsite, which has a distinctive 0.62 µm absorption, likely causing its characteristic colour. A vein on the bottom right of the sample has the strong 1-µm magnesite feature seen in field data (Fig 6), similar in shape and position to olivine (forsterite, fayalite). Our magnesite sample has wider 1um feature than the reference spectrum, indicating that the shoulders of this feature are not diagnostic. The lowest point of this asymmetric feature (~1.03 µm) lines up well with the lowest point of the forsterite absorption. (E) Diffraction peaks from XRD sample of Fe-magnesite vein show that it is a mixture of magnesite and quartz, with no olivine to cause the 1 µm absorption feature.

In Fig. 8, we compute linear mixtures of Fe-bearing magnesite spectra with forsterite and fayalite endmembers, to investigate how the 1-µm feature changes. We note that for this magnesite sample, band centres in the 1-µm feature are centred at ~1.03 and 1.23 µm, compared to 1.05 (1.09) and 1.28 (1.37) for forsterite and fayalite respectively. These similarities are not unexpected, as the wide 1-µm feature is attributed to ferrous iron absorptions in both mineral groups. It is beyond the scope of this work to fully characterize how the 1 µm absorption in carbonate changes with grain size and iron content. This band is noted in the carbonate spectroscopy literature (e.g. Gaffey, 1985), but not systematically studied, while extensive studies of the 1-µm band have been conducted in olivines (e.g. Burns, 1993, and references therein). In olivine, the overlapping absorptions around 1 µm are attributed to ferrous iron in the distorted octahedral M1 and M2 sites. At shorter wavelengths, we see absorptions often associated with ferric iron (e.g. see hematite, lepidocrocite in Fig. 10c). Because the absorption centre is outside the range of our spectrometer, we instead look at peak position between the UV and 1 µm absorptions. Peaks occur at 0.56 and 0.66-0.67 µm in olivine, whereas in this magnesite sample, they are shifted to 0.62-0.75 µm.

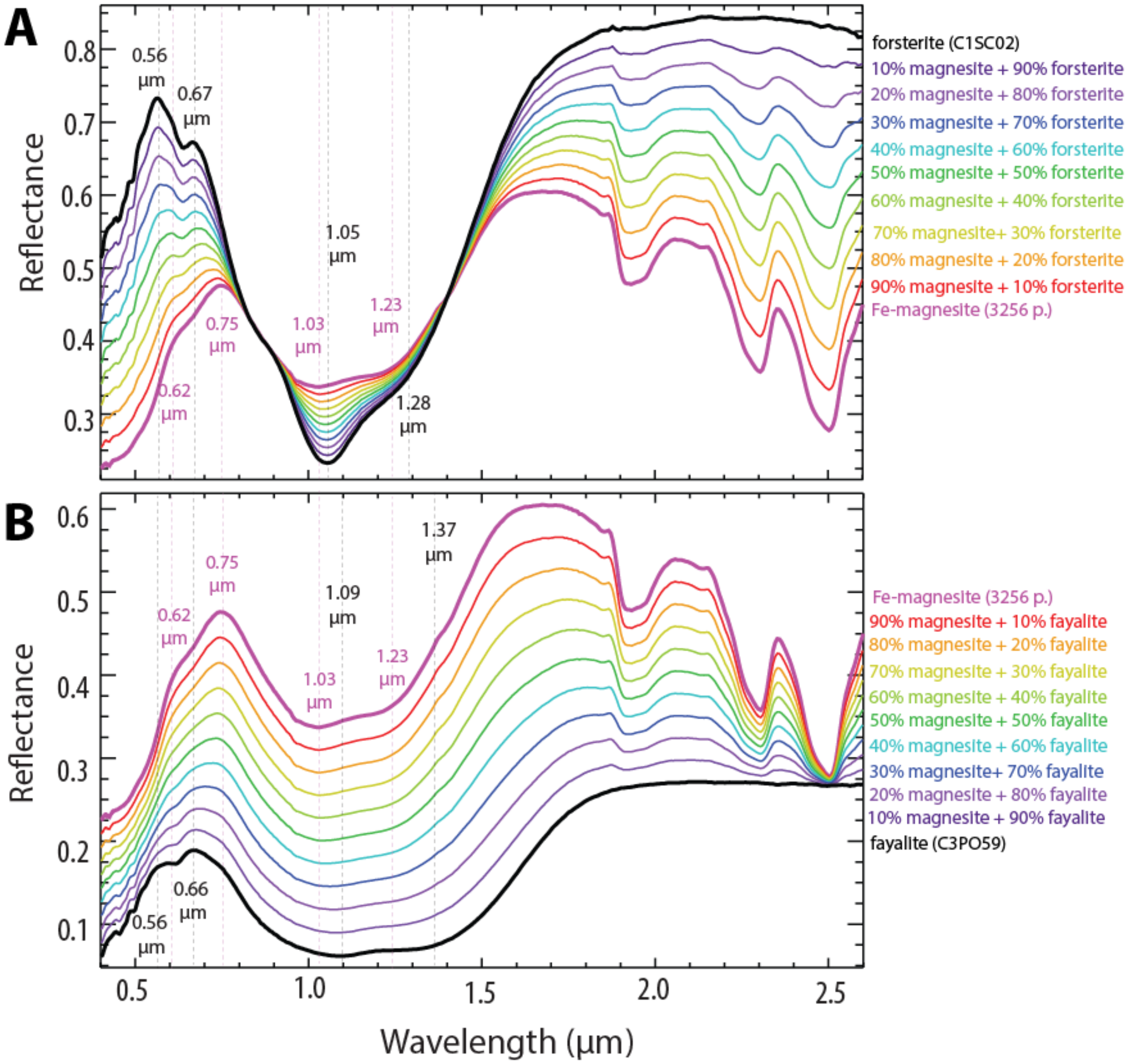

Fig 3-8. Linear mixing of Fe-rich magnesite and olivine. (A) Mixing with forsterite. Reference forsterite sample (RELAB) has a higher overall reflectance than the Fe-bearing magnesite (spectrum from our listvenite sample, Fig Ea, b). Here, the overall shape of the 1-µm absorption is very similar, with band centres offset by ~0.02-0.05 µm. In the VNIR, both forsterite and Fe-magnesite have 2 "peaks" (between absorptions). In forsterite, these peaks are shifted to shorter wavelengths (although minor Fe3+ weathering would alter the shape of this region). (B) Mixing with fayalite. Reference forsterite sample (RELAB) is has a lower overall reflectance than the Fe-bearing magnesite. Here, the overall shape of the 1-µm absorption is noticeably wider in fayalite than in magnesite, with band centres offset by ~0.06-0.14 µm. In the VNIR, fayalite peaks are at very similar positions as forsterite, though the relative heights are reversed.

To determine whether remnant olivine from this altered ultramafic rock could be partially responsible for the large 1-µm absorption (for characterization of olivine-nontronite-carbonate mixtures, see Bishop et al. 2013), we removed a small piece of this sample and crushed it for XRD analysis. In Fig. 7e, we see that the peaks align with magnesite and quartz (RRUFF IDs R040114 and R040031), with no olivine component despite the similar 1-µm absorption feature. Quartz has no absorption features in this wavelength region, so we would not expect to see its spectral signature. Magnesite/olivine sites on Mars have been studied as a potential location for serpentinizing systems, which could provide chemical energy for life—therefore, it is important to note that olivine/magnesite mixtures may look very similar to magnesite spectra alone in the VSWIR wavelength range. Exact band centres may help distinguish Fe-carbonate from olivine absorptions, but if both are present in a mixture, it would be very difficult to estimate proportions of each without knowing the spectral endmembers present (i.e. depth of the 1-µm feature in the carbonate endmember). Here, additional sources of information (e.g. thermal infrared wavelengths, which capture silicate bonds) would be very helpful to distinguish between olivine-rich and Fe-carbonate rich samples.

3.4 Travertine (22.815 N, 57.838 E; Fig. 9-12)

At the travertine site, we see modern carbonate deposits precipitating from hyperalkaline springs on top of dark, veined serpentinite (Fig. 9, 10, 12). The travertine deposit is about 1 m high, imaged from a distance of ~3.5 m. Mountains in the background are >500 m away. These figures are part of the same image, with the right side (Fig. 9, 10) highlighting mineral signatures, and the left side (Fig. 12) showing the range of biological spectral features.

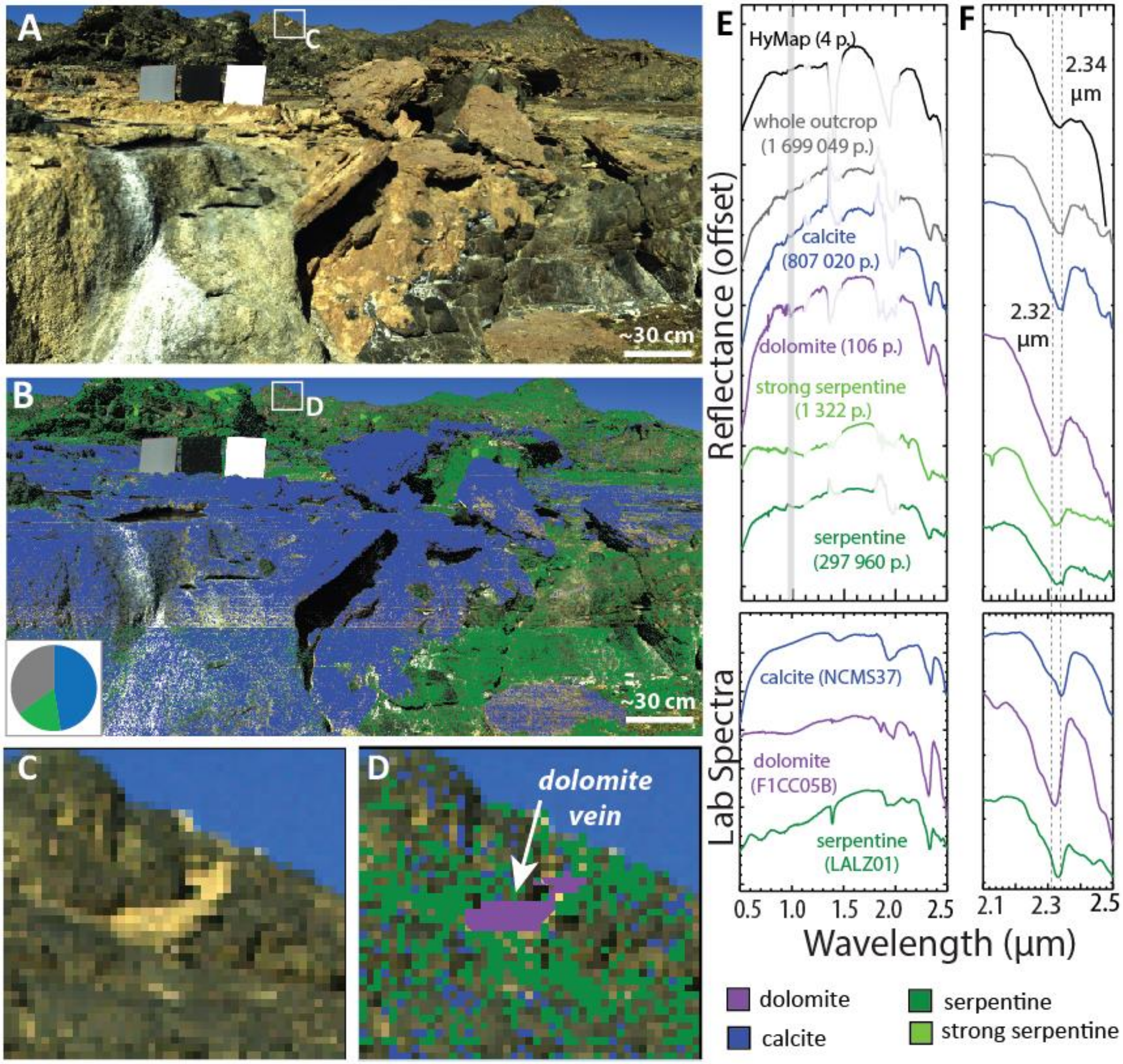

Fig 3-9. Travertine field site (right side of image; 22.815 N, 57.838 E). (a) Light toned carbonates are precipitating on top of dark serpentinite (bottom right). Dark serpentinite mountains are present in the background. Square Spectralon© panels are 30x30 cm. (b) Parameters show that the carbonate is dominated by calcite (blue), while the dark rocks in the foreground and background are serpentine (green). Overall, ~48% of the pixels in this image are classified as calcite, while ~18% are serpentine. Their combined spectrum (grey in E, F) is consistent with calcite, as is the airborne HyMap spectrum for the area. (C, D) A vein in the mountains in the background shows a carbonate with a clear 2.32 µm absorption, consistent with dolomite (purple), in contrast to the 2.34 µm calcite absorptions in the travertine. E, F) Spectra corresponding to coloured regions in B, D. Grey line at 0.97 µm shows the detector join, while atmospheric bands are transparent in field data. Detail from the key 2.1-2.45 µm region is shown in (h).

3.4.1 Calcite and serpentine (Fig. 9)

In Fig. 9, we see a variety of white-grey-tan-brown rocks on top of a dark grey unit in the bottom right, with dark mountains in the background (Fig. 9a). Spectrally, the white-grey-tan-brown rocks in the foreground are consistent with calcite, regardless of the exact colour. In the mountains, we see a vein of carbonate (Fig. 9c, d) where the absorption positions are consistent with dolomite (2.32 µm) rather than calcite. The dark unit underlying carbonate and mountains in the background are consistent with serpentine. In this whole image, ~48% (807 020/1 699 049) of the pixels are calcite, and 18% (297 960/ 1 699 049) are classified as serpentine. Here, both the average spectrum of the whole outcrop and the airborne spectrum from HyMap (Fig. 9e, f) are consistent with calcite, with a strong absorption at 2.34 µm, downturn to 2.5 µm, and no 2.12-µm serpentine absorption. In this case, the spectral dominance of carbonate may be partly due to the high albedo contrast—the serpentinite is very dark, and so while diagnostic absorptions may be relatively deep, the absolute depth is much smaller than similarly deep absorptions in bright materials. When averaged with bright calcite, the strong contrast of calcite absorptions may overwhelm the serpentine features. In Fig. 10, we show linear mixing results between average calcite and serpentine endmembers (Fig. 10a), as well as coarsely-crystalline calcite (Fig. 10b). Using the average endmembers, the diagnostic 2.12-µm serpentine absorption flattens out at ~50% calcite/serpentine (becoming convex at ~70% calcite). The absorption centre shifts from 2.32 µm (serpentine) to 2.34 µm (calcite) by ~40-50% calcite. The mean spectrum for the whole outcrop (grey; Fig. 9e), we see a flat (but not convex) 2.1 µm region and a band shifted to 2.34 µm, as expected for ~50-70% calcite. If instead we use a bright, coarsely crystalline calcite endmember (Fig. 10b), the 2.1-µm region takes on the characteristics of carbonate (narrow absorption at 2.15 µm) by ~40% calcite; the 2.3-µm band centre shifts to calcite wavelengths by ~20% calcite in the linear mixture.

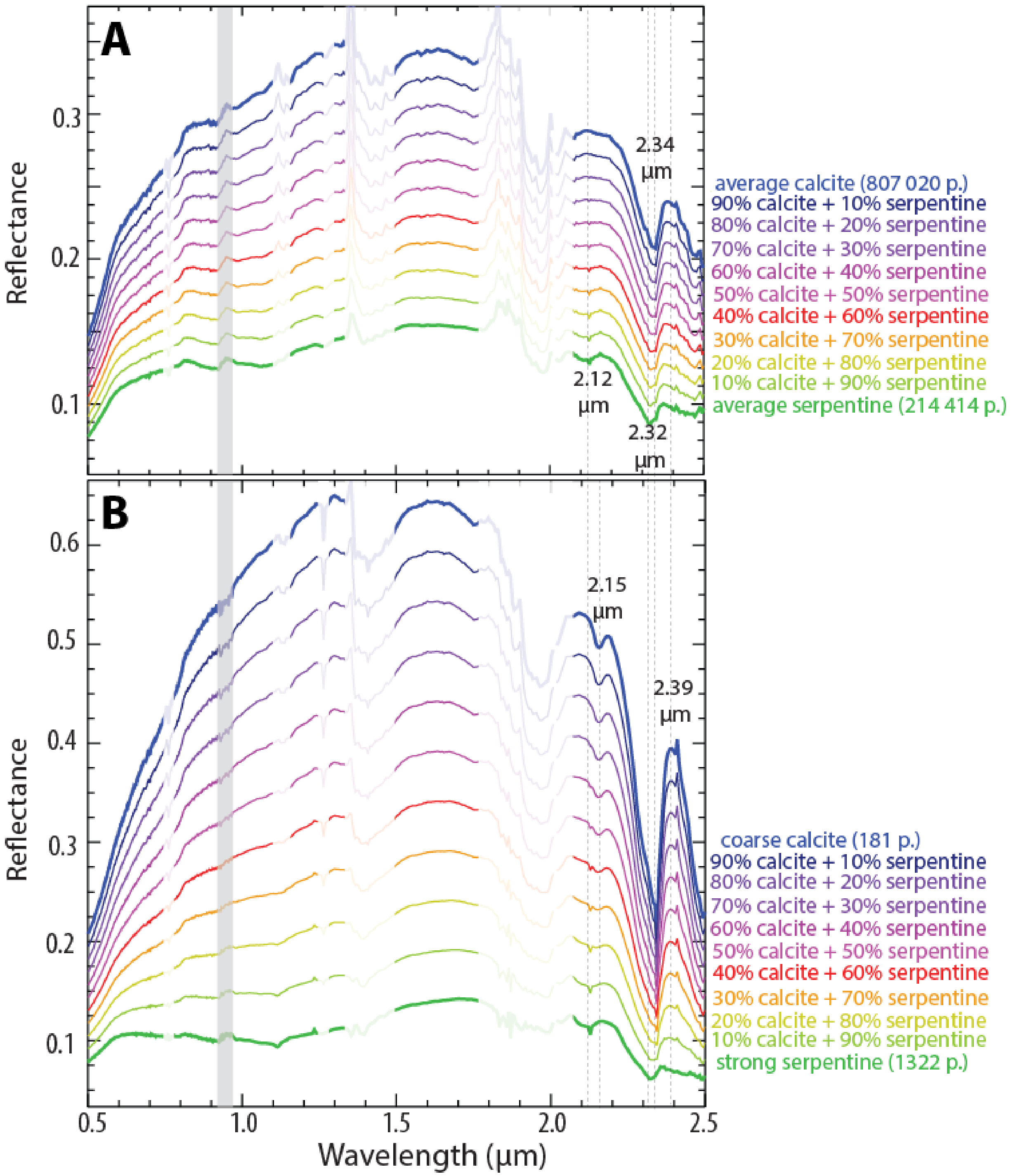

Fig 3-10. Linear mixtures between serpentine and calcite (spectra from travertine field site, Fig 3-9)). (a) Average calcite and serpentine endmembers. Diagnostic serpentine absorption at 2.12 µm flattens out at about 40% calcite/60% serpentine, and becomes convex at ~ 70% calcite. By 40-50% calcite, the serpentine band centre has shifted to 2.34 µm, and the 2.4 µm "peak" is broader and more similar to calcite. (B) Using coarsely crystalline examples (with deep absorptions) from within the scene, we see that the 2.1 µm region takes on a carbonate-like character (narrow, centred at 2.15 µm) by ~40% calcite/60% serpentine. Here, the 2.3-µm band centre and 2.4 µm "peak" shape have shifted to calcite wavelengths by ~20% calcite/80% serpentine.

3.4.2 Calcite natural variability (Fig. 11)

Here, calcite has a variety of colours—white to dark grey appearing to follow an old water spillway overtopping a pond, to a reddish brown colour (Fig. 11a, b). Pixels that are not picked up by our parameters here (e.g. some of the whitish material in the travertine) have shallow absorptions, consistent with fine-grained calcite. Looking at the SWIR spectra (Fig. 11d, e), we see that all have the diagnostic 2.34 and 2.5 µm absorptions, but considerably varying depths. White-grey calcite has the shallowest absorptions, which may be due to fine grained crystals (consistent with recent crystallization in a spillway). Bright spectra with deep absorption features (reddish calcites here) are consistent with coarse crystals; in one case, we see a minor 2.15-µm absorption typically only seen in pure reference samples in laboratory conditions. In VNIR data (Fig. 11c, d), we see a variety of flat to steep red slopes that may reflect trace amounts of iron oxides. Here, the VNIR data can assist in understanding minor compositional differences, but only when we also have the SWIR to confirm the underlying mineralogy.

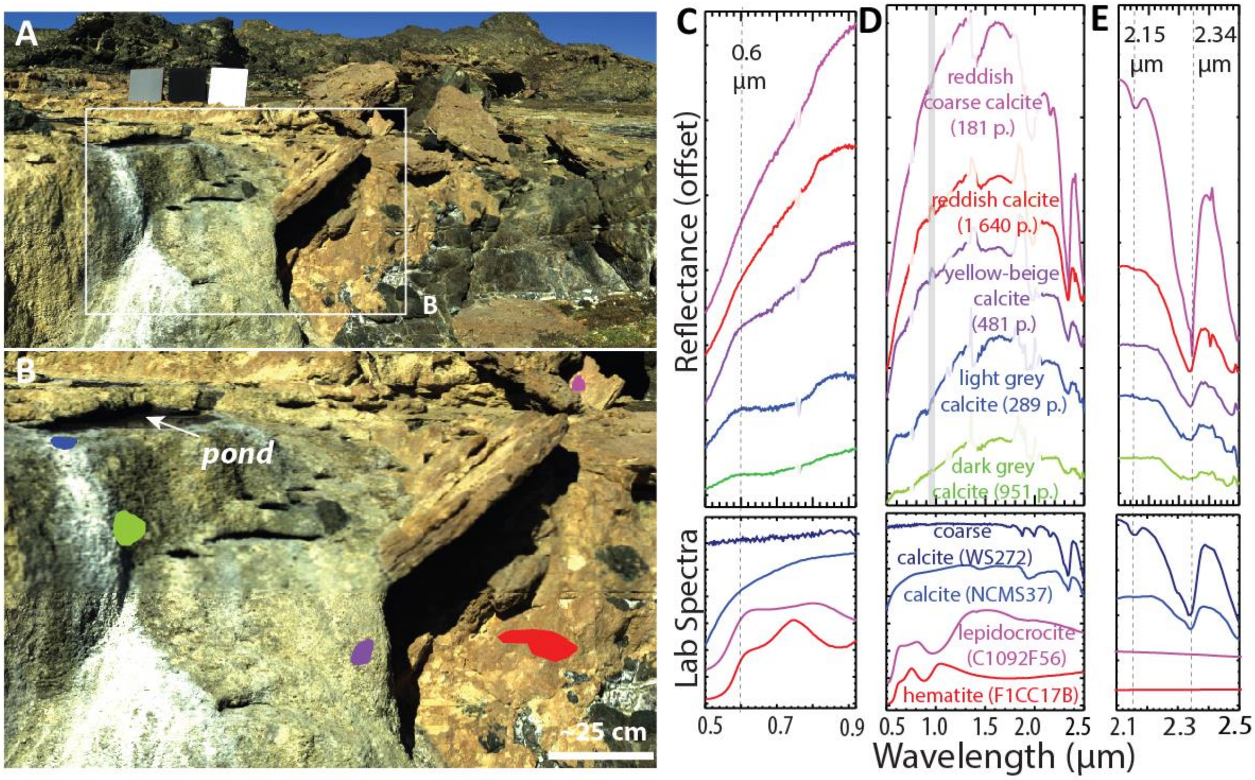

Fig 3-11. Travertine field site (right side of image; 22.815 N, 57.838 E); zoom to highlight diversity amongst calcite spectra in the same scene. (b) Average spectra of each coloured region are show in (C-E). Older calcite appears reddish, while closer to the pond is likely younger. Light and dark grey calcites appear to be within a recent spillway. (c) In VNIR, these calcite spectra have a wide range of slopes, and some (especially yellow-beige calcite (purple), and light grey calcite (blue)) have features at ~ 0.6 µm that may be related to iron oxides (e.g. hematite, goethite). (d) Full spectral range (0.502.5 µm) of these different natural calcite examples, showing the differing overall shapes. (e) All spectra have the 2.34 µm absorption and 2.5 µm slope of calcite, although the band centre is broader and shallower in the dark and light grey calcite spectra (green and blue). This may be due to increased noise related to the shallower band depth; shallow band depths are often associated with fine grained crystals, which would be expected for the most recent calcite deposits, freshly precipitated. Redder, older calcites have deeper band depths, in some cases even minor calcite absorptions (e.g. 2.15 µm) are visible, indicative of coarse crystalline samples.

3.4.3 Biological materials (Fig. 12)

In Fig. 12a, we see the left half of the travertine image, with a bush and active travertine terrace in the foreground. We identify pixels with biological materials using SWIR wavelengths, with their large water-related absorptions at 1.2, 1.4, and 1.9 µm. Dry biological materials also show absorptions at ~1.7 µm and 2.12 µm, related to lignins, proteins, and cellulose (Peterson and Hubbard, 1992; Kokaly et al., 2007; Fig. 12f). To distinguish between fresh biological materials, the VNIR portion of the spectrum is required. Dry vegetation materials (Fig. 12e) have featureless red slopes similar to some of the calcites in Fig. 10c. Green leaves on a bush show evidence of chlorophyll-a at 0.68 µm (e.g. Hubas et al., 2011), which is muted in the brownish vegetation in the near-field and far-field. The cloudy stream, which is forming calcite terraces in the foreground, has a distinctive spectral signature, with a small 0.624-µm (consistent with phycocyanin, a pigment in cyanobacteria) and large 0.869-µm (consistent with bacteriochlorophyll –a) absorption not present in spectral libraries of plant materials (Hubas et al., 2011). Instead, these are consistent with bacterial mats (e.g. Kokaly et al., 2007). In the mid-distance, where we first see the stream appear, this microbial signature is uniquely strong. It might be the case that this is the source of the microbes, or perhaps a source of their food (e.g. upwelling methane). Were we to design a field campaign testing the biological or chemical diversity of this site, we could use imaging spectroscopy to find hotspots of particular interest.

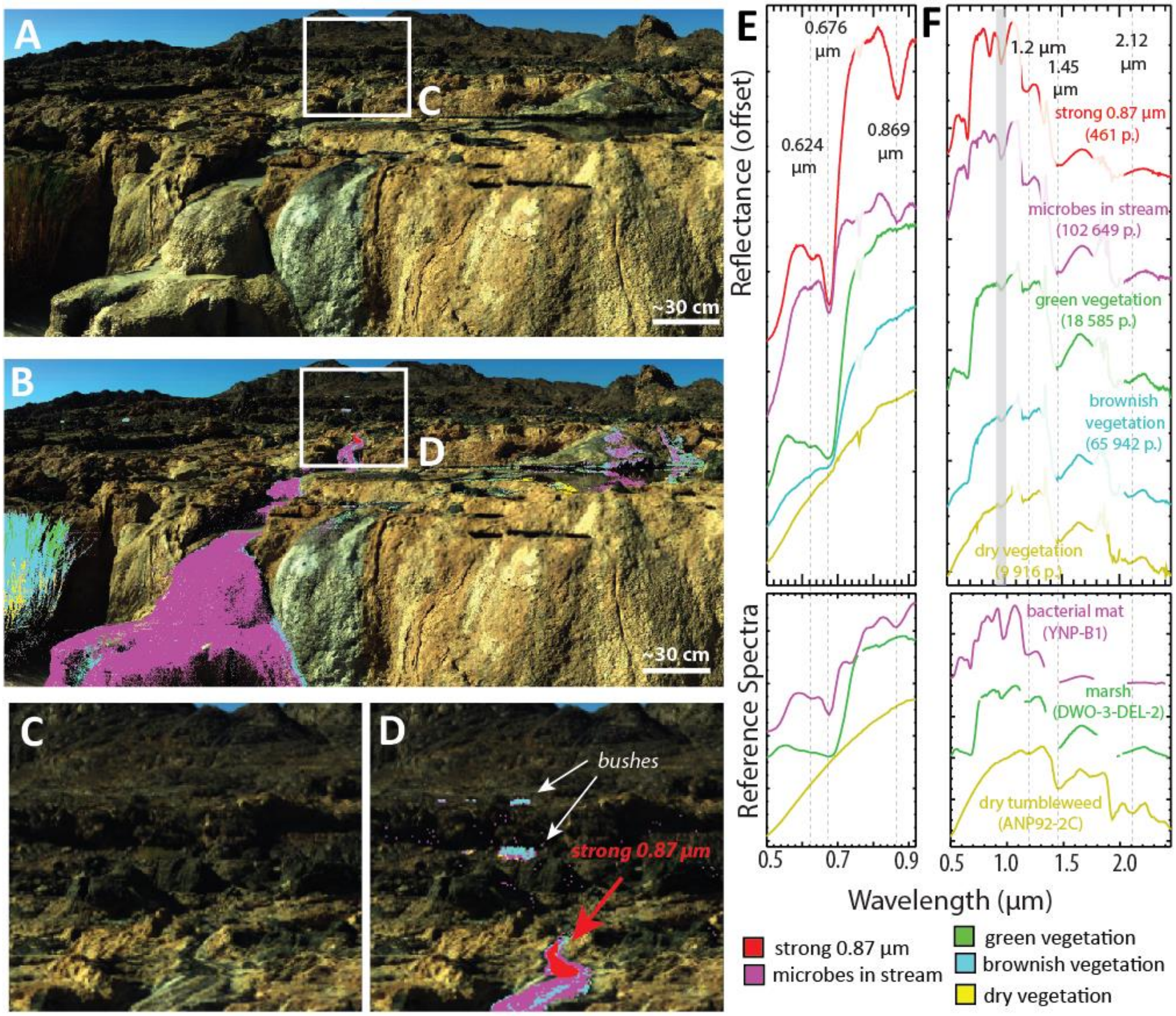

Fig 3-12 (a) Travertine field site (left side of image; 22.815 N, 57.838 E), with active travertine terraces. (b) Different colours reflect different biological materials, with corresponding spectra in panels E, F. In the streams, magenta and red have absorptions at 0.624 and 0.869 µm consistent with microbial mats (phycocyanin and bacteriochlorophyll-a, respectively). Fresh, green vegetation (green) also have chlorophyll-a absorption at 0.676 µm, with a "peak" around 0.550 µm. Brownish vegetation (cyan) lacks the green peak, but still has the "red edge" between 0.68-0.75 µm. Dry vegetation (yellow) lacks diagnostic features in the VNIR, but shares the 1.2 µm absorption with all organic material, as well as the 1.45 and 2.12 µm absorptions related to lignins which emerge when the deep, wide absorptions at 1.4 and 1.9 µm caused by water dry out (double check band assignments). (c, d) In the midground of the image, we can see some individual bushes emerge, as well as a very strong microbial absorption signal. The relative strength of these absorptions at this location indicates that this may be the source region, perhaps due to a localized food source (e.g. methane seep?) or other favourable environmental condition.

4 Discussion

4.1 Advantages of imaging spectroscopy vs. point sampling

Imaging spectroscopy in the field has several advantages over point sampling. Firstly, we can distinguish between very similar phases (like dolomite and calcite), and thereby capture more of the full mineralogical diversity in an outcrop that would otherwise be possible. We also pinpoint rare phases for further targeting/sampling; these rare phases tell us more about the physical/chemical environment (like prehnite). Rare phases such as remnant pyroxenes tell us about the protolith, pointing to ultramafic materials. In extraterrestrial samples, finding small, less altered parts of an outcrop to measure/sample in situ could help us understand both original igneous processes that created the rock (e.g. mantle conditions) as well as fluid processes and later changes in temperature and pressure that have shaped the alteration mineral assemblage. Furthermore, imaging spectroscopy allows us to interpret the mineral phases in their original context, allowing us to better understand their relationships to one another.

4.2 Lessons for carbonate and serpentine detection on Mars

At small spatial scales, we can confidently distinguish between members of a mineral solid solution phase (e.g. calcite-dolomite-magnesite), where multiple phases are present within a scene. In the field, we can generally distinguish between serpentine and carbonate (depending on the spatial resolution and mixing scale), despite their similar absorption features. This is not always possible in airborne or orbital datasets, where we do not know the spectral endmembers present in the scene. With typical, in-scene endmembers, linear mixing can better approximate the actual areal percentages observed in the overall unit (e.g. Fig. 9, 11). However, the exact abundances remain tricky to pin down, as endmembers from within a scene may themselves be mixtures. Having data available at a number of scales (e.g. Fig. 3) is useful to narrow down the possible range of abundances; here, we can use the proportions of veins at different scales to estimate the total amount of mineralization within veins in the rock unit.

5 Conclusions

With a VSWIR imaging spectrometer in the field, we were able to distinguish between different spectrally similar carbonate minerals, as well as identify rare minerals such as small remnant pyroxenes within the matrix of the rock; targeting these for further study could tell us about the original composition of the rock, and/or deeper crustal processes. Other rare minerals, such as prehnite, only form under a small range of temperature and pressure conditions, and so being able to detect it helps to constrain the possible range of past environmental conditions. This ability to fully characterize the mineralogical variability at a site would be very useful on planetary missions, where the number of samples and sites visited are very limited, and it is essential to extract the most information possible from each sample/site. For this kind of mineralogical characterization, both high spectral resolution and full VSWIR spectral range are required; current instruments such as the multispectral VNIR MastCam instrument aboard the Mars Science Laboratory cannot distinguish between similar materials (e.g. prehnite, epidote, chlorite, serpentine). Furthermore, understanding the typical mineralogical endmembers (and their spatial and spectral variability) helps calibrate airborne or orbital hyperspectral imagery. While abundance estimates are still imperfect due to endmember variability (e.g. textures, coatings, brightness, grain size), knowing the average endmembers present within a scene helps us to better estimate abundances from remote imagery datasets. Additionally, multiple scales of imagery can help us further constrain the abundance of different minerals, if they are predominantly found in discrete veins at a variety of scales. This textural information can also help us unravel information about multiple generations of fluid flow; on other planetary bodies, this could help us to understand whether there were multiple pulses of alteration over time, perhaps from different fluid sources, or whether alteration likely occurred at once.

Acknowledgements

Thanks to our field crew Georges Ceuleneer, Yves Daydou, Mathieu Rospabé, Mathieu Benoît, and Layla al-Habsi, and to the family who hosted our campsite. Thanks to Peter Kelemen for advice and introduction to Oman.

3.6 References

Amri, I., et al. (1996). "Tectonic setting for the genesis of oceanic plagiogranites: evidence from a paleo-spreading structure in the Oman ophiolite." Earth and Planetary Science Letters 139(1-2): 177-194.

Barnes, I., et al. (1978). "Present day serpentinization in New Caledonia, Oman and Yugoslavia." Geochimica et Cosmochimica Acta 42(1): 144-145.

Bibring, J.-P., et al. (2005). "Mars surface diversity as revealed by the OMEGA/Mars Express observations." Science 307(5715): 1576-1581.

Bindi, L., et al. (2015). Highlights in mineralogical crystallography, Walter de Gruyter GmbH & Co KG.

Bishop, J., et al. (2008). "Reflectance and emission spectroscopy study of four groups of phyllosilicates: Smectites, kaolinite-serpentines, chlorites and micas." Clay Minerals 43(1): 35-54.

Bishop, J. L., et al. (2013). "Coordinated spectral and XRD analyses of magnesite-nontronite-forsterite mixtures and implications for carbonates on Mars." Journal of Geophysical Research: Planets 118(4): 635-650.

Burns, R. G. and R. G. Burns (1993). Mineralogical applications of crystal field theory, Cambridge university press.

Carr, M. H. (1995). "The martian drainage system and the origin of valley networks and fretted channels." Journal of Geophysical Research: Planets 100(E4): 7479-7507.

Chavez Jr, P. S. (1988). "An improved dark-object subtraction technique for atmospheric scattering correction of multispectral data." Remote Sensing of Environment 24(3): 459-479.

Clark, R. N. (1999). "Spectroscopy of rocks and minerals, and principles of spectroscopy." Manual of remote sensing 3: 3-58.

Clénet, H., et al. (2010). "Thick sections of layered ultramafic cumulates in the Oman ophiolite revealed by an airborne hyperspectral survey: petrogenesis and relationship to mantle diapirism." Lithos 114(3-4): 265-281.

Clenet, H., et al. (2013). "A systematic mapping procedure based on the Modified Gaussian Model to characterize magmatic units from olivine/pyroxenes mixtures: Application to the Syrtis Major volcanic shield on Mars." Journal of Geophysical Research: Planets 118(8): 1632-1655.

Cloutis, E. A. and M. J. Gaffey (1991). "Pyroxene spectroscopy revisited: Spectral-compositional correlations and relationship to geothermometry." Journal of Geophysical Research: Planets 96(E5): 22809-22826.

Cocks, T., et al. (1998). The HyMapTM airborne hyperspectral sensor: The system, calibration and performance. Proceedings of the 1st EARSeL workshop on Imaging Spectroscopy, EARSeL.

Cooley, T., et al. (2002). FLAASH, a MODTRAN4-based atmospheric correction algorithm, its application and validation. IEEE International Geoscience and Remote Sensing Symposium, IEEE.

D. L. Blaney, R. O. G., P. Mouroulis, B.L. Ehlmann, B. Van Gorp, I. McKinley, Jose Rodriguez, A. Lamborn, J. M. Haag, M. Cable (2016). "Ultra Compact Imaging Spectrometer, Abstract # 4067." 3rd International Workshop on Instrumentation for Planetary Missions.

De Sanctis, M., et al. (2015). "Ammoniated phyllosilicates with a likely outer Solar System origin on (1) Ceres." Nature 528(7581): 241.

Edwards, C. S. and B. L. Ehlmann (2015). "Carbon sequestration on Mars." Geology 43(10): 863-866.

Ehlmann, B., et al. (2016). Vswir microimaging spectroscopy for geologic history and identifying and quantifying mineral, ice, and organic abundances on planetary surfaces. 3rd International Workshop on Instrumentation for Planetary Mission.

Ehlmann, B., et al. (2010). "Geologic setting of serpentine deposits on Mars." Geophysical research letters 37(6).

Ehlmann, B. L., et al. (2011). "Evidence for low-grade metamorphism, hydrothermal alteration, and diagenesis on Mars from phyllosilicate mineral assemblages." Clays and Clay Minerals 59(4): 359-377.

Ehlmann, B. L., et al. (2008). "Orbital identification of carbonate-bearing rocks on Mars." Science 322(5909): 1828-1832.

Falk, E. S. and P. B. Kelemen (2015). "Geochemistry and petrology of listvenite in the Samail ophiolite, Sultanate of Oman: Complete carbonation of peridotite during ophiolite emplacement." Geochimica et Cosmochimica Acta 160: 70-90.

Frey, M. and D. Robinson (2009). Low-grade metamorphism, John Wiley & Sons.

Gaffey, S. J. (1986). "Spectral reflectance of carbonate minerals in the visible and near infrared (0.35-2.55 microns); calcite, aragonite, and dolomite." American Mineralogist 71(1-2): 151-162.

Gao, B.-C., et al. (1999). "Atmosphere REMoval Program (ATREM) User’s Guide, Version 3.1." Center for the Study of Earth from Space (CSES), Cooperative Institute for Research in Environmental Sciences (CIRES), Univ. of Colorado, Boulder, Colo.

Green, R. O., et al. (2015). Microimaging Spectroscopy for the Exploration of Small Bodies: First Laboratory Measurements of Carbonaceous Chondrite and HED Meteorites and a Proposed M6 Instrument for In Situ Measurement. 46th Lunar and Planetary Science Conference. Houston, Lunar and Planetary Institute: Abstract #2154.

Microimaging spectroscopy for exploration: Laboratory measurements of carbonaceous chondrite and HED meteorites and a proposed M6 in situ instrument.

Greenberger, R. N., et al. (2016). Detection of organic-rich oil shales of the green river formation, Utah, with ground-based imaging spectroscopy. 2016 8th Workshop on Hyperspectral Image and Signal Processing: Evolution in Remote Sensing (WHISPERS), IEEE.

Halls, C. and R. Zhao (1995). "Listvenite and related rocks: perspectives on terminology and mineralogy with reference to an occurrence at Cregganbaun, Co. Mayo, Republic of Ireland." Mineralium Deposita 30(3-4): 303-313.

Heylen, R., et al. (2011). "Fully constrained least squares spectral unmixing by simplex projection." Geoscience and Remote Sensing, IEEE Transactions on 49(11): 4112-4122.

Hubas, C., et al. (2011). "Tools providing new insight into coastal anoxygenic purple bacterial mats: review and perspectives." Research in microbiology 162(9): 858-868.

Hunt, G. R. (1970). "Visible and near-infrared spectra of minerals and rocks: I silicate minerals." Modern Geology 1: 283-300.

Hynek, B. M., et al. (2010). "Updated global map of martian valley networks and implications for climate and hydrologic processes." Journal of Geophysical Research: Planets 115(E9).

Kelemen, P. B. and J. Matter (2008). "In situ carbonation of peridotite for CO2 storage." Proceedings of the National Academy of Sciences 105(45): 17295-17300.

Kokaly, R. F., et al. (2017). USGS spectral library version 7, US Geological Survey.

Kokaly, R. F., et al. (2007). "Spectral analysis of absorption features for mapping vegetation cover and microbial communities in Yellowstone National Park using AVIRIS data."

Lapotre, M. G., et al. (2017). "Compositional variations in sands of the Bagnold Dunes, Gale crater, Mars, from visible-shortwave infrared spectroscopy and comparison with ground truth from the Curiosity rover." Journal of Geophysical Research: Planets 122(12): 2489-2509.

Michalski, J. R. and P. B. Niles (2010). "Deep crustal carbonate rocks exposed by meteor impact on Mars." Nature Geoscience 3(11): 751-755.

Murchie, S., et al. (2007). "Compact reconnaissance imaging spectrometer for Mars (CRISM) on Mars reconnaissance orbiter (MRO)." Journal of Geophysical Research: Planets (1991–2012) 112(E5).

Murchie, S. L., et al. (2009). "A synthesis of martian aqueous mineralogy after 1 Mars year of observations from the Mars Reconnaissance Orbiter." Journal of Geophysical Research: Planets 114(E2).

Mustard, J. F. and C. M. Pieters (1989). "Photometric phase functions of common geologic minerals and applications to quantitative analysis of mineral mixture reflectance spectra." Journal of Geophysical Research: Solid Earth 94(B10): 13619-13634.

Neal, C. and G. Stanger (1984). "Calcium and magnesium hydroxide precipitation from alkaline groundwaters in Oman, and their significance to the process of serpentinization." Mineralogical Magazine 48(347): 237-241.

Niles, P. B., et al. (2013). "Geochemistry of carbonates on Mars: implications for climate history and nature of aqueous environments." Space Science Reviews 174(1-4): 301-328.

Pelkey, S., et al. (2007). "CRISM multispectral summary products: Parameterizing mineral diversity on Mars from reflectance." Journal of Geophysical Research: Planets 112(E8).

Peterson, D. L. and G. Hubbard (1992). "Scientific issues and potential remote-sensing requirements for plant biochemical content."

Pieri, D. C. (1980). "martian valleys: Morphology, distribution, age, and origin." Science 210(4472): 895-897.

Pinet, P., et al. (2006). Mantle rock surface mineralogy mapping in arid environment from imaging spectroscopy: The case of the Maqsad peridotitic massif in Oman and implications for the spectroscopic study of exposed mafic units on Mars. Proc. Lunar Planet. Sci. Conf. 37th.

Pinet, P., et al. (2003). Hyperspectral remote sensing approach for rock surface mineralogy mapping in arid environment. Proceedings IUGG XXXIII General Assembly, Sapporo (Japon).

Pollack, J. B., et al. (1987). "The case for a wet, warm climate on early Mars." Icarus 71(2): 203-224.

Rempfert, K. R., et al. (2017). "Geological and geochemical controls on subsurface microbial life in the Samail Ophiolite, Oman." Frontiers in microbiology 8: 56.

Roy, R., et al. (2009). "Geological mapping strategy using visible near-infrared–shortwave infrared hyperspectral remote sensing: Application to the Oman ophiolite (Sumail Massif)." Geochemistry, Geophysics, Geosystems 10(2).

Schulte, M., et al. (2006). "Serpentinization and its implications for life on the early Earth and Mars." Astrobiology 6(2): 364-376.

Searle, M. and J. Cox (1999). "Tectonic setting, origin, and obduction of the Oman ophiolite." Geological Society of America Bulletin 111(1): 104-122.

Stern, S., et al. (2015). "The Pluto system: Initial results from its exploration by New Horizons." Science 350(6258): aad1815.

Swayze, G., et al. (1992). "Ground-truthing AVIRIS mineral mapping at Cuprite, Nevada."

Tilton, G., et al. (1981). "Uranium-lead isotopic ages of the Samail ophiolite, Oman, with applications to Tethyan ocean ridge tectonics." Journal of Geophysical Research: Solid Earth 86(B4): 2763-2775.

Van Gorp, B., et al. (2014). "Ultra-compact imaging spectrometer for remote, in situ, and microscopic planetary mineralogy." Journal of Applied Remote Sensing 8(1): 084988-084988.

Viviano-Beck, C. E., et al. (2014). "Revised CRISM spectral parameters and summary products based on the currently detected mineral diversity on Mars." Journal of Geophysical Research: Planets 119(6): 1403-1431.

Web, R. "Reflectance Experiment Laboratory (RELAB) Description and User's Manual."

Wray, J., et al. (2011). "Columbus crater and other possible groundwater-fed paleolakes of Terra Sirenum, Mars." Journal of Geophysical Research: Planets 116(E1).

Chapter 4

CHALLENGES IN THE SEARCH FOR PERCHLORATE AND OTHER HYDRATED MINERALS WITH 2.1-μM ABSORPTIONS ON MARS

E. K. Leask[1], B. L. Ehlmann[1, 2], M. Dundar[3], S.L. Murchie[4], and F.P. Seelos[4]

[1] Division of Geological and Planetary Sciences, California Institute of Technology, Pasadena, CA, USA

[2] Jet Propulsion Laboratory, California Institute of Technology, Pasadena, CA, USA

[3] Indiana University-Purdue University, Indianapolis, IN, USA

[4] Johns Hopkins University/Applied Physics Laboratory, Laurel, MD, USA

Leask, E., et al. (2018). "Challenges in the search for perchlorate and other hydrated minerals with 2.1-μm absorptions on Mars." Geophysical Research Letters 45(22): 12,180-112,189, doi: 10.1029/2018GL080077.

Abstract

A previously unidentified artifact has been found in Compact Reconnaissance Imaging Spectrometer for Mars (CRISM) targeted I/F data. It exists in a small fraction (<0.05%) of pixels within 90% of images investigated and occurs in regions of high spectral/spatial variance. This artifact mimics real mineral absorptions in width and depth and occurs most often at 1.9 and 2.1 μm, thus interfering in the search for some mineral phases, including alunite, kieserite, serpentine, and perchlorate. A filtering step in the data processing pipeline, between radiance and I/F versions of the data, convolves narrow artifacts ("spikes") with real atmospheric absorptions in these wavelength regions to create spurious absorption-like features. The majority of previous orbital detections of alunite, kieserite, and serpentine we investigated can be confirmed using radiance and raw data, but few to none of the perchlorate detections reported in published literature remain robust over the 1.0-μm to 2.65-μm wavelength range.

Plain Language Summary

Many minerals can be identified with remote sensing data by their characteristic absorptions in visible-shortwave infrared data. This type of data has allowed geological interpretation of much of Mars' surface, using satellite-based observation. We have discovered an issue with the Compact Reconnaissance Imaging Spectrometer for Mars instrument's data processing pipeline. In ~<0.05% of pixels in almost all images, noise in the data is smoothed in such a way that it mimics real mineral absorptions, falsely making it look as though certain minerals are present on Mars' surface. The vast majority of previously identified minerals are still confirmed after accounting for the artifact, but some to all perchlorate detections and a few serpentine detections were not confirmed, suggesting the artifact created false detections. This means concentrated regions of perchlorate may not occur on Mars and so may not be available to generate possibly habitable salty liquid water at very cold temperatures.

1 Introduction

The Compact Reconnaissance Imaging Spectrometer for Mars (CRISM) aboard the Mars Reconnaissance Orbiter (MRO) has been collecting visible/short-wave infrared reflectance data (0.4-3.9 μm) since 2006 (Murchie et al., 2007). These data have revolutionized our knowledge of Mars' surface, allowing the identification of mafic, hydrated, and evaporite mineral deposits as well as interpretation of the geological processes that created them (e.g., Mustard et al., 2008; Ehlmann et al., 2008; Bishop et al. 2008a; Murchie et al., 2009a; Wray et al., 2011, Carter et al., 2013). There are several known artifacts in the CRISM dataset that must be taken into consideration when analyzing data, including a sharp feature created by a filter boundary at 1.65 µm and a “sawtooth” pattern caused by imperfect atmospheric correction at ~2 µm (Murchie et al., 2009b; Wiseman et al., 2016). Nonetheless, the data quality is sufficient to discover minerals previously unreported for Mars, map their distribution, and generate new insights into martian environmental processes.

We began this work thinking we had discovered a hydrated phase with a 2.1-µm absorption in some ways similar to perchlorate, present in small exposures widely scattered across the surface of Mars. Upon further investigation, we discovered that it was a previously undescribed artifact, present in a small fraction of I/F (π x radiance from the surface divided by solar irradiance) pixels in ~90% of CRISM images investigated. It mimics the characteristics of real mineral absorptions, covering ~20 consecutive bands, and arises from incomplete handling of spikes in the radiance data by a noise filtration step in the radiance to I/F conversion (Fig. 1b-c).

This artifact creates challenges when searching for mineral phases on Mars, especially those with absorptions in the 1.9 and 2.1-µm wavelength range, as we have found the most frequent multi-band artifacts occur at these wavelengths. Minerals whose detections might be affected include the hydrated and/or hydroxylated phases kieserite, alunite, serpentine, and perchlorate, each of which has specific implications for the geochemical conditions present at the time of formation. Here, we describe the steps taken to identify the artifact and characterize its distribution in the CRISM dataset. We revisit key previously-reported detections of key mineral phases potentially impacted by this artifact by examining whether apparent absorptions persist in less processed data products (radiance and raw data), which were not subjected to noise filtering. Finally, we recommend data processing approaches that mitigate the effects of the artifact on CRISM data interpretation.

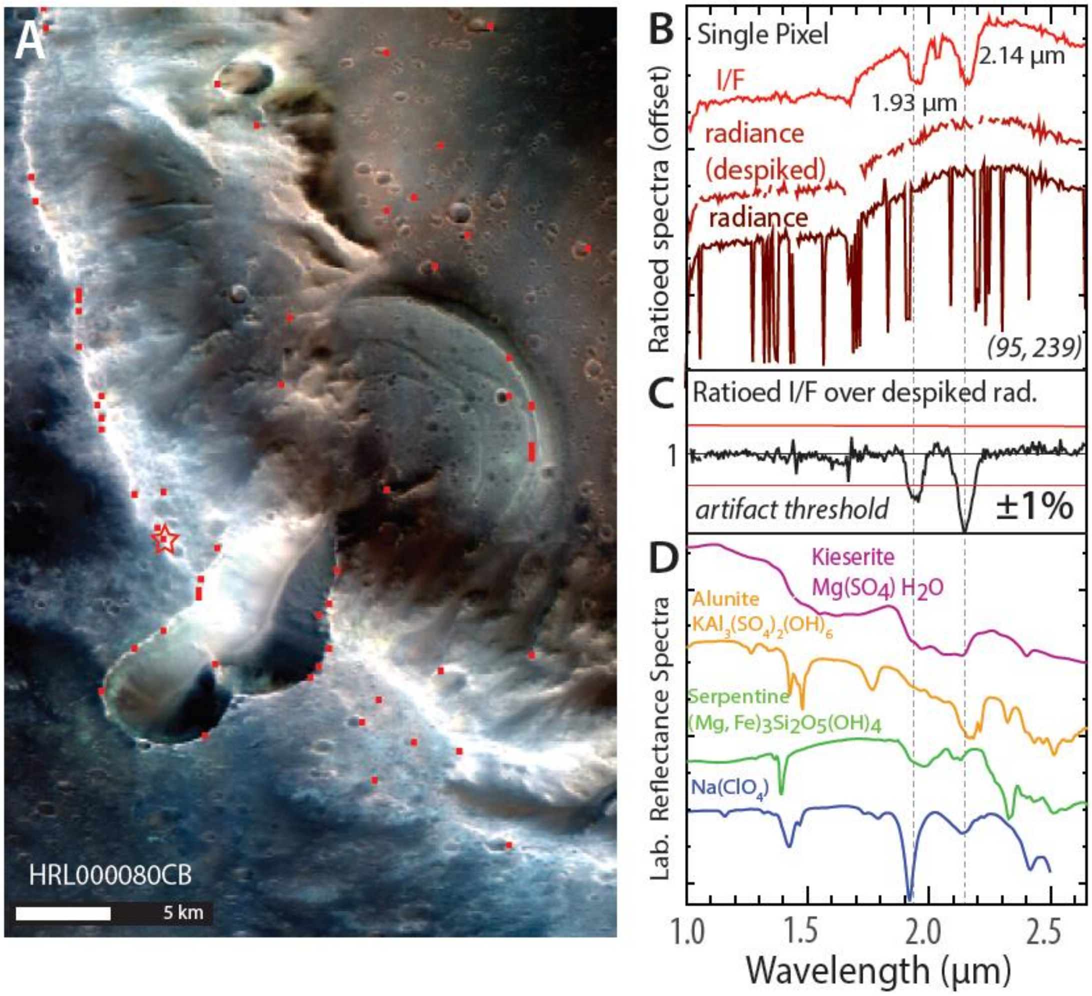

Figure 4-1. Example of the (a) spatial and (b) spectral appearance of the artifact creating the spurious absorptions, shown in ratioed I/F and ratioed radiance. The threshold for an artifact is defined to be where ratioed radiance differs from ratioed I/F by more than 1% (c). Laboratory spectra of minerals with a 2.1-μm absorption are shown (d) for comparison (from USGS spectral library (Clark et al. (2007)) and Hanley et al. (2015)).

2 Materials and Methods

This artifact, which we will refer to as a “spurious absorption”, was first discovered with a multi-step Bayesian clustering algorithm designed to automate detection of rare minerals in CRISM images (implemented by Yerebakan et al. (2014) and Dundar & Ehlmann (2016)). To understand the origin of observed spectral features, we analyzed raw and radiance data in addition to I/F. We employ these earlier data products in the processing pipeline to verify absorption features and differentiate between real features and pipeline-generated artifacts (for details, see Supporting Online Material). Although radiance and raw data are noisy, robust mineral detections can be seen in all types of ratioed data (e.g. Fig. S15).

The CRISM data processing pipeline includes a filtering step between radiance and I/F (Murchie et al., 2016, Appendix N). This filtering is designed to remove sharp, narrow “spikes” in the radiance dataset. Spikes can be positive or negative, and often result from a lag in the response of a detector element when crossing an abrupt brightness boundary (Figs. 1b, S4). Throughout this paper, we use “spike” to mean an abrupt departure from the continuum value, with a maximum of 3 consecutive channels (most often 1). Spikes are generated where particular detector elements are slower than their neighbors in recording an abrupt spatial change in surface brightness. Unlike spikes, “spurious absorptions” (or “absorption-like features”) are typically present over ~20 channels, and have gradual shoulders on either side of the main departure from the continuum value. We present spectra as ratioed data for ease of comparison between datasets; for ratioing, we use a “bland” denominator spectrum constructed from pixels within the same detector column in an image (unless otherwise indicated, “bland” denominators are simple column medians).

3 Results and Discussion

Pixels with 1.9 and 2.1-μm absorptions were identified in 317 of 344 CRISM images examined from across the surface of Mars (Fig. S1, Table S2); another 6 images contained potential identifications, and 21 contained none. To verify whether the apparent absorptions at 1.9 and 2.1 μm were real surface features, we first confirmed that they were present in unratioed I/F data (and not introduced by the choice of denominator). The same spectral features were also confirmed present in advanced products derived from I/F, including targeted empirical records (TERs) and map-projected targeted reduced data records (MTRDRs). The apparent absorptions were present after every iteration of atmospheric correction available in CAT-ENVI, and could be seen even in raw I/F data prior to atmospheric correction.

Next, we checked whether our observed 1.9 and 2.1-μm paired absorption-like features occurred in places that were geologically plausible. Our pixels tend to occur scattered in single or few-pixel groups in areas of topographic roughness, following edges of geologic features (see Figs. 1a, S4). This spatial pattern is unusual, as mineral deposits tend to be found in larger clusters; however, real mineral deposits could plausibly follow topographic features, if erosion were exposing a unique composition from beneath dust. We also observed pixels with paired 1.9 and 2.1-μm spectral features present at rover sites, although corresponding areas of unique composition near traverses have not been flagged by Curiosity or Opportunity. We found a similar spectral pattern in active basaltic dunes at Nili Patera, and seasonal CO_2 frost in Russell Crater. Concentrated hydrated or hydroxylated mineral deposits large enough to be observable from orbit are unlikely to occur within active dunes or seasonal frost, so we began to suspect that the 1.9 and 2.1-µm spectral features might not originate from a real surface phase. We also checked images taken from the 2007 global dust storm—because this is thoroughly mixed dust, we should not see any concentrated mineral phase. The 1.9 and 2.1-µm paired spectral pattern was not found in the dust storm. However, the dust storm images also lacked any areas of strong brightness contrast, as the surface was wholly obscured by dust.

Images with no or potential spurious absorptions usually contained very few areas of strong brightness contrast. The image subset included images from the early part of the mission (2006-2008) as well as images from later in the mission (up to 2014), where IR data became noisier due to reduced cryocooler function (Fig. S2). No clear trend was observed between the number of artifacts detected per image through time. A typical image contains 50-100 ‘artifact’ pixels, as selected by our automated algorithm (see S1.1, Fig. 2a). Spatially contiguous individual artifact detections were almost all in the 1-3 pixel range with a maximum size of 12 contiguous pixels (Fig. S3).

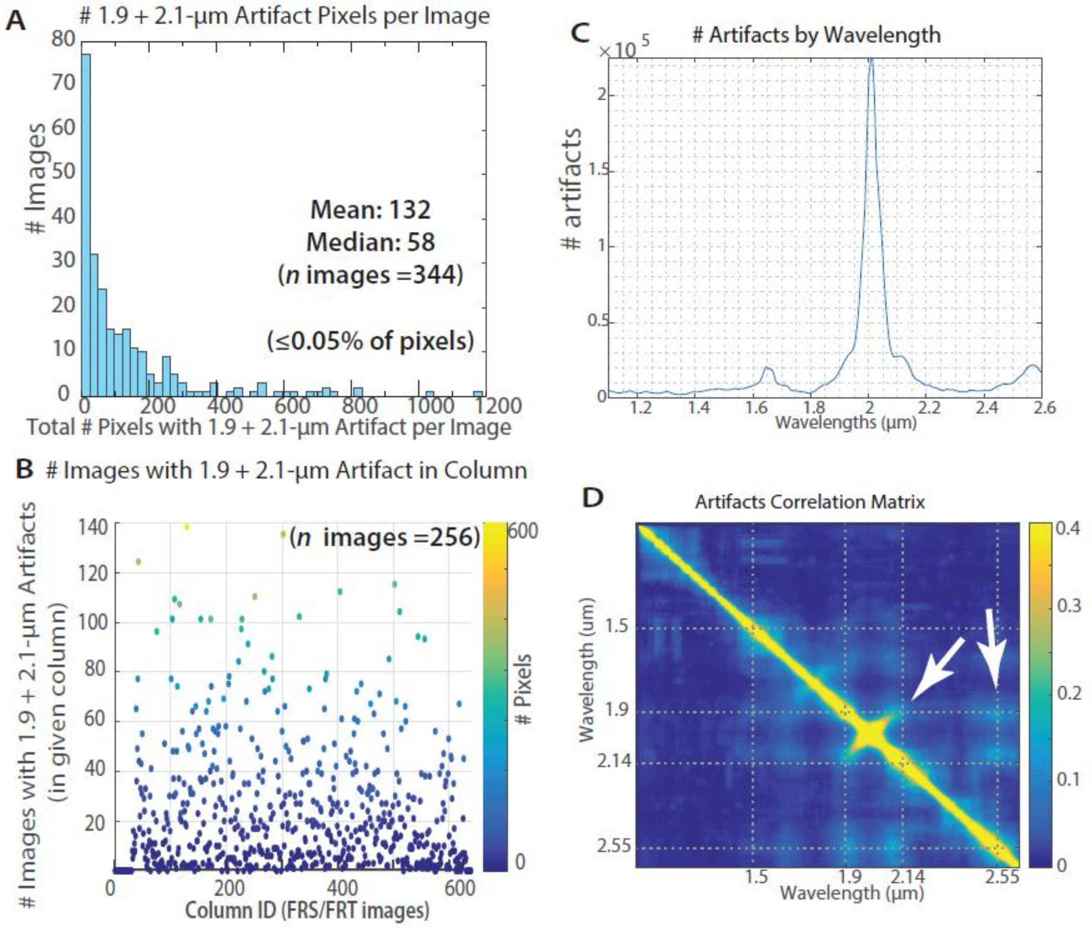

Figure 4-2. Characterization of artifact properties. The distribution of the number of artifacts at 1.9 and 2.1 µm (selected by our algorithm) per image is shown in (a); most images have tens to hundreds of artifacts. These artifacts at 1.9 and 2.1 µm occur preferentially in certain columns across many images (b). Panels on the right aggregate data for 21 images processed from radiance data; (c) shows the total number of artifacts at each wavelength in all the images processed, while (d) is a correlation matrix for the same dataset. Off-axis hotspots in this matrix show where artifacts at different wavelengths tend to co-occur in the same pixels, notably at 1.9, 2.1, and 2.5 µm (arrows).

3.1 Characteristics of the apparent “2.1-µm absorption”

Real mineral phases have consistent spectral characteristics, including shape, depth, and central wavelength of absorptions, and changes in the mineral formula (e.g. solid solution) or mixtures of multiple phases cause systematic variations. In pixels with spectra consistent with our potential mineral phase, we see absorption-like features consistently at 1.9 and 2.1 µm, occasionally with other features at

1.5 and 2.5 µm. The relative depths of the absorption-like features vary, and the band center at ~2.1 µm ranges from 2.10-2.16 µm, without any other systematic changes in spectral properties that might be expected of a changing composition. When we searched outside the automated pixel detections, we found that strong absorption-like features were sometimes present alone at 1.9 or 2.1 µm, less often at ~2.5 µm, and occasionally elsewhere in the spectrum (Fig. S5e-f). We did not systematically evaluate the 2.8-3.9 µm wavelength region due to elevated transient noise effects in this low-signal spectral region (see S2).

3.2 Comparison of ratioed I/F and ratioed radiance data

To evaluate the validity of these absorption-like features, we compared ratioed I/F spectra to ratioed radiance data on a pixel-by-pixel basis to ascertain whether the absorption at 2.1 µm persisted in radiance data. While spectra of valid mineral detections appear similar in ratioed I/F and ratioed radiance (Figs. 3a, S15), the strong absorptions at 2.1 µm in ratioed I/F in pixels selected by our algorithm do not persist in ratioed radiance (Figs. 1b, S5c). For a representative subset of images, every pixel identified with our algorithm as having this 2.1-µm spectral signature was examined to see if the feature was present in ratioed radiance data. In every case, instead of the feature at 2.1 µm, we found spikes in ratioed radiance data.

3.3 Trends in spikes and artifacts

As our initial Bayesian detection algorithm was tuned to find absorptions at 2.1 µm, we searched for similar spurious absorptions at other wavelengths by comparing ratioed I/F and ratioed radiance for 21 images to generate statistics for spectral positions of spikes, spike clusters, and artifacts (Figs. 2c-d, S5-6). We also looked for wavelength-dependence in spikes or clusters of spikes in the radiance data because the spatial distribution of spikes, spike clusters, and artifacts appeared to be similar (Fig. S4).

3.3.1 Wavelength-dependence of spikes in radiance data

To identify single- to few-channel spikes in ratioed radiance data we employed a two-step median filter. For each single-pixel spectrum, the data were compared to a wide (30-band) median filter, and values that differed more than 5% from the median were excluded (obvious spikes). A second (4-band) median filter was then applied, and values that differed more that 1% from this second median were excluded. Although this procedure is effective for identifying spikes, despiked data must be used with care as real narrow absorptions are occasionally misclassified as spikes. For each cube examined, spikes were most common at 1.65 µm (a known filter boundary artifact) and ~2 µm (the centre of the atmospheric CO_2 triplet) (Fig. S5a-b; compare to CO_2 (g) spectrum, Fig. S13c). At longer wavelengths (~2.4–2.65 µm), spikes and clusters of spikes become more common. (Here, a "cluster" is defined as at least 4 spikes within an 11-band spectral interval (Fig. S5)). However, neither spikes nor clusters of spikes preferentially occur at either 1.9 or 2.1 µm. No correlation between spikes at 1.9 and 2.1 µm or any other wavelengths are observed. (Fig. S6a-c).

3.3.2 Wavelength-dependence of spurious absorptions

We searched for all spurious absorption-like features by dividing the ratioed I/F by despiked ratioed radiance; ideally, this ratio should be equal to 1. Bands were identified as containing an artifact if the ratio diverged from unity by >1% (Fig. 1c). Artifacts occur most commonly at 1.65, 2.0 (extending to 1.9 and 2.1 µm), and 2.5 µm (Figs. 2c, S5e-f). Unlike spikes and spike clusters, artifacts centered at different wavelengths do show off-axis trends in the correlation matrix, co-occurring at 1.9, 2.14, and 2.55 µm (Figs. 2d, S6e-f).

3.4 'Bad' detector elements

While pixels selected by our algorithm are found scattered throughout images, there are some columns (corresponding to detector elements) in which artifacts at 1.9 and 2.1 µm occur repeatedly in many images (Fig. 2b). This suggests that certain detector elements are more prone to detector lag (radiance spikes) in these parts of the spectrum. Of 256 full-resolution images investigated, several columns contain artifacts at these wavelengths in more than 100 different images.

4 Assessment of previous mineral detections using the 2.1-µm region

The 1.9-µm absorption indicates surface-adsorbed or mineral-bound water (Hunt, 1977) and occurs in many regions of Mars (e.g. Poulet et al., (2005); Gendrin et al., (2005). The 2.1-µm absorption is far rarer, and related to the presence of either H2O or OH. Its presence – coupled with other absorption features – has specific implications for the presence of particular mineral species and their genetic environments. We assessed previously reported mineral detections that utilize the 2.1-µm region to verify whether this artifact may have affected previously reported work, examining radiance data for CRISM scenes with monohydrated sulfate, alunite, serpentine, and possible perchlorate.

4.1 Kieserite

Kieserite is a monohydrated magnesium sulfate ($MgSO_4·H_2O$), and on Earth it is formed (a) in evaporative basins, (b) through burial and heating of polyhydrated sulfate (at least a few km depth; Roach et al., 2009), or (c) by conversion of polyhydrated sulfate by low water activity groundwater. The detection of kieserite and its discrimination from other phases relies on detection of absorptions at ~1.6, 2.1, and 2.4 µm (Gendrin et al. (2005); Cloutis et al. (2006); Hunt (1971)). We examined the CRISM type spectral region, which is typical of other reported deposits (Viviano-Beck et al., 2015; Roach et al. (2010)). Kieserite is found in a large, contiguous deposit (Fig. S7). Because all absorptions necessary for identification are present in the mean spectrum of all stages of CRISM data, the identification of kieserite in this image is not affected by the 2.1-µm artifact. This is the case for the majority of previously reported kieserite detections on Mars which span hundreds of pixels, whereas the artifact affects only up to ~12 contiguous pixels.

4.2 Alunite

Alunite is a hydroxylated aluminum sulfate mineral ($KAl_3(SO_4)_2(OH)_6$) which forms in acidic conditions, either connected to magmatic fluids or as a product of acidic alteration (Ehlmann et al., 2016 and references therein). The detection of alunite and its discrimination from other phases relies on detection of an absorption at 2.17 µm, a doublet at 1.43 and 1.48 µm, and weaker absorptions at 1.76, 2.32, and 2.52 µm (e.g., Swayze et al., 2006). We examined all three alunite detections currently reported in the peer-reviewed literature: the CRISM type spectral region (Viviano-Beck et al., 2014; Ehlmann et al., 2016), a second region from Ehlmann et al. (2016)/Carter et al. (2013), and the mixed alunite deposit in Wray et al. (2011). For all three exposures, we found that alunite's diagnostic absorptions persisted in both ratioed I/F and ratioed radiance data (Figs. S8-10).

4.3 Serpentine

Serpentine forms when ultramafic rocks are hydrothermally altered in waters with low silica activity (<400°C; Evans, 2004). Serpentine has absorptions at 1.38, 2.32, and 2.52 µm, and its discrimination from other Mg phyllosilicates and mixtures of phyllosilicates and carbonates requires identification of a weaker 2.10-2.12 µm absorption (e.g. Bishop et al., 2008b; Ehlmann et al., 2010). We were able to reproduce spatially contiguous areas (>24 pixels) with a clear serpentine signature in ratioed radiance data from some previously published locations near the Claritas Rise and Nili Fossae (Figs. 3a-b, S11-

12). However, previously reported serpentine spectral signatures from McLaughlin crater (Fig. 3c-d; Michalski et al., 2013) and Chia crater (Fig. 3e-f; Ehlmann et al., 2010) become considerably less diagnostic of the presence of serpentine. The relative depth of the 2.3- and 2.5-µm features could also be consistent with carbonate (e.g. Gaffey, 1986) rather than serpentine or a mixture spectrally dominated by non-serpentine.

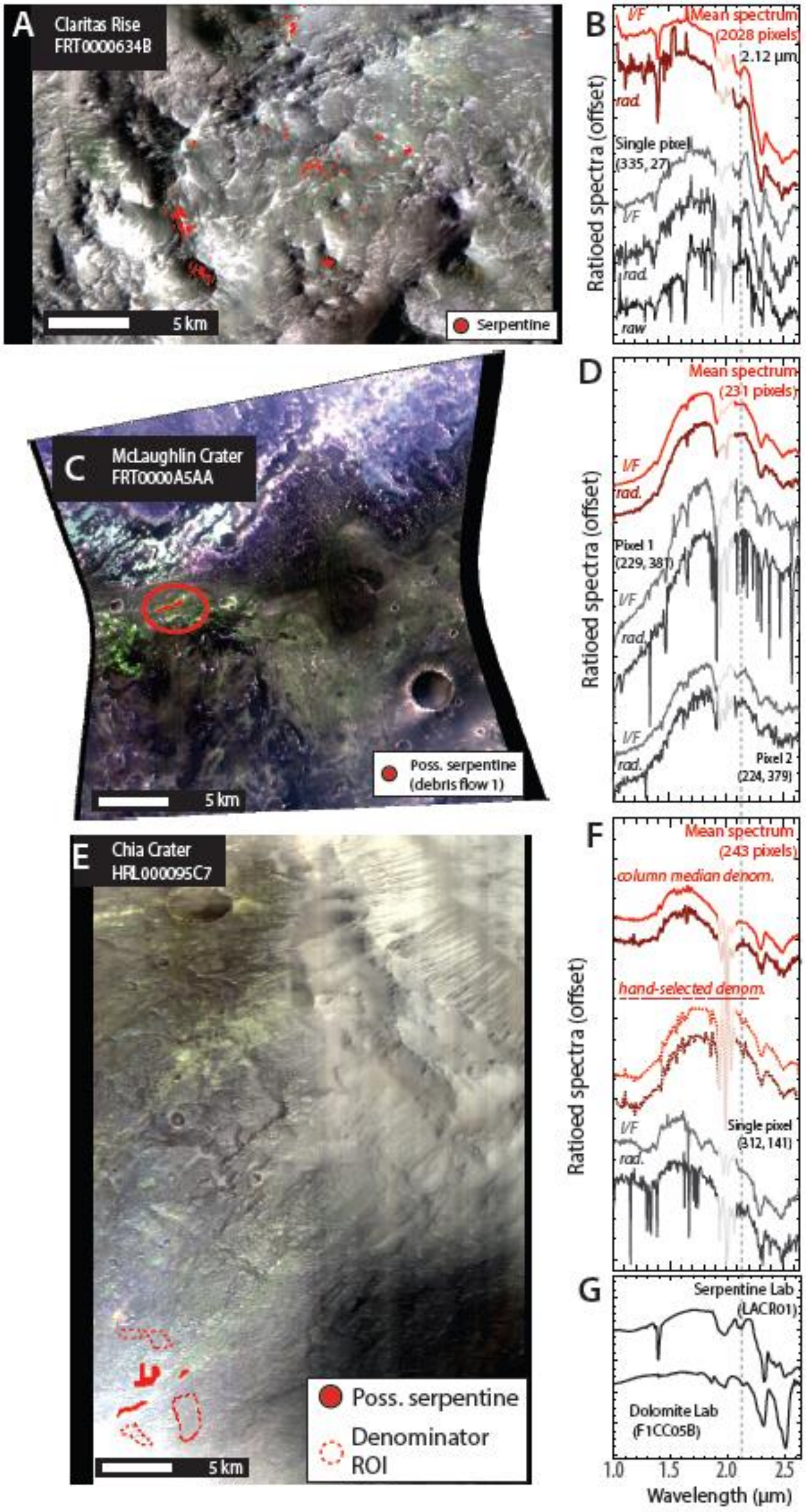

Figure 4-3. Analysis of previously reported serpentine detections. Serpentine detections at Claritas Rise (a-b) remain robust in radiance data in single-pixel and mean spectra. Mean spectra for proposed serpentine detections at McLaughlin (c-d) and Chia (e-f) craters show marginal 2.12-µm absorptions when examined in radiance data. At McLaughlin, some of the proposed serpentine pixels retain a 2.12-µm absorption in radiance data ((d), pixel 2) while others are clearly artifacts ((d), pixel 1). At Chia crater, none of the single pixels examined have a robust 2.12-µm absorption in radiance data when basic column-median ratios are used. However, when spectrally bland regions selected by hand are used for the denominator, a narrow 2.12-µm absorption persists in radiance data.

4.4 Perchlorates

Hydrated chlorine salts (e.g. perchlorates) are found in hyperarid conditions in trace amounts on Earth ($\leq$0.6 wt %; Ericksen (1981)). On Mars, they were measured at 0.4-0.6 wt. % by the Phoenix lander (Hecht et al., 2009) and are also indicated at 0.05-1.05 wt. % in multiple samples measured by MSL (Sutter et al., 2017). Perchlorate minerals can depress the melting point of water to 204K (Hanley et al., 2012), and so have been put forth as a way to maintain liquid brines on the martian surface. They can have multiple cations and are identified by absorptions at 1.43, 1.92, 2.14, and 2.42 µm (sodium perchlorate; Hanley et al., 2015). We examined results from two prior studies that reported detection of hydrated oxychlorine salts, possibly perchlorates and/or chlorates, in remote sensing data (Ojha et al., 2015; Massé et al., 2010).

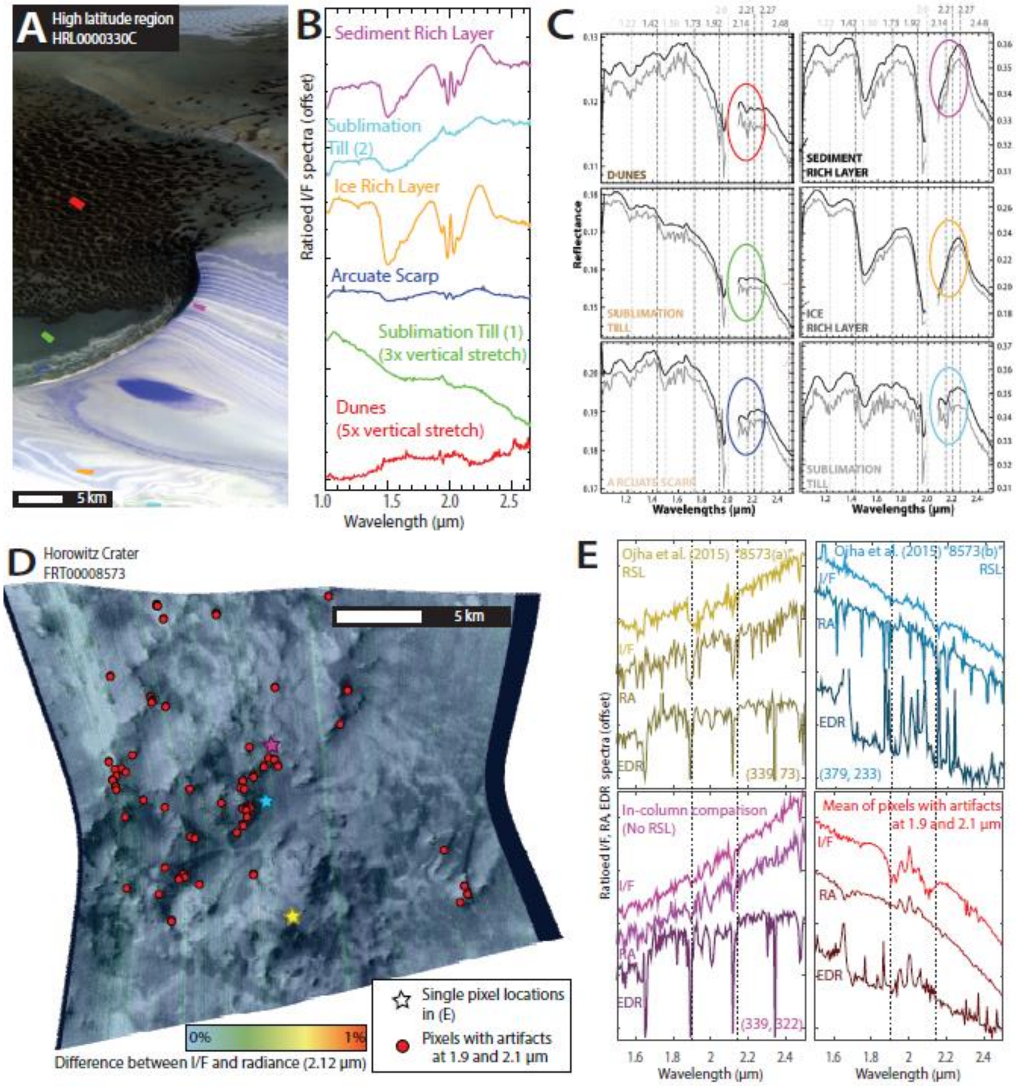

Figure 4-4. Potential perchlorate detections at high-latitudes (a-c) and associated with recurring slope lineae (RSL; d-e). (a) We approximate the regions of interest presented in Massé et al. (2010). (b) mean spectra are ratioed to column averages that exclude ice-rich regions. (c) Unratioed spectra of the regions presented in Massé et al. (2010) as possible perchlorates show a small absorption at 2.14 μm, which disappears in ratioed spectra in (b); it may be a result of an imperfect atmospheric correction. (d) Horowitz Crater, showing distribution of RSLs, pixels with artifacts, and proposed single-pixel perchlorate detections in from Ojha et al. (2015). Corresponding spectra in (e) show that potential absorptions in single-pixel spectra are coincident with column-dependent spikes in raw data. Other artifact pixels are found throughout the image (not correlated with RSL), and the apparent absorptions in I/F do not persist in radiance or raw data (red, (e)).

4.1.1 High latitude perchlorates?

Massé et al. (2010) examined unratioed I/F data from OMEGA (Observatoire pour la Minéralogie, l'Eau, les Glaces, et l'Activité) and CRISM, and found that about 30% of the pixels in a CRISM northern polar image (FRT0000330C) have a small absorption at 2.14 µm, which they suggested might be due to perchlorate (Fig. 4c). They used the targeted reduced data record, version 2 (TRR2) data available at the time. We reprocessed the CRISM image using version 3 (TRR3) data and tested the effects of different atmospheric corrections on unratioed data. The shape and position of the 2.14-µm feature changes, and even disappears completely in some instances, depending on the correction spectrum used (Fig. S13). Since there is a small absorption caused by CO_2 located at 2.15 µm (Fig. S13c), we believe that this proposed perchlorate detection may be the result of an imperfect atmospheric correction. Ratioed data– both I/F and radiance – show clear ice absorptions, but no 2.14-µm absorption (Fig. 4b), regardless of the choice of denominator.

4.1.2 Perchlorates in RSL?

Ojha et al. (2015) presented several possible pixel-scale detections of perchlorates from 2 different sites with recurring slope lineae (RSL), in Horowitz and Palikir craters. They found pixels with an absorption-like feature centered near ~2.14 µm (as well as 1.9 µm), and attributed the absorption to perchlorates, postulating their source was liquid brine from the RSLs. However, our analysis shows that of these pixels (Figs. 4d-e, S14, S16-17), only one might possess a narrow, shallow 2.14 µm absorption in the ratioed radiance and raw data (Fig. 4e, yellow spectra). However, many other pixels in the same column as the single pixel that are far from the RSL have a similar shape, suggesting it may be a column-dependent artifact (e.g. Fig. 4e, purple spectra). Additionally, we located >100 other pixels in the same image with strong spurious 1.9 and 2.1-µm absorptions within I/F data (red, Fig. 4d-e). When these pixels with strong apparent absorptions were investigated in radiance and raw data, the absorptions all disappeared using our data processing methods. This suggests that most minor 2.14-µm absorptions reported for RSL are likely spurious. Robust identification of hydrated chlorine salts thus should include corroboration from radiance data and the presence of a relatively broad, strong 3-µm absorption.

5 Conclusions

We have found a new artifact in CRISM I/F data that mimics the characteristics of real mineral absorptions. The "spurious absorption"-type artifact is most prevalent at 1.9 and 2.1 µm, also common at

~2.5 µm, and occurs less frequently throughout the 1.0-2.65 µm wavelength range examined. It occurs as scattered single- or few-pixel clusters in ~90% of the >300 images we investigated. It appears to be related to the interaction between areas of high spectral or spatial variance in radiance, and a data filtering step designed to remove spikes that is thresholded by the local variance. The spurious absorptions are most prevalent at 1.9 and 2.1 µm because of the interaction of real atmospheric absorptions and the filtering procedure designed to remove the spikes, creating spurious absorptions in adjacent channels which mimic spectral characteristics of real features.

Previously reported detections that utilize the 2.1-µm spectral region, including monohydrated sulfate, alunite, and most serpentine detections, are robust and persist in radiance spectra for most previously reported occurrences; however, a few serpentine spectra were not confirmed, and we were unable to confirm any of the published orbital perchlorate detections using the 1.0-2.65 µm wavelength range. Perchlorate has been proposed as a way to achieve transiently wet, possibly habitable conditions at Mars' surface (Rummel et al., 2014), as well as serve as a marker for recent liquid brines (Ojha et al., 2015). As orbital detections of perchlorate require high concentrations (>~5%), relatively large reservoirs of this mineral (compared to the Phoenix lander detections) have been invoked as a mechanism for allowing liquid water (brines) to exist at temperatures as low as -70°C (Hanley et al., 2012), providing potentially habitable environments on modern Mars (e.g. Rampe et al., 2018). While our non-detection of perchlorate does not preclude the possibility that perchlorates exist in small amounts in martian materials, it means that there is no orbitally-identified major freezing point depressant or evaporite product. Models for RSL formation need not account for the presence of perchlorate-enriched brines, allowing for dry RSL formation mechanisms (e.g. Dundas et al., 2017) or waters of different composition.

The occasional creation of spurious absorptions near atmospheric features interferes in the search for rare mineral phases, especially those such as perchlorate with absorptions in the 1.9 and 2.1-µm regions. However, in no case was the artifact observed to be contiguous over more than 12 pixels. This suggests straightforward steps to mitigate this effect for accurate identification of few-pixel-scale mineral outcrops in CRISM TRR3 I/F data: corroborate the detections using ratioed radiance data, reproduce the detections in multiple I/F images, and (for hydrated minerals) demonstrate occurrence of a 3-µm band due to molecular H2O. Future CRISM data processing pipelines may include further optimizations to the spike-removal procedure to reduce such spurious absorptions.

Acknowledgments and Data

Thanks to K. Seelos and M. Parente for suggestions of tests during presentations of early versions of this work to the CRISM team. Funding for this work was provided in part by an NSERC PGS-D scholarship (E.K.L.), a NASA/JPL grant to B.L.E. to support CRISM investigations, and the Rose Hills Foundation. A part of this research was sponsored by the National Science Foundation (NSF) under Grant Number IIS-1252648 (CAREER) to M.M.D.. The content is solely the responsibility of the authors and does not necessarily represent the official views of NSF. All CRISM data used in this paper are publicly available through the PDS node (http://ode.rsl.wustl.edu/mars/).

4.6 References

Bishop, J., Lane, M., Dyar, M., & Brown, A. (2008). Reflectance and emission spectroscopy study of four groups of phyllosilicates: Smectites, kaolinite-serpentines, chlorites and micas. Clay Minerals, 43(1), 35-54.

Bishop, J. L., Dobrea, E. Z. N., McKeown, N. K., Parente, M., Ehlmann, B. L., Michalski, J. R., et al. (2008). Phyllosilicate diversity and past aqueous activity revealed at Mawrth Vallis, Mars. Science, 321(5890), 830-833.

Carter, J., Loizeau, D., Mangold, N., Poulet, F., & Bibring, J.-P. (2015). Widespread surface weathering on early Mars: A case for a warmer and wetter climate. Icarus, 248, 373-382.

Carter, J., Poulet, F., Bibring, J. P., Mangold, N., & Murchie, S. (2013). Hydrous minerals on Mars as seen by the CRISM and OMEGA imaging spectrometers: Updated global view. Journal of Geophysical Research: Planets, 118(4), 831-858.

Catling, D., Claire, M., Zahnle, K., Quinn, R., Clark, B., Hecht, M., & Kounaves, S. (2010). Atmospheric origins of perchlorate on Mars and in the Atacama. Journal of Geophysical Research: Planets, 115(E1).

Clark, R. N., Swayze, G. A., Wise, R., Livo, K. E., Hoefen, T., Kokaly, R. F., & Sutley, S. J. (2007). USGS digital spectral library splib06a. US geological survey, digital data series, 231, 2007.

Cloutis, E. A., Hawthorne, F. C., Mertzman, S. A., Krenn, K., Craig, M. A., Marcino, D., et al. (2006). Detection and discrimination of sulfate minerals using reflectance spectroscopy. Icarus, 184(1), 121-157.

Dundar, M., & Ehlmann, B. L. (2016). Rare jarosite detection in crism imagery by non-parametric Bayesian clustering. Paper presented at the Hyperspectral Image and Signal Processing: Evolution in Remote Sensing (WHISPERS), 2016 8th Workshop on.

Dundas, C. M., McEwen, A. S., Chojnacki, M., Milazzo, M. P., Byrne, S., McElwaine, J. N., & Urso, A. (2017). Granular flows at recurring slope lineae on Mars indicate a limited role for liquid water. Nature Geoscience, 10(12), 903.

Ehlmann, B., Mustard, J., & Murchie, S. (2010). Geologic setting of serpentine deposits on Mars. Geophysical research letters, 37(6).

Ehlmann, B. L., Mustard, J. F., Murchie, S. L., Poulet, F., Bishop, J. L., Brown, A. J., et al. (2008). Orbital identification of carbonate-bearing rocks on Mars. Science, 322(5909), 1828-1832.

Ericksen, G. E. (1981). Geology and origin of the Chilean nitrate deposits: USGPO: for sale by the Supt. of Docs., GPO.

Evans, B. W. (2004). The serpentinite multisystem revisited: chrysotile is metastable. International Geology Review, 46(6), 479-506.

Gaffey, S. J. (1986). Spectral reflectance of carbonate minerals in the visible and near infrared (O. 35-2.55 microns); calcite, aragonite, and dolomite. American Mineralogist, 71(1-2), 151-162.

Gendrin, A., Mangold, N., Bibring, J.-P., Langevin, Y., Gondet, B., Poulet, F., et al. (2005). Sulfates in martian layered terrains: the OMEGA/Mars Express view. Science, 307(5715), 1587-1591.

Hanley, J., Chevrier, V. F., Barrows, R. S., Swaffer, C., & Altheide, T. S. (2015). Near-and mid-infrared reflectance spectra of hydrated oxychlorine salts with implications for Mars. Journal of Geophysical Research: Planets, 120(8), 1415-1426.

Hanley, J., Chevrier, V. F., Berget, D. J., & Adams, R. D. (2012). Chlorate salts and solutions on Mars. Geophysical research letters, 39(8).

Hecht, M., Kounaves, S., Quinn, R., West, S., Young, S., Ming, D., et al. (2009). Detection of perchlorate and the soluble chemistry of martian soil at the Phoenix lander site. Science, 325(5936), 64-67.

Hunt, G. R. (1971). Visible and near-infrared spectra of minerals and rocks. VI. Sulfides and sulfates. Modern Geology(3), 1-14.

Hunt, G. R. (1977). Spectral signatures of particulate minerals in the visible and near infrared. Geophysics, 42(3), 501-513.

Massé, M., Bourgeois, O., Le Mouélic, S., Verpoorter, C., Le Deit, L., & Bibring, J.-P. (2010). Martian polar and circum-polar sulfate-bearing deposits: Sublimation tills derived from the North Polar Cap. Icarus, 209(2), 434-451.

McEwen, A. S., Dundas, C. M., Mattson, S. S., Toigo, A. D., Ojha, L., Wray, J. J., et al. (2014). Recurring slope lineae in equatorial regions of Mars. Nature Geoscience, 7(1), 53.

McGuire, P. C., Bishop, J. L., Brown, A. J., Fraeman, A. A., Marzo, G. A., Morgan, M. F., et al. (2009). An improvement to the volcano-scan algorithm for atmospheric correction of CRISM and OMEGA spectral data. Planetary and Space Science, 57(7), 809-815.

Michalski, J. R., Cuadros, J., Niles, P. B., Parnell, J., Rogers, A. D., & Wright, S. P. (2013). Groundwater activity on Mars and implications for a deep biosphere. Nature Geoscience, 6(2), 133.

Millour, E., Forget, F., Spiga, A., Colaitis, A., Navarro, T., Madeleine, J.-B., et al. (2012). Mars climate database version 5.

Murchie, S., Arvidson, R., Bedini, P., Beisser, K., Bibring, J. P., Bishop, J., et al. (2007). Compact reconnaissance imaging spectrometer for Mars (CRISM) on Mars reconnaissance orbiter (MRO). Journal of Geophysical Research: Planets (1991–2012), 112(E5).

Murchie, S. L., Mustard, J. F., Ehlmann, B. L., Milliken, R. E., Bishop, J. L., McKeown, N. K., et al. (2009a). A synthesis of martian aqueous mineralogy after 1 Mars year of observations from the Mars Reconnaissance Orbiter. Journal of Geophysical Research: Planets, 114(E2).

Murchie, S. L., Seelos, F. P., Hash, C. D., Humm, D. C., Malaret, E., McGovern, J. A., et al. (2009b). Compact Reconnaissance Imaging Spectrometer for Mars investigation and data set from the Mars Reconnaissance Orbiter's primary science phase. Journal of Geophysical Research: Planets (1991–2012), 114(E2).

Murchie, S. G., Edward; Slavney, Susan. (2016). Mars Reconnaissance Orbiter CRISM Data Product Software Interface Specification, Version 1.3.7.4.

Mustard, J. F., Murchie, S., Pelkey, S., Ehlmann, B., Milliken, R., Grant, J., et al. (2008). Hydrated silicate minerals on Mars observed by the Mars Reconnaissance Orbiter CRISM instrument. Nature, 454(7202), 305-309.

Ojha, L., McEwen, A., Dundas, C., Byrne, S., Mattson, S., Wray, J., et al. (2014). HiRISE observations of recurring slope lineae (RSL) during southern summer on Mars. Icarus, 231, 365-376.

Ojha, L., Wilhelm, M. B., Murchie, S. L., McEwen, A. S., Wray, J. J., Hanley, J., et al. (2015). Spectral evidence for hydrated salts in recurring slope lineae on Mars. Nature Geoscience, 8(11), 829.

Oze, C., & Sharma, M. (2005). Have olivine, will gas: serpentinization and the abiogenic production of methane on Mars. Geophysical research letters, 32(10).

Poulet, F., Bibring, J.-P., Mustard, J., Gendrin, A., Mangold, N., Langevin, Y., et al. (2005). Phyllosilicates on Mars and implications for early martian climate. Nature, 438(7068), 623.

Rampe, E. B., Cartwright, J. A., McCubbin, F. M., & Osterloo, M. M. (2018). The role of halogens during fluid and magmatic processes on Mars, The Role of Halogens in Terrestrial and Extraterrestrial Geochemical Processes (pp. 959-995): Springer.

Roach, L., Mustard, J., Murchie, S., Bibring, J. P., Forget, F., Lewis, K., et al. (2009). Testing evidence of recent hydration state change in sulfates on Mars. Journal of Geophysical Research: Planets, 114(E2).

Roach, L. H., Mustard, J. F., Swayze, G., Milliken, R. E., Bishop, J. L., Murchie, S. L., & Lichtenberg, K. (2010). Hydrated mineral stratigraphy of Ius Chasma, Valles Marineris. Icarus, 206(1), 253-268.

Rummel, J. D., Beaty, D. W., Jones, M. A., Bakermans, C., Barlow, N. G., Boston, P. J., et al. (2014). A new analysis of Mars “special regions”: findings of the second MEPAG Special Regions Science Analysis Group (SR-SAG2): Mary Ann Liebert, Inc. 140 Huguenot Street, 3rd Floor New Rochelle, NY 10801 USA.

Schulte, M., Blake, D., Hoehler, T., & McCollom, T. (2006). Serpentinization and its implications for life on the early Earth and Mars. Astrobiology, 6(2), 364-376.

Sutter, B., Mcadam, A. C., Mahaffy, P. R., Ming, D. W., Edgett, K. S., Rampe, E. B., et al. (2017). Evolved gas analyses of sedimentary rocks and eolian sediment in gale crater, mars: results of the curiosity Rover's Sample Analysis at Mars (SAM) instrument from Yellowknife Bay to the Namib Dune. Journal of Geophysical Research: Planets.

Swayze, G., Desborough, G., Clark, R., Rye, R., Stoffregen, R., Smith, K., & Lowers, H. (2006). Detection of jarosite and alunite with hyperspectral imaging: prospects for determining their origin on Mars using orbital sensors. Paper presented at the Workshop on martian Sulfates as Recorders of Atmospheric-Fluid-Rock Interactions.

Viviano-Beck, C. E. e. a. (2015). MRO CRISM Type Spectra Library. from http://crismtypespectra.rsl.wustl.edu

Wiseman, S., Arvidson, R., Wolff, M., Smith, M., Seelos, F., Morgan, F., et al. (2016). Characterization of artifacts introduced by the empirical volcano-scan atmospheric correction commonly applied to CRISM and OMEGA near-infrared spectra. Icarus, 269, 111-121.

Wolff, M., Smith, M., Clancy, R., Arvidson, R., Kahre, M., Seelos, F., et al. (2009). Wavelength dependence of dust aerosol single scattering albedo as observed by the Compact Reconnaissance Imaging Spectrometer. Journal of Geophysical Research: Planets, 114(E2).

Wray, J., Murchie, S., Ehlmann, B., Milliken, R., Seelos, K., Noe Dobrea, E., et al. (2011). Evidence for regional deeply buried carbonate-bearing rocks on Mars. Paper presented at the Lunar and Planetary Science Conference.

Yerebakan, H. Z., Rajwa, B., & Dundar, M. (2014). The infinite mixture of infinite Gaussian mixtures. Paper presented at the Advances in neural information processing systems.

Chapter 5

EVIDENCE FOR DEPOSITION OF CHLORIDE ON MARS FROM SMALL-VOLUME SURFACE WATER EVENTS INTO THE LATE HESPERIAN-EARLY AMAZONIAN

E. K. Leask[1] and B. L. Ehlmann[1, 2]

[1] Division of Geological and Planetary Sciences, California Institute of Technology, Pasadena, CA, USA

[2] Jet Propulsion Laboratory, California Institute of Technology, Pasadena, CA, USA

Abstract

We investigate the environmental settings of chloride deposits across Mars' southern highlands, looking at all available high resolution imagery, building digital elevation models from stereo pairs, and searching all targeted CRISM images intersecting chloride deposits for accessory minerals like clay, carbonate, and sulphate. We find that the chloride deposits are commonly draped on top of underlying topography, often associated with channels, found at a wide range of elevations, and sometimes perched above deep craters. Where digital elevation models were available, we find that the deposits range in elevation over tens of meters, inconsistent with playa-like environments (which are very flat). Where possible, we measured chloride thickness in the middle of deposits, and found that they were usually <1 m-3 m; we only saw thicker measurements at deposit edges, where draping could skew the measurement. Chloride deposits within larger basins were generally asymmetric, with chloride deposits much higher on the side with inlet channels, indicating that (a) surface water runoff was the most likely source, and (b) the basins were likely not filled completely with water in a deep lake setting, but rather a series of shallow ponds. While chloride deposits are almost all in Noachian terrain, a small number are in channels on top of more recent volcanic terrain (3.4-2.3 Ga), indicating that the processes creating chloride deposits continued through the Hesperian and into the Amazonian. Small amounts of meltwater and/or deliquescence could be an episodic water source, while chloride anions could be derived from surface layer of dust/soil, perhaps brought to the surface by capillary action in clay rich soils prevalent in Noachian terrain.

Plain Language Summary

Chloride salt deposits on Mars are intriguing because they represent the last stage of water present at Mars' surface. They are found across the ancient, clay-rich, southern highlands of Mars, but also sometimes on top of younger volcanic regions, around the edges of the ancient terrain. As a result, we think that they are much younger than the underlying ancient terrain, continuing to form as recently as 2.3 billion years ago. These salt deposits are different to salt flats on Earth, because they occur over a range of elevations and sometimes on slopes, rather than in one flat area. While the martian salts are found in small depressions, they are often perched above much deeper craters which do not contain any chloride. They are also often found in channels. For these reasons, we think that the water source came from surface runoff, rather than deep groundwater welling up to the surface. Small amounts of water could be from occasional melting of surface ice or permafrost (e.g. seasonal, or when a volcano heats it

up), or from minerals that absorb water vapor directly from the air, and turn into a salty liquid. Chloride could come from the top part of the soil; clay-rich soils can form a salt crust when evaporation pulls water and dissolved salt up from the top ~ meter of soil.

1 Introduction

Chloride deposits on Mars, first identified by Osterloo et al. (2008), are of particular interest because they reflect the last surface water present at a given location on the surface, because subsequent water events would dissolve them. These light-toned, indurated features are found throughout the southern highlands, have been described as Noachian to early Hesperian in age, and are small deposits (<1 km^2 -~1000km^2) often found in local topographic depressions, sometimes with channel-like features (Osterloo et al., 2008; Osterloo et al., 2010). In high-resolution imagery, many of these deposits appear to have polygonal fractures and/or ridges, which have been interpreted as salt polygons or desiccation features (Osterloo et al., 2010; El Maarry et al., 2013; Ye et al., 2019). However, unlike many other minerals identified on Mars by remote sensing of characteristic absorption and emission features (clays, sulphates, olivine, pyroxene, silicates), chloride minerals have no such features; instead, they are inferred by ruling out other possible minerals with the same properties (diminished water content in the shortwave infrared OH/H2O absorption and no mid-infrared wavelengths with E~1) that might exhibit the same properties. For example, sulphides and diamonds could also have these properties, but sulphides rarely occur in km^2 exposures and would typically be darker, associated with volcanics if found in topographic lows, and accompanied by sulphate weathering products; large diamond exposures are geologically implausible. Halite (sodium chloride) has been identified in martian meteorites (Bridges and Grady, 2000), and elevated levels of both Na and Cl have been measured in situ on Mars, interpreted as halite (Ming et al., 2006 (Gusev); Knoll et al., 2008 (Meridiani); Thomas et al., 2019 (Gale)).

Previous chloride formation hypotheses include ponding and evaporation of surface water and/or upwelled groundwater (favoured by Osterloo et al., 2010; Glotch et al., 2010; Melwani Daswani and Kite, 2017; El Maarry et al., 2013), from deep lakes or playas, hydrothermal brines (volcanic or impact related), or efflorescent crust. Strictly volcanic sources have been discounted due to lack of spatial association with volcanics and lack of the accessory minerals (sulphates, silica) expected in this setting. On Earth, evaporating lakes and playas tend to leave behind zoned salts (Eugster and Hardie, 1978), corresponding to progressively more soluble minerals (generally carbonates, sulphates, then chlorides), while hydrothermal brines will often deposit silica and sulphates along with chlorides. Thus far, only phyllosilicates have been found in association with chloride minerals (Murchie et al., 2009; Glotch et al., 2010; Huang et al., 2018; Ruesch et al., 2012; El Maarry et al., 2013), found in 10% (Ruesch et al., 2012) to 30 % (El Maarry et al., 2013) of chloride deposits investigated. Deep lakes, as interpreted by Hynek et al. (2015) and Melwani Daswani and Kite (2017), would require large volumes of water present at Mars' surface; therefore, constraining both water depth and timing is important for our understanding of the evolution of water at Mars' surface.

Since the initial detection of chloride deposits, they have been selected as targets for high resolution CRISM (Compact Reconnaissance Imaging Spectrometer for Mars) and HiRISE (High Resolution Imaging Science Experiment) data, and sufficient CTX (ConTeXt Camera) data is available for a global mosaic to provide context for these deposits. CRISM data are used to search for other minerals (e.g. sulphates, carbonates, clays) that might be present with chlorides, and help us understand the water chemistry from which they evaporated. Of the previous global-scale studies, Ruesch et al. (2012) use OMEGA data with spatial resolution better than 2.5 km/pixel; CRISM's spatial resolution is >100x better, so we expect to find smaller deposits below its resolution. El-Maarry et al. (2013) investigated 43 chloride locations with CRISM images, looking explicitly for Fe/Mg phyllosilicates; we expand to all deposits with targeted CRISM images, and search for small deposits of rare, hydrated minerals. High resolution imagery (CTX and HiRISE) are used to understand the context and morphology of deposits, while stereo image pairs are used to build digital elevation models (DEMs) to better understand the stratigraphic relationships between geologic units. These data can help us unravel the outstanding questions about the water source (surface runoff vs. groundwater upwelling), probable chloride source (with accessory minerals and morphology), water volume (deep lakes or ponds), and timing of the deposits.

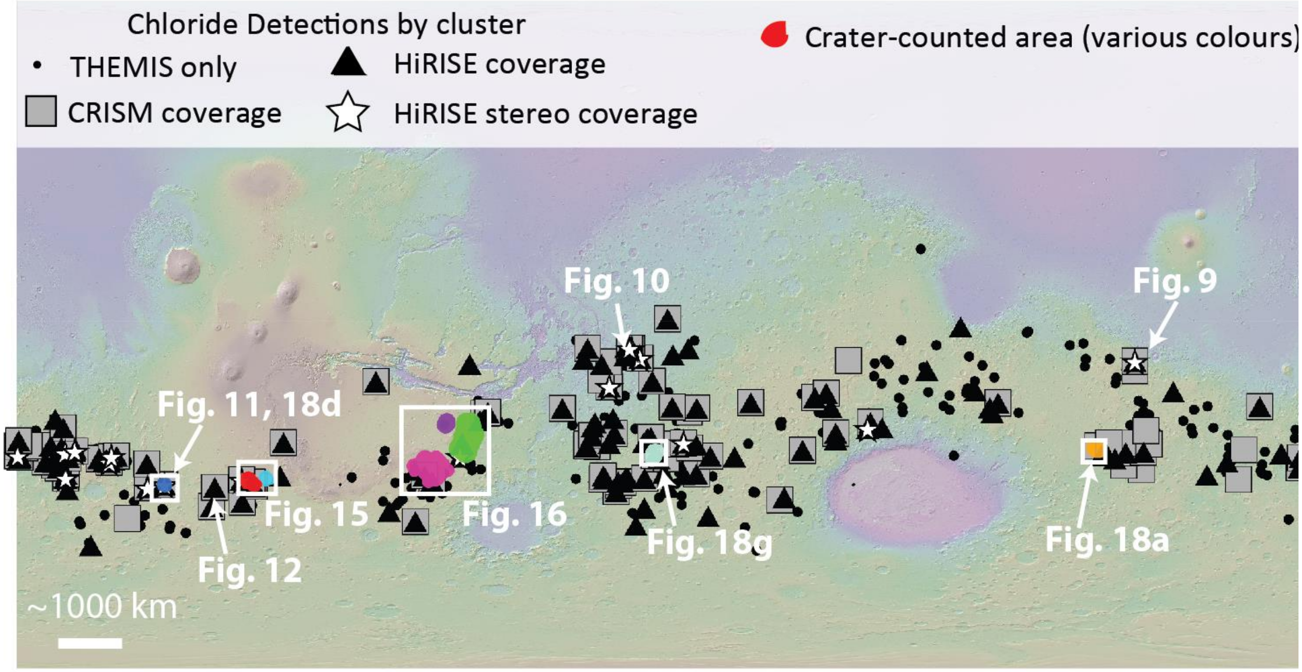

Fig 5-1. THEMIS chloride detections by cluster and type of high-resolution data available. Crater-counted areas are shown as coloured regions to highlight the large areas used for robust age dates. Sites of interest in later figures are identified here, showing the global distribution.

2 Methods

For this work, we exported approximate chloride polygons from JMARS (Osterloo et al., 2010) into ArcGIS, and used CRISM footprints (downloaded from NASA's Planetary Data System (PDS)) to find all CRISM targeted long wavelength data (158 +8 nearby, covering 119/642 chloride deposits), HiRISE (273 images over 177 deposits), and HiRISE stereo images (29 pairs over 21 deposits) that intersected the chloride polygons (Fig. 1). Because there are often many small chloride deposit polygons clustered together, we used ArcGIS tools to draw a 10km buffer around the polygons and aggregated those whose buffers intersected, assuming that they likely shared a genetic relationship due to spatial proximity (e.g. Fig. 2). Instead of 642 initial chloride deposits, we then have 392 chloride deposit clusters (with CRISM coverage in 97 clusters, HiRISE colour in 123 clusters, and HiRISE stereo in 17 clusters). 387/392 deposits have CTX coverage over the chloride deposit.

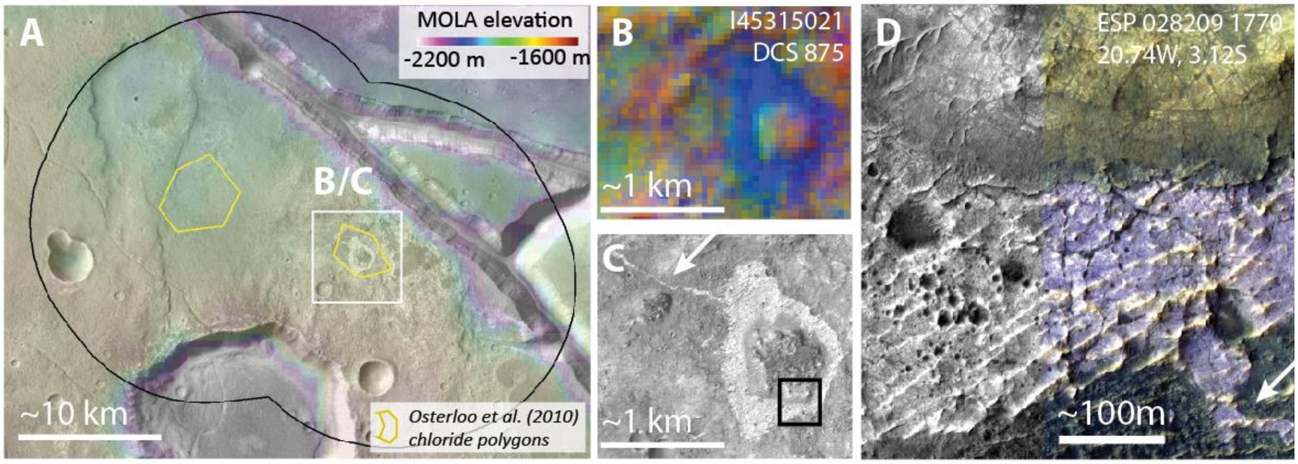

Fig. 5-2. Chloride cluster example with 10km buffer (chaos terrain in Margaritifer Terra, 20.74° W, 3.12° S). (A) Chloride deposits are perched above a crater and deep fractures within the 10 km buffer. (B) Chloride deposit in THEMIS 875 decorrelation stretch (blue tones); fine scale channels not visible at this resolution (100 m/pixel). (C) Same chloride deposit at CTX resolution (6 m/pixel), where fine channels are visible (e.g. white arrow near top of image). (D) Chloride deposit appears light purple in HiRISE colour, making it possible to distinguish boundaries of the chloride deposit when it is adjacent to other light toned fractured units (greyscale (left) vs colour (right) in D). A small chloride-filled channel is present in the lower right (white arrow). Chloride has a sharp contact with surrounding units, and appears to drape SW-NE trending dune-like features.

2.1 CRISM analysis

At full resolution, the CRISM instrument takes hyperspectral images of Mars' surface at ~18 m/pix, covering a wavelength range of 0.36-3.9 μm (Murchie et al., 2007). For this study, we use data from the longer wavelength sensor (~1-3.9 μm; 438 channels) which covers key absorptions for hydrated minerals. Targeted CRISM I/F images (downloaded from PDS) were atmospherically corrected using the CRISM Analysis Toolkit (Morgan et al., 2009) in ENVI (photometrically corrected (division by cos(i)), atmospheric correction using the default 61C4 volcano scan, after McGuire et al. (2009)). Images were then ratioed using a simple column median denominator. If ratioing artefacts were suspected during analysis, a small bland area was chosen as a denominator to ensure that the features persisted using a different denominator. Because many of the CRISM image cubes covering chlorides were taken later in the mission (after cooler difficulties arose), CRISM images are significantly noisier than those earlier in the mission, and so band depth calculations on unsmoothed data tend to show only noise. To mitigate this issue, we used an 11x11x11 spatial/spectral median filter to smooth the image before calculating band parameters. For each CRISM image, we used these band parameter maps calculated on smoothed data in tandem with ratioed, unsmoothed data to verify mineral detections. Specifically, we focused on the band depths at 1.9, 2.1, 2.2, 2.3, and 2.5 μm, in addition to the slope at 2.4 μm. Together, these regions allow detection of hydrated minerals such as Fe/Mg clays (e.g. nontronite, saponite), Al-clays (e.g. kaolinite , montmorillonite), serpentine, carbonate, and mono- and poly-hydrated sulphates, as well as water ice. For images where we found Fe/Mg clays, whose absorptions at 1.9 and 2.3 µm can overlap with carbonates, we also looked at the 3-4 µm part of the spectrum to look for features at 3.4 and 3.9 µm associated with carbonates. However, the smoothing necessary to work with noisy images can also obscure deposits that are <100 pixels in size.

2.2 Morphology and elevation

We use a global CTX mosaic (6m/pix) (Dickson et al., 2018) together with the gridded MOLA (Mars Orbiting Laser Altimeter) elevation product (463 m/pixel, e.g. Smith et al., 2001), available for almost all clusters. Here, within the 10 km buffer connecting all parts of each chloride cluster, we look for: sinuous channels (e.g. Fig. 2c), whether they are sometimes filled with light-toned unit, the range of elevation amongst chloride deposits in the cluster, and the difference between the lowest chloride elevation and the lowest point in the 10 km buffer zone to determine whether the chloride appears to be perched (Fig. 3b, Fig. 4).

We chose to focus on HiRISE colour images (25 cm/pixel, with band centres at 536 nm (blue-green), 694 nm (red), and 874 nm (near infrared); McEwen et al., 2007; Delamere et al., 2010) because in greyscale HiRISE images, fractured clay bearing units can look morphologically indistinguishable from the chlorides (also noted in El Maarry et al., 2013). Where both are present and CRISM data are available to confirm the mineral identification, chloride deposits appear as bright light purple (lacking the red (green in HiRISE colour) tones seen across much of Mars) and contrast with a yellow-beige tones of the clay-bearing units. We therefore use HiRISE colour imagery despite the restricted coverage (HiRISE colour is only available in the central swath of some HiRISE images), to ensure that we do not misidentify clays as chlorides at this resolution. In surveying these images, we looked for colour, fracturing, thickness (e.g. chipping, cutting by fractures, exposure by impact craters), concentric patterns, whether edges of the deposit appeared crisp or diffuse, whether they appear to be draped or in stratigraphy, whether they were at least partially within channels (Fig. 3a).

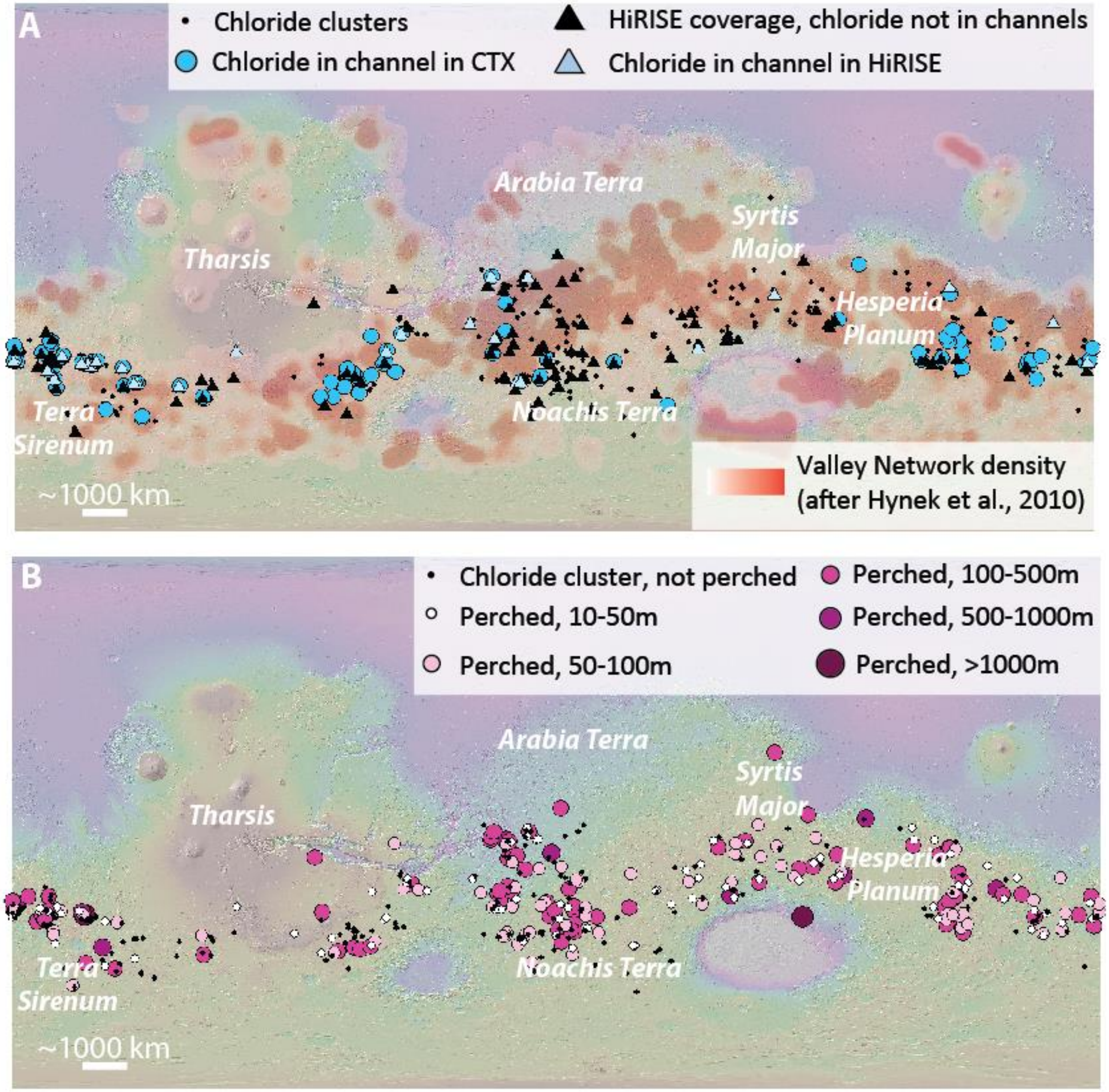

Fig 5-3. (A) Global distribution of chloride deposits within channels at CTX (blue circles) and HiRISE (blue triangles) resolution. The distribution of chloride deposits is similar to the distribution of valley networks (red tones, after Hynek et al. (2010)); this could be due to a related water source for the features, or perhaps later chloride-bearing water exploit existing channel networks. Chloride appears in channels across the globe, although the region south of Syrtis Major has fewer chloride detections within channels, despite the presence of mapped valley networks. This could be due to dust deposition or erosion, which would preferentially obscure/erase fine-scale channel details. (B) Perched chloride deposits (where there is a feature at lower elevation than the chloride within a 10 km buffer, even if the chloride is in a local topographic low) are found across the globe, with no obvious spatial trends. This pattern is consistent with surface runoff (rather than groundwater upwelling) as a primary source of water for the chloride deposits.

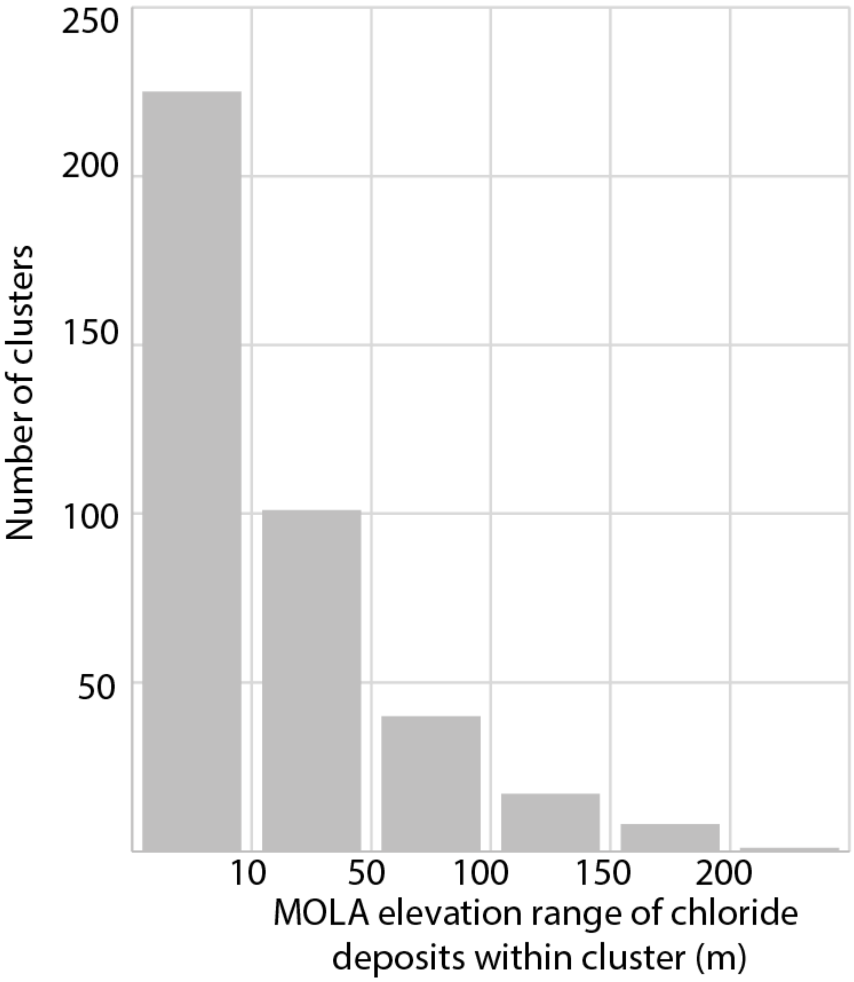

Fig 5-4. Distribution of the range of elevation between chloride deposits within a cluster. Just over half of the clusters (221/392) have <10m elevation difference between parts of a deposit, but a wide range of elevation between proximal chloride deposits (or parts of a contiguous deposit) is also common (max: 300m).

2.2.1 Digital Elevation Models (DEMs)

All HiRISE stereo pairs overlapping chloride deposits and a select subset of CTX stereo pairs were made into DEMs using the Ames Stereo Pipeline (Beyer et al., 2018). These were used to measure the thickness of chloride deposit (where possible), maximum and minimum water depths, and slope/asymmetry of deposits. High resolution LiDAR DEM of Death Valley for comparison with Earth playa topography at similar resolution was obtained through OpenTopography (dataset: Snyder, 2005).

2.3 Age dating

We first used the Tanaka et al. (2014) global geologic map to update the approximate age distribution of the chloride deposits, as the original Osterloo fans et al. (2010) survey used Tanaka (1986) and Greeley and Guest (1987). While almost all of the chloride deposit clusters are found within Noachian terrain, there are a small number of exceptions at the edges of the Tharsis and Hesperia volcanic terrains [see map]. For all of the sites, we used morphological evidence to determine if the chloride post-dates the terrain on which it lies, and used crater counting to establish the maximum possible age of the chlorides where stratigraphic relationships between sufficiently large units permitted it. Unit boundaries were determined based on breaks in slope and morphological similarities in the CTX mosaic. Most bounds were oldest-possible age bounds, established by crater counting units underlying chloride deposits. In one instance, a youngest-possible age bound could be established (see section 3.3). A CTX mosaic base layer was used for crater counting. Craters that very clearly predated the resurfacing event (entirely subdued, no topographic rim expression whatsoever) were excluded; those where the relationship was not clear were included, so as not to skew the count to too young an age. The diameters were calculated in ArcMap and exported to Craterstats2 (developed by G.G. Michael, available: http://hrscview.fu-berlin.de/software.html), using the Mars production function of Hartmann and Daubar (2017) and chronology function of Hartmann (2005) updated by Michael (2013) to determine age dates.

3 Results

3.1 Mineralogy

We find definitive Fe/Mg clay deposits in CRISM images covering 49/119 individual chloride deposits (73/158 CRISM images), or 39/97 aggregated chloride clusters (~40%). Despite explicitly searching for other accessory minerals, we only found 4 locations with any other minerals in the same CRISM image as chlorides. Three of the four are small Al-clay deposits (Fig. 5), identified by absorptions at 1.4, 1.9, and a narrow absorption at 2.2 µm. In one of these locations (Fig. 5d), there is a shoulder at 2.4 µm that could be consistent with sulphate; however, the data are too noisy for certainty. In all three Al-clay instances, the dominant mineral identified is Fe/Mg clay (thousands of pixels), and the small accessory phases (definite Al-clay, possible sulphate mixture) are not in direct contact with the chlorides, and do not appear to be genetically related. Additionally, we find one location with a carbonate spectral signature in the same image as a chloride deposit (Fig. 6). This spectrum has paired strong 2.3- and 2.5-µm absorptions consistent with magnesite (MgCO3; Fig. 6c). Here, carbonate appears to be part of the Fe/Mg clay bearing unit underlying chlorides, and cannot be distinguished morphologically from the clay bearing unit in HiRISE (Fig. 6b). Furthermore, the spectral mean for the clay bearing unit throughout the image has a minor 2.5-µm feature, consistent with a small amount of carbonate mixed with Fe/Mg bearing clays. As with the minor Al-clay detections, the carbonate does not appear to be directly related to the chloride deposit, despite proximity.

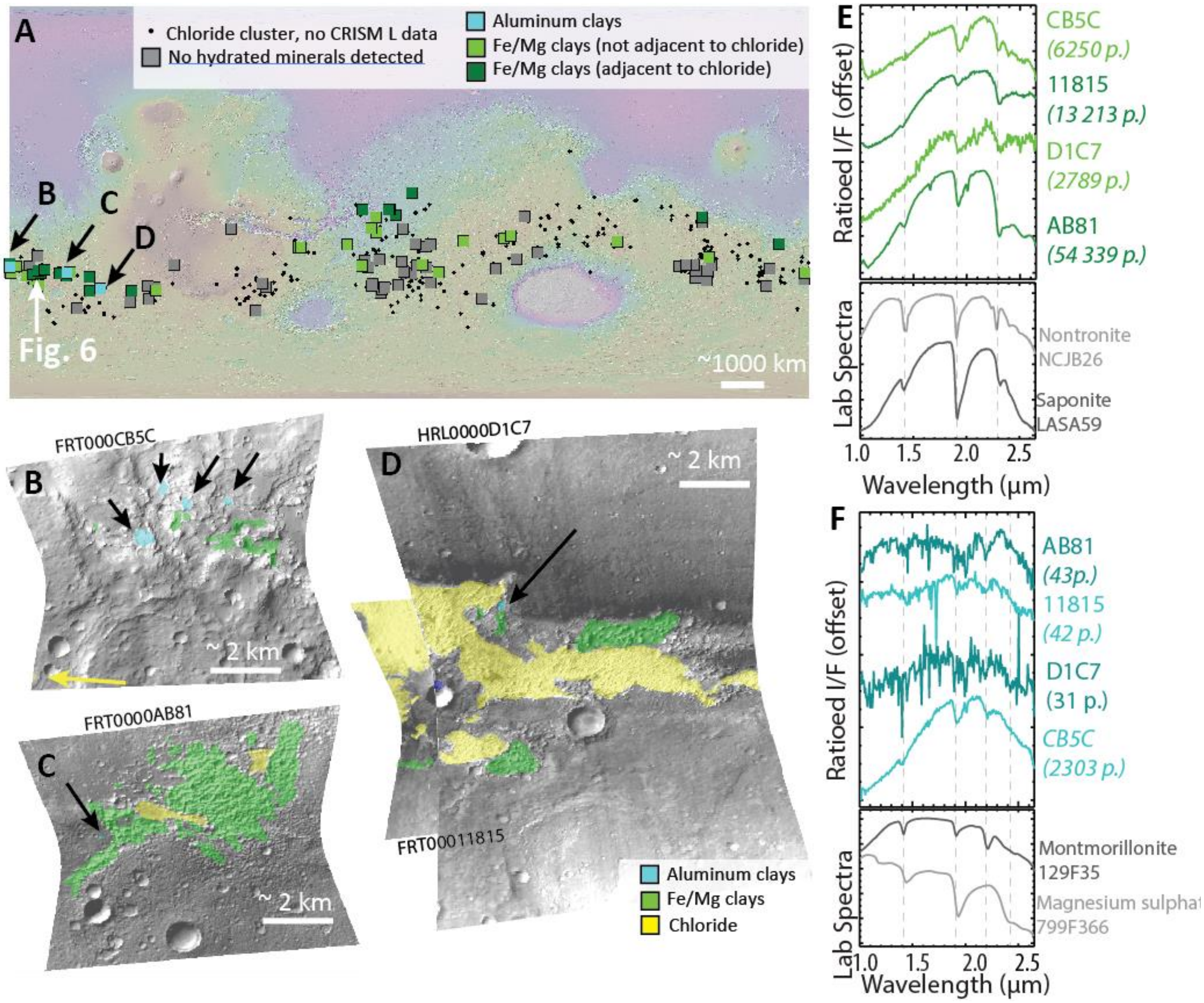

Fig 5-5. Clay/chloride associations across Mars. (A) Fe/Mg clays (green squares) are found with chlorides across Mars, in about half of the images with targeted CRISM coverage. They can occur directly in contact with chlorides (dark green squares), or nearby within the same CRISM image (light green squares). Aluminum clays are only found with chlorides in the Terra Sirenum region, west of Tharsis. (B-D) All sites with chloride and Al clay; corresponding spectra are in E and F. (B) Al clays (cyan) and Fe/Mg clays (green) are found near the edge of a chloride deposit (yellow arrow), not touching the chloride. (C) A large Fe/Mg clay bearing deposit surrounds the chloride (yellow); a small isolated patch of Al-clay is present outside the main clay deposit (black arrow); see spectra in (F). (D) Large chloride deposit in southwest Tharsis region (see fig J for detail) is partially surrounded by Fe/Mg clays, with a small patch of Al-clays (black arrow) detected in 2 overlapping CRISM images (HRL0000D1C7 & FRT00011815). Though noisy, we see these spectra (F) have hints of a 2.4 μm absorption, common in sulphate minerals; they may be Al-clay mixed with sulphate.

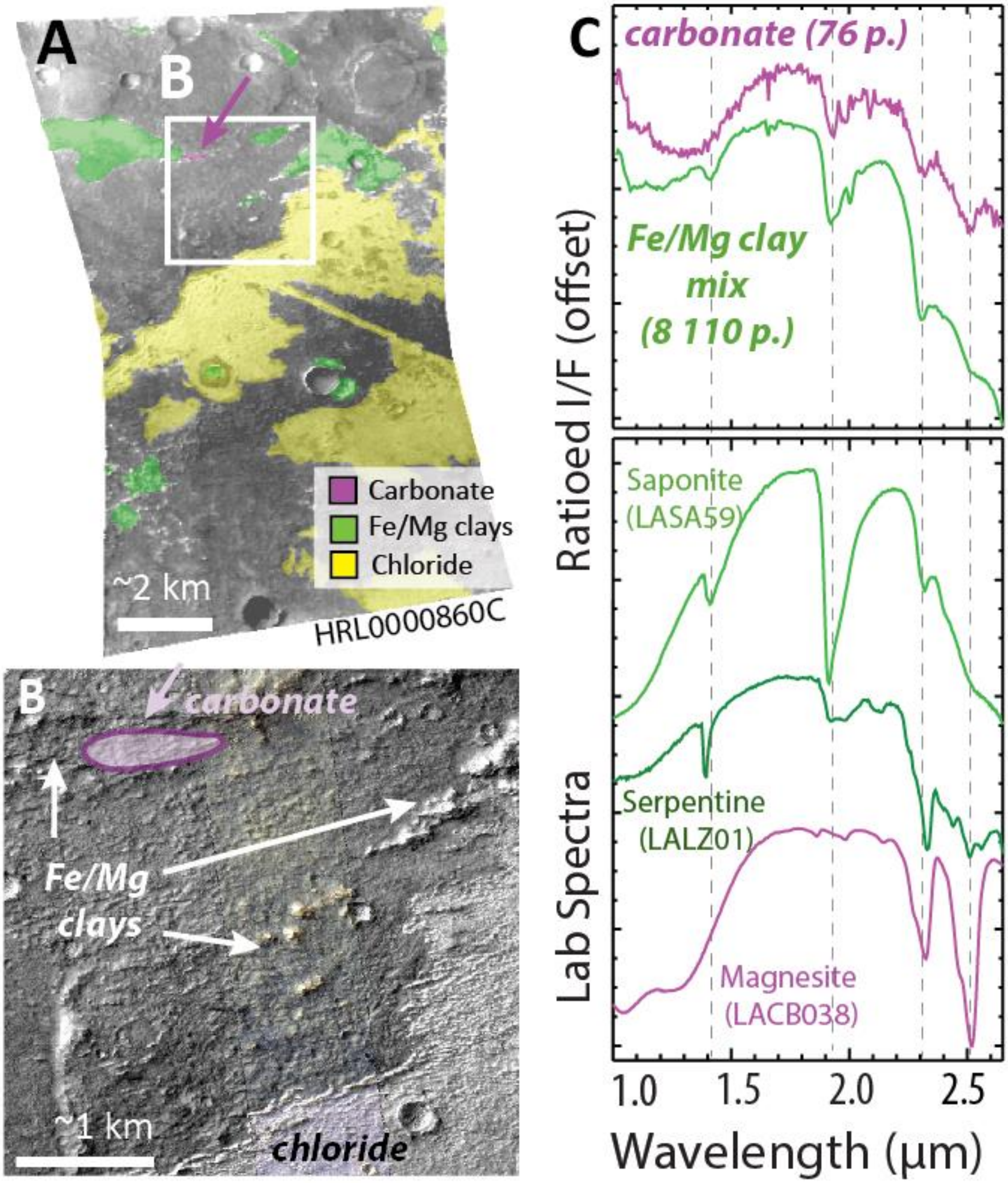

Fig 5-6. (A) Carbonate detected in CRISM image with chloride in Terra Sirenum (154.48°W, 32.62°S; figure location labelled in Fig. 5a). Chloride is draped on top of the Fe/Mg clay bearing unit (e.g. Glotch et al., 2010). (B) Carbonate detection (purple) indistinguishable from Fe/Mg clay bearing unit at HiRISE scale (PSP 006668 1470). (C) Carbonate spectrum has diagnostic paired 2.3 and 2.5 μm absorptions of similar depth (see magnesite (Mg-carbonate) spectrum for comparison). Fe/Mg clay spectrum exhibits a minor 2.5 μm absorption, indicating a likely mixture with carbonate and/or serpentine.

3.1.1 Contact relationships between chlorides and Fe/Mg clays

El Maarry et al. (2013) proposed that a clay substrate might underlie all fractured chloride deposits, positing that desiccation of these clays might be responsible for the fracturing observed. In some instances, it has been shown that the chloride deposits appear to drape on top of clay-bearing units (notably in Terra Sirenum; e.g. Glotch et al., 2010). However, in other locations, a definitive genetic relationship is either inconclusive or the chlorides are inferred to be in underlying units (e.g. Knobel crater, Ehlmann and Buz, 2015; Huang et al. 2018). Here, we look at the contact relationship between chlorides and clays, where they are found in the same image. We find that clays directly touch or surround the chloride deposit in ~50% of instances (45/73 CRISM images with clays, 23/49 chloride deposits, 20/39 chloride clusters); in other cases, the clays are just nearby, but appear unrelated to the chlorides. It appears that while chlorides occur in Fe/Mg clay-bearing terrains, they do not need to be in direct contact with clays in order to form

3.1.2 Water ice

In our search for hydrated minerals, we unexpectedly found spectral signatures for water ice in 8 CRISM images (8 deposits, 7 clusters; Fig. 7). These ice deposits are found on pole-facing slopes between -42.8° S and -27.8° S. All of these images were taken during local winter (Ls 91-151); for 3 clusters, other CRISM images taken during other seasons were available, and these did not show water ice. Therefore, this is most likely a seasonal frost, consistent with the findings of Vincendon et al. (2010), who found seasonal water ice up to 13° S. While the current climate of Mars is too cold/low pressure for liquid water to occur seasonally today, seasonal deposits in the past may have been able to melt, providing a possible source of local, small volumes of water across the southern hemisphere of Mars.

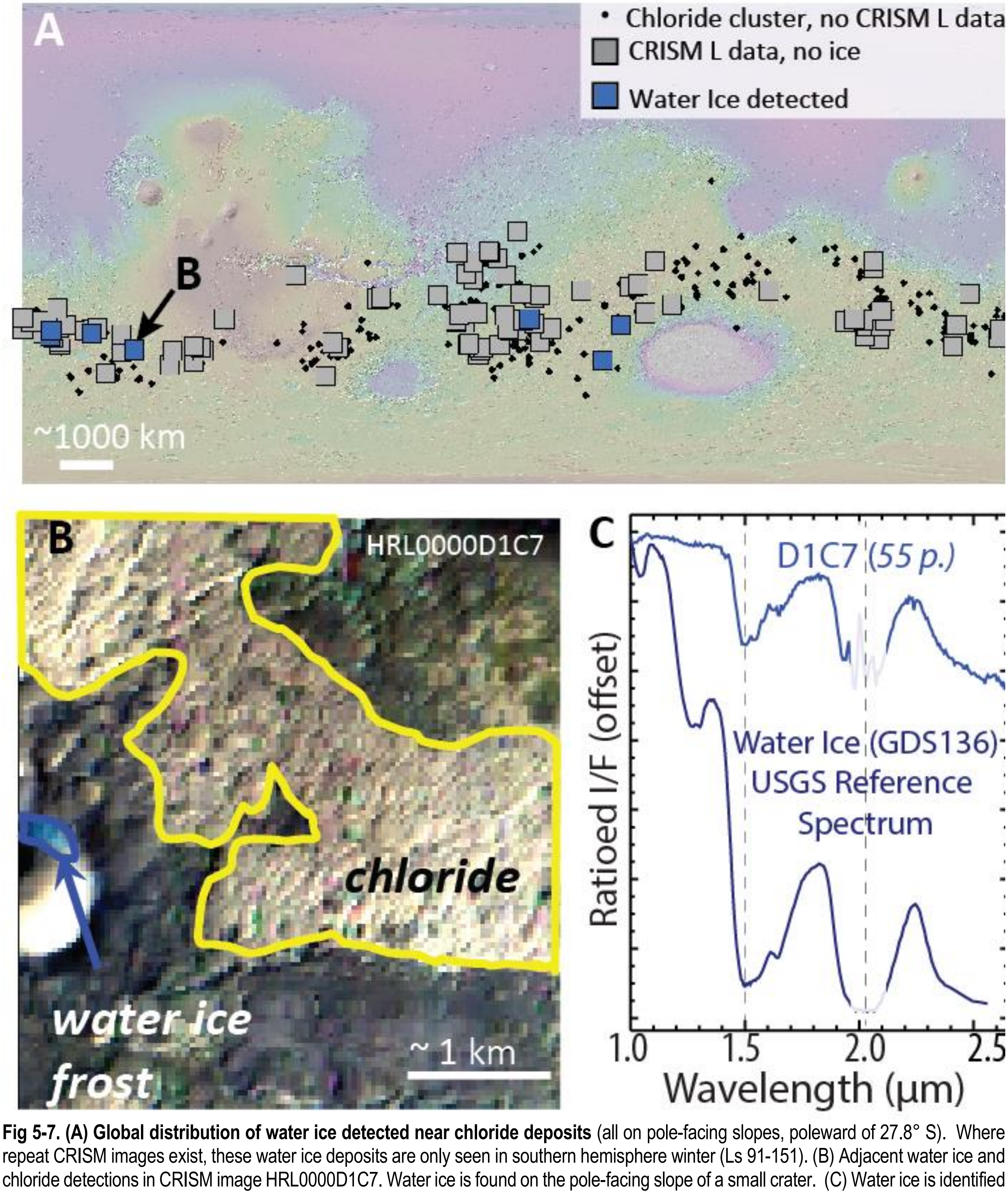

Fig 5-7. (A) Global distribution of water ice detected near chloride deposits (all on pole-facing slopes, poleward of 27.8° S). Where repeat CRISM images exist, these water ice deposits are only seen in southern hemisphere winter (Ls 91-151). (B) Adjacent water ice and chloride detections in CRISM image HRL0000D1C7. Water ice is found on the pole-facing slope of a small crater. (C) Water ice is identified by its large 1.5 and 2.0 µm absorptions. Transient melting of local and/or seasonal ice could have mobilized salt present in soils and transported small volumes short distances to local lows.

3.2 Morphology and Elevation

We find that chloride deposits are often found either nearby or within sinuous features, draped in thin layers on top of underlying topography, and in local lows in intercrater plains, frequently perched above nearby impact crater depressions. Investigating individual deposits, we note that the chloride deposits are often found over a range of elevations, and tend to be at higher elevation on the side of the basin where channels lead into the deposits.

3.2.1 Sinuous features

At the CTX scale, about 70% (269/387) of chloride clusters have sinuous features within the 10 km buffer that extend topographically lower toward the deposit, and in ~20% (82/387) of chloride deposit clusters, a light-toned unit consistent with chloride occurs directly within channels (e.g. Fig. 2a, c; 10a, b; 12b; 16b, c, d). Where HiRISE coverage is available, chlorides are found within sinuous features in ~25% (31/124) of clusters (35/171 deposits) (Fig. 3a). These numbers represent a significant increase from the lower resolution data available for the Osterloo et al. (2010) survey, which found ~8% of the deposits to have sinuous or linear features, interpreted as possible channels.

3.2.2 Thin, draped chloride deposits

Estimating the thickness of chloride deposits on Mars is useful for mass balance calculations (e.g. Melwani Daswani and Kite, 2017; Milliken et al. 2009), and to help us constrain plausible depositional environments. Previous thickness estimates are often in the 1-15 m range (Glotch et al., 2010; Hynek et al., 2015; Melwani Daswani and Kite, 2017). In our survey of HiRISE colour images, we looked for places where chloride deposits appear to be "chipped," cross-cut by impact craters, or exposed in fractures to understand the typical deposit thickness (e.g. Fig. 8), measuring with HiRISE DEMs where available. We focus on places in the middle of chloride deposits (rather than the edges), as these are more likely to represent that average thickness (Fig. 9e, 10e). In places without HiRISE stereo coverage, we see fractures cutting through chloride deposits, revealing that they do not extend into the subsurface (Fig. 8a-d); elsewhere, we see small impact craters (~10 m diameter) exposing dark material from beneath the chloride deposit (Fig. 8e, 10f). Where we do have HiRISE stereo coverage, the chloride thickness often appears to be below the vertical resolution of HiRISE DEMs where available (<1m), up to ~3m thick

(Table 1). Chloride deposits often appear to be draped on underlying topography (e.g. Fig. 2d; Fig. 11c, d, e), and ponded in local lows (e.g. Fig. 9c, d; Fig. 10c), where taller ridges/knobs are not coated with chloride. This is consistent with later, shallow water bodies depositing chloride on top of the extant topography.

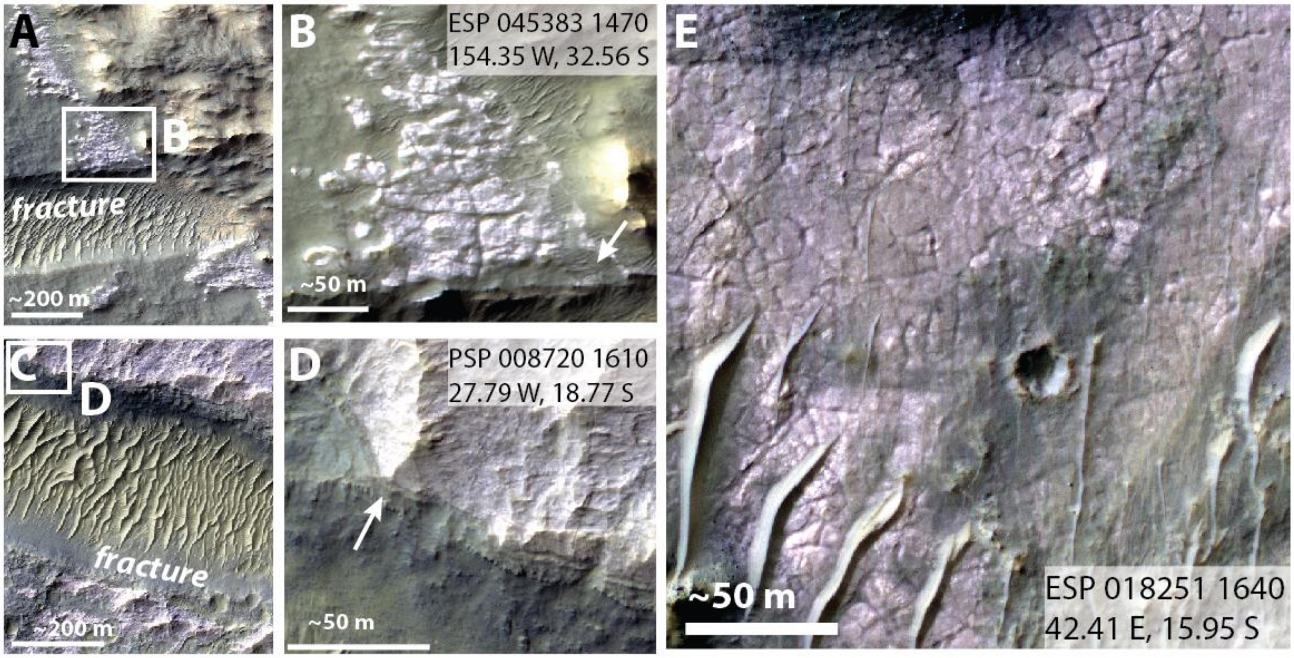

Fig 5-8. Examples where chloride thickness is exposed through fractures or impact craters (no HiRISE stereo data available for thickness measurements). (A) Light purple chloride fringes channel edge, and is cross-cut by later fracture. (B) Close-up shows polygonal fracturing in chloride, and that the chloride does not extend into the subsurface where exposed by the fracture (white arrow). (C) Light purple chloride is present on both sides of the fracture. Zoom in (D) shows that the chloride layer is draped on top of underlying topography, and does not extend into the subsurface. (E) An impact crater has punched through a light purple, fractured chloride unit (linear dunes present in bottom half of image). All ejecta from this ~15 m diameter crater are dark toned, indicating that the chloride is only a thin layer at the surface.

Chl FID covered by HiRISE DEM	Chl Automated Cluster FID (10km buffer)	Latitude	Longitude	HiRISE Stereo Pairs	Deposit Thickness (Near centre, not edge)	Range of deposit elevations	Slope calculations (within a contiguous		
							Elevation change (m)	Distance (km)	Slope (%)
96,97	51	-39.381	216.57	ESP_016201_1405_RED+PSP_010900_1405_RED	1-3m	~18 m	16	0.58	2.76
69	56	-38.816	221.077	ESP_055206_1410_RED+ESP_046200_1410_RED; PSP_003160_1410_RED+ESP_047413_1410_RED	<1m	100m	35	6.8	0.51
119	70	-37.566	242.76	ESP_031918_1420_RED+ESP_023716_1420_RED	n/a	20-30m	26	1.3	2.00
227	81	-37.24	193.564	ESP_026276_1425_RED+ESP_017784_1425_RED	n/a	~15 m in image, >100m in channels (MOLA)	6	1.7	0.35
292	81	-36.776	193.523	ESP_046201_1430_RED+ESP_055220_1430_RED; ESP_050394_1430_RED+ESP_050684_1430_RED; ESP_046201_1430_RED+ESP_046346_1430_RED	n/a	~15 m in image, >100m in channels (MOLA)	21	2.8	0.75
623	128	-32.893	205.615	ESP_017243_1465_RED+PSP_009318_1465_RED; PSP_007380_1470_RED+PSP_010597_1470_RED; PSP_005811_1470_RED+PSP_006668_1470_RED	<1 m to ~3m	MOLA ~95 m	13	0.78	1.67
73	142	-31.572	206.379	ESP_016043_1480_RED+ESP_016188_1480_RED	~1m	>18 m	11	0.45	2.44
341	143	-31.456	303.603	ESP_027406_1485_RED+ESP_036333_1485_RED	<1 m thick	>25m	19	1.46	1.30
326	152	-31.207	180.188	ESP_052768_1485_RED+ESP_036509_1485_RED	<1 to 3 m	15 m	27	2.7	1.00
28	164	-30.254	358.196	ESP_044929_1495_RED+ESP_052880_1495_RED	1-3 m	>50 m (MOLA)	5	0.8	0.63
200	164	-30.413	358.044	ESP_044929_1495_RED+ESP_052880_1495_RED	1-3 m	>50 m (MOLA)	5	0.25	2.00
204	172	-29.979	196.115	ESP_016017_1495_RED+ESP_016162_1495_RED	n/a (Poss <<1 m)	20 m	60	2.6	2.31
422	246	-24.081	57.377	ESP_049898_1560_RED+ESP_049832_1560_RED	n/a	25m	25	0.48	5.26
26	360	-6.417	131.935	ESP_057570_1735_RED+ESP_056950_1735_RED; ESP_044502_1735_RED+PSP_008780_1735_RED	<<1 m	23m	23	2.2	1.05
187	370	-5.601	353.862	ESP_016565_1745_RED+ESP_016499_1745_RED; ESP_016354_1745_RED+PSP_007058_1745_RED; ESP_016288_1745_RED+ESP_016433_1745_RED	1-2m	>20m	7	0.27	2.59
44	377	-3.123	351.545	PSP_008917_1770_RED+PSP_007770_1770_RED	~2-4m	>100m	30	3.4	0.88
180	379	-3.052	350.963	PSP_007981_1770_RED+PSP_008851_1770_RED	n/a	15m	24	2.8	0.86
587	211	-27.706	5.825	ESP_016380_1520_RED+ESP_019716_1520_RED	n/a	MOLA ~100 m	33	4.5	0.74
640	162	-30.549	193.48	ESP_017283_1490_RED+ESP_017428_1490_RED	~<2m	20m (100m in MOLA)	15	3.8	0.39
219	327	-13.118	345.259	PSP_007032_1665_RED+ESP_011317_1665_RED	n/a	~5m	14	2.9	0.48

Table 5-1. Thickness, elevation range, and maximum slope for chloride deposits with HiRISE stereo coverage

3.2.3 Perched chloride deposits

We use gridded MOLA data, available for all deposit clusters, to investigate local topographic trends. While almost all chlorides are present in local lows (as noted in Osterloo et al., 2008, 2010), most (228/392; 58%) are not the lowest elevation within the 10 km buffer (e.g. Fig. 2a). Of these perched deposits, about half (103/228) have a drop of >100m, and ~7% (17/228) are >500m (Fig. 3b). For the majority of these perched chloride deposits, they are in intercrater plains above an old impact crater. There do not appear to be region-specific trends, i.e., perched chloride deposits occur throughout the southern highlands.

Osterloo et al. (2010) noted that while chlorides were widespread in the southern highlands, they were missing in major basins; our findings are consistent with this, but also demonstrate that the trend holds at smaller scales, where chlorides will often be found in intercrater plains but not in adjacent crater bottoms, even when (a) craters are so degraded that there is not a significant crater rim to prevent spilling over, and (b) CRISM images pick up other minerals in crater floors, so it is not a case of being obscured by dust (e.g. Cross crater, Columbus crater). This perched distribution is consistent with small volumes of water (insufficient volumes to spill over into nearby craters), derived from surface water runoff; a groundwater source would first fill topographic lows such as old, degraded craters, before spilling out onto intercrater plains.

3.2.4 Multi-elevation and asymmetric chloride deposits

In gridded MOLA elevation data, 171/392 (44%) of chloride deposit clusters have >10m elevation difference between different parts of the same deposit or cluster (median is 40m, max is 300m) (Fig. 4). This is very different from playa salt deposits on Earth, often invoked as a likely analogue for martian chlorides (e.g. Osterloo et al., 2010; Glotch et al., 2010; Ye et al., 2019; Huang et al., 2018; El Maarry et al., 2013). On Mars, contiguous chloride deposits typically have slopes around 1% (~0.5-5%; see Table 1), while terrestrial salt flats have slopes around 0.05% (one to two orders of magnitude flatter). Here, we show detailed information for a subset of four chloride sites on Mars, as well as two examples of chloride deposits on Earth.

3.2.4.1 Chloride adjacent to Knobel crater (near Gale)

This extensive, multipart chloride deposit (Fig. 9) is in a small basin, with an apparent channel leading into it from the southwest. Previous studies (Ehlmann & Buz, 2015; Huang et al., 2018) have interpreted chloride to be in stratigraphic layers, with small patches of chloride in erosional windows. While chloride does appear to be in a layer, covered by ejecta, in one part of the deposit (Fig. 9b), we also see small pond-like chloride deposits with crisp edges within the ejecta (Fig. 9c), and other patches consistent with ponds at a variety of elevations (~50 m over 8 km) (e.g. Fig. 9d, f). In Fig. 9d, we also see a small knob (black arrow) within the chloride deposit that only has traces of the purplish chloride on it, consistent with a draped chloride layer. In the lowest part of the basin, we see a few chloride-free mesa tops, despite being surrounded by chloride (Fig. 9e, f). If these mesas were part of a capping unit overlying chloride, we would expect to see the same unit at similar elevations around the deposit edge. Instead, we see a contiguous layer of chloride sloping down to the basin, from elevations well above the mesa top. These observations are consistent with an existing chloride deposit, hit by an impact crater (providing a chloride source at high elevation around the crater rim), and reworked by small volumes of water to form the predominantly draped morphologies observed. Basin-filling volumes of water would leave behind chlorides on mesa tops, rather than only ~6m up the sides as we observe. A chloride source around the crater rim would explain the asymmetry in elevation of the deposit (the contiguous layer along a slope (5-7 km in cross section, Fig. 9f), without rising to matching elevations on the far side of the basin).

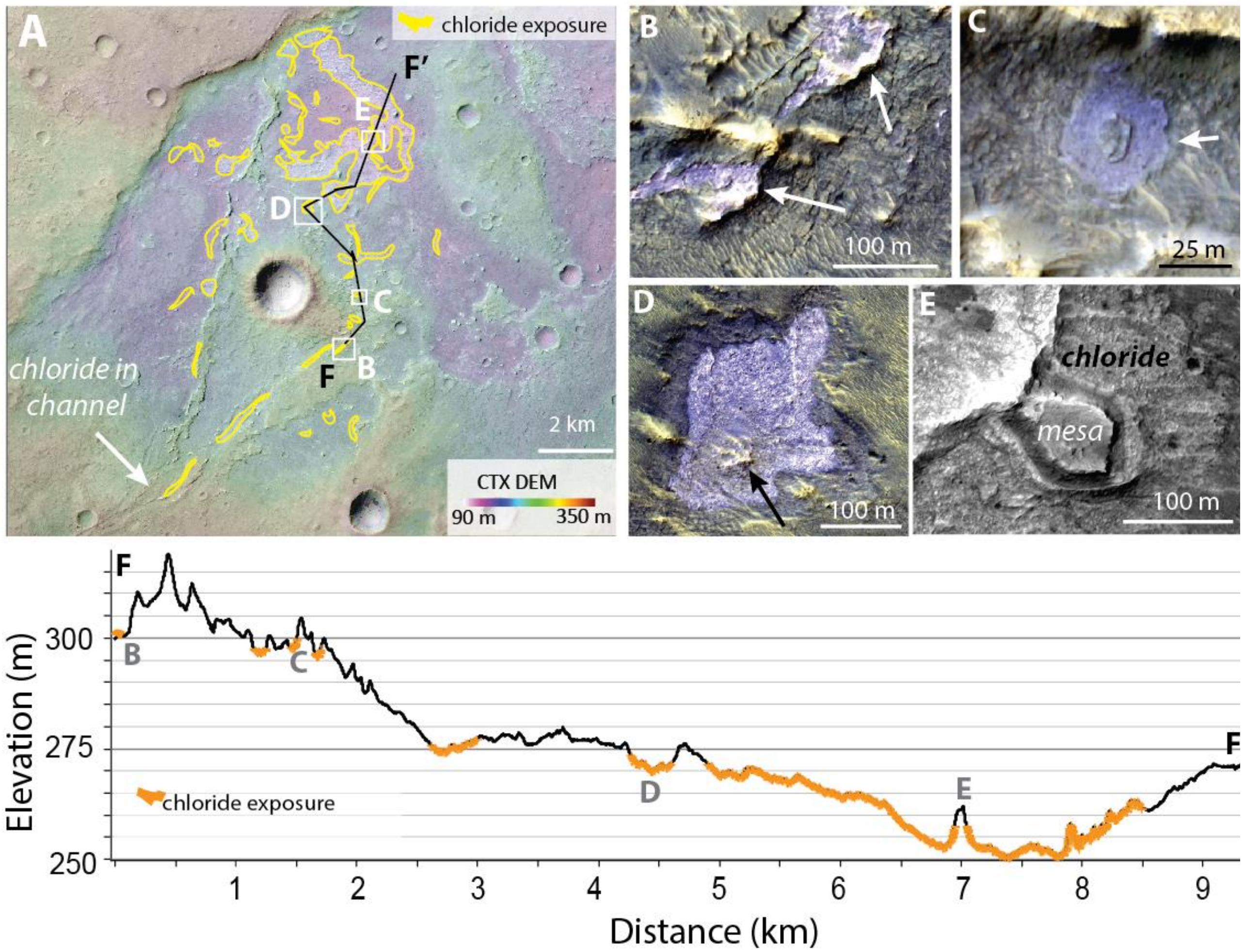

Fig 5-9. Chloride deposit adjacent to Knobel crater (132.0 E, 6.4 S; CTX DEM built from P20_008780 1727 XN and F22_044502 1732 XN). A) Light toned chloride unit (outlined in yellow) is found at a wide range of elevations (~250-300 m MOLA; see cross section F), and is partially found in an inlet channel, pointing to a surface water runoff source. Inferred stratigraphic relationships vary across the deposit; in (B), a chloride deposit (purple in HiRISE colour (ESP 044502 1735)) is in a layer atop a small cliff edge, about 10 m above the bottom right part of the image. This chloride layer may pre-date the impact crater in the centre of (A). Also in the impact ejecta are small, thin patches of inferred chlorides such as that in (C; PSP 008780 1735) which appear to drape underlying topography; we interpret these as small ponds that occurred after the impact event, with remobilization perhaps driven by local impact heating. (D) Larger patches of chloride, with crisp edges corresponding to topographic lows, are also consistent with ponding (ESP 044502 1735). Here, we see that the purple chloride unit does not fully cover the topographic high (black arrow) indicating the chloride is draped on underlying topography. (E) A flat-topped mesa is not covered by chloride, despite being surrounded by light toned, fractured chloride. This mesa is at a lower elevation than nearby contiguous chloride deposits (see cross section F-F'); if the chloride were in a stratigraphic layer rather than draped, we would see other exposures of a non-chloride layer at this elevation, instead of contiguous chloride. Chlorides are found from the basin bottom up to ~ 6 m up the mesa, indicating that the maximum water depth was ~ 6 m. (F) Cross section derived from HiRISE DEM (stereo pair: ESP 044502 1735 & PSP 008780 1735) showing chloride at a wide range of elevations, and in some cases following slopes (e.g. 6-7 km between D and E); this could result from small volumes of briny runoff sourced in the impact ejecta, and carried downhill, ponding to a max water level of ~ 6 m in the lowest areas.

3.2.4.2 Chloride adjacent to Meridiani Planum

This deposit exists within a larger basin (Fig. 10a), and has chloride-filled channels leading into it from the east. Around the edge of the deposit, a crater with a set of concentric rings likely records stages of evaporation (Fig. 10c). We measure chloride thickness where it is exposed in the deepest parts of the basin, as draping around the edges may lead to artificially thick measurements. In Fig. 10d, we see a gap within the fractured chloride unit that is ~1.5 m deep. Elsewhere, a small impact crater ~10 m in diameter (Fig. 10e) exposes only dark toned material, corroborating the idea that the chloride layer is relatively thin (~1m).

While chloride is present at a range of elevations (Fig. 10f), it is only on the side of the basin where the channels are leading in; there is no matching chloride on the opposite side of the basin, as we would expect if the basin had been filled to the level of the highest chloride deposit. This asymmetry is typical in martian chloride deposits. Further evidence of shallow water levels is seen in Fig. 10b, where a channel leads into a high-elevation chloride deposit, which in turn spills over into the main basin. If the water had filled up to the level of the higher-elevation deposit, a mound within the main chloride deposit should have evidence of chloride on top of it. Instead, we see no trace of chloride on the mound/island, despite being surrounded by chloride on all sides. This limits the maximum water depth to ~5-10 m at most, markedly different from the interpretation of Hynek et al. (2015) and Melwani Daswani and Kite (2017), who argue for lakes > 100m deep, based on the overall basin shape. We think that the basin was carved during an earlier, wetter era; small briny water volumes then followed into these existing depressions, not filling them completely.

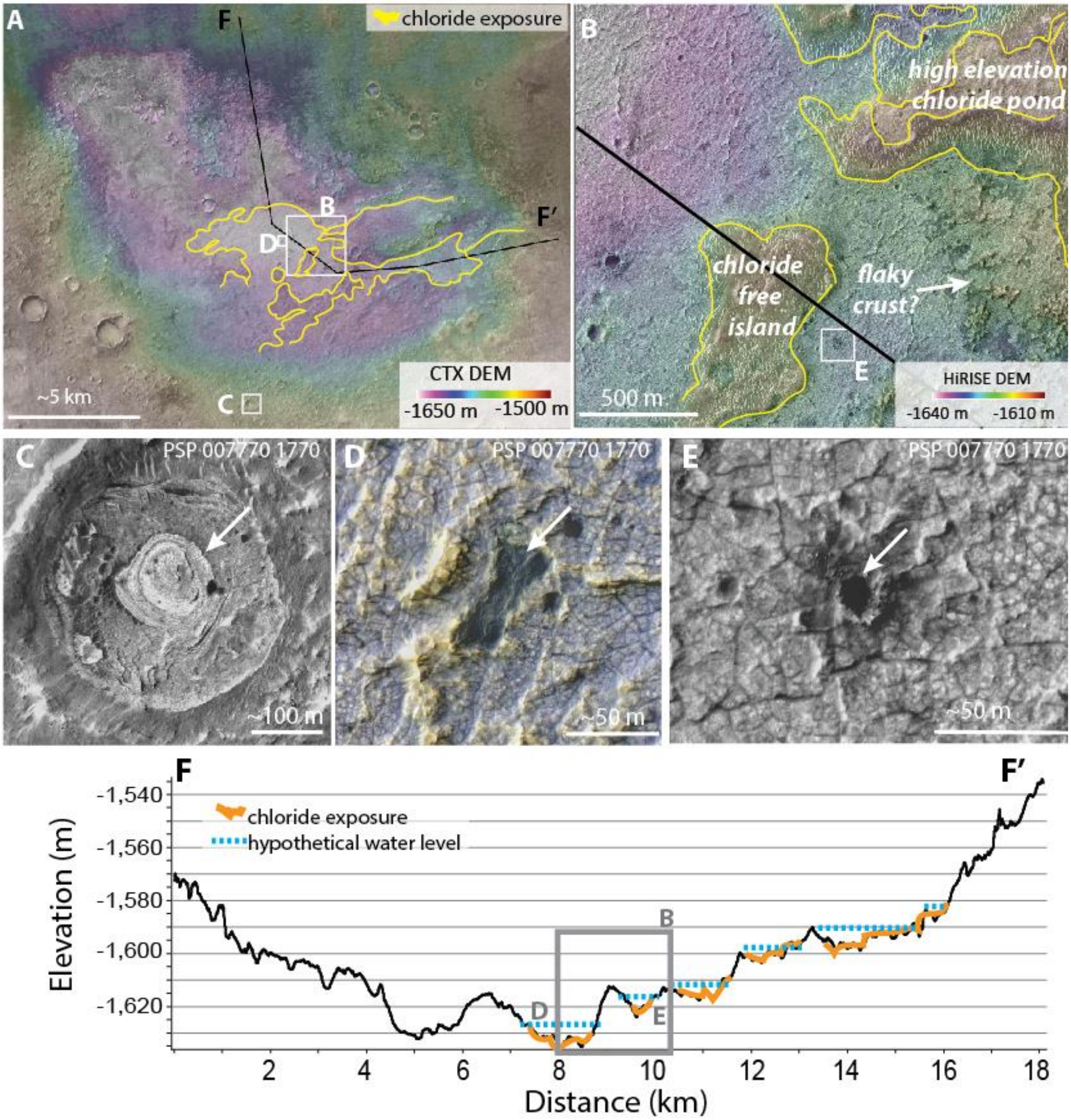

Fig 5-10. Chloride deposit near Meridiani Planum (8.5 W, 3.1S; CTX stereo pair P17 007770 1794 & P20 008917 1763). (A) Light toned chloride unit (outlined in yellow) is present over ~ 50m of elevation, including in channels leading into the main deposit. (B) HiRISE DEM (PSP 008917 1770 & PSP 007770 1770) shows a small stream leading into a higher elevation pond (top right), and a spill point into the deeper basin 15-30 m below. Chloride-covered basin floor elevation ranges by ~15 m. Fractured chlorides on basin floor sometimes have crust-like morphologies, similar to Death Valley analogue (see Fig 13). A mound at an intermediate elevation between the pond and the basin floor is chloride-free, suggesting that water levels never reached that elevation (max 5-10 m deep, possibly even shallower). (C) Concentric rings in a small crater suggest multiple stages of evaporation. (D) Chloride deposit thickness, measured near the centre of the deepest part of the basin is ~ 1.5 m. Fractures in chloride appear to continue across minor topographic changes, indicating that it is a single layer draped on top of underlying topography. (E) A small impact crater punches through the chloride deposit, spreading dark ejecta (depth of crater ~ 40cm).

3.2.4.3 Southwest Tharsis chloride

In this deposit, a mostly contiguous layer of chloride fills the majority of a basin (Fig. 11a). Channels lead into the deposit (white arrow, Fig. 11a; many channels leading down from the Noachian highlands, Fig. 11b), which is emplaced atop the edge of the volcanic unit (Fig. 11b). The chloride is purple-white and fractured in HiRISE colour (Fig. 11c-e), and appears to be a thin layer draping underlying topography. The thin chloride unit appears to be chipping off a ridge line in Fig. 11c (thickness below HiRISE DEM resolution), while in Fig. 11d, we see chloride coating underlying lineations that are < ~3 m high; taller features (black arrows) are left uncovered. In Fig. 11e, chloride <0.5-1 m thick is clearly draped on top of an underlying ridge (white arrow). In cross section (Fig. 11f), we see chloride exists at a range of elevations (~55 m). Once again, the elevation distribution is asymmetric, with the chlorides existing at higher elevations on the southern side of the deposit, where channels feed in. A flat-topped volcanic unit is present to the north, with no chloride detections on top of it; the maximum water level had to be lower than this elevation as an upper limit (~20 m max water depth).

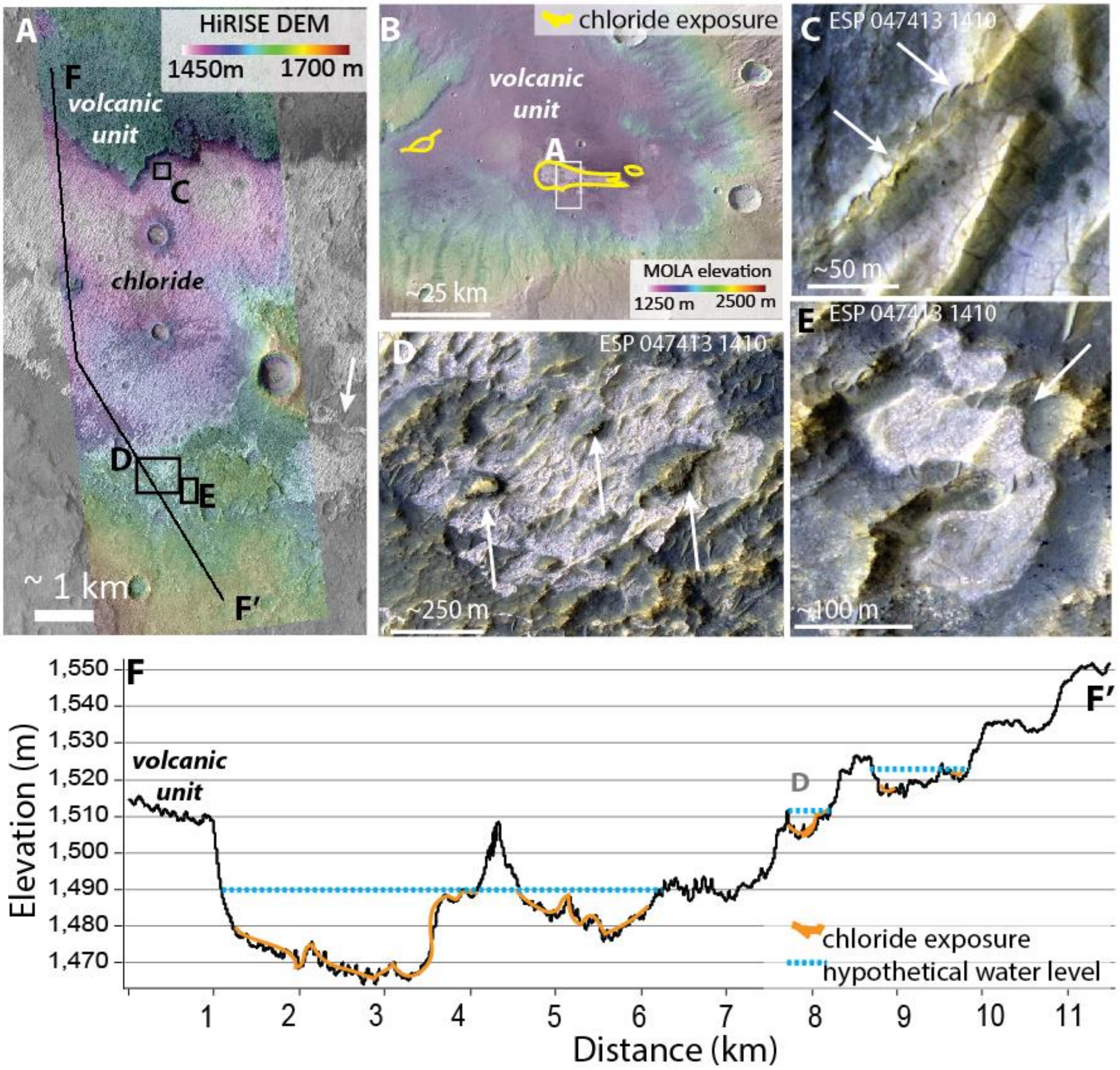

Fig 5-11. Chloride deposit in southwest Tharsis (see Fig 18d-f for age dating). (A) Light toned, ridged chloride unit is present in topographic low. Small, chloride filled channels lead into the main deposit (white arrow). (B) In context, this chloride deposit is surrounded by channels, leading downhill from Noachian highlands onto flat volcanic plains. (C) Purple-white, fractured chloride appears draped on top of underlying ridged topography, covering ridges up to ~3 m high, and sometimes appearing to chip away from the ridge crest (white arrows; thickness below HiRISE DEM resolution). (D) Chloride covered some ridges, but topography taller than ~ 3 m is not coated with chloride (white arrows), indicating that the water level was less than ~ 3m deep at the time of deposition. (E) Light toned, fractured chloride deposit very clearly draped underlying topography (e.g. ridge indicated by white arrow). Chloride here is <0.5-1m thick. (F) Chloride deposits exist at a wide range of elevations (>50 m), and over slopes in contiguous parts of the deposit (e.g. 3-4 km in cross section F). Upper parts of the deposit (9-10 km) are at elevations up to 10 m higher than the flat top of the volcanic unit, indicating that this deposit was likely fed by surface water runoff from the south, and the basin never filled to capacity (else, we would see evidence of chlorides atop the volcanic unit). Chloride deposits appear to curve upwards towards the base of the volcanic unit, indicating that the basin they sit in was carved after the deposition of the volcanics.

3.2.4.4 South Tharsis chloride

Here, a number of small chloride deposits are found within a larger basin (Fig. 12a). Chloride-filled channels lead into some of the deposits (e.g. white arrow, Fig. 12b, c). One small deposit has rounded edges with concentric rings (Fig. 12d). These rings show that the chloride-depositing pond was about the same size as the deposit we see today (not part of a basin-filling contiguous deposit), and suggest multiple stages of ponding/evaporation. While CTX and HiRISE stereo coverage are not available, we note that even at MOLA scale, the chloride deposits cover a range of elevations (~120 m).

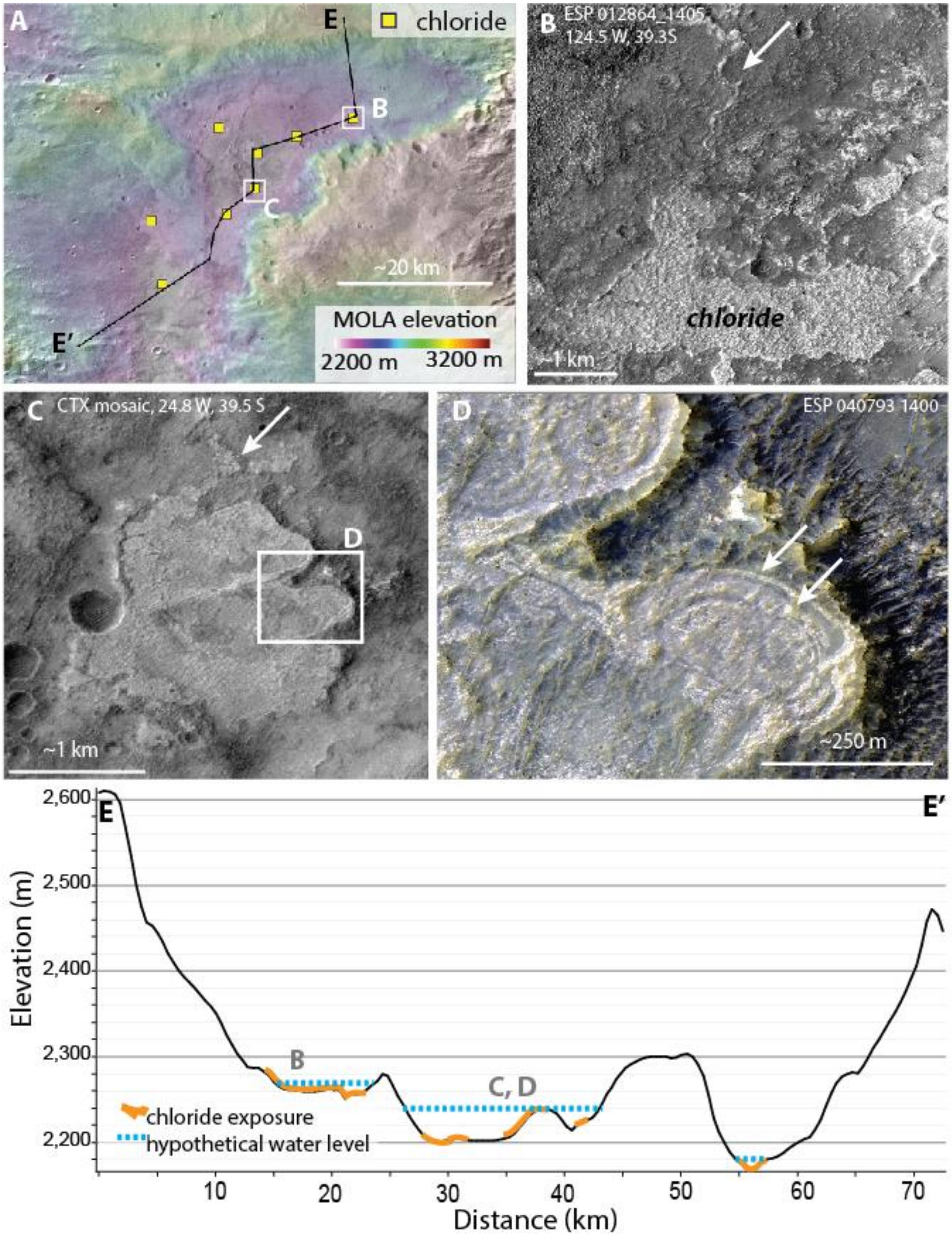

Fig 5-12. Chloride deposit cluster in south Tharsis region. (A) A number of small chloride deposits are present within a larger basin, at a range of elevations (Note: neither full CTX not HiRISE stereo images were available for this site, so MOLA elevations are used). (B) A small, chloride-filled channel (white arrow) leads down into the main deposit (ESP 012864 1405). (C) Another chloride deposit; this one appears raised, and has rounded edges (D) as well as an apparent channel leading into it (white arrow). (D) (ESP 040793 1400) Rounded edges of deposit appear to have concentric rings (white arrows), consistent with multiple stages of ponding/evaporation. This morphology also indicates that the chloride likely formed in a pond this size, with the rings around the edge--and that this is not a remnant of a much larger, basin-filling deposit. (E) Cross section shows series of independent chloride deposits over a range of ~120 m elevation.

3.2.5 Earth analogues

On Earth, chloride deposits are often found in marginal marine basins or playa environments, although they can also be found in Antarctic dry valleys. Marginal marine environments require a connection to a large body of water over a long time; there is no evidence of such a body near chloride deposits on Mars, so we focus on the other two environmental settings. Neither is a perfect analogue for the chloride deposits we see on Mars. Here, we present an example of each, to show the ways in which martian chlorides are similar to those on Earth, and the ways in which they differ.

3.2.5.1 Death Valley, California (Playa)

On Earth, chloride minerals are most commonly associated with arid playa environments, such as the halite salt flats in Badwater Basin (Death Valley, California; Fig. 13a). These environments have meter-scale polygonal ridges and/or fractures (Fig. 13d, e) very similar to the characteristics of martian chlorides. However, these environments are extremely flat, as cycles of flooding and evaporation level the topography (Fig. 13b). In cross section, we see <1 m elevation change over ~2.5 km (Fig. 13c; LiDAR data from Snyder, 2005); this is very dissimilar to the martian chloride examples. In addition, playa environments are typically thick deposits (building the flat layer), alternating between flood and evaporative layers. No evidence of horizontal layering is exposed in any chloride deposit on Mars with HiRISE data available.

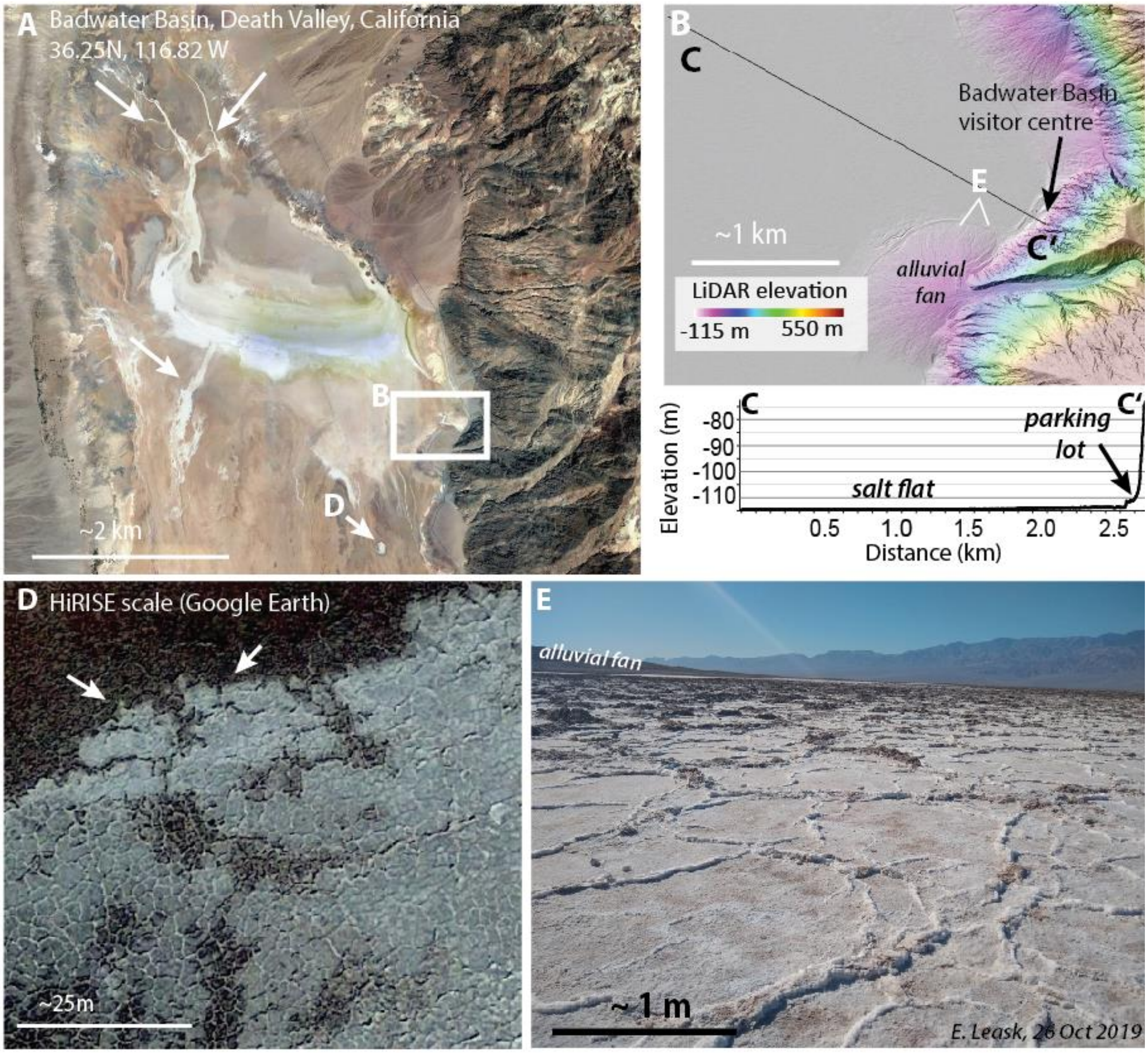

Fig 5-13. Chloride deposit in Badwater Basin (Death Valley, California (Earth)). (A) Light toned chloride deposit fills topographic low, with chloride-filled channels leading into the main deposit (white arrows). (B) LiDAR data (analogous to HiRISE DEM) show a very flat basin bottom; in cross section (C) we see that the salt deposit has less than ~1m elevation change over ~2 km, with a step change to the flat-topped parking lot ~ 2m above the salt flat. This minimal slope is not similar to any martian deposits observed, despite morphological similarities. (D) Google Earth image (analogous to HiRISE scale) of chloride; flaky, crust-like edges (white arrows) and polygonal fractures and ridges are very similar to martian chloride deposits. (E) Chloride deposit from the ground--note bright white colour, polygonal features, and overall flatness of deposit (roughness on the order of ~ 10 cm; photo E. Leask).

3.2.5.2 McMurdo Dry Valleys, Antarctica (Special case, paternoster lakes)

One of the most saline bodies of water on Earth (Meyer et al., 1962) is in the Antarctic Dry Valleys—Don Juan Pond (Fig. 14a) is 90% pure $CaCl_2$, with an overall salinity of ~ 40% by mass. This pond is in the valley bottom, with a bright white ring of salt around a shallow muddy patch (Fig. 14c). Salt crusts show a sharp contact at the edge (Fig. 14d), with salt encrusting short boulders (~< 10 cm). Both groundwater (e.g. Toner and Sletten, 2013) and deliquescence plus snowmelt (Dickson et al., 2013) have been proposed as water sources for Don Juan Pond. Dickson et al. (2013) observe seasonal flow of chloride-rich brines on top of a permafrost layer, where the salinity is attributed to surface/near surface deliquescence. Downstream in the valley is Lake Vanda, which has chloride-rich bottom waters (Angino and Armitage, 1963). These are special saline examples of paternoster lakes—glacial-fed lakes that are connected by streams, occurring at different elevation steps (Fig. 14b)—here there is about ~15 m elevation difference, over 10-15 km. The elevation ranges of these chloride-rich water bodies are similar to martian chloride deposits, but they do not exhibit the polygonal fracturing/ridges that we see in playa environments and on Mars.

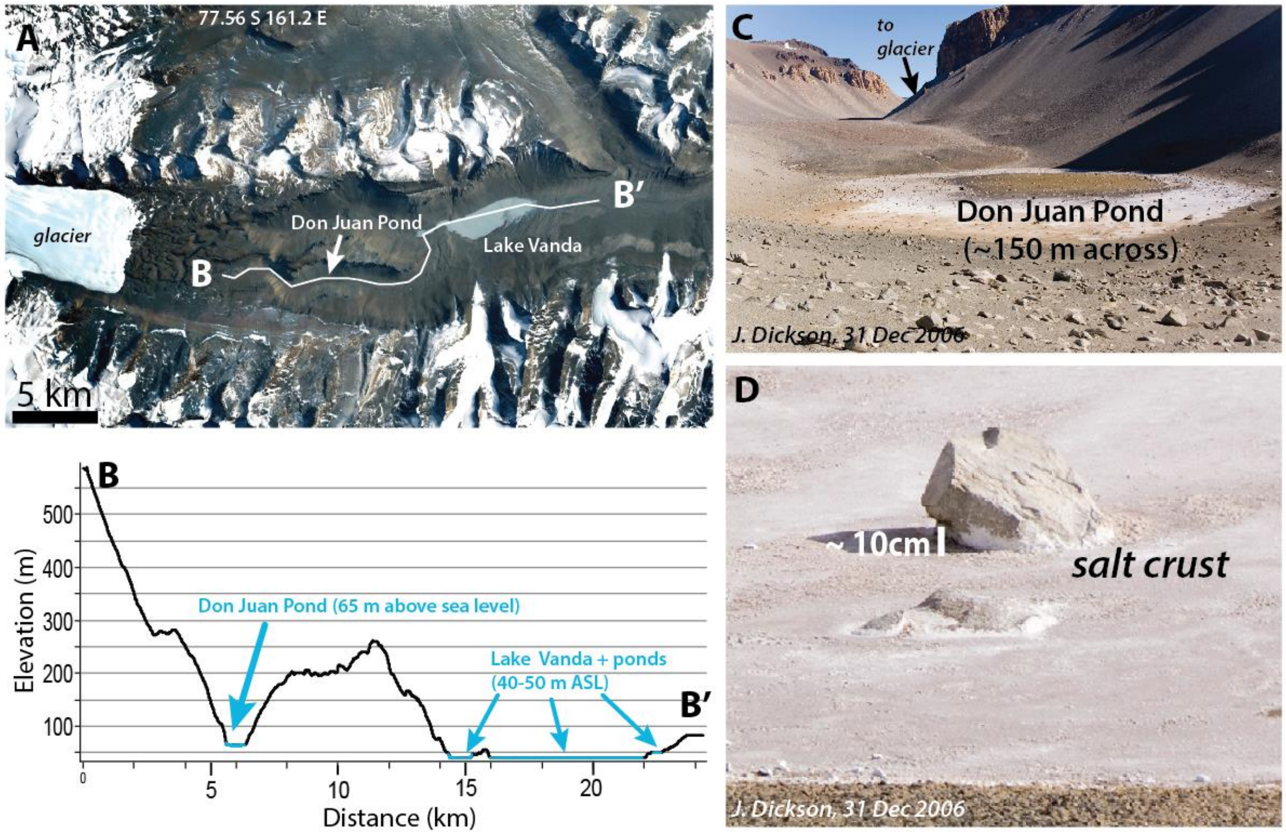

Fig 5-14. Chloride deposit in McMurdo Dry Valleys, Antarctica (Earth). (A) Google Earth image shows a glacier in the upper parts of the valley, and the location of Don Juan Pond (40% salt by mass) and Lake Vanda (also rich in $CaCl_2$) are within the valley. (B) These salty water features are at different elevations (range ~25 m), and connected by channels. This kind of elevation range, with separate bodies sometimes connected by channels, is more similar to the typical elevation distribution seen on Mars. (C) Don Juan Pond (photo J. Dickson), showing the white salt crust and very shallow water level (muddy patch) within the larger valley, downstream from the glacier. (D) Close-up of sharp salt contact (bottom edge) and salt crust that has covered shorter boulders, climbing up ~ 10 cm.

3.3 Age Dating

Osterloo et al. (2010) used published maps from 1986 (Tanaka) and 1987 (Greeley and Guest) for approximate ages of chloride deposits; using these boundaries they found that most deposits were Noachian in age, with ~24% in the Hesperian. Using the updated Tanaka et al. (2014) global map of Mars with unit ages, we find that only 7 deposits (/642) remain in Hesperian terrain—the rest are Noachian, consistent with work by Hill and Christiansen (2019). Osterloo et al. (2010) dated the terrain underlying chloride at 3 sites, finding ages ranging from 3.9-3.7 Ga, while Davila et al. (2011) dated one of the same sites at 3.6 Ga. Similarly, Hynek et al. (2015) date the Meridiani chloride site to be younger than 3.6 Ga, while Huang et al. (2018) date the Knobel terrain to ~3.7 Ga. In this work, we selected a number of sites where morphologic features indicated that chloride had been deposited on top of the volcanic terrain (e.g. chloride within channels carved into a volcanic plain, or deposited on top of a surface with wrinkle ridges) to obtain oldest-possible age bounds. In only one location (S Tharsis, Fig. 15) were we able to also obtain a firm youngest-possible bound, using cross cutting fracture relationships.

3.3.1 Icaria Fossae/South Tharsis

In the Icaria Fossae region (south of Tharsis), several chloride detections are located on terrain cross cut by fractures (fossae) (Fig. 15a, within red region). Looking closer, the chloride deposits are clearly cut by the fractures (Fig. 15b, c), indicating that the chloride was deposited prior to fracturing (but after the underlying terrain was formed). Boundaries for the red region were drawn based on a change in slope marking the boundary between a resurfaced (and fractured) basin, and highland regions. Nearby, a similar flat basin exists where the same suite of fractures cutting the chlorides are erased through resurfacing (Fig. 15d). This surface must be younger than the chloride deposits, allowing both an upper and lower age bound to constrain the chloride age in this location. The terrain underlying chloride (red) is dated at 3.3 Ga, while the nearby (blue) basin was resurfaced at 2.0 Ga. This means that the chlorides must have been deposited after 3.3 Ga but before 2.0 Ga. (In the global scale Tanaka et al. (2014) map, these terrains are respectively classified as late Noachian highlands and early Hesperian volcanics).

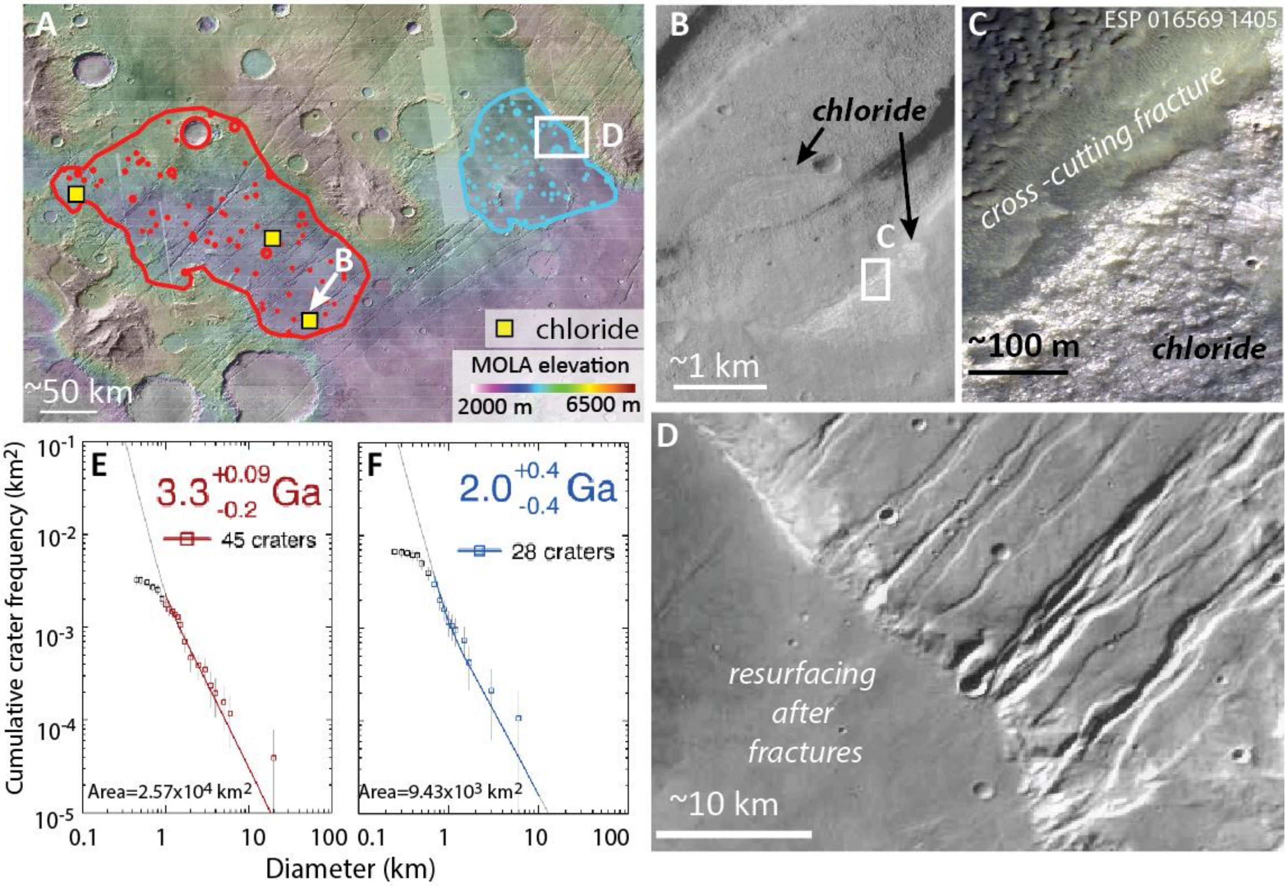

Fig 5-15. Age dating of chloride in south Tharsis (113.75 W, 39.39 S). (A) Chloride deposits are found on heavily fractured terrain (red outline), but not on nearby smooth, resurfaced terrain (light blue). (B, C) Chloride deposit is cut by a fracture, indicating that the chloride deposition happened after the terrain formed, but before the fracturing occurred. (D) Fractures are completely resurfaced by later event, leaving a smooth, easily dated terrain that must be younger than the fractures. (E) Age date of red unit underlying chloride deposits (3.3 Ga); chlorides must be younger than this age. (F) Age date of light blue, resurfaced unit (2.0 Ga); chlorides must be older than this, as the same suite of fractures that came after chloride deposition are filled in by this unit.

3.3.2 East Tharsis (Bosporos & Thaumasia Plana)

On volcanic units east of Tharsis, we see chlorides present at three distinct elevations (Fig. 16a). In a small basin in Thaumasia Planum (outlined in purple), chloride is deposited within a channel (Fig. 16b); see Fig. 17 for further detail about this region. The underlying terrain has a resurfacing age of 3.3 Ga (older age preserved in larger craters is 3.7 Ga) (Fig. 16e). At the lowest elevation (outlined in green) is a large unit with chloride infilling parts of channels cut into the volcanic terrain (Fig. 16c); this unit was resurfaced at ~3.4 Ga, with craters >~10 km pointing to an older age of 3.7 Ga (Fig. 16f). Finally, we have another large area with many chlorides (Bosporus Planum, outlined in pink in Fig. 16a). Many of these chlorides are also within clear channels (Fig. 16d), indicating that they were deposited after the volcanic unit was emplaced and eroded. This terrain is dated at 3.3 Ga (Fig. 16g). (In the global scale Tanaka et al. (2014) map, these terrains are all classified as late Noachian volcanics).

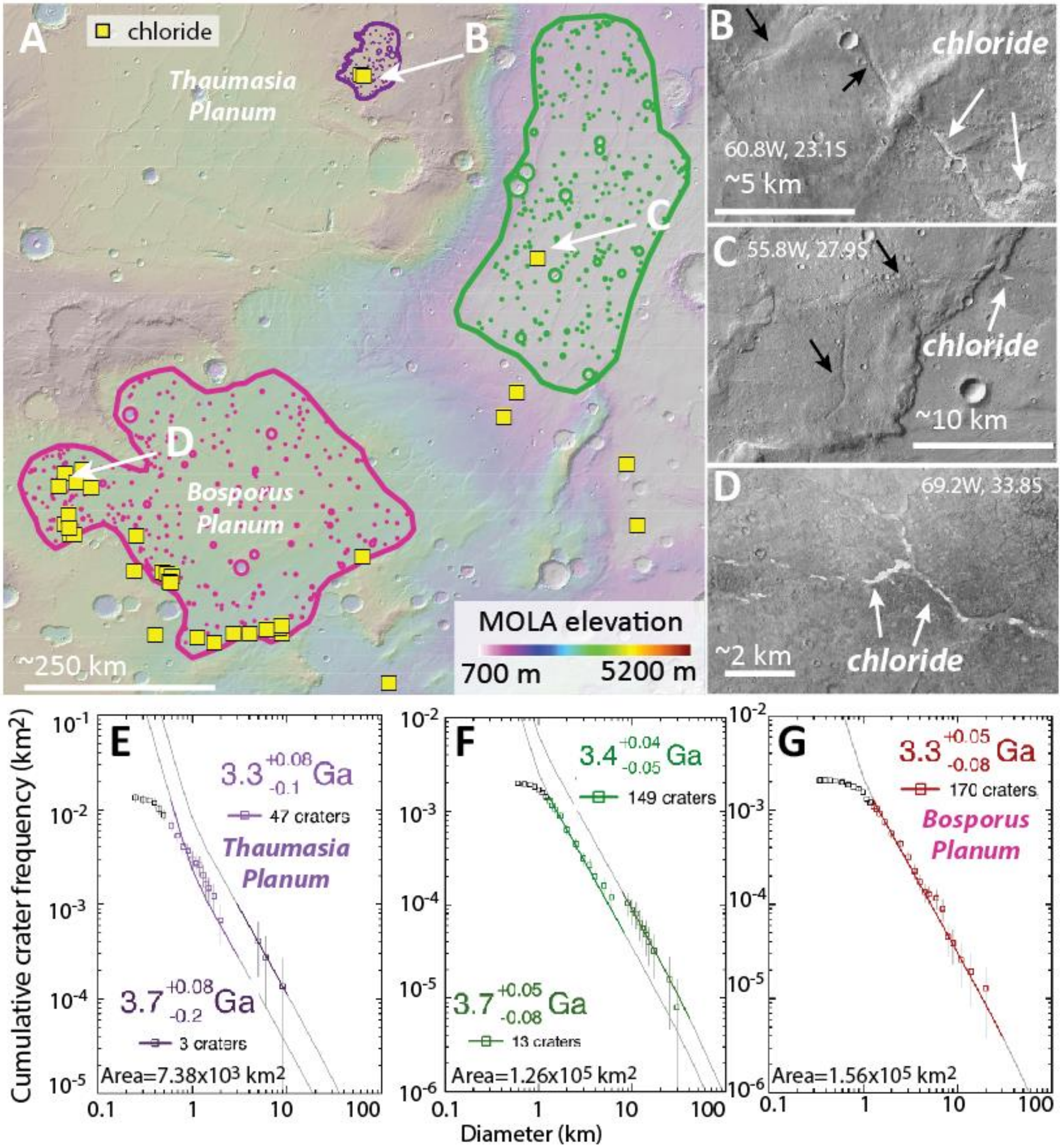

Fig. 5- 16 Age of chloride deposits in East Tharsis. (A) Three regions with chloride are defined by topographic boundaries (at different scales). (B) In the small purple region, light toned chloride deposit is found within a channel. Similarly, in the green region, the chloride deposit partially infills a channel at the surface. The pink region in Bosporus Planum contains many chloride deposits, many of which are also in channels (D). Since the chlorides are within fine-scale channels, we interpret them to post-date resurfacing events for these regions. (E) Small site at Thaumasia Planum (purple) has a resurfacing age of ~ 3.3 Ga (resurfaced terrain ~ 3.7 Ga). (F) Large green region downhill from Thaumasia Planum has a very clear resurfacing age of ~3.4 Ga, resetting craters smaller than ~ 10 km diameter, and an older trend at 3.7 Ga. (G) Craters in Bosporus Planum (pink) yield a uniform age of ~ 3.3 Ga.

In detail, these chloride deposits on volcanic terrain appear to be immediately downhill from remnants of Noachian highland material (e.g. Fig. 17). Here, the THEMIS chloride detection is within a channel in the relatively flat volcanic floor unit, next to topographic highs with plenty of Fe/Mg clays (green in Fig. 17a, spectra in Fig. 17d). In this clay-rich terrain, HiRISE colour images show possible small chloride deposits (Fig. 17b, c). Small chloride deposits such as these, formed in clay-rich Noachian terrain, may have been transported down onto the nearby volcanic material by small amounts of meltwater, creating the larger deposits detected by THEMIS.

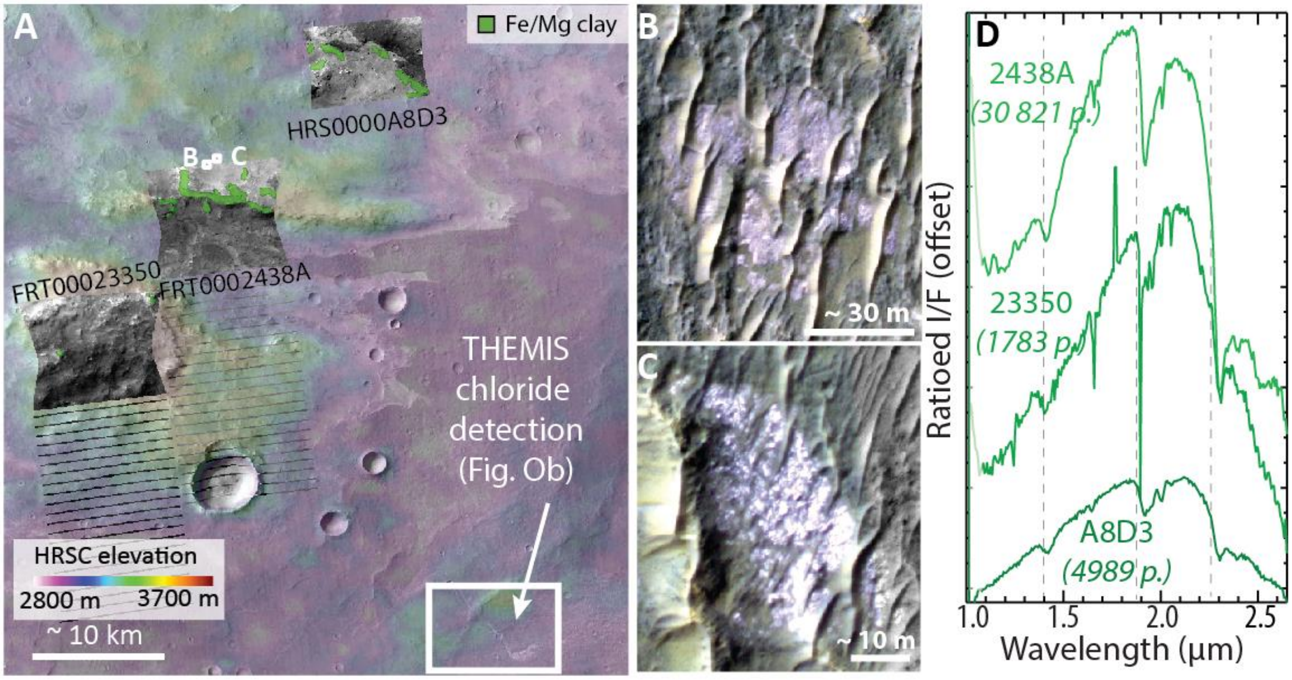

Fig 5-17. Possible evidence for remobilization of chloride deposits (Detail from Thaumasia Planum chloride deposit, purple in Fig. 16). (A) While chloride deposit (white box) is on volcanic plains, hills to the left have strong clay signatures (green in CRISM images; clay spectra shown in D). Elevation data from HRSC DEM: h0460_0000.da4.53 (CTX stereo pairs unavailable). Associated with these clays are small suspected chloride deposits (light purple in Figs (B, C); ESP 026694 1575). Similar small chloride crusts developed in association with clay rich-soils could then have been dissolved and transported downhill in channels, redepositing chloride away from the clay-rich source area.

3.3.3 East Hesperia Planum

At the eastern edge of Hesperia Planum, chlorides are detected atop volcanic terrain (Fig. 18a). More chlorides are present in the Noachian highlands nearby. The chloride in Hesperia Planum is located within a channel (Fig. 18b), indicating that it was emplaced after the volcanic unit. This unit has a resurfacing age of 3.4 Ga (older age is 3.6 Ga); chlorides must be younger than 3.4 Ga. (In the global scale Tanaka et al. (2014) map, this unit is classified as early Hesperian volcanic).

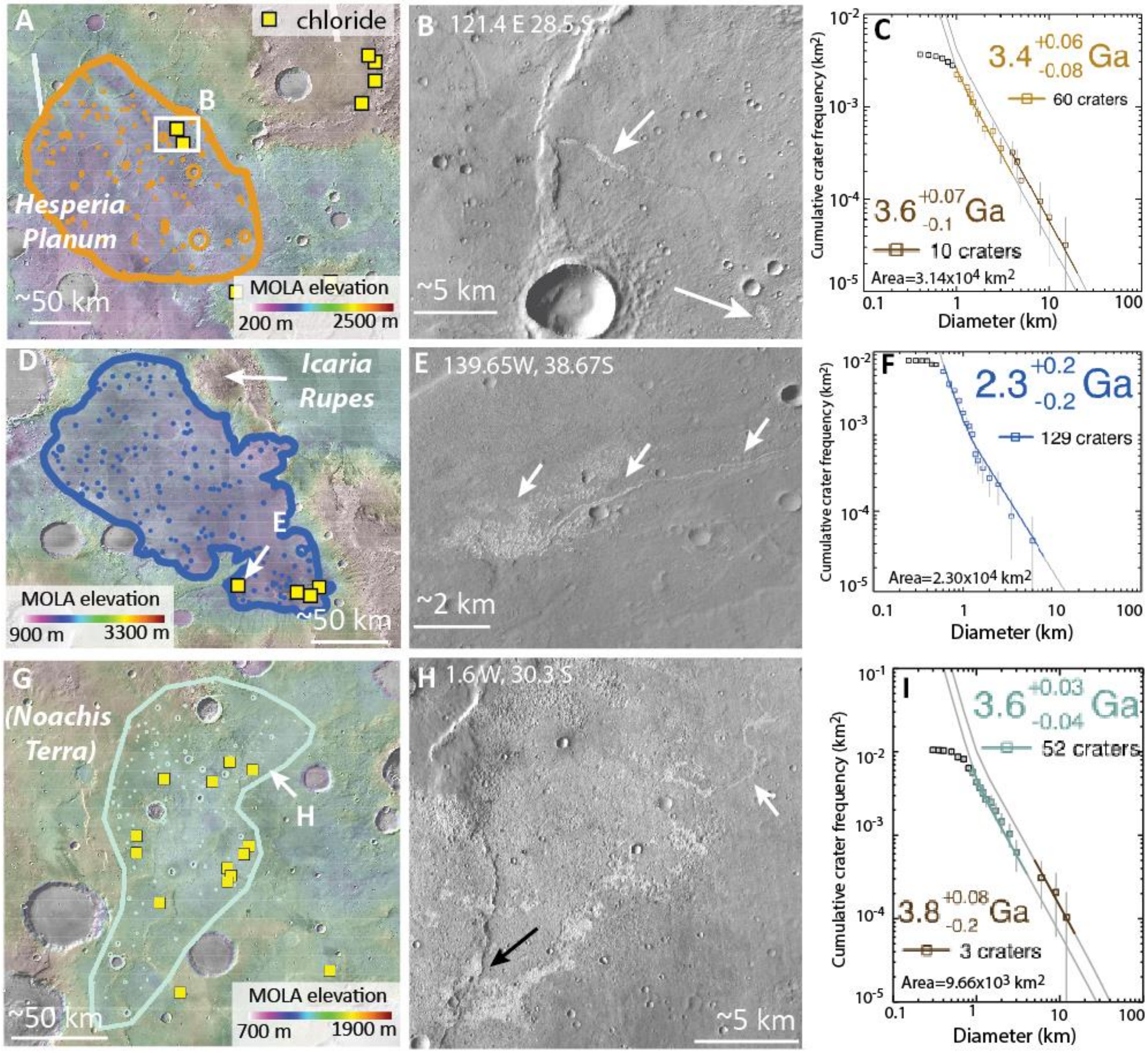

Fig 5-18. Age of other chloride-bearing terrains on Mars. (A) Chloride deposit is on the eastern edge of Hesperia Planum. Nearby chloride deposits present in adjacent Noachian highlands. (B) Chloride on top of Hesperian lava flow is present within a channel (possibly a collapsed lava tube), suggesting that it was deposited after the emplacement of the lava flow. (C) Crater counting results from orange area in (A) shows a resurfacing age of 3.4 Ga (older surface ~ 3.6 Ga). (D) Southwest Tharsis site (detail in Fig J) is part of a large, smooth unit (likely lava flow). (E) Chloride deposit is present within channels on top of the lava flow unit, indicating that the chlorides are younger than the volcanic unit. (F) Crater counting for this region in southwest Tharsis yields an age of 2.3 Ga; this chloride deposit must be younger than ~2.3 Ga. (G) Cluster of chloride deposits on a volcanic unit in Noachis Terra; region and craters used are outlined in light cyan. (H) Chloride is present within channels on top of this unit (white arrow), and spills over a wrinkle ridge (black arrow). (I) Crater counting for this unit gives a resurfacing age of ~3.6 Ga (older surface ~3.8 Ga).

3.3.4 SW Tharsis

Chlorides are present on top of a smooth volcanic unit southwest of Tharsis, (Fig. 18d), where they are sometimes found in channels (Fig. 18e; for further detail, see Fig. 11). This large, flat volcanic unit is dated at 2.3 Ga; since the chlorides are on top of it, they must be younger than ~2.3 Ga. (In the global scale Tanaka et al. (2014) map, this unit is classified as early Hesperian volcanic).

3.3.5 Noachis Terra

Here, chlorides are on top of an older volcanic unit (flat area with wrinkle ridges; Fig. 18g). Again, chlorides are clearly on top of this unit, present in channels (white arrow in Fig. 18h) and spilling over a wrinkle ridge (black arrow, Fig. 18h). This unit has a resurfacing age of 3.6 Ga (underlying terrain dated to 3.8 Ga). (In the global scale Tanaka et al. (2014) map, this unit is classified as late Noachian highland).

While the majority of chloride deposits are on Noachian and early Hesperian terrain (3.9-3.6 Ga), we have identified several deposits that are on significantly younger terrain—several ~3.3-3.4 Ga (Hesperian), and even one that appears to be on top of Amazonian terrain (younger than 2.3 Ga). In all cases, these deposits on younger volcanic terrain are immediately adjacent to Noachian highlands, rather than in the centre of a volcanic plain, suggesting that their source may originate in the Noachian highlands despite their younger ages.

4 Discussion

4.1 Water source

In our analysis, all lines of evidence point to surface water runoff; we see deposits that are perched, even at a local scale, even more channels in CTX and HiRISE datasets, draping textures, and elevations that are not consistent with a groundwater-fed playa environment. Furthermore, our observations suggest that the chlorides were deposited from small volumes of water, rather than deep lakes as suggested in Hynek et al. (2015) and Melwani Daswani and Kite (2017). Evidence for small volumes of water includes layer thicknesses often <1 m, ponding at multiple elevations, asymmetry in deposits (high on one side, where channels lead in, and much lower on the other side), and draping textures where slightly higher topographic highs (>4 m) are generally not covered by chlorides. A larger volume of water would have been able to hold more chloride, and so deposits would be more likely to form a flat layer rather than reflecting underlying topography. Our revised thickness estimates, generally <~1m thick layers, are also consistent with small volumes of water.

One possible source of small volumes of surface water could be meltwater runoff, either seasonal or episodic (perhaps driven by obliquity changes, or related to heating from volcanism). A few locations show evidence of multiple stages of water levels (concentric rings in Fig. 10c, 12d), which could reflect multistage evaporation or repeated wet/dry cycles. Today, we only see thin seasonal water frosts in the southern highlands of Mars (Fig. 7; Vincendon et al., 2010), which would likely not provide enough brine for the km-scale chloride deposits we observe, even if temperatures and pressures were high enough to allow for melting rather than sublimation. But in the past, such surface ice deposits (perhaps in addition to subsurface ice in permafrost) may have been more widespread, thicker, and able to melt and provide a water source for chloride deposits. Alternatively, rare episodes of precipitation (e.g. due to volcanic outgassing) could provide a source of surface runoff; such precipitation might already be enriched in chlorine (e.g. Nekvasil et al., 2019).

4.2 Ion source

Possible chloride ion sources include volcanism (atmospheric, fumaroles, or magmatic sources), leaching and alteration from igneous crust, or remobilization of older deposits. Associated cations (e.g. sodium) are likely derived from leaching/weathering. In agreement with previous work (e.g. Osterloo et al., 2010; Ruesch et al., 2014), we do not believe that direct volcanic sources are likely, given the spatial anti-correlation with large volcanic provinces (e.g. Fig. 3, where Tharsis, Syrtis Major, and Hesperia volcanics are largely devoid of chlorides). However, chlorine emitted into the atmosphere through volcanic processes could settle out across the planet, in a surface coating enriched in chlorine (e.g. Cl-rich Mars dust, as in Schmidt et al., 2018).

Leaching chloride directly from dust, soils, or igneous materials (e.g. chlorapatite, glasses) is easier to achieve at higher temperatures and water/rock ratios, but work by Melwani Daswani and Kite (2017) indicates that it is possible even from igneous materials over decades of seasonal melting; chlorine in more mobile phases in dusts or soils is likely much easier to leach. Widespread Fe/Mg clays across the Noachian highlands are an indication that significant alteration has already taken place, and chloride ions may already have been released into more mobile phases through earlier alteration processes. Chloride deposits may preferentially form on clay-rich soils, which are known on Earth to be less permeable than most soils (e.g. Warrence et al., 2003); small volumes of water which might otherwise quickly infiltrate into the subsurface might instead evaporate at the surface, creating thin chloride crusts available for remobilization in the next cycle (e.g. Fig. 17, 19). In addition, capillary action in clay-rich soils can create salt crusts at the surface, accessing salts in the top meter of soil and bringing them to the surface (e.g. Provin and Pitt, 2001). This could be one mechanism for separating chloride and sulphate anions, to create the relatively pure chloride deposits observed on Mars. Small volumes of meltwater at a later date could mobilize small salt deposits (such as those in Fig. 17), and aggregate them in local topographic lows. Small volumes of low temperature water would preferentially dissolve just the most soluble salts (chlorides), providing an additional mechanism for separating chlorides from expected other carbonate or sulphate anions. An alternative source for small volumes of water is deliquescence, where salt minerals present in the soil can adsorb water vapor from the air, and form a concentrated brine when the relative humidity is high enough (as observed in Antarctica; Dickson et al., (2013)).

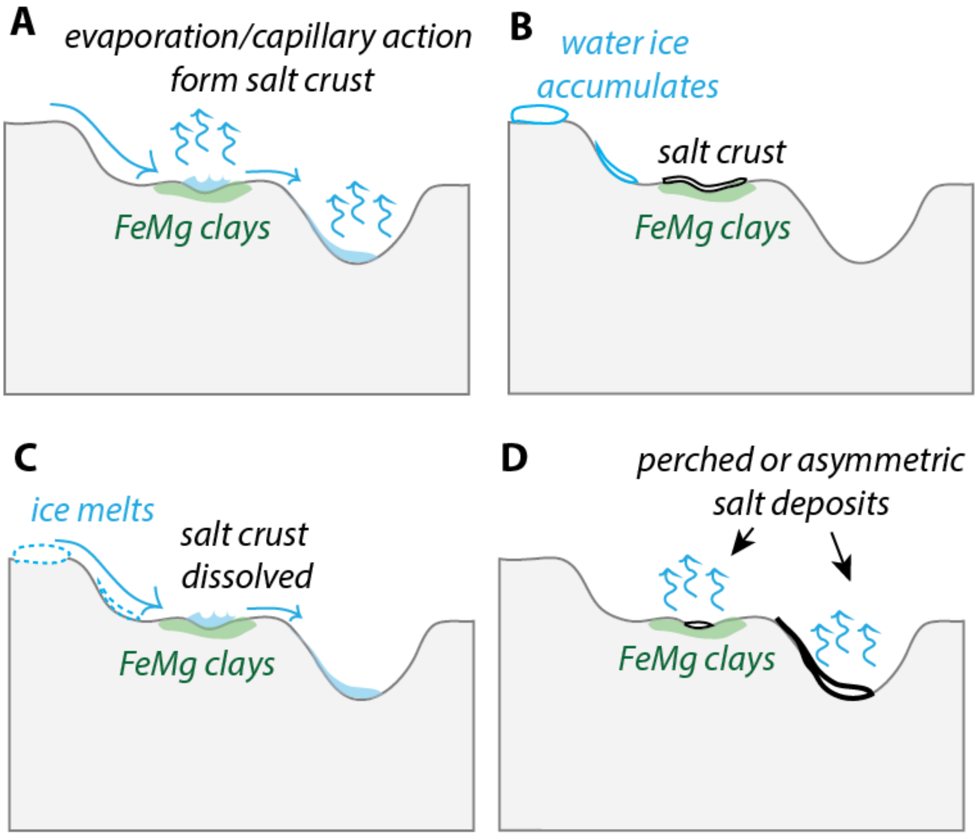

Fig. 5-19. Schematic diagram for chloride formation (A) At the end of a surface water epoch, evaporation/capillary action forms a salt crust in regions with impermeable clays. (B) Water ice accumulates (e.g. at elevation, or on pole-facing slopes). (C) Ice melts, sending small volumes of meltwater downstream. Previously deposited salt crusts may be dissolved, creating briny waters, redepositing in local topographic lows. (D) Freezing/evaporation occurs, leaving perched and/or asymmetric salt deposits (rather than basin-filling rings of salt).

4.2.1 Order of magnitude estimation

Chloride contents of soils and dust on Mars are typically ~1wt.% (Berger et al., 2016; Schmidt et al. 2018) with maximum measured amounts of ~3 wt.%. Filiberto & Treiman (2009) used data from martian meteorites to infer a parental magma composition of ~0.3 wt% Cl. Using these ranges (0.3-3 wt% Cl), we estimate (a) how much material contains enough chloride to generate all chloride deposits observed, and (b) how much material contains enough chloride to account for a median chloride deposit (~10 km^2, ~1m thick). Across the southern highlands, the total area of the chloride deposits is ~14 000 km^2 (Osterloo et al., 2010). Assuming a layer ~1 m thick of 25% halite (Glotch et al., 2016), this translates to ~$1x10^{14}$ mols Cl. If the surface material was 0.3-3 wt% Cl, and had a density of typical rocky materials (3 000 kg/m^3), this amount of chlorine would be present in a layer 0.7-7 mm thick across the southern highlands (area ~6.5 $x10^7$ km^2). But these processes appear to be more local, involving small amounts of water moving to local topographic lows, and so a more appropriate metric might be to investigate how much of the surrounding area would need to be leached to create a typical chloride deposit (10 km^2, 1 m thick). Using the same assumptions, we find that chloride from the top 3cm-30cm would need to be leached over a 1000 km^2 area (for reference, ~1000 km^2 is the typical order of magnitude area included within the 10 km buffer zone around a deposit, e.g. Fig. 2a). Since we know capillary action in clay rich soils can access the top meter or so, these numbers mean leaching from the top soil layer is a plausible chlorine source.

4.3 Significance of Mineral Assemblages/Lack Thereof

Previous studies have noted the lack of association with other minerals (sulphate, carbonate) typically found with chloride deposits on Earth (Ruesch et al., 2012; El Maary et al., 2013), as well as the apparent relationship with Fe/Mg clays. Even using machine learning techniques, and searching every targeted CRISM image that intersects chloride, we were unable to find any small deposits of accessory minerals that might help us to further narrow down the composition of the brine from which the chlorides were deposited. Laboratory work by Glotch et al. (2016) and Ye & Glotch (2019) constrains these deposits to be ~25% chloride material, but mixed with <5% (and typically <1%) minerals like sulphate or clay which have significant absorptions in the visible-shortwave infrared region. Even small amounts of these accessory minerals show through in mixtures with halite. However, a very pure halite crust a few mm to cm thick would mask underlying materials, although we never see anything but Fe/Mg clay minerals exposed where impact craters have broken through a chloride layer.

On Earth, clay-rich soils are known to hinder infiltration and drainage, and so ponding and evaporation at the surface is more likely to occur. Pure halite crusts develop on clay-rich soils through capillary action, when evaporation pressure is strong (e.g. arid and/or low pressure atmosphere). This process could be occurring on Mars as well, accounting for the presence of clays near most chloride deposits. Chemically, the presence of clays signals that initial igneous crust has been significantly aqueously processed, perhaps releasing both cations and anions through leaching (e.g. Milliken et al., 2009), and leaving them in a mobile phase that is easily dissolved and transported.

4.4 Timing

Although chloride deposits are found overwhelmingly in Noachian terrain (at the global scale (Tanaka et al., 2014) and select local deposits (e.g. Osterloo et al., 2010)), their morphologies and elevation distributions are consistent with being draped on top of the surface. Therefore, we can only say that the vast majority of chloride deposits happened in the Noachian or later. In only one case were we able to obtain a youngest-possible age date to bracket chloride formation (prior to 2.0 Ga). Generally, chloride deposits themselves are too small to obtain reliable age dates from direct crater counting. We dated several regions where chlorides were clearly on top of a volcanic unit, and found that resurfacing ages for these units ranged from Hesperian to Amazonian (3.6-2.3 Ga). Since these areas are typically large (>7 000 km^2), we do not think that the age dates are artificially young due to a small sample size.

Taking into account both our age dates and those of previous studies, we believe that chloride deposits may have started to form as early as the late Noachian, but that the processes creating these deposits continued until at least ~2.3 Ga. For one deposit, chloride formation must have occurred at least 2 billion years ago. Furthermore, many chloride deposits are present in intercrater plains, in places that could accumulate dust over time, and chloride minerals are soft and easily abraded. Given the crisp, fresh appearance of these deposits, we think that a significant proportion of them may be on the younger side of the age range. The persistence of episodes of small volumes of water into the Amazonian is consistent with other recent work in Gale crater (e.g. Grant et al., 2019; Martin et al., 2017).

4.5 Spatial distribution of chlorides

A puzzling fact about the chloride deposits is that they are almost all in the southern parts of the southern highlands, and not in the more northern parts (e.g. Mawrth, NE Syrtis) where we still see plenty of other mineral detections. As noted in previous work, chloride deposits follow the same approximate distribution as the valley networks (Hynek et al., 2010; see Fig. 3a). This band is centred farther south than would be expected for a zone of maximum precipitation, based on Mars' current orientation. Bouley et al. (2016) propose that the valley networks formed prior to the Tharsis bulge; the mass of Tharsis later caused Mars' poles to shift, such that this bulge was on the equator. They demonstrate that the densest valley networks line up with the zone of maximum expected precipitation, based on a model of Mars' shape and orientation with Tharsis removed. While we think that the chloride deposits likely occurred after this shift (Hesperian/Amazonian), it is possible that chloride deposits detectable at THEMIS resolution require pre-existing valley networks to efficiently aggregate and transport small volumes of brine into a larger deposit. Alternatively, this zone could have hosted the largest amounts of surface/subsurface ice after the Noachian, which could have slowly melted over time, and provided a water source for the chloride deposits.

5 Conclusions

Chloride deposits found across the southern highlands of Mars likely represent small volumes of surface water, deposited in existing topographic lows such as old channels and lake basins. Within these basins, chloride deposits tend to be draped on top of underlying topography, and at a range of (asymmetric) elevations, unlike playa environments on Earth. Despite being found in local topographic lows, many chloride deposits are within 10 km of a deeper crater with no signs of groundwater upwelling or chloride deposits, indicating that deep upwelling groundwater is probably not responsible for these deposits. Instead, we believe that surface runoff is the most likely water source, from potential sources like seasonal or episodic melting of ice or permafrost, or deliquescence. Chloride anions may be leached from the top layer (<1 m) of soil/dust in the highlands, where clay-rich soils provide a mechanism to wick brines up to the surface, forming a pure salt crust. Weathering of basalt to clay also releases cations, which could combine with chloride to form the observed deposits. Measured chloride enrichments in martian dust may be a result of volcanic aerosols settling out on the surface. While the vast majority (97%) of chlorides are found within the Noachian highlands, a small number are found in channels on top of younger volcanic plains, around the edges of these volcanic provinces. Chloride bearing brines may have formed in the Noachian highlands, and been transported downhill and deposited on top of younger terrain (3.4-2.3 Ga). Thus, we believe that Mars' chloride deposits continued to form into the Amazonian, despite being found predominantly in Noachian terrain.

5.6 References

Berger, J. A., Schmidt, M. E., Gellert, R., Campbell, J. L., King, P. L., Flemming, R. L., . . . VanBommel, S. J. (2016). A global Mars dust composition refined by the Alpha-Particle X-ray Spectrometer in Gale Crater. Geophysical research letters, 43(1), 67-75.

Beyer, R. A., Alexandrov, O., & McMichael, S. (2018). The Ames Stereo Pipeline: NASA's Open Source Software for Deriving and Processing Terrain Data. Earth and Space Science, 5(9), 537-548.

Bishop, J. L., Perry, K. A., Darby Dyar, M., Bristow, T. F., Blake, D. F., Brown, A. J., & Peel, S. E. (2013). Coordinated spectral and XRD analyses of magnesite-nontronite-forsterite mixtures and implications for carbonates on Mars. Journal of Geophysical Research: Planets, 118(4), 635-650.

Bridges, J., & Grady, M. (2000). Evaporite mineral assemblages in the nakhlite (martian) meteorites. Earth and Planetary Science Letters, 176(3-4), 267-279.

Carter, J., Poulet, F., Bibring, J. P., Mangold, N., & Murchie, S. (2013). Hydrous minerals on Mars as seen by the CRISM and OMEGA imaging spectrometers: Updated global view. Journal of Geophysical Research: Planets, 118(4), 831-858.

Delamere, W. A., Tornabene, L. L., McEwen, A. S., Becker, K., Bergstrom, J. W., Bridges, N. T., . . . Keszthelyi, L. (2010). Color imaging of Mars by the high resolution imaging science experiment (HiRISE). Icarus, 205(1), 38-52.

Dickson, J., Kerber, L., Fassett, C., & Ehlmann, B. (2018). A Global, Blended CTX Mosaic of Mars with Vectorized Seam Mapping: A New Mosaicking Pipeline Using Principles of Non-Destructive Image Editing. Paper presented at the Lunar and Planetary Science Conference.

Ehlmann, B. L., & Buz, J. (2015). Mineralogy and fluvial history of the watersheds of Gale, Knobel, and Sharp craters: A regional context for the Mars Science Laboratory Curiosity's exploration. Geophysical research letters, 42(2), 264-273.

Ehlmann, B. L., Mustard, J. F., Murchie, S. L., Poulet, F., Bishop, J. L., Brown, A. J., . . . Milliken, R. E. (2008). Orbital identification of carbonate-bearing rocks on Mars. Science, 322(5909), 1828-1832.

El-Maarry, M. R., Pommerol, A., & Thomas, N. (2013). Analysis of polygonal cracking patterns in chloride-bearing terrains on Mars: Indicators of ancient playa settings. Journal of Geophysical Research: Planets, 118(11), 2263-2278.

Eugster, H. P., & Hardie, L. A. (1978). Saline lakes Lakes (pp. 237-293): Springer.

Glotch, T. D., Bandfield, J. L., Tornabene, L. L., Jensen, H. B., & Seelos, F. P. (2010). Distribution and formation of chlorides and phyllosilicates in Terra Sirenum, Mars. Geophysical research letters, 37(16).

Glotch, T. D., Bandfield, J. L., Wolff, M. J., Arnold, J. A., & Che, C. (2016). Constraints on the composition and particle size of chloride salt-bearing deposits on Mars. Journal of Geophysical Research: Planets, 121(3), 454-471.

Hartmann, W., & Daubar, I. (2017). Martian cratering 11. Utilizing decameter scale crater populations to study martian history. Meteoritics & Planetary Science, 52(3), 493-510.

Hartmann, W. K. (2005). Martian cratering 8: Isochron refinement and the chronology of Mars. Icarus, 174(2), 294-320.

Hill, J., & Christensen, P. (2019). New Constraints on the Formation Ages of the Chloride-Bearing Deposits in the martian Southern Hemisphere. LPI Contributions, 2089.

Huang, J., Salvatore, M. R., Edwards, C. S., Harris, R. L., & Christensen, P. R. (2018). A Complex Fluviolacustrine Environment on Early Mars and Its Astrobiological Potentials. Astrobiology, 18(8), 1081-1091.

Hynek, B. M., Osterloo, M. K., & Kierein-Young, K. S. (2015). Late-stage formation of martian chloride salts through ponding and evaporation. Geology, 43(9), 787-790.

Knoll, A. H., Jolliff, B. L., Farrand, W. H., Bell III, J. F., Clark, B. C., Gellert, R., . . . Johnson, J. R. (2008). Veneers, rinds, and fracture fills: Relatively late alteration of sedimentary rocks at Meridiani Planum, Mars. Journal of Geophysical Research: Planets, 113(E6).

McEwen, A. S., Eliason, E. M., Bergstrom, J. W., Bridges, N. T., Hansen, C. J., Delamere, W. A., . . . Keszthelyi, L. (2007). Mars reconnaissance orbiter's high resolution imaging science experiment (HiRISE). Journal of Geophysical Research: Planets, 112(E5).

McGuire, P. C., Bishop, J. L., Brown, A. J., Fraeman, A. A., Marzo, G. A., Morgan, M. F., . . . Pelkey, S. M. (2009). An improvement to the volcano-scan algorithm for atmospheric correction of CRISM and OMEGA spectral data. Planetary and Space Science, 57(7), 809-815.

Melwani Daswani, M., & Kite, E. (2017). Paleohydrology on Mars constrained by mass balance and mineralogy of pre-Amazonian sodium chloride lakes. Journal of Geophysical Research: Planets, 122(9), 1802-1823.

Michael, G. (2013). Planetary surface dating from crater size–frequency distribution measurements: Multiple resurfacing episodes and differential isochron fitting. Icarus, 226(1), 885-890.

Milliken, R., Fischer, W., & Hurowitz, J. (2009). Missing salts on early Mars. Geophysical research letters, 36(11).

Ming, D. W., Mittlefehldt, D. W., Morris, R. V., Golden, D., Gellert, R., Yen, A., . . . Ruff, S. W. (2006). Geochemical and mineralogical indicators for aqueous processes in the Columbia Hills of Gusev crater, Mars. Journal of Geophysical Research: Planets, 111(E2).

Morgan, F. (2009). CRISM Data Users' Workshop CAT Tutorial.

Murchie, S., Arvidson, R., Bedini, P., Beisser, K., Bibring, J. P., Bishop, J., . . . Clancy, R. (2007). Compact reconnaissance imaging spectrometer for Mars (CRISM) on Mars reconnaissance orbiter (MRO). Journal of Geophysical Research: Planets, 112(E5).

Murchie, S. L., Mustard, J. F., Ehlmann, B. L., Milliken, R. E., Bishop, J. L., McKeown, N. K., . . . Wiseman, S. M. (2009). A synthesis of martian aqueous mineralogy after 1 Mars year of observations from the Mars Reconnaissance Orbiter. Journal of Geophysical Research: Planets, 114(E2).

Osterloo, M., Hamilton, V., Bandfield, J., Glotch, T., Baldridge, A., Christensen, P., . . . Anderson, F. (2008). Chloride-bearing materials in the southern highlands of Mars. Science, 319(5870), 1651-1654.

Osterloo, M. M., Anderson, F. S., Hamilton, V. E., & Hynek, B. M. (2010). Geologic context of proposed chloride-bearing materials on Mars. Journal of Geophysical Research: Planets, 115(E10).

Provin, T., & Pitt, J. L. (2001). Managing soil salinity. Texas FARMER Collection.

Ruesch, O., Poulet, F., Vincendon, M., Bibring, J. P., Carter, J., Erkeling, G., . . . Reiss, D. (2012). Compositional investigation of the proposed chloride-bearing materials on Mars using near-infrared orbital data from OMEGA/MEx. Journal of Geophysical Research: Planets, 117(E11).

Smith, D. E., Zuber, M. T., Frey, H. V., Garvin, J. B., Head, J. W., Muhleman, D. O., . . . Zwally, H. J. (2001). Mars Orbiter Laser Altimeter: Experiment summary after the first year of global mapping of Mars. Journal of Geophysical Research: Planets, 106(E10), 23689-23722.

Snyder, N. (2005). Transient response of a desert river to forced diversion: Furnace Creek Wash, Death Valley National Park, California. Lidar data acquisition and processing completed by the National Center for Airborne Laser Mapping (NCALM - http://www.ncalm.org). NCALM funding provided by NSF's Division of Earth Sciences, Instrumentation and Facilities Program. EAR-1043051., distributed by OpenTopography. . doi: 10.5069/G9P848VX

Survey, G., Greeley, R., & Guest, J. (1987). Geologic map of the eastern equatorial region of Mars.

Tanaka, K. L. (1986). The stratigraphy of Mars. Journal of Geophysical Research: Solid Earth, 91(B13), E139-E158.

Tanaka, K. L., Skinner Jr, J. A., Dohm, J. M., Irwin III, R. P., Kolb, E. J., Fortezzo, C. M., . . . Hare, T. M. (2014). Geologic map of Mars. United States Geological Survey Sci. Invest.(Map, scale 1: 20,000,000)(in review).

Thomas, N., Ehlmann, B., Meslin, P. Y., Rapin, W., Anderson, D., Rivera-Hernández, F., . . . Mangold, N. (2019). Mars Science Laboratory Observations of Chloride Salts in Gale Crater, Mars. Geophysical research letters.

Tosca, N. J., & McLennan, S. M. (2006). Chemical divides and evaporite assemblages on Mars. Earth and Planetary Science Letters, 241(1-2), 21-31.

Vincendon, M., Forget, F., & Mustard, J. (2010). Water ice at low to midlatitudes on Mars. Journal of Geophysical Research: Planets, 115(E10).

Warrence, N. J., Bauder, J. W., & Pearson, K. E. Basics of salinity and sodicity effects on soil physical properties.

Weiss, D. K., & Head, J. W. (2014). Ejecta mobility of layered ejecta craters on Mars: Assessing the influence of snow and ice deposits. Icarus, 233, 131-146.

Ye, B., Huang, J., Michalski, J., & Xiao, L. (2019). Geomorphologic Characteristics of Polygonal Features on Chloride-Bearing Deposits on Mars: Implications for martian Hydrology and Astrobiology. Journal of Earth Science, 1-10.

Ye, C., & Glotch, T. D. (2019). Spectral Properties of Chloride Salt-Bearing Assemblages: Implications for Detection Limits of Minor Phases in Chloride-Bearing Deposits on Mars. Journal of Geophysical Research: Planets, 124(2), 209-222.

Google Earth Pro v 7.1.5.1557, (5 September 2015), Death Valley, California

36.2047 N, 116.7904 W, Eye alt: 150 ft. Maxor Technologies 2019. http://www.earth.google.com [October 2019]

Google Earth Pro v 7.1.5.1557, (5 September 2015), Death Valley, California

36.2548 N, 116.8272 W, Eye alt: 23.5 km. TerraMetrics 2019. http://www.earth.google.com [October 2019]

Google Earth Pro v 7.1.5.1557, (31 Dec 1998), McMurdo Dry Valleys, Antarctica

77.5647 S, 161.2139 E, Eye alt: 60 km. USGS Landsat 7. http://www.earth.google.com [November 2019]

Chapter 6

A HISTORY OF ALTERATION IN TERRA SIRENUM, MARS: EVIDENCE FOR CHEMICALLY DISTINCT WATERS FORMING SULPHATES VS. CHLORIDES INTO THE AMAZONIAN

E. K. Leask[1], B. L. Ehlmann[1, 2], and M. Dundar[3]

[1] Division of Geological and Planetary Sciences, California Institute of Technology, Pasadena, CA, USA

[2] Jet Propulsion Laboratory, California Institute of Technology, Pasadena, CA, USA

[3] Indiana University-Purdue University, Indianapolis, IN, USA

Abstract

Terra Sirenum, a region in the Noachian highlands southwest of Tharsis, is unique in the number, proximity, and diversity of orbital detections of secondary minerals, including chlorides, many sulphates, carbonates, clay minerals, and hydrated silica. We combine mineralogical information, high-resolution imagery, and elevation models to investigate the geologic context of these secondary minerals, to better understand the sources of water and ions for each type of deposit, as well as their spatial/temporal relationships. Carbonates, where present, are part of Noachian basement rocks exposed through cratering processes, and do not appear to be part of any evaporative sequence. We have found numerous small detections of the acid sulphate minerals alunite and jarosite throughout the region, which mirror the dominant clay cation in the regions they are found—Al phyllosilicates and Fe phyllosilicates, respectively—suggesting that the cations are leached in situ. We interpret a previously-discovered kaolinite-rich unit overlying iron/magnesium clays across northeast Terra Sirenum as remnants of a widespread felsic ash unit, rather than a pedogenic weathering sequence. Sulphate and chloride detections are decoupled, with sulphates precipitated from volcanism-associated groundwaters, while chloride detections are consistent with surface water runoff, in some instances clearly post-dating volcanic units capping sulphate detections. Volcanic resurfacing of craters in the region gets progressively younger from west to east across our study area, with the youngest dates nearest Tharsis. From age dates across the region, episodic, localized sulphate- and chloride-forming processes continued to occur from ~3.5-<2 Ga; we hypothesize that their decoupling points to disconnected episodic surface and groundwater reservoirs, perhaps separated by a permafrost layer.

Plain Language Summary

In Mars research, a major outstanding question is trying to understand how Mars evolved from a water-rich planet to the dry planet we see today: whether the water went underground or was still at the surface in smaller amounts for some time, and whether the water was salty, acidic, or sulphur-rich, as these have implications for whether or not life could have survived. We look at a large region southwest of Mars' biggest volcanoes, which is known for having a large number of different types of water-related minerals. Different minerals form under different conditions (acidity, temperature, composition), so we can use these diverse mineral detections to infer the properties of the water that deposited them. We also use high resolution imagery to understand how the minerals are (or are not) related to one another. Here, we find that acidic, sulphate minerals are present only in deep areas with indications of volcanic activity,

meaning the water likely came from groundwater with acid and sulphur added from nearby volcanism. Age dating of the units associated with sulphates shows that they get progressively younger from west to east, towards the big, thick volcanic region; we think that this volcanic unit could be acting like a blanket, keeping rock molten underground for longer than in other regions. Chloride minerals (e.g. table salt) are found in small ponds and channels at a wide range of elevations, including on top of some of the sulphate-associated volcanics; we think that these come from episodes of surface water runoff, perhaps from melting ice, dissolving and transporting small amounts of chloride present in the dust/soil at the surface. On Earth, sulphate and chloride minerals are often found together, evaporating one after the other from the same body of water. However, these same minerals in close proximity on Mars appear to have come from totally separate water bodies, despite happening at around the same time (between ~3.5 and 1.4 billion years ago). We think this means that these surface and groundwater reservoirs were fully separated for this time, perhaps by a permanently frozen layer between them, preventing episodes of melted water at the surface from going deep into the ground, and stopping groundwaters heated by molten rock from making it all the way up to high elevations. Furthermore, previously-described patterns of aluminum-rich clays on top of iron/magnesium rich clays in this area have been interpreted as weathering sequences, which implies a large volume of water moving from the top down to wash iron and magnesium out from the clays, leaving behind mostly aluminum. Instead, we interpret the aluminum-rich clays as part of a regional aluminum-rich volcanic ash layer, deposited on top of widespread, older iron/magnesium clays; this interpretation only needs a small amount of water to create the observed pattern of aluminum clays over iron/magnesium clays.

1 Introduction

Though Mars' surface is dry today, there are many lines of evidence that point to widespread surface water in its past. Since the first Mars imagers in the 1970s, we have observed deep, branching valley networks (e.g. Masursky et al., 1977) carved into the southern highlands, and many thousands of hydrated mineral deposits have been detected with imaging spectroscopy, first OMEGA (Observatoire pour la Minéralogie, l'Eau, les Glaces, et l'Activité) in 2005 (Poulet et al., 2005; Bibring et al., 2005), followed by CRISM (Compact Reconnaissance Imaging Spectrometer for Mars) (e.g. Murchie et al., 2009). With these detections came a division of Mars' history into 3 mineralogical eras (Bibring et al., 2006): a clay-rich, wet early Mars in the Noachian, followed by a sulphate-rich period in the Hesperian, and finally a dry Amazonian era, with punctuated volcanism. However, several recent works have found evidence of surface water and diagenesis into the Amazonian, suggesting that episodic surface waters may have existed on Mars as recently as ~2.5-2.0 Ga (Martin et al., 2017; Morgan et al., 2018; Grant and Wilson, 2019; Leask and Ehlmann, in prep.). Here, we investigate the relationships between alteration minerals to better understand the timing, source, and compositions of the waters in which they formed.

We focus our study on Terra Sirenum, an ancient region in the Noachian highlands just southwest of Tharsis, which contains a large number of diverse secondary minerals, including chlorides, carbonates, clay minerals, hydrated silica, and a plethora of sulphates, including kieserite, szomolnokite, gypsum, alunite, and jarosite (Osterloo et al., 2010; Wray et al., 2011, Ehlmann et al., 2016, Pajola et al., 2016). Terra Sirenum also hosts the proposed Eridania palaeolake—a series of connected basins that were likely filled with water in the Noachian (Irwin et al., 2002; Michalski et al., 2017), as well as two craters (Columbus and Cross) previously studied for their array of sulphate mineralogies, suggestive of acidic lake or spring settings (Wray et al., 2011; Ehlmann et al., 2016). Unique, regionally widespread detections of aluminum-rich clays have also been found in this area (Wray et al., 2011) and several instances of aluminum-rich clays over iron/magnesium rich clays have been interpreted as weathering sequences (Carter et al., 2015).We use the spatial proximity of all these different minerals in conjunction with high resolution imagery and digital elevation models to explore possible genetic relationships between secondary minerals throughout the region. Salt minerals on earth are often part of an evaporative sequence (e.g. Eugster & Hardie, 1978), and understanding relationships between carbonate, sulphates, and chlorides helps us understand how water reservoirs on Mars have evolved through time. We investigate likely sources for water and ions for each deposit, combining data from a number of orbital datasets to understand composition (CRISM & THEMIS (Thermal Emission Imaging System), texture (CTX (Context Camera) and HiRISE (High Resolution Imaging Science Experiment), and elevation (MOLA (Mars Orbiting Laser Altimeter), and DEMs (digital elevation models) from CTX and HiRISE stereo pairs) thereby determining stratigraphic relationships and the environmental history of water in the Terra Sirenum region.

2 Methods

2.1 Mineral detection and analyses

In this work, we focus on minerals associated with water, especially evaporites/chemical precipitates (chlorides, sulphates, and carbonates) and hydrated silicates. For chloride mineral identification, we use the dataset provided by Osterloo et al. (2010), based on decorrelation stretched THEMIS infrared data (~100 m/pixel, with 9 bands 6-15 µm; Christiansen et al., 2004). We verify each detection and refine the boundaries of their regions of interest. For detailed cross-sections, we focus on the detections that are corroborated in CRISM data, where ratioed data show a bright, red slope with no major absorptions, and an inverted 3-µm water feature, indicating that they are drier than their surroundings. To investigate clay and sulphate mineralogy over this large region, we use both targeted and mapping CRISM (Compact Reconnaissance Imaging Spectrometer for Mars, aboard the Mars Reconnaissance Orbiter (MRO)) datasets, as well as a machine learning algorithm on the targeted dataset to classify pixels belonging to different mineral categories (Dundar et al., submitted). In particular, this was useful in finding small mineral deposits and rare minerals. All mineral detections are verified by hand, using traditional spectroscopic techniques. CRISM (and THEMIS) datasets used in this work can all be downloaded from NASA’s Planetary Data System.

2.1.1 CRISM multispectral mapping tiles

We mosaicked 36 CRISM multispectral mapping tiles (calibrated to Lambert albedo) for unbiased spectral coverage of our study area, covering about ~50% of the region in long strips (see Fig 1). This dataset has 72 spectral channels (0.41-3.92 µm), and a spatial resolution of 256 pixels/degree (converts to ~232 m/pixel in our region; cite DPSIS, section 3.5.1). To enhance spectral features, we ratioed the pixels in this mosaicked dataset by the column median; given the large area covered by this mosaic, we assume that the column median is bland, as the phyllosilicate mineral deposits we are investigating are much, much smaller than the ~1500 km column height. Mineral detections in the mapping dataset were corroborated with targeted, full-resolution CRISM data where available. Due to the lower spectral resolution of the mapping dataset, we only categorize locations with hydrated minerals, indicated by a 1.9-µm absorption, and by the presence of a 2.2-µm or 2.3-µm absorption, associated with Al- and Fe/Mg- bearing clays, respectively (see Table 1). We use this mapping dataset in conjunction with a global CTX (Context camera) mosaic, described below.

Group	Mineral Name	Formula	Diagnostic absorptions (µm)
Clay (Fe/Mg)	Saponite	$Ca_{0.25}(Mg,Fe)_3((Si,Al)_4O_{10})(OH)_2 \cdot nH_2O$	1.42, 1.92, 2.31, (2.39)
	Nontronite	$Na_{0.3}Fe_2((Si,Al)_4O_{10})(OH)_2 \cdot nH_2O$	1.42, 1.92, 2.29, (2.40)
Clay (Al-rich)	Montmorillonite	$(Na,Ca)_{0.33}(Al,Mg)_2(Si_4O_{10})(OH)_2 \cdot nH_2O$	1.41, 1.92, 2.20
	Kaolinite	$Al_2(Si_2O_5)(OH)_4$	1.41, 1.92, (2.16), 2.20
Sulphates	Monohydrated sulphates (kieserite, szomolnokite)	$(Mg,Fe)SO_4 \cdot H_2O$	1.63, 2.10-2.14, 2.40
	Gypsum	$CaSO_4 \cdot 2H_2O$	1.44, 1.76, 1.95, 2.21, 2.47
	Polyhydrated sulphates	$(Mg,Fe)SO_4 \cdot nH_2O$ (n>1)	1.43, 1.93, shoulder at ~2.40
	Bassanite	$CaSO_4 \cdot 0.5H_2O$	1.43, 1.92, 2.49
	Alunite	$KAl_3(SO_4)_2(OH)_6$	(1.43), 1.48, 1.76, 2.17,2.52
	Jarosite	$KFe^{3+}{}_3(SO_4)_2(OH)_6$	1.47, 2.27, shoulder at ~2.4
Carbonate	Dolomite	$CaMg(CO_3)_2$	1.92, 2.32, 2.51
Chloride	Halite	NaCl	(none)
Other Silicates	Analcime (zeolite)	$Na(AlSi_2O_6) \cdot H_2O$	1.42, (1.79), 1.92, 2.50
	Hydrated Silica	$SiO_2 \cdot nH_2O$	1.43, 1.94, 2.22

Table 6-1. Relevant mineral groups, names, formula, and diagnostic absorptions

2.1.2 CRISM targeted images

CRISM targeted infrared (IR) I/F images have 438 spectral channels (1.0-4.0 µm), and have a spatial resolution ~18-36 m/pixel (Murchie et al., 2007). In total, 167 targeted CRISM I/F images were processed (out of 562 in the region), selected based on a variety of factors, including: (1) date of image (younger images are typically less noisy than those later in the mission, due to cooler failures); (2) images with previously identified minerals of interest, to test whether the machine learning algorithm could replicate results; (3) where CTX imagery and/or CRISM mapping data indicated the presence of erosion or alteration processes; and (4) completeness of spatial coverage throughout the region.

Each image was processed using the machine learning algorithm described in Dundar et al. (submitted); essentially, pixels in each column with the least variability were averaged to create a “bland” denominator for ratioing to remove residual, column-dependent noise that is characteristic of the CRISM dataset. A 3-band median filter was applied to the ratioed I/F image to mitigate spikes, and the resulting spectra were parametrized based on band depths and ratios between different wavelengths (after Pelkey et al., 2007 and Viviano-Beck et al., 2014; details in Dundar et al., *submitted*). Parametrized spectra from published mineral detections were used as a training dataset. The classifier categorized each pixel as belonging to the closest mineral class, either with a probability or a maximum likelihood designation in different iterations of the algorithm.

Mineral detections were then verified using traditional, manual techniques. CRISM I/F images were autoratioed using a column median for simplicity, verified with local, manual denominator choices where the mineral detection could have been the result of a feature in the denominator. Mineral deposits that were identified using machine learning techniques were manually verified; this was especially useful to find small clusters (~30-100+ pixels). Regions of interest shown in figures 5-13 were drawn by hand, based on the machine learning assignments and customized band parameter maps.

2.2 High resolution imagery

2.2.1 Global CTX mosaic

We use a global CTX mosaic (Dickson et al., 2018) as a base layer for geologic interpretation, and interpolation between nearby mineral identifications. These data from the Context (CTX) camera on MRO are greyscale images, with a spatial resolution of ~6 m/pixel. In the course of this study, we noticed a similar light-toned, eroded texture associated with kaolinite/alunite deposits found across Terra Sirenum, and used the CTX mosaic to map similar light-toned, eroded units across the region. Targeted CRISM data intersecting these regions were processed (if not included in the initial list), and the regions of interest mapped in ArcGIS were imported to ENVI, where spectral means were calculated for each region using the CRISM mapping data mosaic.

2.2.2 HiRISE images

HiRISE images (High Resolution Imaging Science experiment on MRO; ~25 cm/pixel) were used to understand the detailed textures of deposits and their surroundings, looking especially for features like lava flows, cones, layering, veining, and stratigraphic relationships. Colour HiRISE (only available for some images, and only in the central swath) are especially helpful for distinguishing between light-toned phases, e.g. where different clays are juxtaposed, or clays and evaporites.

2.3 Digital Elevation Models

To help understand the relationships between mineral deposits, we use 3 different scales of digital elevation models (DEMs) in this work, including a global MOLA layer (Mars Orbiting Laser Altimeter on Mars Global Surveyor; 463 m/pixel), and DEMs derived from stereo CTX and HiRISE images, using the Ames Stereo Pipeline (Beyer et al., 2018).

2.4 Age dating from crater counts

For 7 sites with clay/sulphate alteration mineralogy, we conducted crater counts. These sites were chosen for the quality and quantity of targeted CRISM and HiRISE data available. We selected two sites to represent the Eridania basin (sites chosen have adjacent chloride deposits). Several other works have dated parts of these basins—overall ages are generally 3.5-3.7 Ga, roughly consistent with our age of 3.5 Ga for both sites (e.g. Irwin et al., 2002; Pajola et al., 2016; Michalski et al., 2017), although some works report ages as young as 1.5 Ga for small areas within the basins (e.g. Adeli et al., 2015). Sites crater-counted in this work are within largely flat, resurfaced crater basins; these are the surfaces we used for age-dating. Because of the difficulty always accurately determining whether a crater existed before or after a resurfacing event (HiRISE data are not always available to help), we counted all visible craters >~400 m diameter within the bounds, using the global CTX mosaic as a base layer. Since smaller craters are obliterated by resurfacing while larger ones tend to remain, several of these sites show two trends, where smaller craters define a younger trend, and larger craters define an older trend (pre-resurfacing);. Crater diameters were calculated in ArcMap, and exported to Craterstats 2.0 (Michael & Neukum, 2010). Age dates were determined using the Mars, Hartmann and Daubar (2016) production function and Hartmann (2005) (updated Michael (2013)) chronology function.

3 Results

3.1 Regional trends

3.1.1 CTX mosaic and multispectral mapping data

While investigating Al-clay and sulphate detections in northeast Terra Sirenum, we noticed a very similar morphology in several of the deposits—at the CTX scale, they contain light-toned, cliff-forming units around the edges of craters, with yardang-like linear, streamlined ridges and mesas, embayed by a dark-toned, flat-lying crater floor unit (see sections 3.3.3-3.3.7 below, and associated figures). Where HiRISE is available, they are finely layered (~1-10 m thick), with planar lamination. For unbiased coverage of these deposits, we mapped all similar light toned, eroded units from the CTX global mosaic, and used the CRISM multispectral mapping data to find spectral averages for each region, if sufficient data was available (Fig. 1). For many of these regions, a clear 2.2 or 2.3 μm signal is present in multispectral data, indicating the presence of either Al- or Fe/Mg-rich clays. Sites with dominant Al-rich clays (2.2 μm) are also more likely to show a 1.4-μm absorption, and sometimes appear to have a steep shoulder at 2.4 μm often associated with sulphates (notably Columbus and Cross craters, as well as "Kahnawake" crater). None of the eroded, light-toned exposures identified as Fe/Mg clay-rich show fine layering at HiRISE scale, nor do they have the yardang-like, aligned linear ridges, but instead have disconnected knobs and inverted channels (see figures 4-7, discussed below). There is a clear spatial pattern in the dominant clay mineral type, with Fe/Mg clays present across the region, and dominantly Al-rich clays occurring exclusively in the northeastern parts of our study area. Several of these sites were previously noted in Wray et al. (2011); we expand on their work, processing targeted CRISM observations taken as a result of their investigation. This pattern is corroborated by targeted CRISM data (Fig. 2a), and appears to follow the same distribution as alunite vs. jarosite detections (discussed below, section 3.1.2).

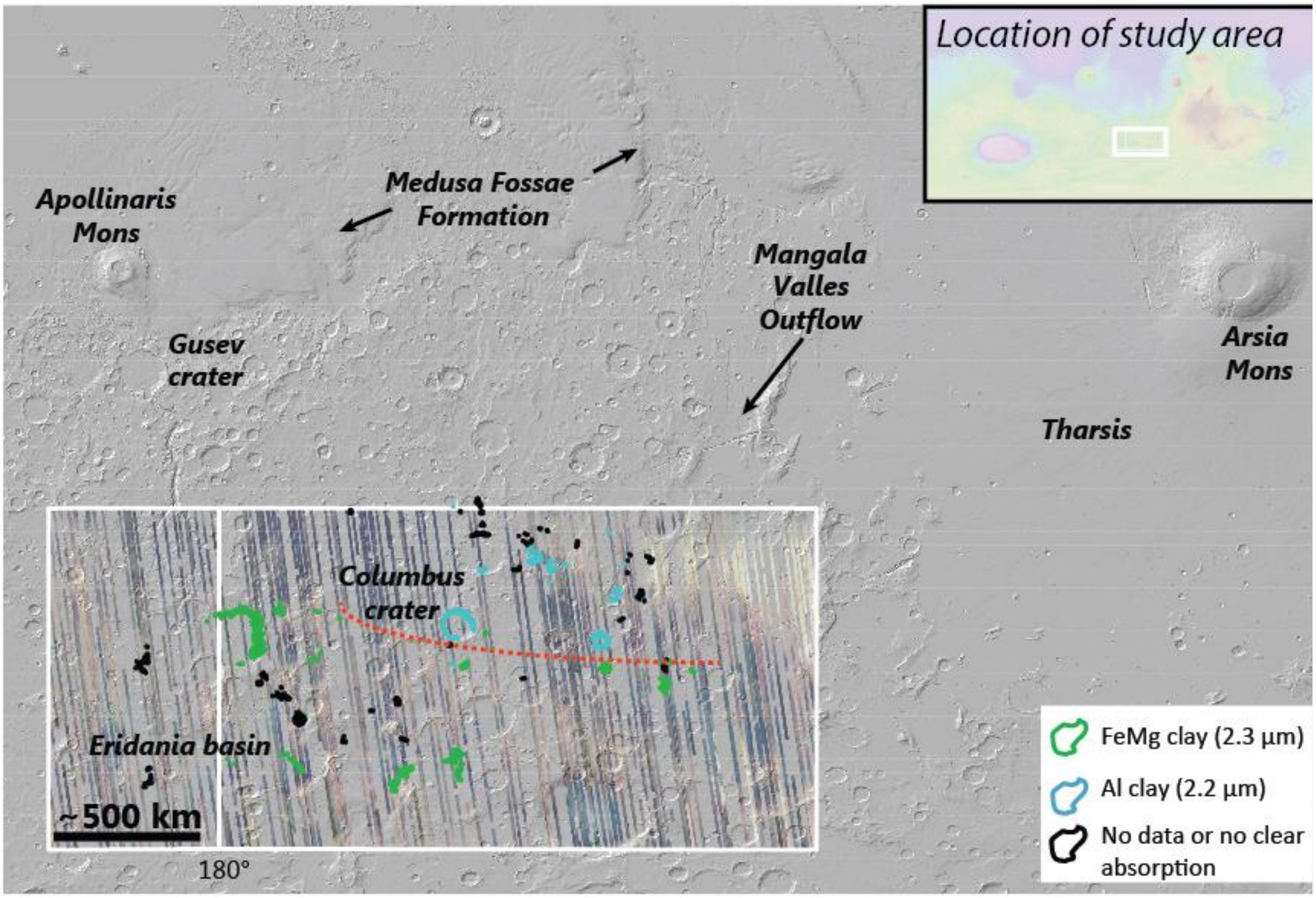

Fig. 6-1. Terra Sirenum study area in context, showing nearby features including volcano Apollinaris Mons, Medusa Fossae Formation deposits, and Mangala Valles mixed volcanic/fluvial outflow channel. Stripes show CRISM ratioed, joined Lambert albedo mapping tiles used in this study. Polygons show outlines of light toned eroded units delineated in global CTX mosaic; black outlines have no data/no clear absorptions, while green outlines have an absorption at 2.3 µm consistent with Fe/Mg clays, and cyan outlines have an absorption at 2.2 µm consistent with Al clays. Red dashed line delineates transition from majority Fe/Mg clay detections to dominant Al-clay exposures to the northeast.

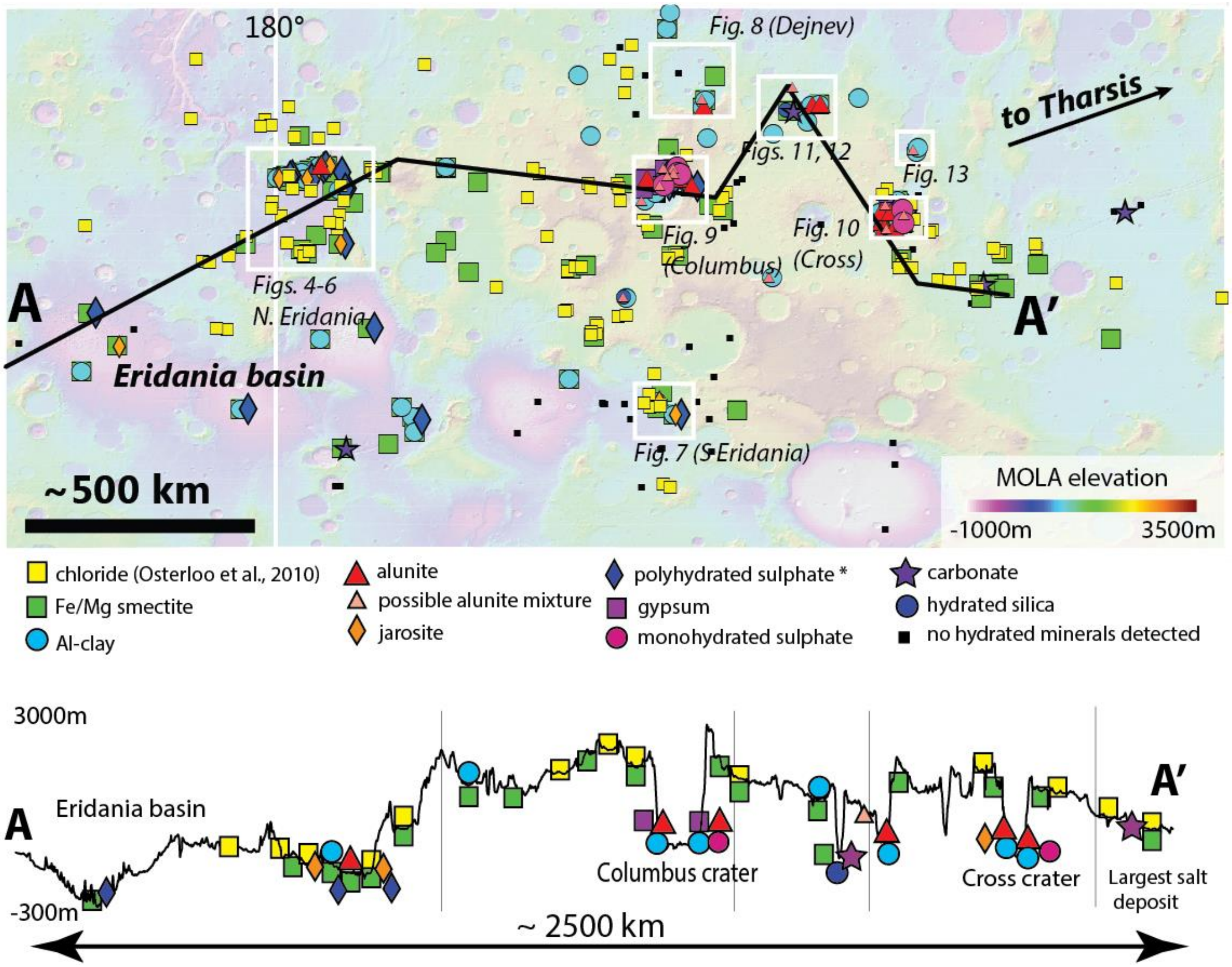

Fig. 6-2. Distribution of alteration mineral detections in Terra Sirenum. Chlorides and iron/magnesium clays are found throughout the region, at a wide range of elevations, while sulphates are almost exclusively found in deep basins. Aluminum clays often occur with either iron/magnesium clays, or with sulphates in basins.

3.1.2 Targeted CRISM data

Terra Sirenum has widespread detections of clay minerals, sulphates, and chlorides, as well as a handful of carbonates and hydrated silica detections (Fig 3a). Locations where no secondary minerals are detected tend to be in dusty locations, and/or later, noisier images (black squares in Fig 3a). Both Fe/Mg and Al-rich clays are found throughout the region, although there are more and larger detections of Al-rich clay (likely montmorillonite, kaolinite (see Table 1 for mineral formulae); cyan circles in Fig 3a) in the northeastern part of the region. Al-clays in the southwestern areas are small deposits (see sections 3.3.1, 3.3.2 below) in areas dominated by Fe/Mg clay minerals (e.g. saponite nontronite; green squares in

Fig 3a). Carbonates, where present, appear to be mixed in with Fe/Mg clay-bearing materials, and not separate evaporite units (see section 3.3.6 below). The two hydrated silica detections are present in very different mineral assemblages and geologic settings; one is in a central peak, near carbonates and Fe/Mg clays (section 3.3.6), while the other in adjacent to a possibly volcanic mound, and associated with kaolinite and a possible small alunite detection (this site is explored in Wray et al., 2011 (intercrater site 3)). A wide variety of sulphate minerals are found in Terra Sirenum; distinctive gypsum and monohydrated sulphates (kieserite and szomolnokite) are restricted to Columbus and Cross crater basins (for details, see Wray et al. (2011) and Ehlmann et al. (2016)), while small detections of alunite, jarosite, and polyhydrated sulphates are more widespread. Here, we use polyhydrated sulphate as the most likely interpretation (due to proximity to other sulphates) for a phase with a 1.9-µm absorption and strong shoulder at 2.4 µm (see Fig. 5c), but other minerals (notably zeolites like analcime) have very similar spectral shapes; this ambiguity has been previously noted in the literature (e.g. Wray et al., 2010). Acid sulphates alunite and jarosite are found throughout Terra Sirenum, in small patches within units dominated by Al- and Fe/Mg-rich clay units, respectively. That is, they are found associated with clays of the same cation. Sulphates always occur with at least a small amount of Al-rich clays nearby, although not all Al-rich clay deposits have associated sulphate detections from orbit. Chloride detections (Osterloo et al., 2010; yellow squares in Fig 3a) are scattered across the region, although missing in the deepest basins (southern Eridania, Newton crater, Cross crater, Columbus crater).).

3.1.3 Regional cross section

Each of the three main groups of alteration minerals (clays, sulphates, and chlorides) shows a different relationship with elevation throughout Terra Sirenum (Fig 3b). Both Fe/Mg and Al-rich clays are found at all elevations, from the deepest basins to the intercrater plains in the highlands (-600 to 2700m). Sulphates are found almost exclusively in crater basins (exception shown in Figs. 11 and 12), although these are at different absolution elevations throughout the region (~-600 to 1600 m). Chlorides are found in local topographic lows at a wide range of absolute elevations (~300 to 2700m). Neither hydrated silica nor carbonate detections show any correlation with elevation.

3.2 Age dates

To understand the timing of the different units we observed, we counted craters present at each site described below. All appeared to have experienced resurfacing events, with relatively flat, dark, even units filling approximately circular basins (or in the case of Fig. 3g, a series of circular basins). The basin areas range from ~780 km^2 ("Ohsweken", Fig. 3f) to ~32 000 km^2 (N Eridania, Fig. Ma; see Table 2 for a summary of areas, ages, and crater counts).

Crater counts in both North and South regions in Eridania (Figs 2a,b) show a single age of 3.5 Ga, indicating that the entire area was last resurfaced in the Hesperian. These are also the only two regions dominated by Fe/Mg clays. Dejnev (Fig. 3c) shows 2 distinct episodes of resurfacing, at around 3.5 Ga (consistent with the nearby Eridania basins), and again around 2.9 Ga (near the Hesperian/Amazonian boundary). Columbus crater appears to have been fully resurfaced at ~3.5 Ga, with a second resurfacing event affecting smaller craters at ~3.2 Ga. Though the area is smaller, Cross crater also shows a resurfacing age at about 3.5 Ga, and again at 2.2 Ga, resetting ages for the smaller crater diameters. "Ohsweken" has the least robust age dates, with an area of <1000 km^2; it appears to have been resurfaced at ~1.8 Ga, although this age could be artificially young due to the bias from its small size. However, the nearby "Kahnawake" crater has an even younger resurfacing age (1.4 Ga), despite having an area similar to Columbus. The larger size fraction at "Kahnawake" yield a maximum age of 2.6 Ga. Together, it appears that the resurfacing ages get progressively younger as we move from west to east across our study area, starting out ~3.5 Ga (Hesperian in the Eridania region, and as young as ~1.4 Ga (Amazonian) at the easternmost site, "Kahnawake.")

Site	Area (km^2)	N craters	Diameter range (km)	Age estimate (Ga)
N Eridania	31 600	100	1-15	3.5 +/-
S Eridania	23 600	110	0.75-15	3.5 +/-
Dejnev	15 200	70	0.6-1	2.9
		35	1-7.5	3.5
		3	7.5-15	3.8
Columbus	5 760	35	0.6-1	3.2
		15	1-10	3.5
Cross	2 360	23	0.5-1	2.2 +/-0.4
		2	1-3.5	3.5 + 0.1 -0.4
		2	3.5-10	3.8 +0.09 -0.3
Crater_161W_26S/Ohsweken	784	14	0.4-1	1.8
		3	1-3	3.7
Crater_157W_27S/Kahnawake	4 280	58	0.4-0.65	1.4
		17	0.65-5	2.6

Table 6-2. Results of age dating and crater counts

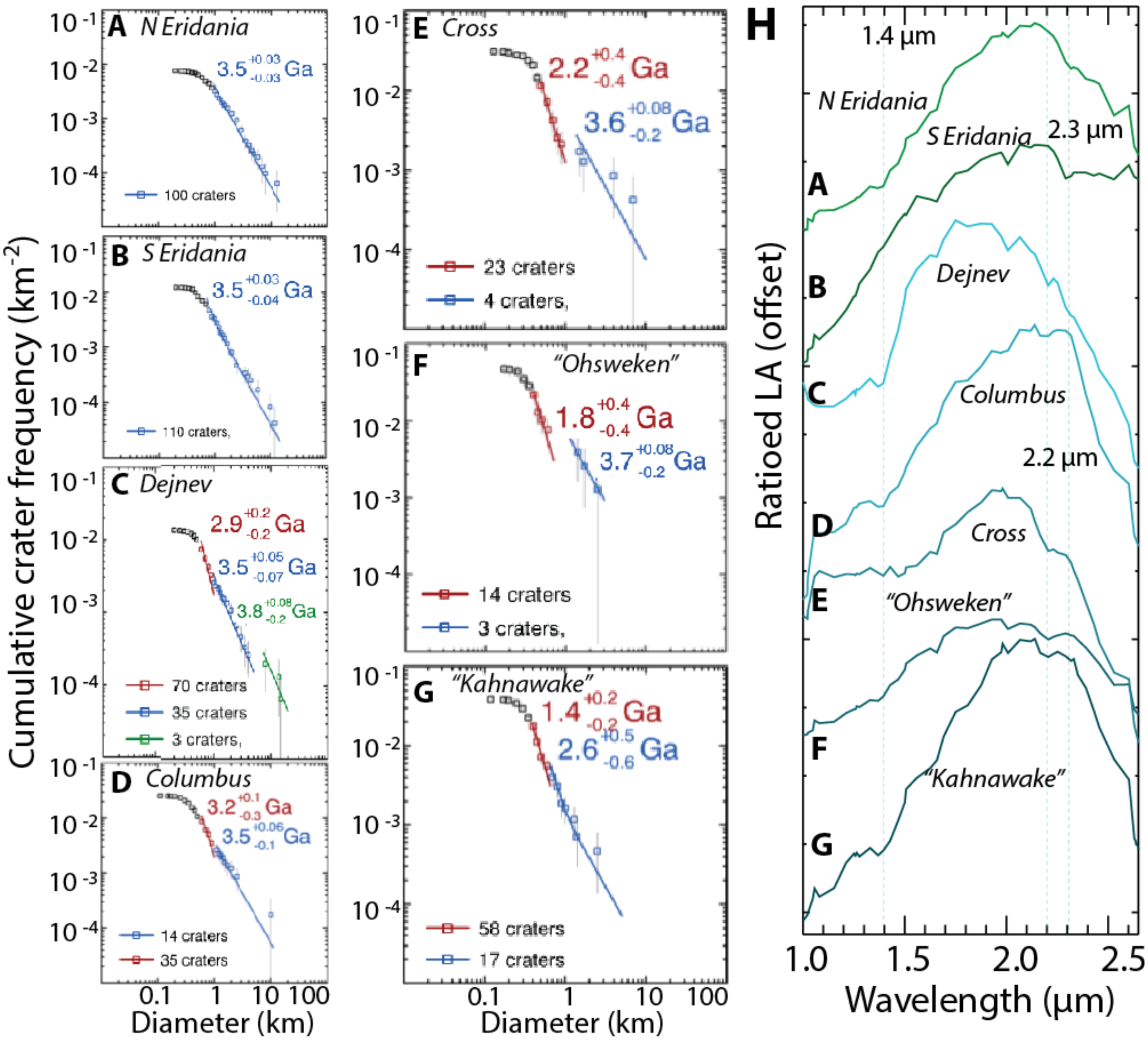

Fig. 6-3 Age dating volcanic resurfacing above clay (+/- sulphate) units. (A-G) N Eridania (3.5 Ga), S Eridania (3.5 Ga), Dejnev (resurfaced ~ 2.9 Ga, 3.5 Ga, 3.8 Ga), Columbus (resurfaced ~3.2 Ga, and 3.5 Ga), Cross (resurfaced ~2.2 Ga and 3.6 Ga), "Ohsweken" (resurfaced ~1.8 Ga and 3.7 Ga), "Kahnawake" (resurfaced ~1.4 Ga and 2.6 Ga). H) Multispectral means from polygons shown in (A-G), showing a clear 2.3-µm absorption (dominant Fe/Mg clays) in Eridania (A & B), and dominant Al-clays (2.2-µm absorption) elsewhere (C-G).

3.3 Mineralogy & morphology—examples

Here, we have chosen seven sites in Terra Sirenum with clay and sulphate detections—with nearby chloride where possible— to explore in detail, examining the morphology and relationships between hydrated-mineral bearing materials to infer the geologic history. These sites encompass the variations and trends observed across the region.

3.3.1. Northern Eridania

Northern Eridania basin straddles the 180 meridian, and is part of a series of connected basins interpreted as a palaeolake (e.g. Irwin et al., 2002). It was proposed as a potential landing site for Mars 2020, in part due to its mineralogical diversity (e.g. Pajola et al., 2016) because clays, sulphates, and chlorides are in close proximity. We confirm a stratigraphic relationship of Al-clays overlying Fe/Mg clay-bearing units in the northern part of the basin (Fig 4a; detail in Fig 5), previously described in Wendt et al. (2013), Adeli et al. (2015), Carter et al. (2015), and Pajola et al. (2016). Several of these works also note a dark capping unit above the light-toned, Al-clay bearing unit, which we also observe throughout the basin (e.g. Fig 4e, f). This dark capping unit is interpreted as volcanic in origin, given wrinkle ridges apparent within it (Fig. 4c). In some places, this unit is below light toned knobs, instead of capping them; where this is the case, it embays the older light-toned unit (Fig 4d).

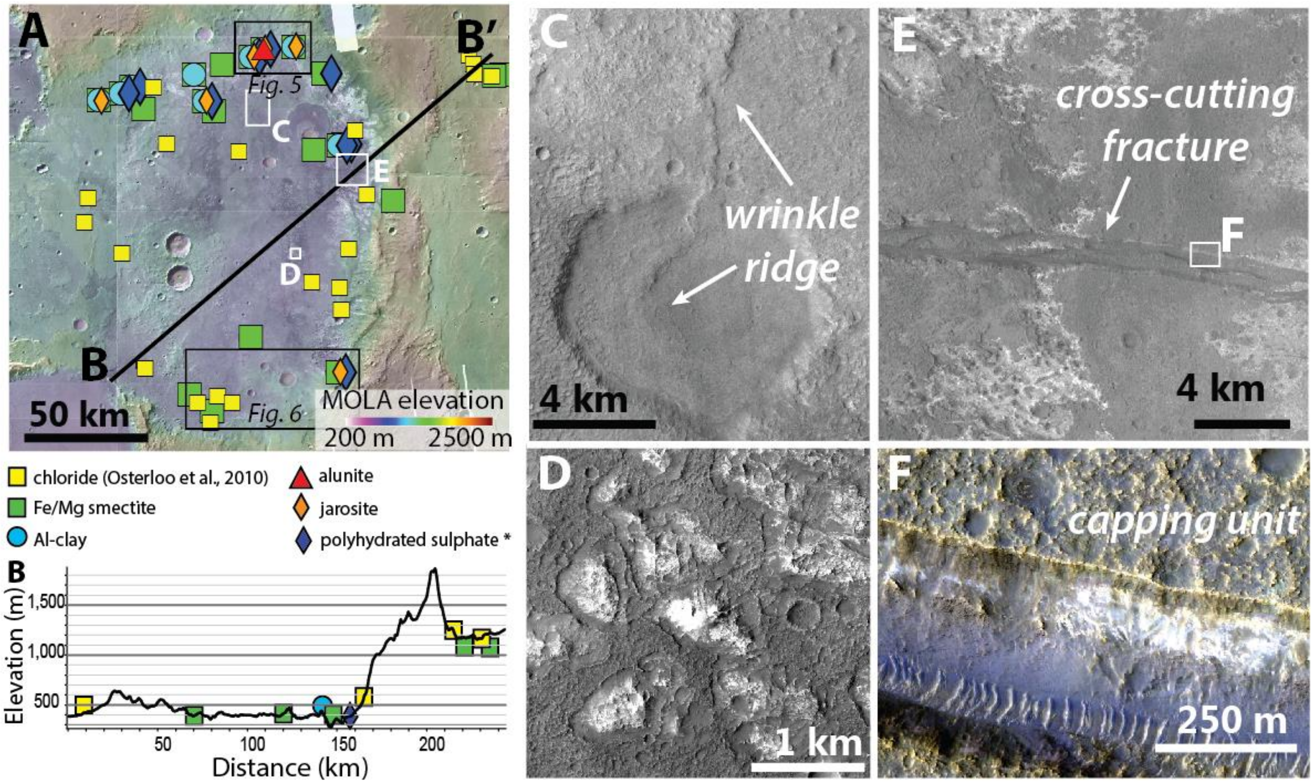

Fig. 6-4. Northern Eridania overview figure, showing sulphates, chlorides, and clays throughout the basin. Chlorides are also perched outside the basin, just above, indicating that the source of water is likely surface runoff rather than groundwater upwelling. C-F) Evidence for volcanic resurfacing—a wrinkle ridge appears to drape underlying topography (C); lava appears to embay Fe/Mg clay knobs (D; ESP 047309 1500); Dark capping unit is cross-cut by a fracture (E) exposing a light toned unit below (F; ESP 022294 1505).

Two previous authors (Carter et al., 2015 and Pajola et al., 2016) note the presence of sulphates in the northern section of this basin, including polyhydrated sulphate (or a zeolite), and small jarosite and alunite detections (Figs 5-7). Jarosite is identified by its absorption centred at 2.27 µm, and steep shoulder at ~2.4 µm; here, jarosite is likely mixed with Al-clay, with a secondary absorption centre at 2.20 µm, and 1.42 µm absorption instead of 1.47 expected for pure jarosite (see Table 1). Alunite is identified in individual pixels by its absorptions at 1.48, 1.76, and 2.17 µm. Here, the minor 1.76-µm absorption is lost when we average all pixels in the regions of interest, also likely due to mixing with Al-clays (Fig 5i). However, the paired shifts of the minor 1.4-µm feature closer to 1.5 µm and the 2.2-µm feature closer to 2.17 µm is consistent with alunite. We confirm these detections, and find 9 discrete small jarosite deposits in 6 images in the area, including previously unreported jarosite and polyhydrated sulphate in the southern part of the basin (Fig 5i, 6f). In HiRISE, we see that the Al clay and sulphate deposits are typically associated with bleached and veined textures respectively (Fig 5c-h, Fig 6e), unlike the draped morphology seen with the chlorides. Neither the bleached layer (particularly evident in HiRISE colour) nor the intensely veined sulphate areas occur at consistent elevations throughout the region (Fig 5b, Fig 6b). The stratigraphic position is, however, consistent. Always under a dark capping unit, this bleached layer (~3-15 m thick) ranges in elevation over 150 m. No fine layering in the light toned units is observed in any HiRISE image in this region.

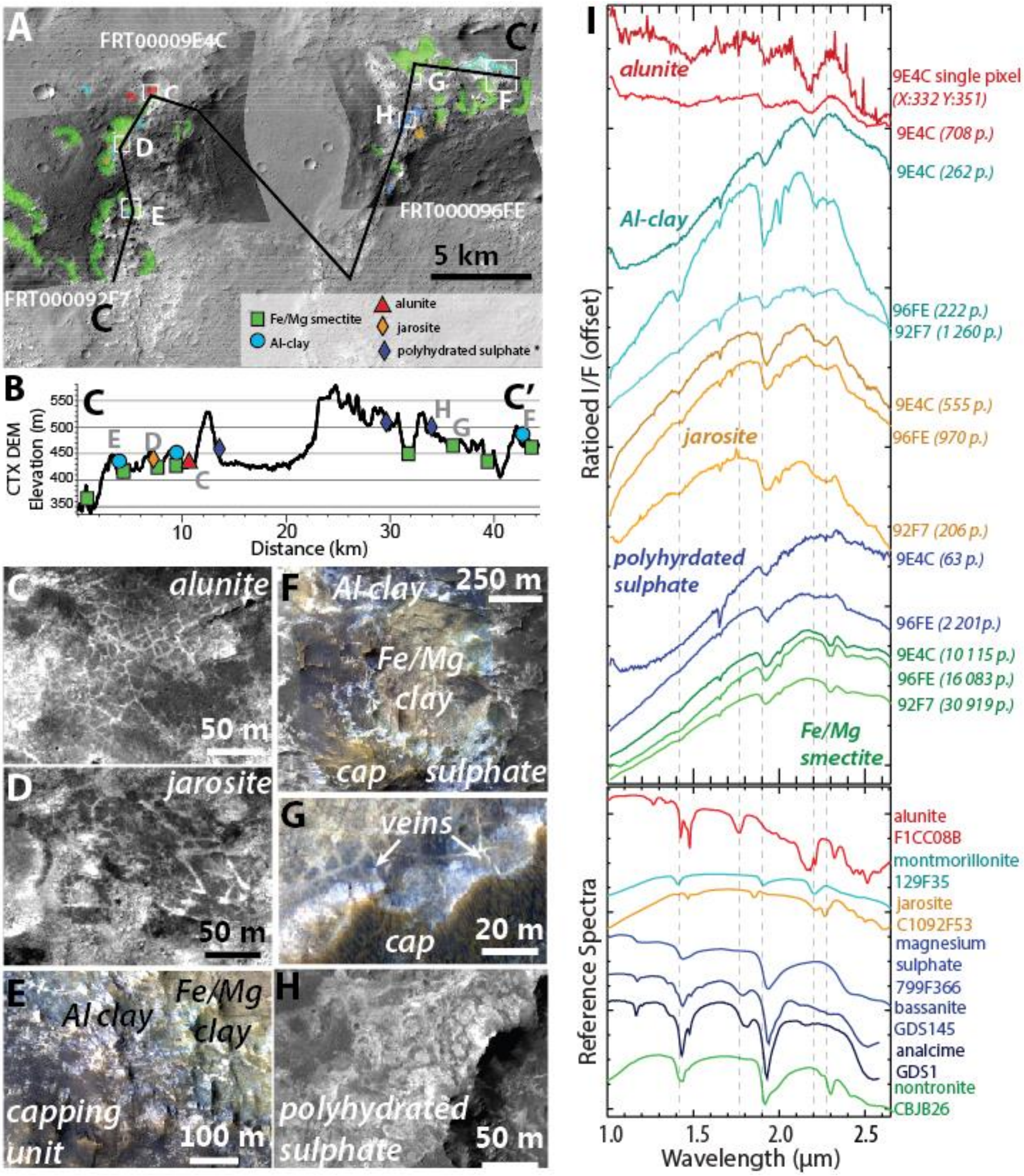

Fig. 6-5 Sulphate and clay exposures, northern side of N Eridania. They occur at a wide range of elevations (410-565 m, 420-500 m within cross section in (B)), displaying the same bleached appearance for ~3-15m under a dark capping unit (e.g. E, F, G). No fine layering in Al clays here—instead, we see intense veining wherever we see Al clays and sulphates (C, D, G, H). Alunite is distinguished by its 1.48 and 2.17 μm absorptions, although the 1.75-μm absorption is not strong in the mean spectrum; Al clay (eg. montmorillonite) has absorptions centred at 1.41 and 2.20 μm instead. Jarosite is differentiated from Fe/Mg smectite by its absoption centred at 2.27 μm vs. 2.30 μm, and the steep shoulder at 2.4 μm. Polyhydrated sulphate and minerals such as bassanite and analcime (a zeolite) all have similar spectra, with absorptions at 1.9 μm and shoulder at 2.4 μm; for simplicity, we call all of these detections polyhydrated sulphate. (C, D--ESP042285 1515; E--ESP030206 1510; F--ESP058610 1515; G, H--PSP006893 1515)

Chloride detections (Osterloo et al., 2010) overlie the dark capping unit— a consistent interpretation amongst previous authors (Wendt et al., 2013; Adeli et al., 2015; Pajola et al., 2016). Chloride deposits appear to be a thin layer (where intersected by fresh impact craters, Fig 6c), with defined, crenulated edges, draping underlying topography (Fig. 6b, d), and even have small, chloride filled channels leading into larger deposits (arrow in Fig 6c). We note that chloride deposits are not restricted to the basin itself, but also present outside the basin, >700 meters above (Fig 4b), and not found in the smaller, deeper, connected crater basin to the southwest.

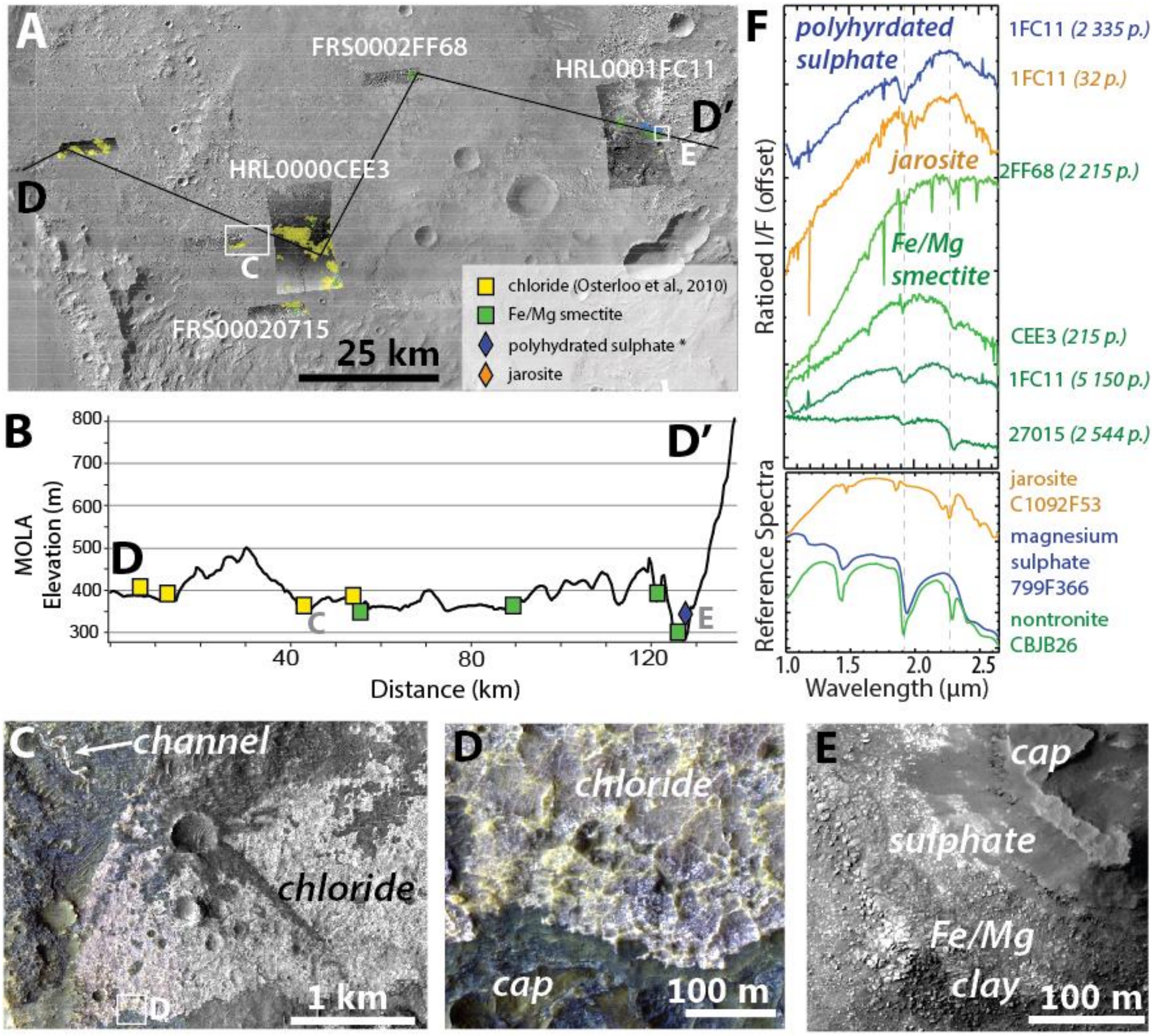

Fig. 6-6 Chloride, clay, and sulphate exposures, southern side of N Eridania. Here, we see chloride on top of clays, and above the dark capping unit (B). Chlorides have crusty edges (C, D) and a draped appearance, and a possible channel leading in (white arrow in C). Sulphates are exposed below capping unit (B, E), bright toned but with a rubbly appearance. (C, D--ESP047876 1480; E--ESP023705 1485)

3.3.2. S Eridania

This site is in the easternmost basin of the chain of basins forming the southern part of the Eridania palaeolake, and is chosen for the proximity of robust chloride detections to multiple clay types and sulphate. Here, we see a light-toned unit on the eastern side of Fig 7a, exposed from beneath a dark, flat capping unit. Once again, clay bearing patches are present within the light-toned unit, the majority of which are Fe/Mg clays (green in Fig 7a). Small amounts of Al-rich clays are found either directly beneath the capping unit or in remnant knobs, mixed with or adjacent to sulphate detections (Fig 7b, d, f); these knobs are above the underlying Fe/Mg clay bearing unit. However, while the patchy Al-clay and sulphate detections are above Fe/Mg clays (and immediately under a capping unit, where it exists), they are not at a consistent elevation throughout the site, varying by ~140m (Fig Fb). Al-clay and sulphate bearing units exhibit a bleached/veined texture in HiRISE colour, very similar to that in the N Eridania site (Fig 7e). No fine-scale layering is observed in HiRISE images in any of the clay-bearing units.

The dark, scarp-forming, competent capping unit lacks obvious wrinkle ridges, and has clear channels carved into the top of the unit, continuous with a network of inverted channels where the substrate is exposed. It is ~10-20 m thick, and could be a volcanic layer on top of the sedimentary clay and channels unit, in line with Wendt et al., (2013), Adeli et al., (2015), and Michalski et al., (2017), or possibly a basaltic sandstone. Chloride deposits follow channels carved into the dark capping unit (Fig 7a, yellow outlines). Where erosion has occurred (eastern, light toned part of this image), some of these chloride-filled channels transition into inverted channels. In places (e.g. Fig 7c), remnant chloride (light purple) is present within the preserved levees of the inverted channel. These chloride detections are found ~20-40 m above surrounding Fe/Mg clays (cross section, Fig 7b), and range in elevation by more than 160m across the site. Despite their relative elevation, the chlorides were likely the last mineral to form; the channels and clays likely formed in the same environment (e.g. sandstone channels in a clay-rich floodplain), with the chlorides later deposited in the last channels. Aeolian erosion could then have exposed the channels and clays, creating the observed inverted topography.

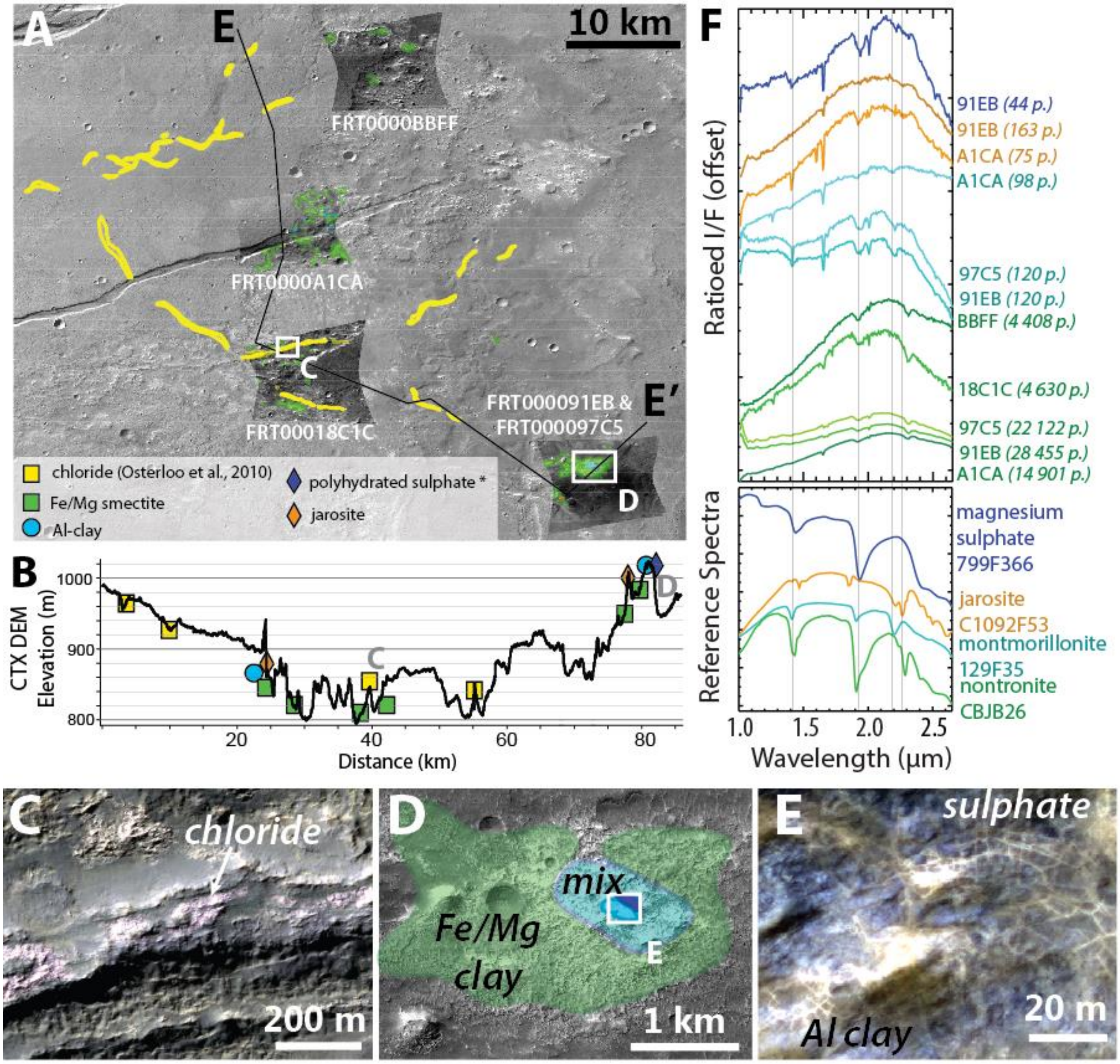

Fig. 6-7 Chlorides, clays, and sulphates in SE Eridania. Chlorides are found in channels, sometimes within inverted topography (A, C). Channels are carved into a dark toned capping unit, likely volcanic resurfacing. Under the capping unit, a light toned unit is exposed by erosion. This light toned unit has small Al-clay exposures (above Fe/Mg clay; see Fig B, D); possible polyhydrated sulphates and jarosite are found with the Al clays (Fig B, D, E). At HiRISE scale, these are veined (E), similar in appearance to those found in N Eridania. (CTX DEM--B18_016505, B21_017929; B21_017784, B22_018061; C--ESP026276 1425; D, E--PSP 006708 1420; 166.75 W, 36.52 S)

3.3.3 Dejnev crater

Dejnev is a large old, degraded crater just northeast of Columbus crater (Fig 3). Wray et al. (2011) note the presence of an Al-clay bearing unit in Dejnev, and note that the morphology is similar to Columbus crater (see section 3.3.4 below). Chloride deposits exist ~50 km west of the crater, but none are found within it (Fig. 8a). A fresh impact crater ~35 km NW of Dejnev shows both Fe/Mg (green) and Al clay (cyan) in its ejecta (Fig. 8b), with Al-clay as the further (uppermost) ejecta, indicating that there is Al clay in the subsurface outside the crater. Within Dejnev, we see wrinkle ridges on a flat, dark crater floor unit; this is consistent with volcanic resurfacing. Furthermore, while the crater rim is dissected, there are no clear channels breaching the crater to bring in sediment to form a flat capping unit, as seen in Gale crater. Fe/Mg clays are found in ejecta excavated from deep beneath this capping unit. Around the southern edge of the crater, we see an erosional pattern where there are quasi-linear gaps in the capping unit (Fig 8d). In a few places, elongated, light-toned, finely layered units are present within the gaps in the capping unit (e.g. Fig 8e). For the most part, these do not have a strong spectral signature, although some appear to have Al-clay (Fig 8d; outside HiRISE coverage). Al-clay (e.g. montmorillonite; identified by its sharp 1.41-and 2.20-µm absorptions) is predominantly found in a light toned, massive unit ~200m thick just above this layered unit, around the southern edge of the crater, as well as in mounds within the crater, not covered by the capping unit. In some places, the capping unit embays the edges of the massive Al-clay unit, suggesting that the Al-clay unit predates the capping unit. The Al-clay bearing unit erodes into a fine-grained material, forming a smooth talus slope to the crater floor (Fig 8e). We find new possible alunite detections associated with the Al-clay unit, In two different images in the crater (A900 and 10817)—band centre closer to 2.17 than 2.20, consistent with alunite (Fig 8g). The spectrum from FRT00010817 has more spectral features diagnostic of alunite, including a shoulder at 2.4 µm, wider 1.4-µm absorption (doublet to 1.48) than pure Al-clay, and even a small 1.75-µm absorption. Possible alunite detections do not appear to be morphologically distinct from the massive Al-clay unit (Fig 8e); no crust-like edges or desiccation cracks that would likely accompany alteration in an acid-saline lake setting.

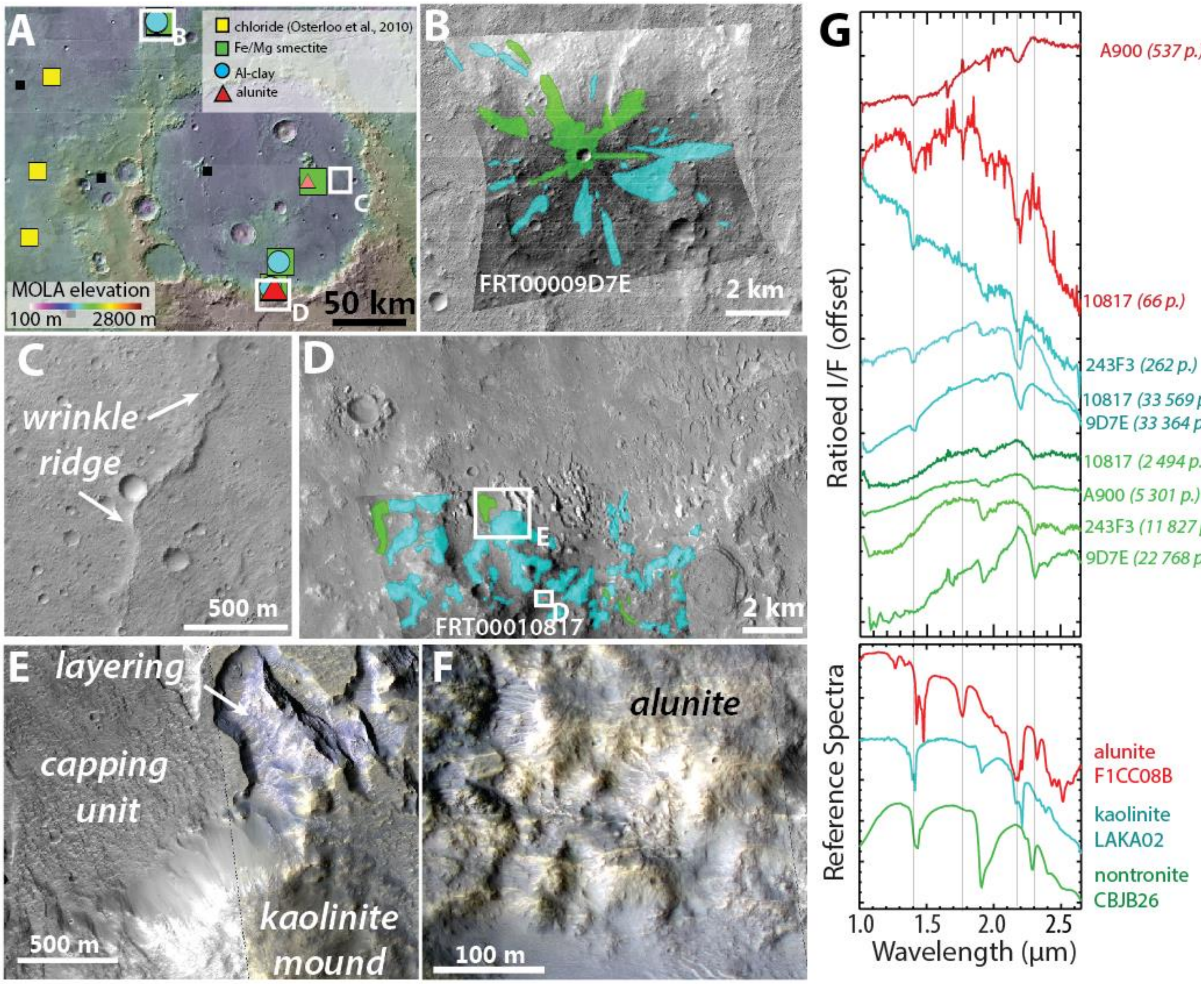

Fig. 6-8 Clays and possible alunite in Dejnev crater. Al clays in massive light toned unit at crater edge, and in hills in northern part of crater, and exposed by a fresh impact just outside the crater (A, B, D). Deeper Fe/Mg clays are exposed by crater ejecta, both inside and outside Dejenev (A, B). Light toned layered unit which appears to underlie massive Al clays (and sometimes has slight Al clay signature (E)) is embayed by dark-toned, flat topped unit (likely volcanic, given wrinkle ridges (C)). Hints of alunite in massive Al-clay unit do not seem to have unique texture (no crust-like edges or fracturing expected if ponded water(F)). (D, E, F--ESP011560 1535. 164.6 W, 26.2 S)

3.3.4 Columbus crater

For a detailed account of the sulphate and clay deposits in Columbus crater, see Wray et al. (2011). As in Dejnev (above), there are numerous chloride detections in intercrater plains around Columbus crater (yellow squares, Fig 9a), but nothing within the crater itself. Within the crater, Fe/Mg clay detections are rare, limited to small exposures in crater walls and in ejecta exposed from beneath the crater floor unit. Al-clay and sulphate detections are concentrated in a light-toned ring around the crater, and in mounds within the crater that have not been resurfaced. This discontinuous, polygonally fractured ring (Fig 9b, c) is unique in Terra Sirenum, and has been interpreted as evidence of a groundwater-fed palaeolake (Wray et al., 2011). Columbus crater is also unique in its wide range of sulphate minerals, including bassanite, gypsum, kieserite, jarosite, alunite, and polyhydrated sulphates. Gypsum is identified by its asymmetric triplet absorption at 1.44 µm, in addition to a small absorption at 1.76 µm, deep 1.95-µm absorption, minor 2.2-µm absorption, and typical sulphate shoulder at ~2.47 µm (Fig 9e). Light toned, fine planar layers are exposed in mesas on the crater floor, embayed by a dark, flat lying crater floor unit. As with Dejnev, there are no clear channels breaching the crater rim as a possible sediment source—furthermore, the dark capping unit has many wrinkle ridges (Fig 9b). It is interpreted as volcanic in origin, post-dating the emplacement of the eroded finely-layered mesa unit. These layered mesa units have weak, patchy Al-clay and sulphate spectral features, but on the whole do not show a clear spectral signature. However, immediately below these mesas (and not elsewhere on the dark, flat capping unit), a strong kaolinite spectral signature is observed.

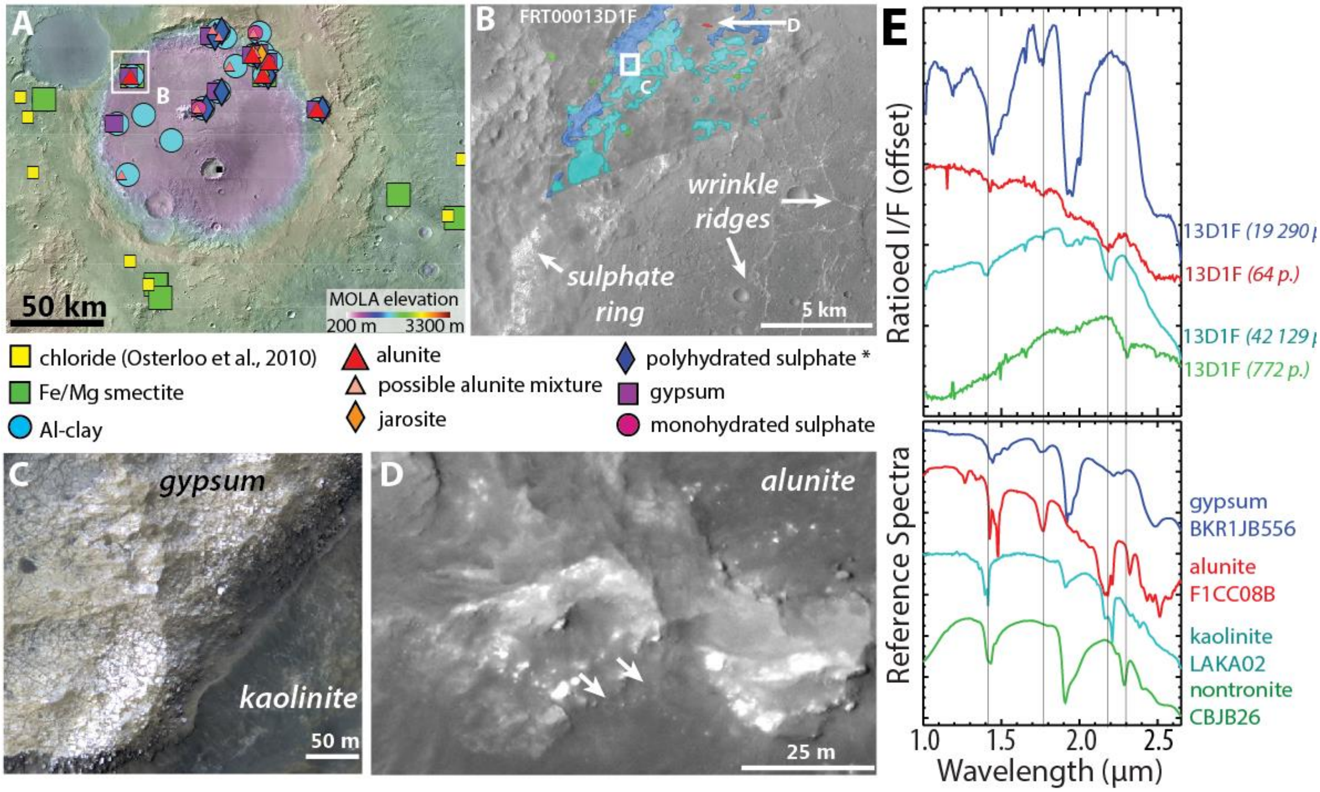

Fig. 6-9 Variety of clays and sulphates in Columbus crater, with chlorides nearby in intercrater plains (A). Sulphates are concentrated in a ring around the edge (A, B)—here, we see a fractured gypsum/sulphate ring (C), above Al-clays. Small amounts of alunite are present in light toned knobs (D). Wrinkles in the flat bottom of the crater indicate volcanic resurfacing (B) . (C, D--ESP013960 1510)

3.3.5 Cross crater

East of Columbus, Cross crater has a number of different clay and sulphate minerals within the basin, while chlorides are only present outside the rim of the crater (Fig. 10a). For a detailed account of Cross crater clay/sulphate deposits, see Ehlmann et al. (2016). As in Dejnev and Columbus, limited Fe/Mg clays are found within wall exposures or impact ejecta (Fig 10a, b). Around the edges of the crater floor there is a discontinuous light toned unit; in the northern parts of the crater, it has been eroded in a quasi-linear, yardang-like morphology, while along the southern edge, it appears to be a narrower, coherent bench above the crater floor (Fig. 10a, b). The lowermost parts of these light toned units are finely layered (Fig 10c, d), while the upper parts (nearest the crater rim) are massive, light toned mounds, and appear to be covered with small, light-toned linear dunes and/or yardangs at HiRISE scale (Fig 10e). Here, Al-clay spectral features are found within the massive unit (and/or light-toned dunes), as well as in the layered unit (at least 150 m thick). Alunite is found in patches within the massive upper unit, and not in the underlying layered unit. These aluminous, acid sulphate deposits have been interpreted as the result of an acidic, sulphurous groundwater source, such as upwelling fluids in contact with a magmatic source (Ehlmann et al., 2016). Jarosite, szomolnokite, and polyhydrated sulphate are also identified in Cross crater. As in Dejnev and Columbus craters, dark-toned, flat unit fills the central portion of the crater floor, here embaying light-toned mounds (possibly part of a central peak complex). No wrinkle ridges are observed, and a small channel breaches the crater rim to the east; this dark toned crater floor unit could be volcanic or sedimentary in origin.

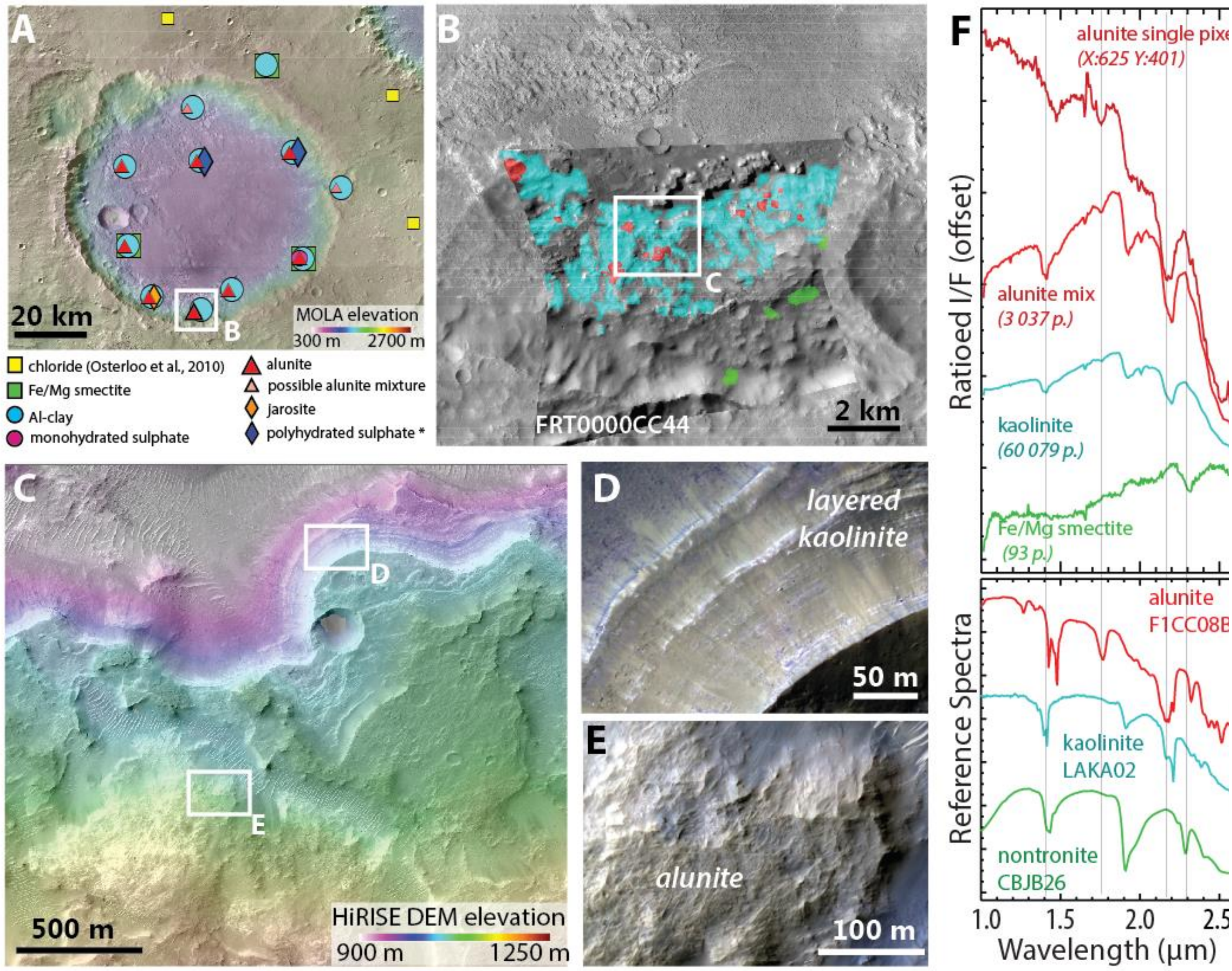

Fig. 6-10 Alunite at Cross Crater. Chloride detections are present in the intercrater plains above Cross Crater, and diverse sulphates within it (A). (B) Alunite (red) is concentrated in several places within the kaolinite-bearing unit (cyan). Layered, cliff-forming units associated with kaolinite (C, D) are found below a massive unit with alunite (E). Spectra from FRT0000CC44 (B) are shown in (F). (D, E--PSP010228 1490; HiRISE DEM from PSP010228 1490, ESP016320 1490)

3.3.6 Crater_161W_26S/ “Ohsweken”

Located east of Dejnev, this crater was identified in Wray et al. (2011) as having Al-clay deposits, as well as a similar texture to Columbus and Cross crater floors. Following the IAU convention, we have chosen the name of a small town on Earth to refer to this crater—Ohsweken. In Figs 11 and 12, we show both this crater and a nearby, fresh crater to the southwest whose ejecta is spilling over into “Ohsweken” (Fig 11a). In the central peak unit of this fresh crater, Fe/Mg phyllosilicates are identified (Fig 11a-c; 12a). In the same unit, we see small detections of both hydrated silica and probable carbonate (Fig 12a-c), neither of which is morphologically distinctive in the central peak unit. We interpret these as part of the basement rock, exposed by the impact, rather than a later sedimentary deposit (which we expect would be texturally distinctive at the HiRISE scale). This association of carbonate with basement rock is consistent with other carbonate detections in Terra Sirenum (Leask and Ehlmann, in prep.; Michalski et al., 2017). Fe/Mg clays are also present in the wall rock of “Ohsweken” (Fig 11, 12j), again likely part of a basement unit exposed through the cratering process.

“Ohsweken” is adjacent to a previously reported intercrater Al-clay and alunite detection (Wray et al. 2011; Ehlmann et al., 2016; Fig 11a, c, 12d). While this site is not in a crater basin, it has many of the same morphological characteristics—light toned, finely layered, cliff-forming units, eroded into yardangs (Fig 12e, f). A small, isolated knob nearby may be a volcanic edifice (although this is not definitive). Here, alunite is inferred in noisy data due to the band centre of an absorption at 2.17 µm, although the additional absorptions at 1.48 and 1.76 are not observed (Fig 11c).This alunite detection is ~600 m above the other detections on the crater floor of “Ohsweken” (Fig 11b).

Within “Ohsweken” crater, elongated, aligned mesas of light-toned, finely-layered units are concentrated along the inside of the southern crater rim, although limited exposures are also present inside the northern rim, where they are exposed from beneath the nearby fresh crater’s ejecta (Fig 11a). In the southeastern part of the inner crater rim, the light toned layered unit is topped by a couple of massive mounds, with smooth talus slopes indicating that they are likely made of a soft material (as in Dejnev, section 3.3.3; see Fig 12l, n). Al-clay (including clear kaolinite) is found within these mounds, as are small, localized alunite detections (Figs. 11c, 12j, n). The alunite detections in HRL000132BC have all diagnostic absorptions, including a wide 1.4-µm absorption, 1.75 µm, 1.92, 2.17, and shoulder at 2.4 µm (Fig 11c). Elsewhere, Al-clay is often associated with the finely layered light toned units (Fig 12 g-k, n), but once again, the signature is strongest immediately below these units, and only weak and intermittent within the layered unit itself. This Al-clay signature is found on top of a flat, dark-toned unit which embays the quasi-linear mesas (Fig 12g, h). This dark toned crater floor unit has a few features that could be interpreted as wrinkle ridges (Fig 12g), and no channels breach the crater rim, leading us to interpret the dark floor unit as likely volcanic in origin.

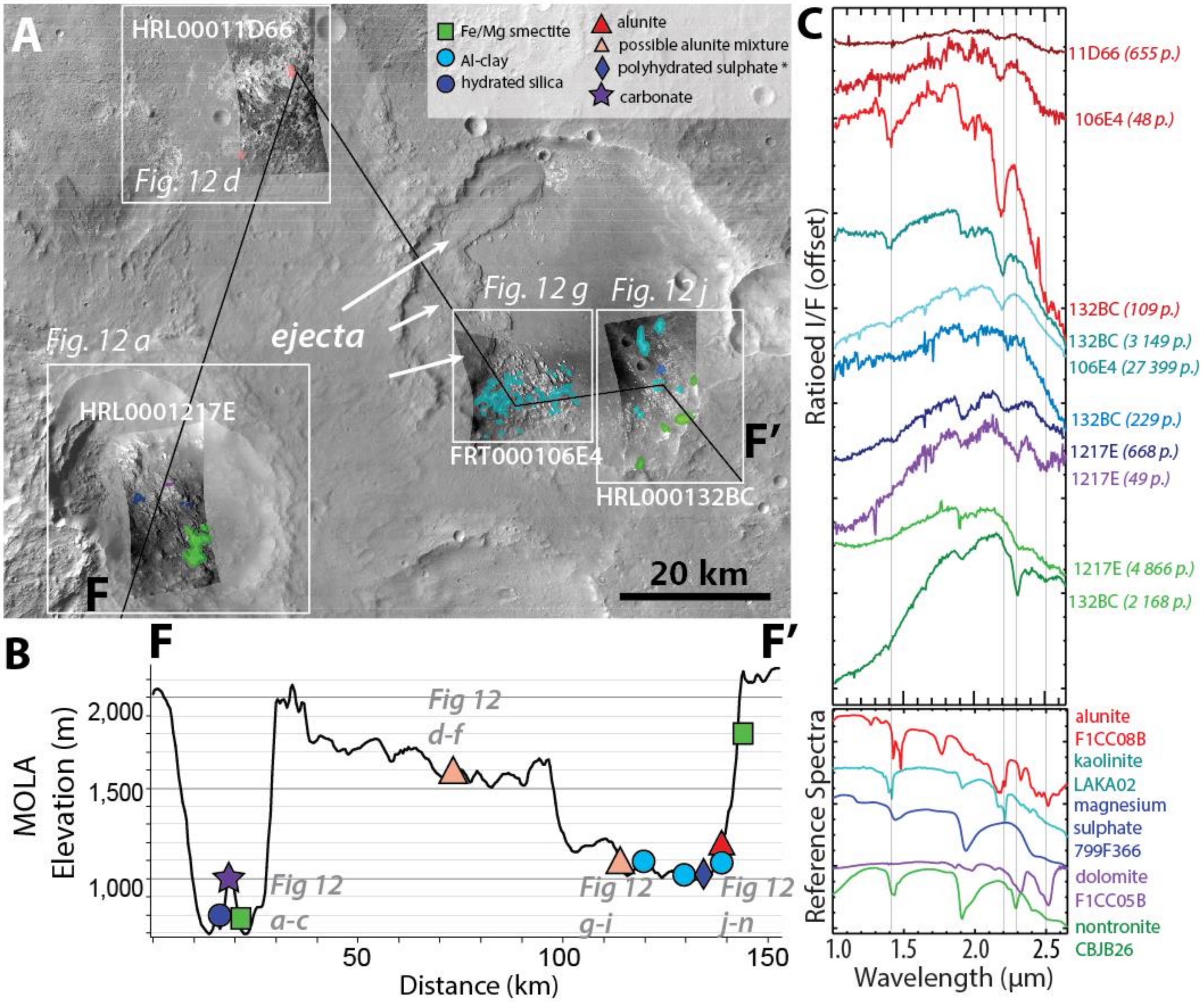

Figs. 6-11 (this page) and 6-12 (next page) “Ohsweken”crater. Light toned, Al-clay, layered unit exposed in craters but also intercrater plains (A). Hints of alunite found with this unit—definitively in massive unit in 132BC, overlying a light toned, finely layered unit. Carbonate and Fe/Mg smectites are exposed in central peaks and crater walls (A, B); ejecta from one of these craters mantles layered kaolinite in FRT000106E4, indicating that the crater post-dates deposition of the layered kaolinite unit. Fig 12. (a-c) Carbonate exposed in the central peak of a fresh crater, deeper than nearby alunite (Fig 11b), indicating that acidic fluids were not widespread in the subsurface. Finely layered units with Al-clay and alunite are sometimes present in intercrater plains, (Fig 11a, b; 12d-f), not just in basins (Fig 12g, j). Light toned, layered, cliff-forming units (~ 80 m high) are streamlined, indicating soft rock and aeolian erosion (Fig 12e,f,g). These mesas are sometime embayed by a flat, dark toned unit with wrinkle ridges (likely basalt) (Fig 12e, f,j, k). Alunite is concentrated in a zone within a powdery kaolinite mound (Fig 12j, l) above the layered cliff-forming unit (Fig 12k, n). (HiRISE DEM--ESP013907 1535, ESP013485 1535)

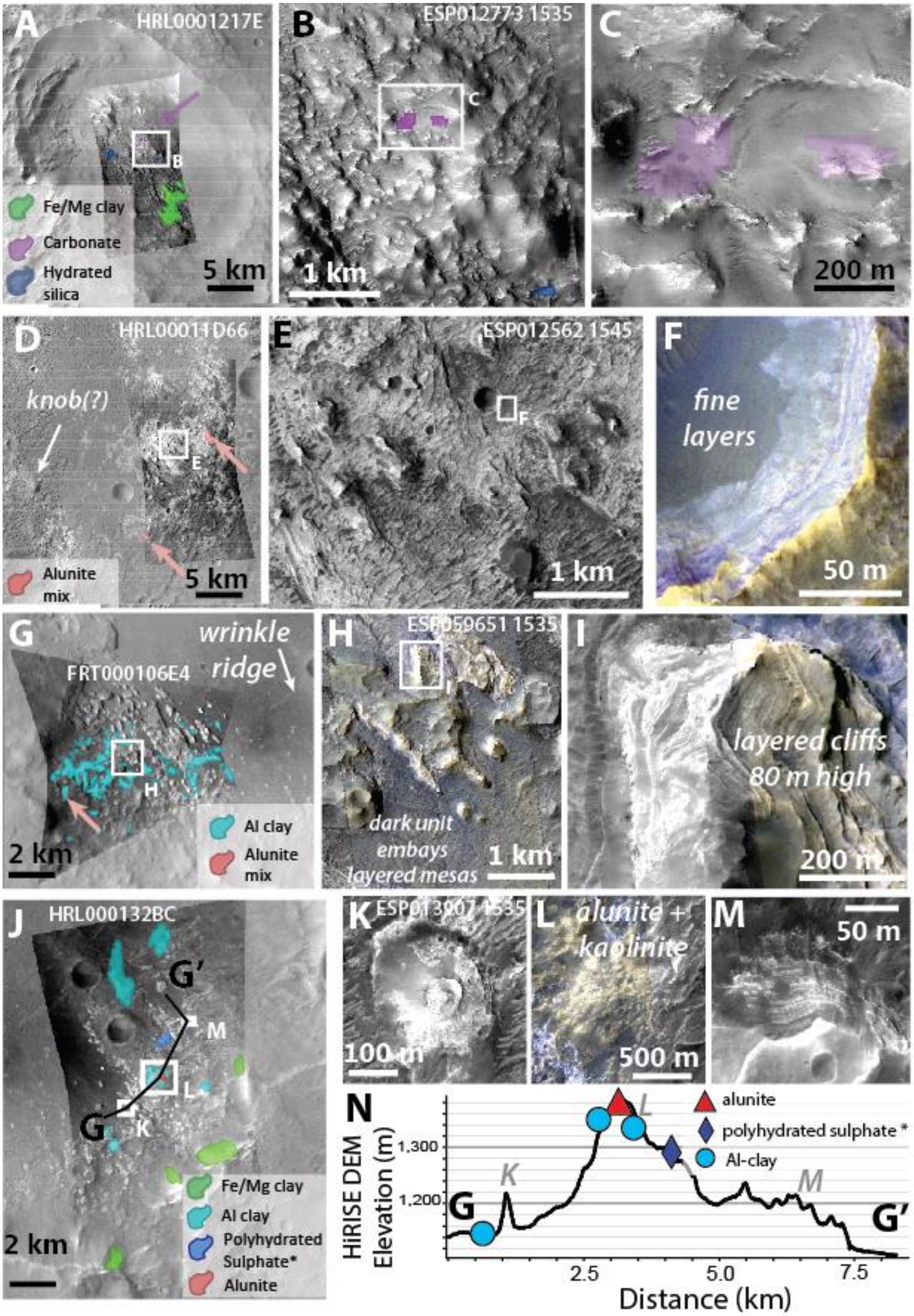

(Fig 6-12, see caption on previous page)

3.3.7 Crater_157W_27S/ “Kahnawake”

This crater, located east of “Ohsweken,” was described in Wray et al. (2011) as having Al-clay signatures in multispectral data and a similar texture to Cross/Columbus. We assign it the name “Kahnawake,” used herein. It was recently surveyed by Hemmi and Miyamoto (2017), who investigated the morphology of the cones present throughout the crater floor unit (Fig 13). Exposed around the inner edge of the crater, underneath the dark, flat capping unit (~10 m thick) are finely-layered, light toned, cliff-forming units >100m thick (Fig. 13a, b). These units are streamlined, eroded in a quasi-linear, NW-SW trend consistent with aeolian erosion (Fig 13c). Spectrally, the layered cliff-forming units are usually bland, with occasional weak Al-clay or polyhydrated sulphate spectral features. However, at the base of these cliffs is a very strong kaolinite signature (strongest where yellowish in HiRISE colour, Fig 13d, e, g; cyan in Fig 13c). Weaker Al clay signatures are still present in the darker floor units; in HiRISE colour, we see that in these places, the dark floor units are partially covered with light toned material (Zoom on Fig 13e). Traces of a bright, polygonally fractured unit around the base of the cliffs are too small to identify with CRISM data. This fractured unit looks morphologically similar to the sulphate ring in Columbus crater, and likely formed through subaerial desiccation, meaning there was once surface water (lake or pond) in this crater. However, it is not clear whether the polygonally fractured unit was deposited after erosion of the cliffs, forming in the modern topographic low and eroding back, or whether it is part of a continuous unit underlying the thick, finely layered, cliff-forming unit. A degraded channel ~15 km long breaches the rim of the southwest part of the crater, supporting the hypothesis that there was once a lake in this crater.

Localized zones of probable alunite are identified by a wide 1.4 µm, 1.92 µm, and 2.17 µm absorption centre, with a drop-off at 2.4 µm. Some single pixels within these regions also show a small 1.75-µm feature (Fig 13g). The strongest alunite spectral features are within mounds ~300 m above the top of the cliffs, near the crater rim (pink/red, Fig 13a); at the time of writing, there is no HiRISE coverage of these detections. Another possible alunite/Al-clay detection is within the layered cliff-forming unit; in HiRISE colour, there appear to be traces of a white substance at different elevations within the cliff-forming unit (Fig. 13f).

A dark, lobate unit (~10 m thick) partially fills a valley between cliff-forming units (Fig 13d). This unit is morphologically consistent with a basalt lava flow; given this morphology and the presence of cones on the capping unit in the crater floor (Fig 13b), we interpret the dark toned capping unit as volcanic in origin.

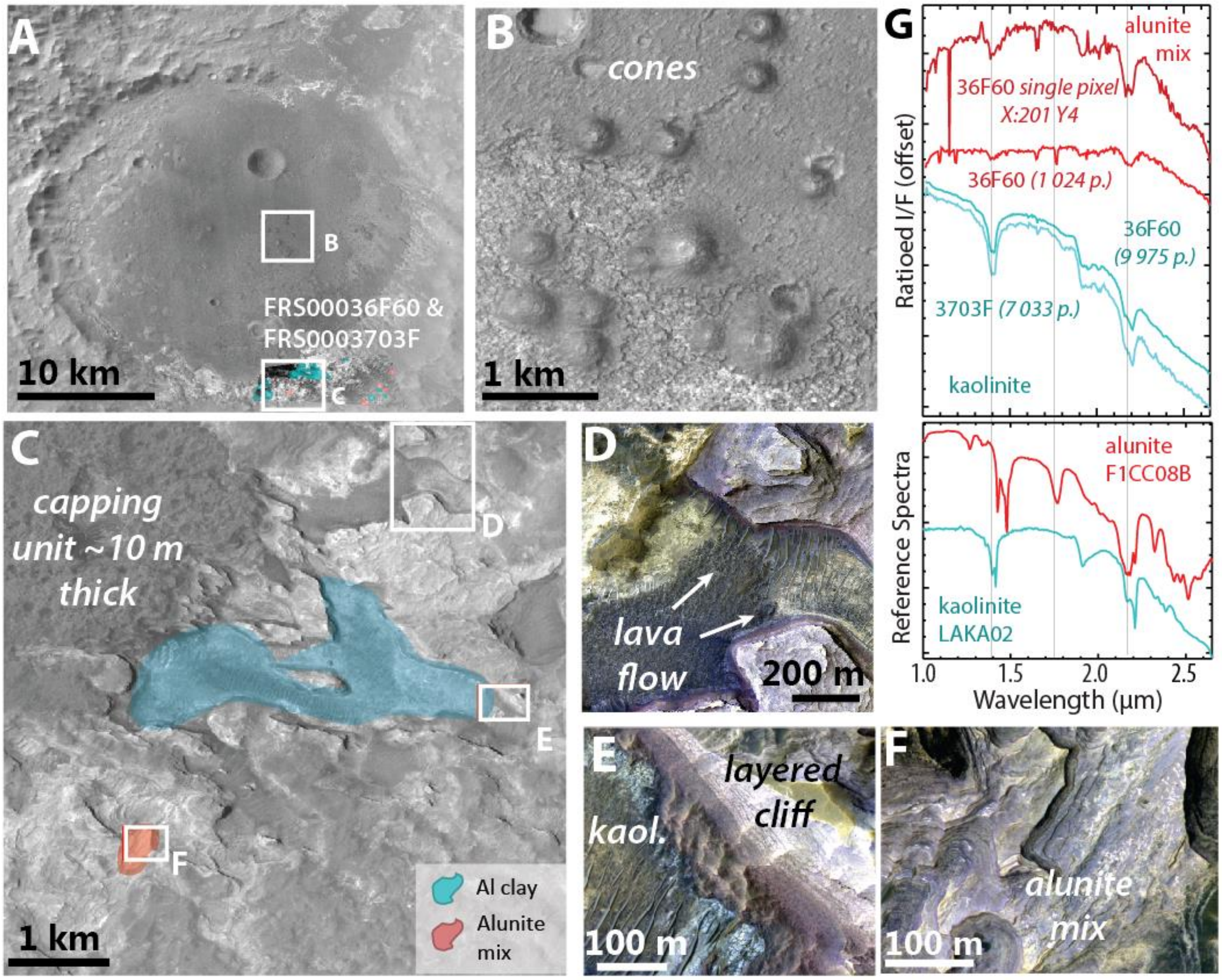

Fig. 6-13. "Kahnawake" crater. Flat-topped, dark unit ~ 10 m thick (A) with cones (B) overlies finely layered, light-toned cliff forming unit, ~100 m high (C-F). A dark toned, lobate lava flow appears to spill onto eroded floor unit (D). Kaolinite signature is strongest at cliff bases (C), sometimes in light toned mounds, and sometimes mixed with possible alunite (light red in A, C). Here, the possible alunite spectra have a wider 1.4 μm absorption than kaolinite (see G), and a 2.2-μm absorption shifted closer to 2.17 μm, with a minor 1.75-μm absorption in some single-pixel spectra. In HiRISE, the alunite mixture appears to be within the layered cliff-forming unit. (HiRISE DEM--ESP 047150 1520; ESP 041282 1520. HiRISE in D--ESP 041282 1520; E--ESP047150 1520; F--ESP049009 1520)

4 Discussion

4.1 Environmental settings for Al-clay bearing units

Aluminum rich clays (kaolinite, montmorillonite) form where an aluminous protolith exists, or through extensive leaching of iron/magnesium clays, where more mobile ferrous iron and magnesium cations are preferentially removed, leaving behind aluminum. Extensive leaching can be caused by high water/rock volumes, akin to laterites in warm and wet environments on Earth (weathering sequences), or through acidic waters. In Terra Sirenum, we find Al-clay deposits throughout the region, at a wide range of elevations (-300m in Eridania to 2600m in intercrater plains; Fig 3a, b). Where materials underlying Al clays are exposed (through erosion or impact processes; e.g. Fig 4f,h, 7d, 8b,d), they are consistently identified as Fe/Mg clays. This stratigraphic relationship of Al-clays overlying Fe/Mg clays is typical of laterites, but could also be explained by a felsic ash overlying altered basaltic materials. If the Al-clays were created through leaching at the surface, we would expect to see a diffuse contact between Al-clay and Fe/Mg clay units (as seen in soil horizons), where often a colour change is the main signifier of the mineralogical difference. Alternatively, if the Al-clay were attributed to a felsic ash unit, we would expect to see a sharp contact and morphological difference between the Al-clay bearing unit and underlying Fe/Mg clays. If extensive leaching occurred in the subsurface (due to upwelling groundwater), we would expect to see zones of alteration focused in veins as pathways for the upwelling fluids.

Investigating the relationships between Al and Fe/Mg clays across Terra Sirenum, we observe two distinct categories: in Eridania basin, Al-clays are a minor component (not observed in multispectral mapping data), and are present within a light-toned unit ~3-15m thick, with no discernible layering, under a dark capping unit. Fine, white veins are associated with this unit, where HiRISE colour coverage exists (e.g. Fig 5e, f, g, 7d). Outside of Eridania, where Al-clays are found, they are usually the dominant clay mineral (absorption present at the scale of multispectral mapping data). They are associated with thick (60-150+ m), cliff-forming, light-toned, wind-sculpted, finely-layered units, most often found around the inside edge of craters, but also sometimes in intercrater plains (e.g. Fig 11b, 12d-f).

4.1.1 Al-clays in Eridania basin

Al-clay bearing units in Eridania have been previously interpreted as pedogenic weathering sequences, as they overlie Fe/Mg clay units (Carter et al., 2015; Adeli et al, 2015; Pajola et al., 2016). These Al-clay units are relatively thin (3-15m thick), and have a diffuse contact with underlying Fe/Mg clays (Fig 5), sometimes with veins cutting across both Al and Fe/Mg clay units. Because of this diffuse contact and lack of morphological difference between the two clay types, we rule out an Al-rich ash layer as a possible cause for Al concentration, and agree with previous work that leaching is the most likely cause for the observed Al-clay units. However, veining directly below and into the Al-clay units signals the presence of subsurface fluid pathways that could provide fluid for leaching, rather than alteration occurring at the surface. Heavily veined areas are associated with sulphates, including acid sulphates jarosite and alunite (Fig 5c, d, h; 7e; see section 4.2.1 below), suggesting that the mineralizing fluids were acidic. Furthermore, the Al-clay unit is found immediately below a capping unit interpreted as a basalt lava flow, given wrinkle ridges in the unit (Fig 4c,f; 5e-g). On Earth, the heat associated with basalt flows can cause intense alteration where they are emplaced on top of clay units. Permeability boundaries could contribute to enhanced alteration at the contact between clay and basalt, if upwelling acidic groundwater were trapped beneath a basaltic cap. The >150m elevation variability in different exposures of thin Al-clay units within a basin (Fig 5b, 6b, 7b) would not be expected if alteration occurred as a result of a standing body of water, whether fed by groundwater or surface water—but would be expected if the alteration is driven by contact with a capping basalt unit.

While we cannot rule out pedogenic weathering, we prefer the interpretation that acidic water associated with a volcanic capping unit caused subsurface alteration to Al-clays. This interpretation accounts for the diffuse boundary between Al and Fe/Mg clays, veined texture, association with acid sulphates, and variable elevation of a thin zone of alteration. Notably, while extensive pedogenic weathering would require a warm and wet environment, the alternative volcanic hypothesis is equally plausible under cold and icy conditions, where the energy for alteration is provided by the basalt.

4.1.2. Thick, finely-layered, cliff-forming units associated with Al-clays in NE Terra Sirenum

Outside Eridania basin, most light-toned eroded units in Terra Sirenum (mapped from CTX) are identified as Al-clay bearing, with an absorption at 2.2 µm in multispectral mapping data (Fig 1). These units are mostly around the inside edges of crater basins, but are also present in intercrater plains (e.g. Fig 12d-f). Where HiRISE data are available, these units exhibit fine laminations, and are often sculpted into yardangs and elongated mesas (Fig 8d,e; Fig10b-d, 11a, 12d-m; 13c-f). Where targeted CRISM data is available, Al-clay minerals are corroborated. However, while the Al-clay signal is associated with the light-toned, cliff-forming units at the ~100m/pixel scale, at higher resolution we see only weak and intermittent Al-clay spectral signatures within the layered unit (with the exception of Cross crater); the strongest kaolinite and montmorillonite signatures are instead found at the base of these layered units, on the dark-toned crater floor unit which embays the layered mesas, or in mounds on top of the layered unit (Fig 8d, Fig 11g-i, Fig 13c; also noticed in Wray et al., 2011). Although Al-clay signatures are found on a dark crater floor unit at the base of light-toned, layered mesas, they are not found elsewhere on the dark toned crater floor unit. At HiRISE scale, a patchy, diffuse light toned unit (sometimes in dunes) is present on top of the dark floor unit, suggesting that the Al-clay signature may be related to material eroded from the light-toned layered unit. Where kaolinite is present in massive mounds on top of the light-toned, layered unit, it is usually found in conjunction with alunite (see section 4.2.1 below).

In Fig 14, we plot the thickness of the layered unit associated with Al-clays (or the thickness of Al clays themselves, if no layered unit exists). Thicknesses of the layered unit are minimum thicknesses, as we do not see the base of the unit, while the thicknesses of Al clays in Eridania show the maximum observed thickness in the region. These thicknesses are plotted against distance from Arsia Mons (Tharsis), a nearby volcanic vent. Overall, the thickness of the layered unit declines with increasing distance from Arsia Mons, although the exposure of the layered unit in Cross Crater is thicker than that exposed in "Kahnawake."

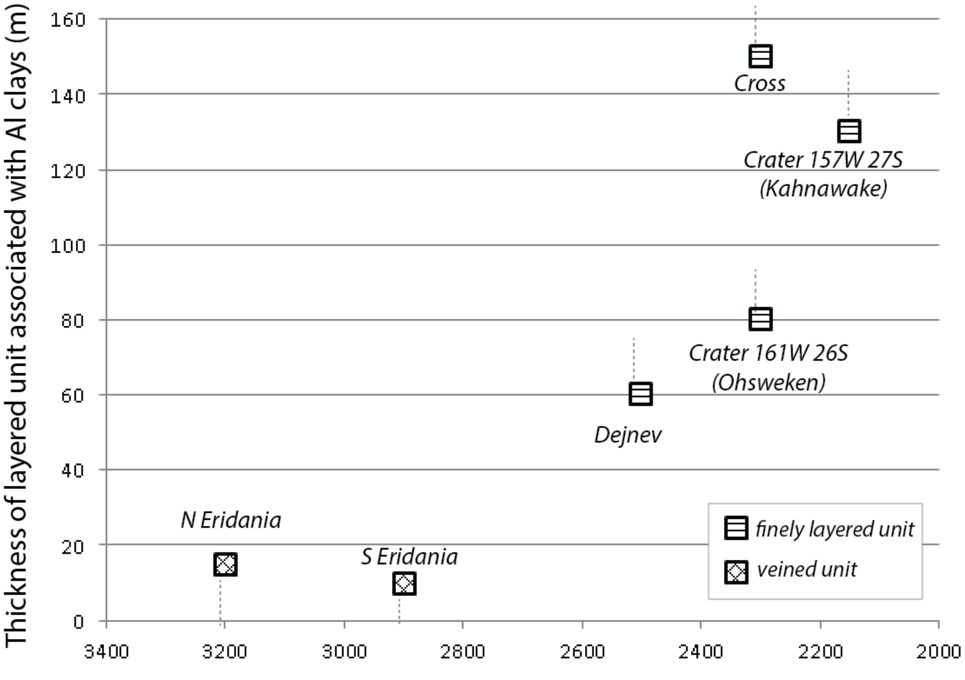

Fig. 6-14 Thickness of Al-clays (or layered unit associated with Al-clays) vs. distance from Tharsis. Dashed lines pointing downward indicate a maximum possible thickness, while those pointing upward indicate that the thickness plotted here is a minimum bound.

4.1.2.1 Aluminum concentration mechanism: extensive leaching or a difference in protolith?

As in Eridania, Al-clay deposits elsewhere in Terra Sirenum appear to overlie Fe/Mg clays, and so are similar to pedogenic weathering sequences caused by extensive leaching at the surface. However, unlike Eridania, we do not see the contact with underlying Fe/Mg clays; instead, we only see these underlying Fe/Mg clays when they are brought to the surface in impact ejecta (e.g. Fig 8b), and so cannot use the nature of the contact to differentiate between a leaching scenario concentrating aluminum, or a difference in protolith. We note that the finely-layered morphology associated with Al-clay detections is not found associated with Fe/Mg clays in Terra Sirenum, and so it is unlikely that they are part of a continuous unit, with Fe/Mg clays always hidden in the subsurface.

Detections of Al-clays in NE Terra Sirenum do not appear to be correlated with channels or dense channel networks (as in S Eridania, Fig 7). If the Al-clays were caused by high volumes of surface runoff, we would expect the most intense alteration (largest Al-clay detections) to occur where the densest channel networks are (e.g. Eridania); this is not observed. Similarly, if the Al-clays were solely due to extensive leaching from regional groundwater upwelling, we would expect to only find them in deep crater basins and/or at consistent elevations; while many of the best preserved examples are in crater basins, there are numerous Al-clay detections outside these basins (see Figs 1, 3). Also, we would expect to see the most extensive Al-clay alteration in the deepest basins (e.g. Eridania)—again, this pattern is not observed. Small detections of acid sulphate clays are found both in Eridania and in the rest of Terra Sirenum, so we do not believe that waters in Eridania were less acidic than those in the rest of Terra Sirenum. Thus, we do not believe that extensive leaching—whether due to surface runoff, groundwater upwelling, or enhanced acidity—is likely to be the cause of this spatial trend in dominant clay mineralogy.

Alternatively, a regional felsic ash deposit on top of Fe/Mg clay basement rocks could account for the observed spatial trend in dominant Al-clay mineralogy. A felsic ash layer would be expected to have the same layered morphology inside and outside crater basins, and to exist at a wide variety of elevations as we observe here. Such a layered unit would be preferentially preserved in sheltered crater basins, and could be soft enough to be sculpted into yardangs, while competent enough to form cliffs and mesas.

Ash layers are typically thickest near the point of origin, tapering off with distance from the source. Here, we note that the light toned, layered units generally decrease in thickness with increasing distance from Tharsis. Additionally, a felsic ash unit comprised of mostly feldspars and quartz would be spectrally unremarkable in the wavelength range covered by CRISM, as is observed. Fine grained feldspars and felsic glasses would readily alter to Al-clays with a small amount of water; this softer material would be expected to erode out of the cliff-forming unit, potentially explaining the strong Al-clay signatures immediately below these light-toned, layered cliffs. A regional layered felsic ash unit, draped on top of underlying widespread Fe/Mg clays, is therefore consistent with all our observations, and thus our preferred hypothesis for the observed distribution of Al-clays in Terra Sirenum.

4.2 Sulphate deposit formation

Sulphate deposits are found across Mars, and generally inferred to post-date clay alteration (e.g. Bibring et al., 2006). They are often interpreted as caused by upwelling groundwaters (e.g. Meridiani Planum; McLellan et al., 2005, Valles Marineris; e.g. Roach et al., 2010), possibly magmatic in origin. Sulphates precipitate from sulphurous, usually acidic waters, and can precipitate at the surface—e.g., in an evaporative playa-like setting, in a layer with desiccation cracks, or in mounds where springs intersect the surface—or they can precipitate in veins in the subsurface, filling cracks caused by earlier desiccation or by hydraulic fracturing (Caswell and Milliken, 2017). We note that in Terra Sirenum, acid sulphate alunite is found where the dominant clays are Al-rich, while jarosite is found where Fe/Mg clays are the dominant mineral—this indicates that cations for these acid sulphate minerals are likely leached in situ, not carried in with the water. In order to form, sulphates require a water source (upwelling groundwater or surface runoff) as well as a sulphate anion source (e.g. leaching, remobilization of older deposits, magmatic volatiles, or atmospheric volcanic aerosols). We explore the possible water and anion sources for sulphate deposits in Terra Sirenum below.

4.2.1 Groundwater vs. surface water source for sulphates

If the water source for sulphates in Terra Sirenum were surface water runoff or precipitation, we would expect to see sulphates at a wide range of elevations, associated with channels or in topographic lows at the end of channels, where surface water flow is concentrated. If sulphate precipitated from surface water, we would expect it to be in a desiccated, fractured layer draping topography, perhaps also filling in pre-existing fractures in the near-subsurface. While we see some limited sulphate exposures near channels in Eridania (e.g. Fig 7), sulphates are not found directly within or adjacent to channels. Here, sulphates are associated with veined textures (Fig 5), which could be either desiccation cracks infilled by percolating surface water, or hydraulic fractures. While these are at the limit of HiRISE resolution, light toned veins do not always meet at orthogonal angles, and so may be more consistent with hydraulic fracturing, where the groundwater responsible for fracturing the rock is the most likely source of mineralization (e.g. Caswell and Milliken, 2017). Here, overpressure causing fracturing could be driven by upwelling magmatic fluids encountering a strong capping unit, rather than strictly due to overburden pressure and burial. In Columbus crater, we see sulphate present in a fractured layer at an approximately constant elevation (consistent with evaporation at the surface); however, there is no evidence for channels breaching the crater to provide surface water. Elsewhere (Cross, "Kahnawake"), degraded channels lead into the crater, but sulphates are restricted to small, localized patches in mounds—not consistent with evaporation from a sulphurous lake or pond fed by surface runoff.

While both Fe/Mg and Al clays are found at a wide ranges of elevations, both in craters and intercrater plains, sulphates are found almost exclusively in crater basins, between -300-1800 m MOLA (800-1000 m below the highest clays and chlorides). The single exception is shown in Fig 11a, b, just above "Ohsweken," where there are stronger alunite detections in mounds within the crater. Ring fractures could provide a conduit for upwelling groundwater to intersect the surface above the crater basin. This almost total restriction to basins points to a likely groundwater source for sulphurous water, similar to other sulphate deposits across Mars. However, within basins, sulphates are often not at the lowest elevation—in Dejnev, Cross, "Ohsweken," and "Kahnawake," alunite is typically in mounds above layered kaolinite. This morphology is consistent with groundwater springs intersecting the surface, precipitating alunite directly around springs/vents, surrounded by intense kaolinite alteration. These mounds are found at the inside edge of craters, where faults may act as conduits for upwelling, acidic groundwater, and on top of a light toned layered unit interpreted as a felsic ash (see section above). This felsic ash unit would act as a local source for aluminum cations to form kaolinite and alunite rather than the iron/magnesium mineralogy more common on Mars. Post-emplacement mineralization from fluids upwelling in ring faults could contribute to the parts of the light toned layered units nearest crater rims being best preserved.

Given that sulphates are almost entirely restricted to basins, and mostly found in veins (consistent with hydraulic fracturing) or mounds (consistent with springs), we infer that the most likely water source was upwelling groundwater.

4.2.2 Sulphate anion source

Sulphate anions could be derived from leaching, volcanic/atmospheric deposits, remobilization of older deposits, or magmatic volatiles. Volcanic aerosols would be found at all elevations (atmospheric deposit); since we only find sulphates at lower elevations, we rule this out as a likely sulphate source. Widespread leaching would need to occur to release sulphate for the observed deposits (typically 1 % of a martian basalt; Schmidt et al., 2018). While this is possible, there is no clear mechanism to concentrate sulphate released through leaching into the localized deposits observed. Also, acidic waters appear to be focused, rather than widespread in the subsurface, given the common association with concentrated alteration in mounds (interpreted as springs/vents). In a central peak uplift in a crater adjacent to "Ohsweken" (Fig 11, 12), we see carbonate; had acidic, sulphate rich waters permeated the whole area, we would expect them to have dissolved carbonate. This crater formed after the emplacement of light toned layered units in "Ohsweken," as its ejecta mantles the layered unit (Fig 11). The carbonate is ~50-150 m below the elevation of alunite-bearing mounds, in an adjacent crater, ~100 km away). Given the mound morphology of the alunite, we expect that they were formed by upwelling springs, and so it is unlikely that the groundwater would not have been at the same elevation as the carbonates in the adjacent crater—pointing to the focused nature of upwelling fluids in the subsurface.

As sulphates are found across Terra Sirenum, for remobilization of buried deposits to be the source of sulphate, buried deposits would need to exist throughout Terra Sirenum—while this is not impossible, we might expect to see evidence of sulphates in ejecta, which we do not observe. However, without drilling cores, we cannot rule this out as a possible source.

However, the simplest explanation for the source of sulphate anions in Terra Sirenum is through upwelling magmatic volatiles. This is consistent with their likely groundwater source and focused nature, and bolstered by the proximity to volcanic units throughout Terra Sirenum. In all sites, sulphates are associated with a dark capping unit, frequently with wrinkle ridges and generally interpreted as volcanic in origin. At "Kahnawake" crater, we see even stronger evidence of a volcanism, with a lobate basalt flow (Fig 13d) and cones (Fig 13b). Exsolved magmatic volatiles could mix with a groundwater reservoir, or even locally melt a frozen groundwater reservoir and increase the volume of water available to cause local alteration. Thus, these sulphates could have formed either under a warm and wet or a predominantly cold and icy Mars climate.

4.3 Chloride deposit formation

Unlike sulphate deposits, which are found almost exclusively in basins, chloride deposits in Terra Sirenum are scattered throughout the highlands and usually not observed in deep crater basins (except N Eridania). Similarly to sulphates, chloride deposits require both a water source and an anion source (Cl-).

If the water source were groundwater, we would expect to see chlorides in basins and at lower elevations, missing from the highlands. Instead, we see chlorides throughout the highlands (generally in local topographic lows; see Osterloo et al., 2010; Leask and Ehlmann, in prep.), pointing to a surface water source. This is consistent with finding of chloride within channels (e.g. S Eridania, Fig 7a, c); any surface water (whether a large or small volume) is likely to make its way to existing channels; larger volumes of surface water could potentially erode their own channels. The last, briny surface water present within these channels could evaporate to create deposits we observe. Chloride deposits are also morphologically consistent with formation at the surface: they are typically in a thin, draping layer, polygonally fractured, and with crust-like edges to the deposit (Fig 6 c, d). These features are all expected from an evaporite deposit forming in a small lake or pond, desiccating and fracturing after the water evaporates. Given a surface water source, possible chloride anion sources include atmospheric/volcanic aerosols, or leaching from surface deposits (e.g. dust, soil, or upper portions of bedrock). These sources are present at all elevations, and precipitation or meltwater could mobilize chloride (especially if it is already in a labile form, not locked away in bedrock), and redeposit the chloride in ponds at slightly lower elevations (see Leask and Ehlmann, *in prep*.).

The lack of chlorides in deep basins is puzzling, as we would expect surface water to pond in the deepest regional lows. If chlorides were never deposited in the deepest basins, it could point to small water volumes, lacking enough water to spill over into the deep basins before drying out. Alternatively, perhaps the substrate in deep basins was more permeable, and brines percolated into the subsurface without leaving chloride crusts at the surface. Or, chlorides may have been deposited in deep basins but redissolved by later waters, or buried through resurfacing processes.

4.4 Relationship between salt minerals (chlorides, sulphates, and carbonates)

Carbonates, where present, are associated with a basement unit uplifted in central peaks of craters or in crater walls, and so are likely part of an earlier Noachian history of alteration. Despite the proximity of chlorides and sulphates in this region of Mars (within 10 km in Eridania), they appear to be completely genetically independent, not part of the same evaporative sequence as often seen on Earth (Eugster and Hardie, 1978). In Eridania, sulphates are found beneath a capping unit, while chlorides are found in channels on top of the same capping unit, with no spectral signature of sulphates associated with them. Work by Ye and Glotch (2019) demonstrates that <5% sulphate mixed with chloride would be visible spectroscopically. Given this separation despite physical proximity, and our interpretation of chlorides as derived from surface waters vs. sulphates are precipitated from upwelling groundwaters, the chloride and sulphate deposits in Eridania likely formed from two distinct reservoirs, either coeval or separated in time.

In all cases except “Ohsweken” and “Kahnawake,” chloride deposits exist around the top of craters with sulphate deposits in them. A possible explanation for this is that chlorides were deposited prior to sulphate emplacement and/or resurfacing, and dissolved or buried. Alternatively, the chlorides could have been deposited after sulphate emplacement and resurfacing, but simply been in volumes of water too small to spill over into deeper craters. In Eridania (both northern and southern sites), we see that chlorides are deposited in channels carved into a capping unit dated at 3.5 Ga. Just southeast of our study area, a chloride deposit is draped on top of a unit dated at 2.3 Ga (see Leask and Ehlmann, *in prep*.). This suggests that the processes forming chlorides in Terra Sirenum occurred between at least 3.5 and 2.3 Ga. Capping units associated with sulphates are dated between 3.5-1.4 Ga (see section 4.5 below), suggesting that chloride and sulphate forming processes may have been occurring in tandem throughout the Hesperian and into the Amazonian, with intermittent meltwaters at the surface dissolving labile chlorides in small volumes of water and redepositing them in concentrated, pure chloride deposits nearby, while upwelling magmatic groundwaters associated with episodic volcanism created sulphate deposits around the edges of craters. The lack of communication between these reservoirs could point to vertical stratification, which could be explained by a permafrost layer, keeping periodic meltwater at the surface from infiltrating and mixing with groundwater reservoir (e.g. Head and Marchant, 2014).

4.5 Age trends

The basin resurfacing ages become progressively younger moving west to east across our study area, from ~3.5 Ga in the Eridania region, to an age between 1.4- 2.6 Ga in the easternmost “Kahnawake” site. Sites nearer Eridania have ages ~3.2-2.9 Ga (Columbus and Dejnev). If sulphates are associated with volcanism, this suggests that the same style of processes creating sulphates occurred over ~1-2 billion years, as global volcanism became localized in a few centres (e.g. Tharsis). These ages and spatial distribution are consistent with the history of volcanic activity on Mars proposed by Werner (2009), with widespread volcanism until 3.7-3.5 Ga, followed by retreat to only places with a thick insulating crust (e.g. Schumacher and Breuer, 2007).

4.6 Interpreted History

Here, we integrate our preferred interpretations into a single possible history of alteration in Terra Sirenum (Fig. 15).

(1) Late Noachian (<<3.5 Ga): Eridania paleolake dries out. Carbonates may form with clay-bearing units in the surface or subsurface.

(2) 3.5 Ga: Eridania is volcanically resurfaced; Al-clays form at the contact between Fe/Mg clays and a basaltic cap. Sulphate-bearing veins form in the underlying, lithified Fe/Mg clay bearing unit, possibly related to upwelling groundwater. Dejnev, Columbus, and Cross craters all experience a volcanic resurfacing event around this time too.

(3) After 3.5, before 3.2 Ga: Widespread felsic ash layer emplaced, and begins to be eroded into mesas. Perhaps deposited by an early eruption similar to formation of Medusa Fossae formation.

(4) 3.2-1.4 Ga: Craters in Terra Sirenum experience volcanic resurfacing (retreating over time to the east, towards Tharsis). Eroded felsic ash units are embayed by basaltic units. Upwelling groundwaters with magmatic volatiles form springs at the surface, causing localized acid sulphate alteration in mounds. Acidic waters cause alteration of felsic ash to Al-clay. Volcanism provides local heat source for enhanced alteration and/or melting of permafrost.

(5) <3.5 to <2.3 Ga: Channels form in capping unit in Eridania. Intermittent, small volumes of meltwater dissolve labile chloride at the surface (e.g. in dust), and redeposited chloride in channels and small ponds across Terra Sirenum.

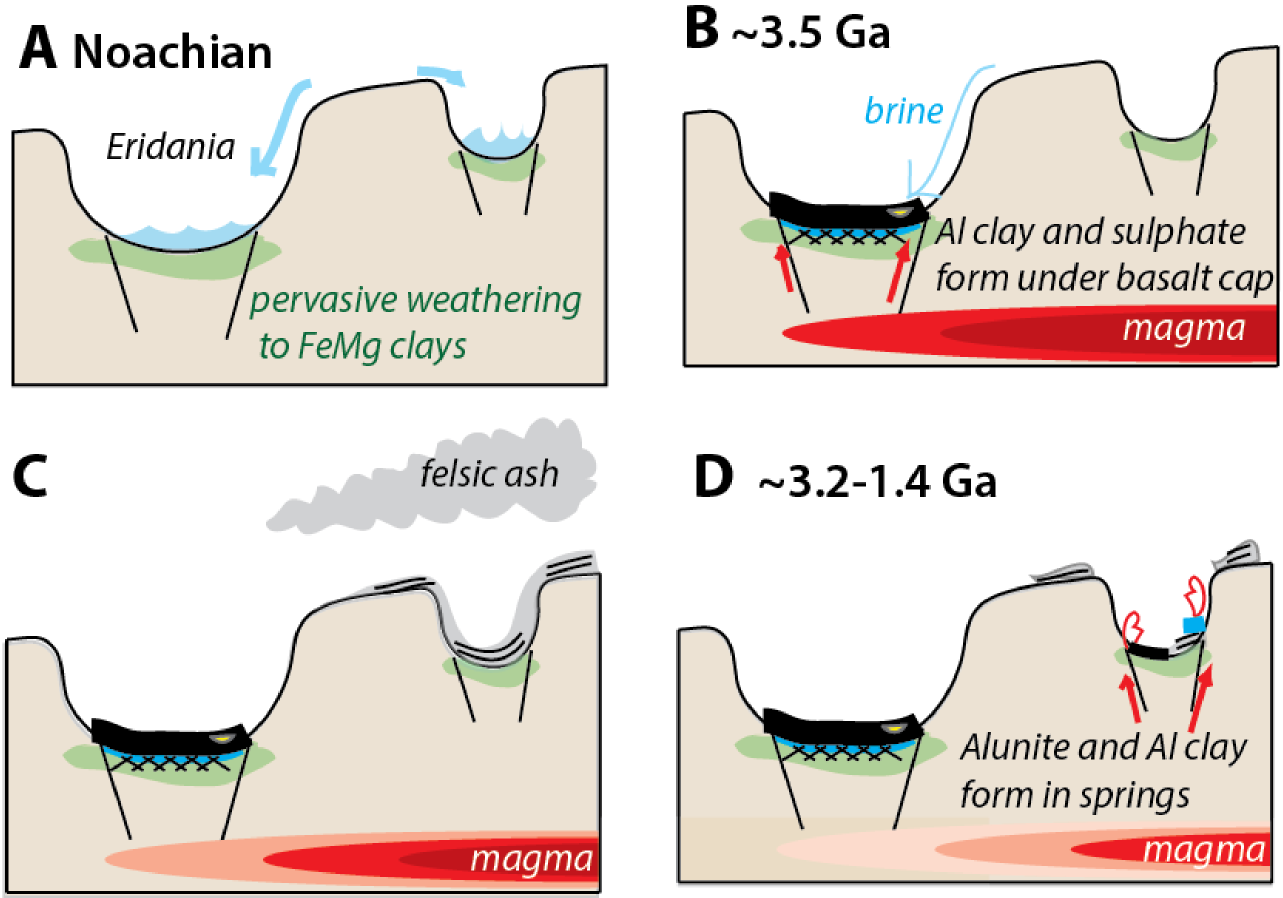

Fig. 6-15 Interpreted history of alteration in Terra Sirenum. (a) In the Noachian, extensive surface hydrological systems cause pervasive weathering of basaltic crust to Fe/Mg clays, especially in basins. (b) Around 3.5 Ga, basaltic flows resurface Eridania basin, contributing to enhanced leaching where in contact with clays, generating a thin layer of Al-clay. Sulphates are deposited in veins under the basaltic cap, possibly due to magmatic volatiles in upwelling groundwater. Small volumes of brine, washed down from the highlands, form chloride deposits in small ponds and channels on top of the capping unit. (c) A layered, felsic ash unit is emplaced in northeastern Terra Sirenum. (d) Between 3.2-1.4 Ga, the felsic ash is eroded back, and areas of active volcanism retreat towards Tharsis (eastward). Ring fractures around craters act as conduits for upwelling, acidic/sulphurous waters, focusing them in springs around the edges of craters, forming alunite/kaolinited mounds and altering the felsic ash unit to Al-clays.

5 Conclusions

Despite the close proximity of chlorides, carbonates, and sulphates in Terra Sirenum, these minerals do not appear to be genetically related. Chloride deposits appear to be related to surface water runoff, present at most elevations throughout the region in small ponds and within old channels. Sulphates are typically adjacent to or underneath volcanic morphologies, and almost always in deep crater basins, indicating that they are likely formed by upwelling groundwaters with magmatic contributions of sulphate and acidity. This indicates the presence of two chemically and spatially distinct water reservoirs in Terra Sirenum through the Hesperian and into the Amazonian; a permafrost layer is a possible explanation for this total separation between episodic surface and groundwater events. Carbonates are rare, and mixed in with basement rock units (often Fe/Mg clay bearing), only exposed in crater peaks and walls. Small amounts of Al-rich clays are associated with sulphates in the western part of the study area (Eridania), while widespread, thick, finely layered kaolinite-bearing units are present throughout the northeastern parts of Terra Sirenum. We interpret this as a felsic ash unit, providing an aluminum source for the numerous small alunite detections found in conjunction with this unit. The age of volcanic resurfacing appears to get younger moving west to east across our study area (~3.5 Ga to ~1.4 Ga), indicating that widespread Hesperian volcanism might contract through the late Hesperian into the Amazonian.

6.6 References

Adeli, S., et al. (2015). "Geologic evolution of the eastern Eridania basin: Implications for aqueous processes in the southern highlands of Mars." Journal of Geophysical Research: Planets 120(11): 1774-1799.

Beyer, R. A., et al. (2018). "The Ames Stereo Pipeline: NASA's Open Source Software for Deriving and Processing Terrain Data." Earth and Space Science 5(9): 537-548.

Bibring, J.-P., et al. (2005). "Mars surface diversity as revealed by the OMEGA/Mars Express observations." Science 307(5715): 1576-1581.

Bibring, J.-P., et al. (2006). "Global mineralogical and aqueous Mars history derived from OMEGA/Mars Express data." Science 312(5772): 400-404.

Carter, J., et al. (2015). "Widespread surface weathering on early Mars: A case for a warmer and wetter climate." Icarus 248: 373-382.

Caswell, T. E. and R. E. Milliken (2017). "Evidence for hydraulic fracturing at Gale crater, Mars: Implications for burial depth of the Yellowknife Bay formation." Earth and Planetary Science Letters 468: 72-84.

Christensen, P. R., et al. (2004). "The thermal emission imaging system (THEMIS) for the Mars 2001 Odyssey Mission." Space Science Reviews 110(1-2): 85-130.

Dickson, J., et al. (2018). A Global, Blended CTX Mosaic of Mars with Vectorized Seam Mapping: A New Mosaicking Pipeline Using Principles of Non-Destructive Image Editing. Lunar and Planetary Science Conference.

Ehlmann, B. L., et al. (2016). "Discovery of alunite in Cross crater, Terra Sirenum, Mars: Evidence for acidic, sulfurous waters." American Mineralogist 101(7): 1527-1542.

Eugster, H. P. and L. A. Hardie (1978). Saline lakes. Lakes, Springer: 237-293.

Grant, J. A. and S. A. Wilson (2019). "Evidence for late alluvial activity in Gale crater, Mars." Geophysical research letters.

Hartmann, W. and I. Daubar (2017). "martian cratering 11. Utilizing decameter scale crater populations to study martian history." Meteoritics & Planetary Science 52(3): 493-510.

Hartmann, W. K. (2005). "martian cratering 8: Isochron refinement and the chronology of Mars." Icarus 174(2): 294-320.

Head, J. W. and D. R. Marchant (2014). "The climate history of early Mars: insights from the Antarctic McMurdo Dry Valleys hydrologic system." Antarctic Science 26(6): 774-800.

Hemmi, R. and H. Miyamoto (2017). "Distribution, morphology, and morphometry of circular mounds in the elongated basin of northern Terra Sirenum, Mars." Progress in Earth and Planetary Science 4(1): 26.

Irwin, R. P., et al. (2002). "A large paleolake basin at the head of Ma'adim Vallis, Mars." Science 296(5576): 2209-2212.

Martin, P., et al. (2017). "A two-step K-Ar experiment on Mars: Dating the diagenetic formation of jarosite from Amazonian groundwaters." Journal of Geophysical Research: Planets 122(12): 2803-2818.

Masursky, H., et al. (1977). "Classification and time of formation of martian channels based on Viking data." Journal of Geophysical Research 82(28): 4016-4038.

McLennan, S. M., et al. (2005). "Provenance and diagenesis of the evaporite-bearing Burns formation, Meridiani Planum, Mars." Earth and Planetary Science Letters 240(1): 95-121.

Michael, G. (2013). "Planetary surface dating from crater size–frequency distribution measurements: Multiple resurfacing episodes and differential isochron fitting." Icarus 226(1): 885-890.

Michalski, J. R., et al. (2017). "Ancient hydrothermal seafloor deposits in Eridania basin on Mars." Nature communications 8: 15978.

Morgan, A., et al. (2018). Global distribution of alluvial fans and deltas on Mars. Lunar and Planetary Science Conference.

Murchie, S., et al. (2007). "Compact reconnaissance imaging spectrometer for Mars (CRISM) on Mars reconnaissance orbiter (MRO)." Journal of Geophysical Research: Planets 112(E5).

Murchie, S. L., et al. (2009). "A synthesis of martian aqueous mineralogy after 1 Mars year of observations from the Mars Reconnaissance Orbiter." Journal of Geophysical Research: Planets 114(E2).

Osterloo, M. M., et al. (2010). "Geologic context of proposed chloride-bearing materials on Mars." Journal of Geophysical Research: Planets 115(E10).

Pajola, M., et al. (2016). "Eridania Basin: an ancient paleolake floor as the next landing site for the Mars 2020 rover." Icarus 275: 163-182.

Pelkey, S., et al. (2007). "CRISM multispectral summary products: Parameterizing mineral diversity on Mars from reflectance." Journal of Geophysical Research: Planets (1991–2012) 112(E8).

Poulet, F., et al. (2005). "Phyllosilicates on Mars and implications for early martian climate." Nature 438(7068): 623.

Roach, L. H., et al. (2010). "Hydrated mineral stratigraphy of Ius Chasma, Valles Marineris." Icarus 206(1): 253-268.

Schmidt, M. E., et al. (2018). "Dusty rocks in Gale crater: Assessing areal coverage and separating dust and rock contributions in APXS analyses." Journal of Geophysical Research: Planets 123(7): 1649-1673.

Schumacher, S. and D. Breuer (2007). "An alternative mechanism for recent volcanism on Mars." Geophysical research letters 34(14).

Viviano-Beck, C. E., et al. (2014). "Revised CRISM Spectral Parameters and Summary Products Based on the Currently Detected Mineral Diversity on Mars." Journal of Geophysical Research: Planets.

Wendt, L., et al. (2013). "Knob fields in the Terra Cimmeria/Terra Sirenum region of Mars: Stratigraphy, mineralogy and morphology." Icarus 225(1): 200-215.

Werner, S. C. (2009). "The global martian volcanic evolutionary history." Icarus 201(1): 44-68.

Wray, J., et al. (2011). "Columbus crater and other possible groundwater-fed paleolakes of Terra Sirenum, Mars." Journal of Geophysical Research: Planets 116(E1).

Wray, J. J., et al. (2010). "Identification of the Ca-sulfate bassanite in Mawrth Vallis, Mars." Icarus 209(2): 416-421.

Ye, C. and T. D. Glotch (2019). "Spectral Properties of Chloride Salt-Bearing Assemblages: Implications for Detection Limits of Minor Phases in Chloride-Bearing Deposits on Mars." Journal of Geophysical Research: Planets 124(2): 209-222.

Chapter 7

SUMMARY, IMPLICATIONS, AND OUTSTANDING QUESTIONS

In this work, we have explored natural mineral systems on Earth and Mars using visible-shortwave infrared imaging spectroscopy at a wide range of scales, from sub-millimeter scales in the laboratory to >200m/pixel in CRISM mapping datasets. In chapters 2 and 3, we used prototype imaging spectrometers in the laboratory and field to characterize mineralogic and spectral diversity in samples and outcrop, demonstrating how a similar instrument could be used in planetary missions to: (1) calibrate orbital datasets; (2) plan sampling and targeting, based on a comprehensive understanding of the mineral phases present at a site; (3) characterize the geologic/environmental setting of any samples taken. In this new era of returned sample missions, where we can maximize the amount of information we can obtain from a sample, fully understanding its environmental setting and geologic context becomes even more crucial, to understand how different processes may have affected the sample over time.

An instrument such as this on the surface of Mars could help us to find mineralogical traces of Mars' ancient atmosphere—for instance, if carbon dioxide is sequestered in carbonate veins of varying composition, we could trace these changes in composition and obtain a suite of samples that reflect these changes; thus far, we rely on imagery and limited multispectral data in the VNIR, which are insufficient to distinguish between many alteration minerals (e.g. clays, carbonates, and sulphates). While quantification of mineral abundances remains a difficult question, in situ spectral endmembers and textural observations (e.g. veining) are helpful in constraining possible abundance estimates. Going deeper, this type of instrument is capable of finding the least-altered remnant protolith, even where it is only present in small places in outcrop or hand samples. These regions may record the deeper crustal conditions, in cases where a rock has been brought to the surface (e.g. through impact processes). Finding these rare exposures in altered terrains—and being able to then sample them—could help us understand environmental conditions deep within Mars' ancient crust.

In chapter 4, we set out to search for perchlorate mineral detections in the CRISM dataset; instead, we found a systematic artifact in the data processing pipeline that mimics perchlorate-like absorptions. We had initially hoped that we had found traces of perchlorate across Mars, visible at the ~20m/pixel scale—which would have had enormous implications for the possibility of liquid water at the surface of Mars today, given perchlorate's ability to depress the freezing point of water by ~70 C. Instead, we reinforced the importance of exploring alternative hypotheses and potential data artifacts, especially in cases where the results have far-reaching ramifications.

In chapters 5 and 6, we look at secondary minerals in their geologic context, focusing on chlorides and sulphates. This kind of detailed work, combining data from many different datasets at different scales including mineralogy, textures (high resolution imagery), and elevation, allows us to interpret the relationships between mineral deposits and their likely formation environments. In line with previous work (Osterloo et al., 2010; Ruesch et al., 2012; Glotch et al., 2010), we find that the chlorides are found in local topographic lows, and appear to drape underlying topography rather than being exposed in erosional windows. However, these previous papers prefer a playa-like environment interpretation, likely groundwater fed, and probably pre-dating the Hesperian sulphate-rich emplacements. With additional high resolution digital elevation models, we find that the chloride deposits are inconsistent with playa-like environments; unlike flat playas, chloride deposits on Mars are often sloped, and asymmetric on different sides of a basin, only following an equipotential elevation for small areas (pond-like) within larger basins. We interpret this elevation pattern as consistent with a surface water runoff source, creating a thin layer (<1-3m thick) of chloride where channels debouche into small basins. As these small brine volumes dry out, they create chloride deposits within the older channels they occupy. Here, we do not have sufficient HiRISE DEM data to directly measure the thicknesses of deposits in channels; the thicknesses of chloride within channels may be even smaller than those in basins (e.g. mms to cms), as we would expect the thickest deposits within the basins themselves.

Additionally, we find a small number of chloride deposits on Hesperian and Amazonian terrain, indicating that the surface water process creating these deposits continued until at least ~2.3 Ga. Dating of nearby sulphates places them in the same age range, although sulphates and chlorides never appear in the same sequence. These results push the established range for sulphate formation on Mars into the Amazonian, consistent with recent results from other methods (e.g. age dating of jarosite at Gale crater; Martin et al., 2017)). Furthermore, sulphates are found almost exclusively in basins in Terra Sirenum (and associated with volcanic resurfacing), while chlorides are predominantly in the intercrater plains. These different elevation patterns are consistent with a surface water source for chlorides, in contrast to an upwelling groundwater source for sulphates. If these chloride-forming and sulphate-forming processes were both occurring episodically throughout the Hesperian and into the Amazonian, the two water reservoirs must have been kept separate; else, we would expect to find sulphates and chlorides together, as often found on Earth (e.g. Eugster and Hardie, 1978). (It should be noted that chloride could be found mixed within the sulphate deposits, and would not be distinguishable; however, laboratory studies by Glotch et al. (2016) and Ye and Glotch (2019) have demonstrated that the reverse is not true; if sulphates were associated with the martian chloride deposits (>1-5% abundance), we would detect them.) Chemically distinct surface and groundwater compositions point to disconnected water reservoirs; this observation fits in with the hypothesis that Mars' surface and subsurface water reservoirs may have become separated as Mars froze, with a permafrost layer separating ephemeral surface waters from a deeper reservoir (e.g. Head and Marchant, 2014).

In chapter 6, we also note that many of the sequences of Al-clays over Fe/Mg clays in Terra Sirenum are consistent with a felsic ash layer, rather than weathering sequences (as previously interpreted, e.g. Carter et al., 2015). Thick Al-clay weathering sequences (laterites) on Earth form in tropical environments, where warm temperatures and intense rainfall leach Fe and Mg cations from the soil, leaving Al cations behind. Thus, widespread weathering sequences on Mars would imply a similar climate with high volumes of water passing through. Our alternative interpretation of these units only requires minor alteration of felsic ash to Al-clay; hence it could be consistent with either a warm and wet past Mars, or a cold and icy climate scenario. This is one of the outstanding questions in Mars science—we know Mars once had flowing rivers, but a consensus has not been reached on whether Mars was once warm and wet for a prolonged time (e.g. Pollack et al., 1987; Craddock and Howard, 2002) or whether it was predominantly cold and icy, and only occasionally above the melting point (e.g. Squyres and Kasting, 1994; Wordsworth et al., 2013).

Several of the chapters in this work contain possible avenues of exploration for future landed missions. An onboard imaging spectrometer would improve our ability to sample and target thoroughly, and find phases we might have otherwise missed. In micro-imaging mode, it could allow for petrographic-type analysis, looking at the textures of mineral mixtures to better understand their origin and history. Landed missions in chloride or sulphate deposits—especially sample return missions— could look at fluid inclusions for a record of fluid composition. For example, if chloride deposits have built up over multiple cycles, as suggested by concentric rings in a couple of locations, we could analyze fluid or atmospheric inclusions in each layer to trace how they change through time. Sulphate deposits that appear to be directly connected to volcanics in Terra Sirenum may bring up volatiles from deep magma chambers, again trapped in inclusions; with isotopic measurements of samples like these, we could perhaps scratch the surface in better understanding Mars' depths.

7.1 References

Carter, J., et al. (2015). "Widespread surface weathering on early Mars: A case for a warmer and wetter climate." Icarus 248: 373-382.

Craddock, R. A. and A. D. Howard (2002). "The case for rainfall on a warm, wet early Mars." Journal of Geophysical Research: Planets 107(E11): 21-21-21-36.

Eugster, H. P. and L. A. Hardie (1978). Saline lakes. Lakes, Springer: 237-293.

Glotch, T. D., et al. (2010). "Distribution and formation of chlorides and phyllosilicates in Terra Sirenum, Mars." Geophysical research letters 37(16).

Glotch, T. D., et al. (2016). "Constraints on the composition and particle size of chloride salt-bearing deposits on Mars." Journal of Geophysical Research: Planets 121(3): 454-471.

Head, J. W. and D. R. Marchant (2014). "The climate history of early Mars: insights from the Antarctic McMurdo Dry Valleys hydrologic system." Antarctic Science 26(6): 774-800.

Martin, P., et al. (2017). "A two-step K-Ar experiment on Mars: Dating the diagenetic formation of jarosite from Amazonian groundwaters." Journal of Geophysical Research: Planets 122(12): 2803-2818.

Osterloo, M. M., et al. (2010). "Geologic context of proposed chloride-bearing materials on Mars." Journal of Geophysical Research: Planets 115(E10).

Pollack, J. B., et al. (1987). "The case for a wet, warm climate on early Mars." Icarus 71(2): 203-224.

Ruesch, O., et al. (2012). "Compositional investigation of the proposed chloride-bearing materials on Mars using near-infrared orbital data from OMEGA/MEx." Journal of Geophysical Research: Planets 117(E11).

Squyres, S. W. and J. F. Kasting (1994). "Early Mars: How warm and how wet?" Science 265(5173): 744-749.

Wordsworth, R., et al. (2013). "Global modelling of the early martian climate under a denser CO2 atmosphere: Water cycle and ice evolution." Icarus 222(1): 1-19.

Ye, C. and T. D. Glotch (2019). "Spectral Properties of Chloride Salt-Bearing Assemblages: Implications for Detection Limits of Minor Phases in Chloride-Bearing Deposits on Mars." Journal of Geophysical Research: Planets 124(2): 209-222.

Appendix

SUPPORTING INFORMATION FOR CHAPTER 4: CHALLENGES IN THE SEARCH FOR PERCHLORATE AND OTHER HYDRATED MINERALS WITH 2.1-μM ABSORPTIONS ON MARS

Introduction

This supporting information includes further details about data processing methods, i.e., the algorithm to automate pixel identification and the processing pipeline for CRISM data, as well as a discussion about the use of the 3-μm wavelength region in identifying minerals in single-pixel CRISM spectra. Supplementary figures further detail the spatial, temporal, and spectral distribution of the artifact, and provide further examples of robust single-pixel mineral detections. CRISM image cubes analyzed in this study are listed in Table S2, and summarized in Table S1.

S1. Extended description of methods and data processing

S1.1. Pixel clustering algorithm

CRISM I/F data were downloaded from the NASA Planetary Data System, and atmospherically corrected using CAT-ENVI (v3.1) tools. A photometric correction (division by cosine of the incidence angle) and an empirical atmospheric correction using the default volcano scan (VS61C4) (McGuire et al., 2009) were applied. Image cubes were ratioed to enhance the contrast of minor absorptions, using bland pixels selected from within each column. An unsupervised, Bayesian clustering algorithm was then run on these data, to find and group similar spectra. The center of each cluster generated by this algorithm was manually inspected to identify corresponding minerals. Although the initial detection of the pattern of interest in this study (pixels with 1.9 and 2.1 μm absorptions) was achieved using an unsupervised clustering algorithm, the detections require manual inspection for identification. The unsupervised algorithm was applied to a select set of data mainly from the Nili Fossae and Mawrth Vallis regions to collect a training set representing known spectral signatures and mineral phases. This training dataset was then used to train a supervised version of the non-parametric Bayesian model of Yerebakan et al. (2014), which in turn was used to process all images included in this study from multiple regions of Mars.

S1.2. CRISM data processing

To understand the origin of the observed spectral features, we also analyzed the reduced data record (RDR) radiance data as well as the instrument experimental data records (EDRs) that report raw data in units of data number (DN). EDRs are the rawest forms of instrument data available, and radiance data are calibrated but not divided by solar radiance. In the CRISM data processing pipeline, both precede the more commonly utilized I/F data (IOF). Version 3 I/F data, radiance data, and raw EDRs were all downloaded from NASA's Planetary Data System (PDS). CAT-ENVI was used to convert the PDS format into ENVI format. We employ the earlier data products in the processing pipeline to verify absorption features and differentiate between real features and pipeline-generated artifacts. Although radiance and EDR data are noisy, robust mineral detections can be seen in all types of ratioed data (Figs. 3b, S17).

Typical CRISM processing starts with an EDR, which is the raw, uncalibrated DN detected by the sensor. A simplified description of processing to radiance is: (1) subtraction of the dark background, (2) division by the integration time to obtain a DN accumulation rate, and (3) division by a flat field and instrument responsivity (see CRISM DPSIS, Appendix L for processing details). These steps are expressed algebraically as

$$\text{radiance} =((\text{data number}-\text{dark})/(\text{integration time}))/((\text{flat field})(\text{instrument responsivity}))$$

Radiance data are converted to I/F by the following equation:

$$I/F =(\text{radiance}*\pi*[\![(\text{distance between sun and Mars})]\!]^{2})/(\text{solar flux})$$

(In the equation above the solar flux is the solar irradiance at Earth). In addition, the CRISM data processing pipeline includes a filtering step between radiance and I/F (described in Appendix N of the CRISM DP SIS on the PDS). This filtering is designed to remove sharp, narrow "spikes" in the radiance dataset. Some spikes are positive and result from transient excursions of the dark value in a particular detector element. Other spikes are either positive or negative, and result from a lag in the response of a detector element when crossing an abrupt brightness boundary (Fig. 1b, S4). Thus, spikes can appear upward or downward toward a constant offset when data are acquired with substantial albedo change between successive image lines.

We used the radiance data in two ways: construction of I/F without filtering, and construction of ratioed radiance data. Ratioed radiance was constructed by dividing by the column median at a given wavelength, as a way to remove the strong exponential drop-off of solar radiation and as a rough atmospheric correction (assuming a constant atmosphere throughout a scene). A few individual cases were tested using spectrally bland pixels within a column, selected by hand, to ensure that real absorptions were not being eliminated in the process of ratioing. Aside from any effects from data filtering, ratioed radiance should be equivalent to ratioed atmospherically and photometrically corrected I/F, because the intermediate processing steps are multiplicative.

S2. Discussion of 3-µm region

For the purposes of this paper, we focused on the 1-2.65 µm wavelength region, although CRISM data are available to 3.9 µm. Data from the longer wavelength region (2.7-3.9 µm) are considerably noisier than at shorter wavelengths, and there is another filter zone boundary at ~2.7 µm (analogous to the one at 1.65 µm) which introduces further complications when interpreting absorptions across this boundary. Also, thermal radiation starts to become a complicating factor at these longer wavelengths; surface temperature, atmospheric temperature, and the temperature of the instrument itself all need to be considered when calibrating data.

Full spectra (1-3.9 µm) are shown in figures S15-17; all data are ratioed for simplicity (numerators and denominators can be found in the supplementary data table). We first present single pixel data from well-characterized mineral regions on Mars (Fig. S15). Unlike the characteristic absorptions at shorter wavelengths, none of the ~3 µm absorptions persist in I/F, radiance, and raw datasets. The ~3-µm H2O-related absorption in kieserite is very broad (Fig S15a), and so we might not expect to see a strong signal in CRISM data. However, laboratory spectra for both alunite and serpentine have a sharp, clear absorption at 2.7-2.8 µm, a metal-OH vibration. Alunite (Fig S15b) appears to have that characteristic absorption in I/F data, but the radiance data are very noisy, and the region appears flat in raw data. Serpentine (Fig S15c) appears to have the characteristic absorption in raw data, but long wavelength ratioed values are improbably high in both I/F and radiance. This may be a problem introduced by the choice of denominator in ratioing, although the same pixels (column median) are used as a denominator in I/F, radiance, and raw datasets. It is also possible that the surface temperature of the serpentine region is warmer than its surroundings (perhaps because of aspect/sun angle), adding more thermal radiation to the reflectance values at longer wavelengths. For all these single-pixel examples, even though the mineral signatures are strong and clear in all datasets in the 1-2.65 µm range, the ~3-µm absorption is not consistent in I/F, radiance, and raw data. Thus, we de-emphasize use of the ~3-µm region in the main text and generally for verifying our mineral detections.

Figures S16-17 show all proposed RSL perchlorate pixels, in addition to two other pixels for comparison. Denominators used for ratioing match the denominators given in Ojha et al. (2015) where available, else column medians are used as denominators. Proposed perchlorate pixels from high-latitude regions were not included in this analysis, as an ice absorption at 3 µm dominates the spectrum in this wavelength range. Four pixels from Horowitz Crater (FRT00008573) are shown in Fig. S16. In panel (a) (spectrum 8573b from Ojha et al. (2015)), there is a broad absorption centered at ~3.2 µm in both I/F and radiance data. However, the absorption in perchlorate minerals is centered at ~2.8 µm (Hanley et al., 2015). Similarly, panel (b) (spectrum 8573a from Ojha et al. (2015)) may also have a noisy absorption at longer wavelengths, but it does not appear to coincide with the perchlorate absorption position. Panel (c) depicts a non-RSL pixel from the same column as panel (b); many of the spikes in the data are located at the same wavelengths in both of these pixels, and the long wavelength I/F data have a very similar structure. This in-column similarity means it is possible that the apparent absorptions are caused by column-dependent noise rather than a real surface signal. Panel (d) shows a clear, broad absorption in long wavelength data in I/F, radiance, and raw data, centered at ~3.3 µm. However, this pixel is not from a region with RSLs, and the apparent absorptions at 1.9, 2.1, and 2.5 µm do not persist in radiance or raw data—while it has a 3 µm feature, it cannot be identified as a perchlorate.

Proposed perchlorate pixels from Palikir Crater are shown in Fig. S17 (see Fig. S14 for focused look at the shorter wavelength region). While these spectra do no show robust 1.9- and 2.1-µm absorptions clearly above the level of noise, they do all appear to have a narrow but distinct 3-µm absorption in I/F. Though noisy, several of those absorptions appear to be present in radiance data too. However, ~3-µm absorptions are common over much of Mars in hydrated mineral phases, and do not uniquely identify perchlorate. Also, all six pixels come from 2 adjacent columns, and could be affected by column-specific noise (note the similar shape of spectra in (b) and (c) of Fig. S17).

Supplementary Figures

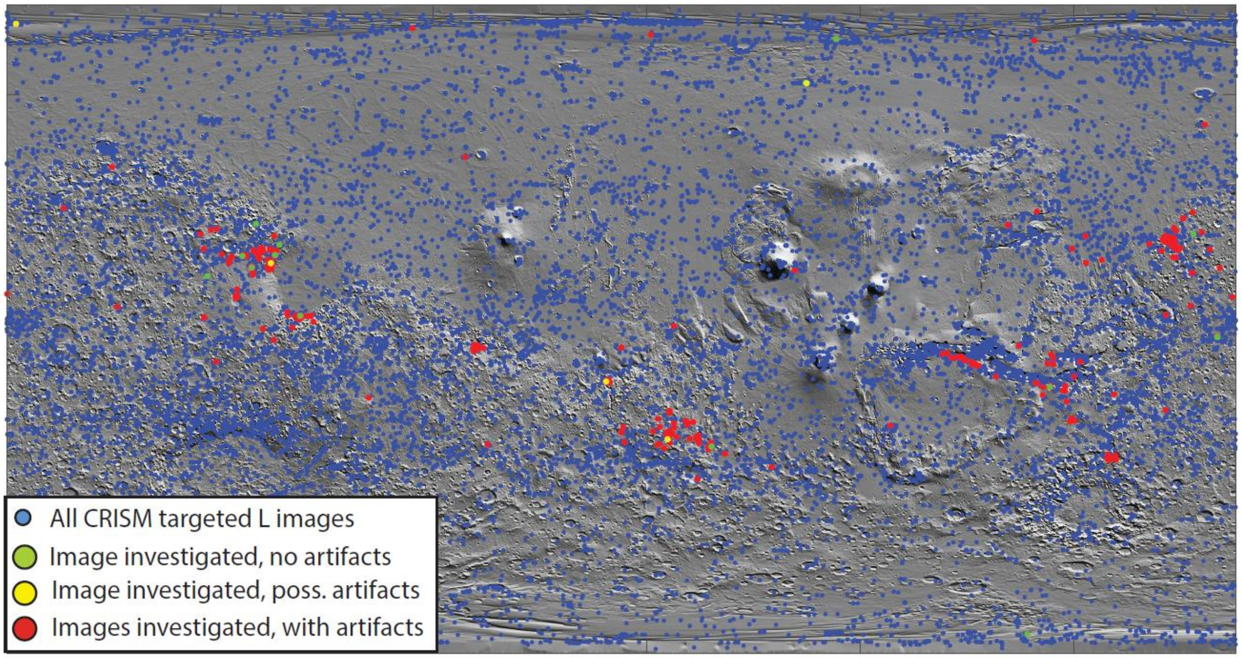

Figure S1. Spatial distribution of targeted CRISM ‘L’ (infrared) images (blue), with larger symbols for the 344 images investigated with our algorithm (red where artifact pixels were detected, green where detections are marginal, and yellow for no detections).

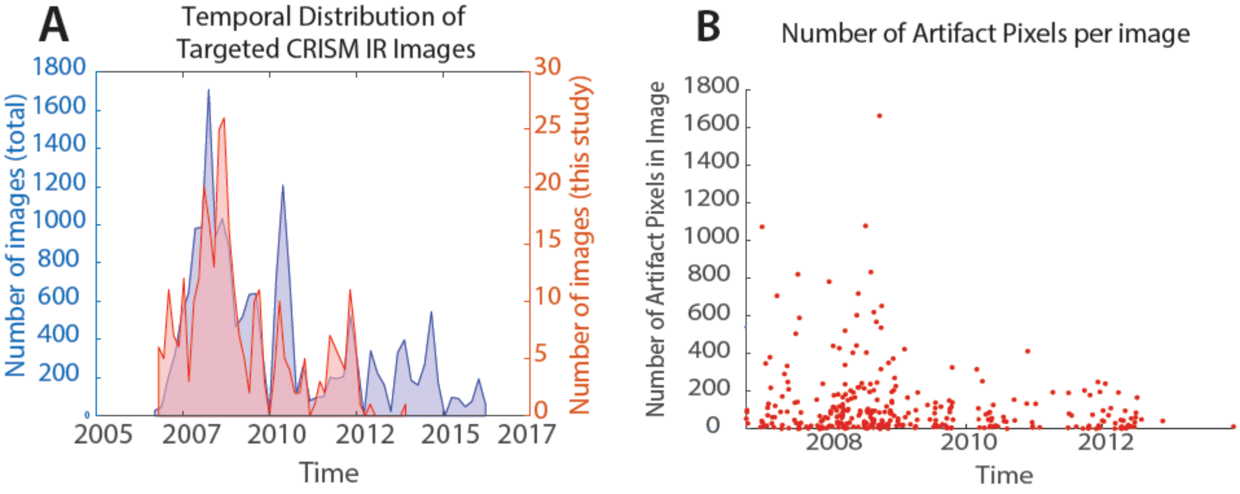

Figure S2. a) Temporal distribution of all targeted CRISM “L” data (blue) and images investigated in this study (red) (Note different axis scales). b) Number of artifact pixels per image through time; note that it is independent of time (i.e. artifacts are not restricted to later, noisier images)

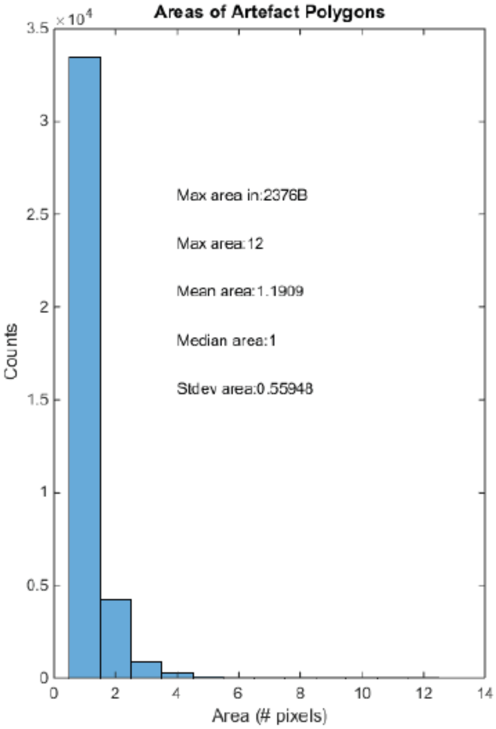

Figure S3. Artifact area statistics for all 344 images investigated with our automatic detection algorithm. Most artifacts are a single pixel; the largest contiguous area with the artifact signal was 12 pixels. Other minerals are detected in contiguous areas over tens or hundreds of pixels.

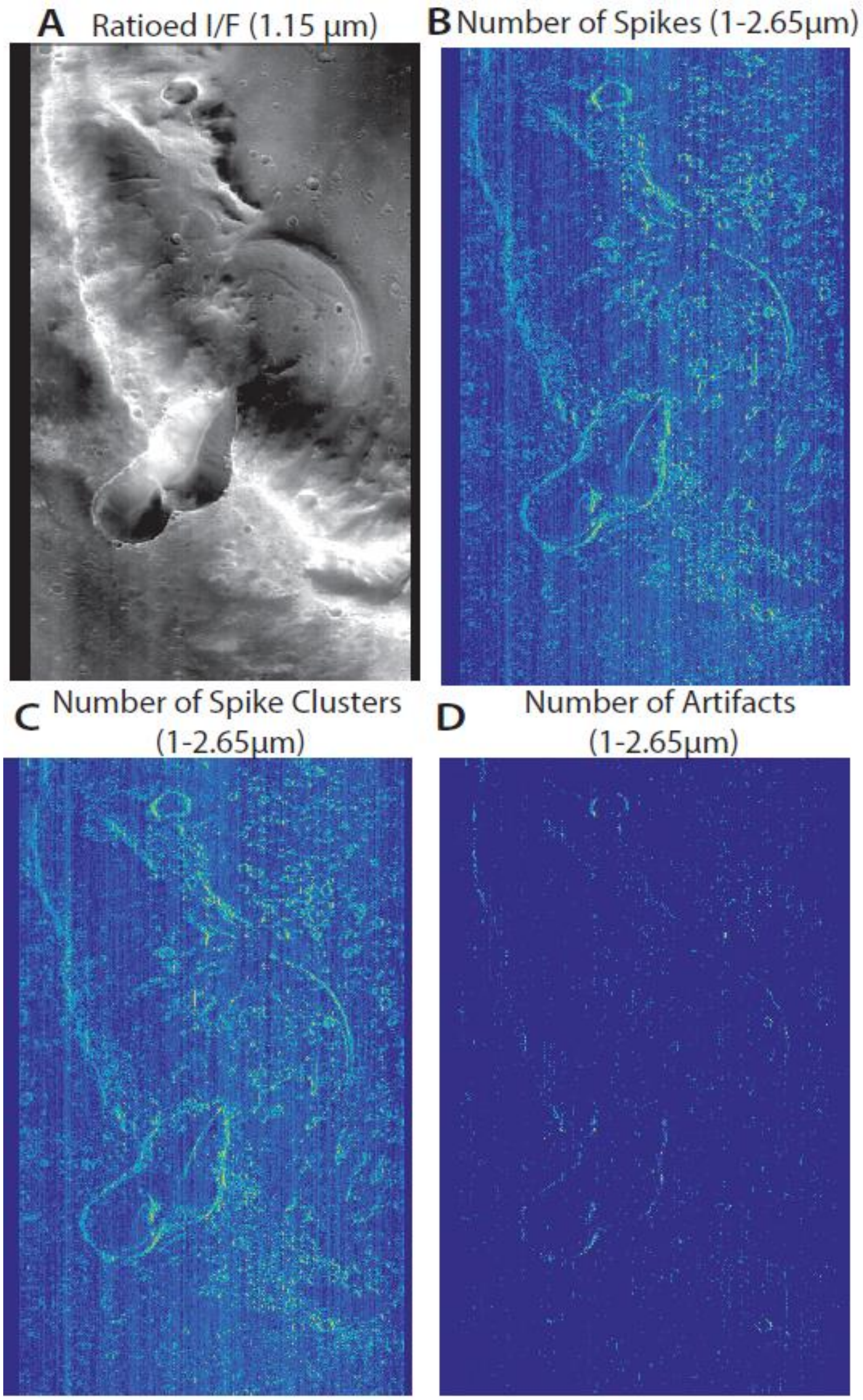

Figure S4. Spatial distribution of spikes, spike clusters, and artifacts in a single image (HRL000080CB), with the ratioed reflectance (brightness) at a single wavelength band for comparison (a). Spikes, spike clusters, and artifacts tend to coincide with abrupt changes in brightness along topographic boundaries, or occur frequently in a column (vertical striping).

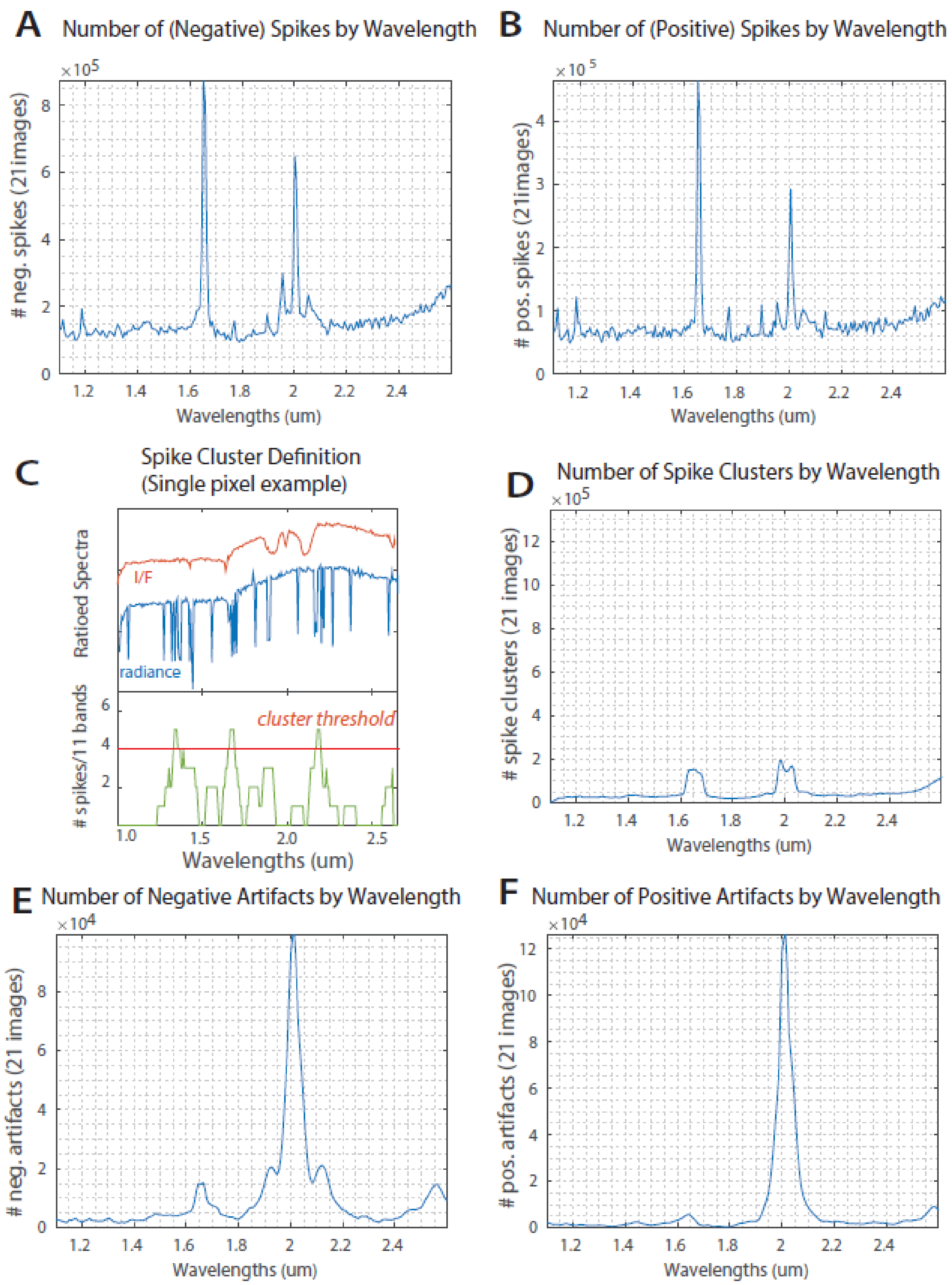

Figure S5. Spectral distribution of spikes, spike clusters, and artifacts (data shown are for a subset of 21 images processed from radiance data and compared to I/F). Panels a & b show that positive (upward) and negative (downward) spikes preferentially occur at 1.65 µm and ~2 µm, corresponding with a filter boundary and CO_2 triplet respectively (see Fig. S13c for a typical martian atmospheric spectrum). These patterns are both caused by abrupt, narrow features that are misclassified as spikes by our simple 2-step median despiking algorithm; true spikes (as defined in the main text) are found at similar levels throughout the spectrum, although they are more common at wavelengths > 2.4 µm. c, d) We define "spike clusters" to be where >4 spikes occur within a moving window of 11 bands; they are more common at 1.65 and 2µm (not 1.9 and 2.1 µm, which we would expect if spike clusters were responsible for our artifact). Panels e & f show where negative and positive artifacts occur between 1-2.65 µm ("artifact" here is defined in the main text; see Fig. 1c). Note that negative (absorption-like) artifacts in (e) have minor peaks at 1.9 and 2.1 µm, which are not present in positive artifacts (f).

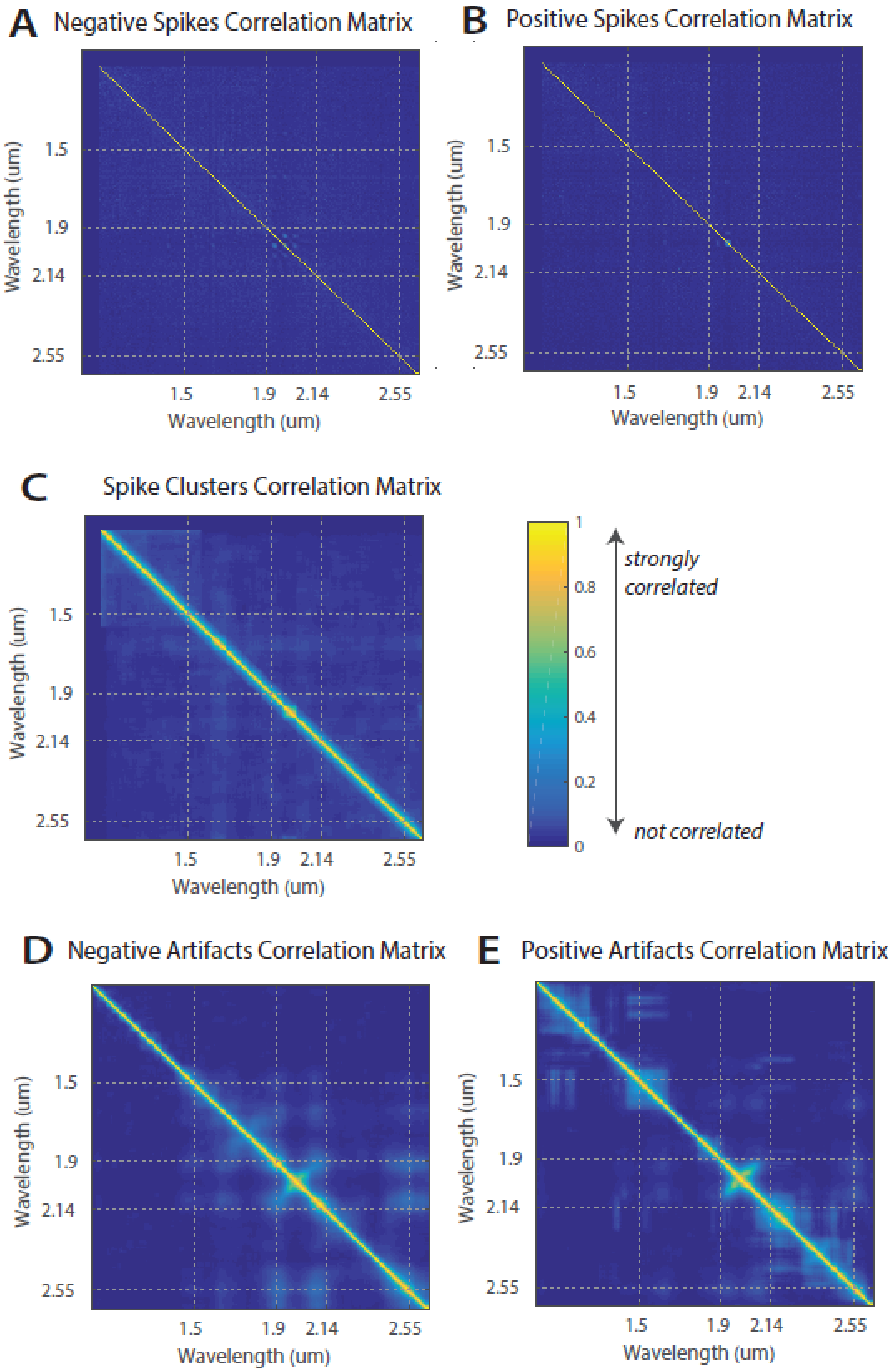

Figure S6. Correlation matrices for spikes, spike clusters, and artifacts. Neither positive (upward) spikes, negative (downward) spikes, nor spike clusters (a-c) show strong off-axis 'hotspots' which would indicate that they preferentially co-occur at certain wavelengths. However, both positive and negative artifacts show clear patterns of correlation (off-axis 'hotspots'), most strongly at 1.9 and 2.1 µm.

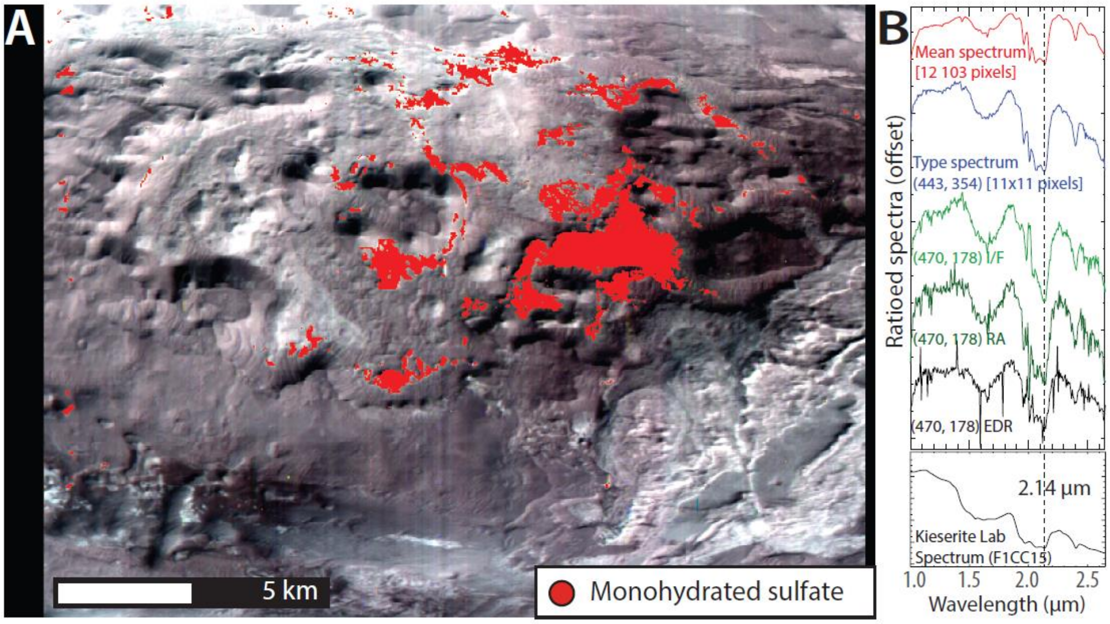

Figure S7. (a) Monohydrated sulfate (most likely kieserite) is found in thousands of pixels in this image, in spatially contiguous regions in FRT0000A91C. (b) The diagnostic absorptions are consistent in single-pixel I/F, radiance, and raw data, as well as the mean ratioed radiance spectrum for the highlighted pixels (b).

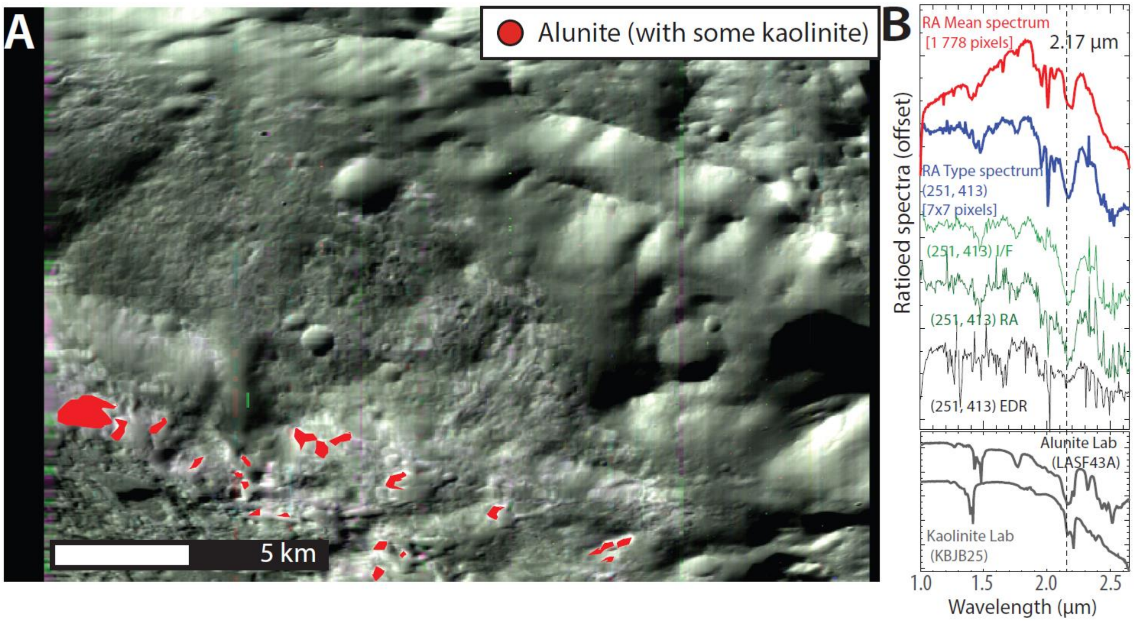

Figure S8. (a) Alunite in Cross Crater (Terra Sirenum; FRT0000B252) is found in a spatially coherent areas in a single geologic unit (not scattered single pixels). (b) Mean and single pixel spectra show that the diagnostic absorptions remain in ratioed radiance and raw data.

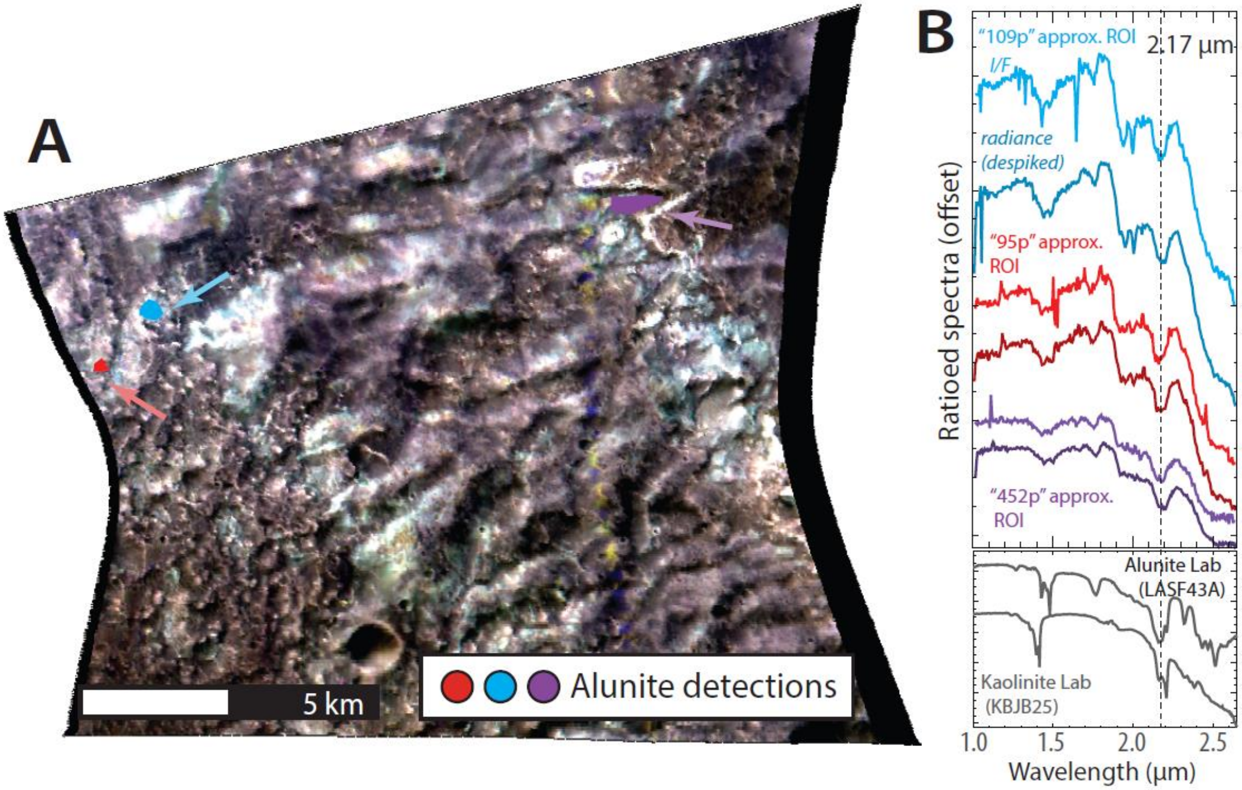

Figure S9. (a) Alunite in Columbus Crater (with some kaolinite mixed in; FRT00013EEF), after Wray et al. (2011). (b) Mean spectra (ratioed I/F and ratioed despiked radiance) for each region shown in (a).

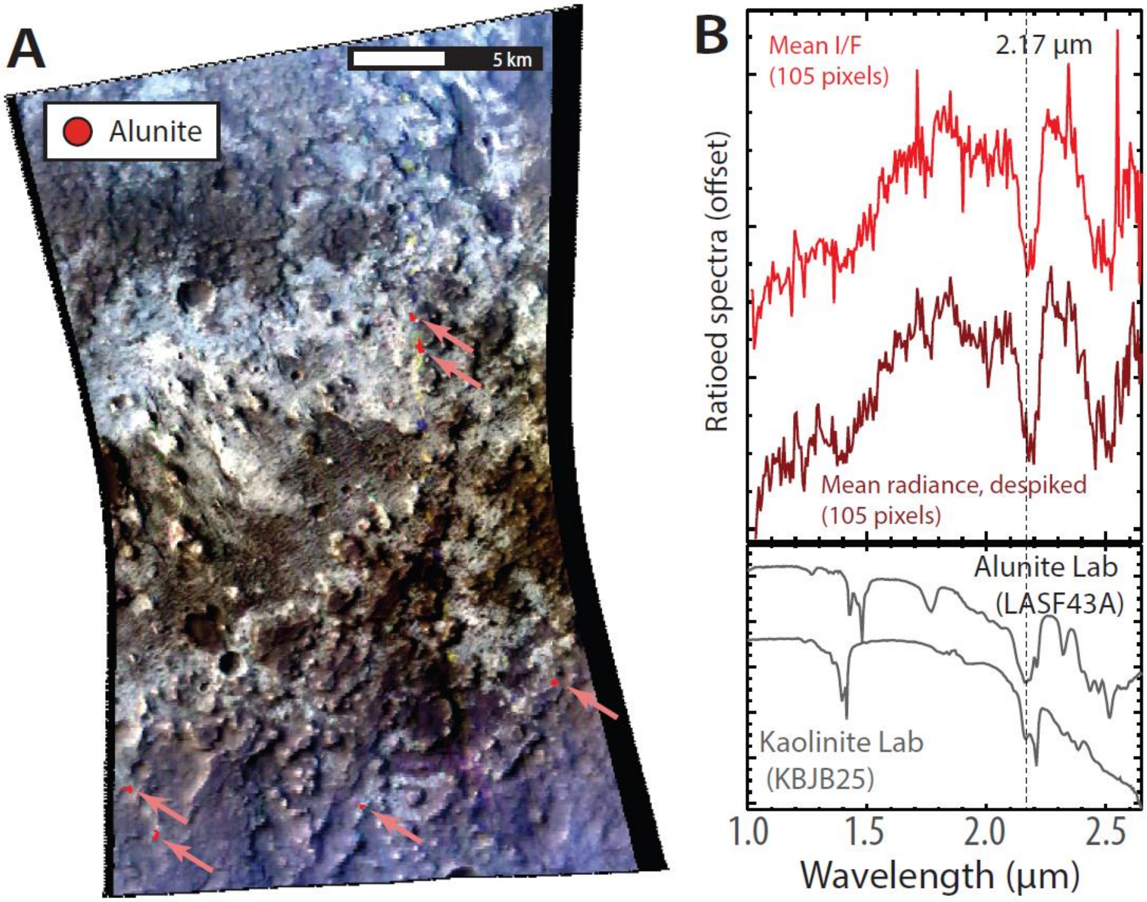

Figure S10. (a) Intercrater alunite deposits (dispersed; HRL00011D66); individual ROIs are 16-25 pixels (after Ehlmann et al., 2016; Carter, 2015 (personal communication). (b) Mean spectra of all highlighted pixels combined; note that alunite's diagnostic absorptions are present in both ratioed I/F and despiked ratioed radiance spectra.

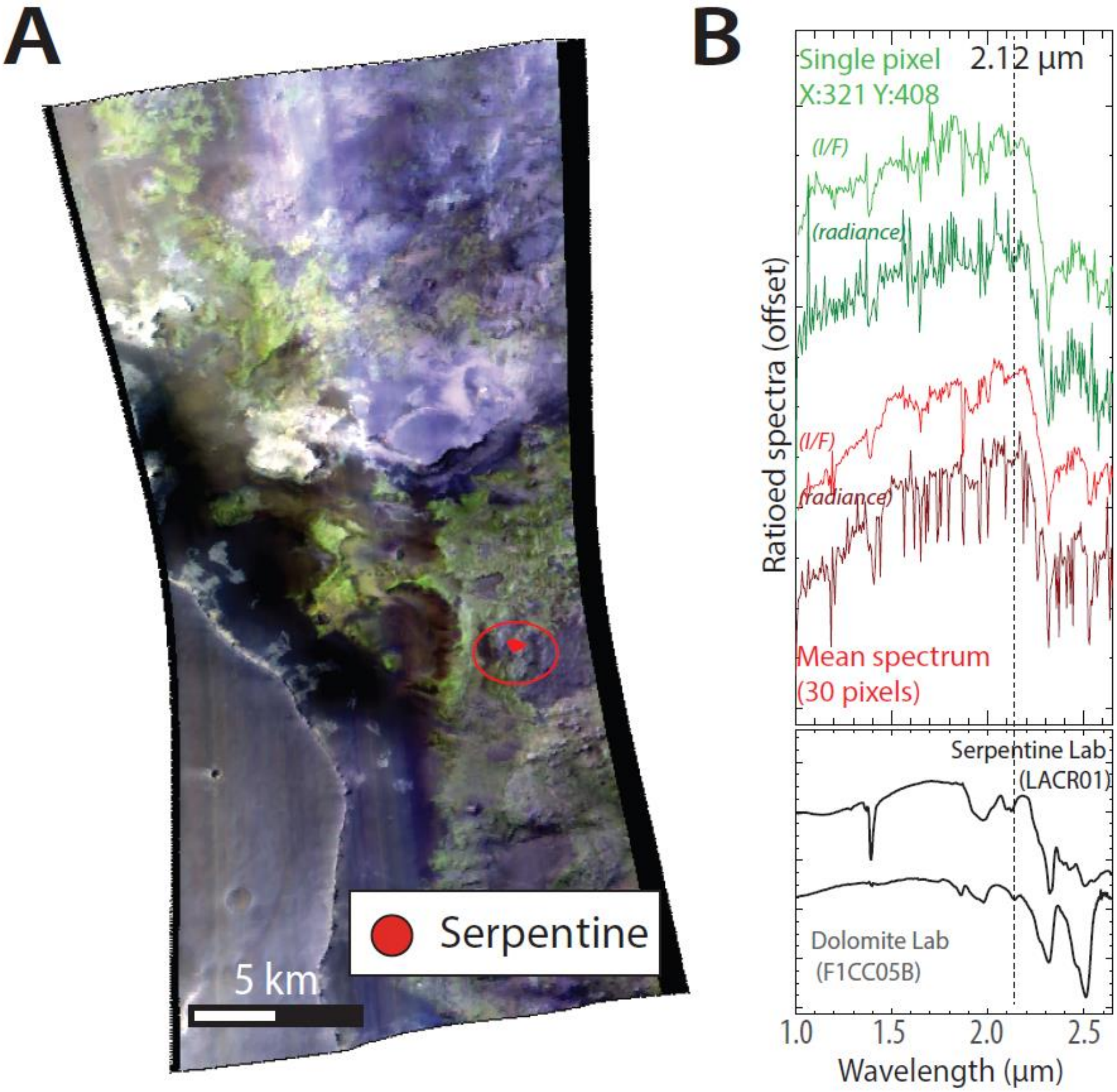

Figure S11. (a) Northeast Syrtis (HRL0000B8C2) serpentine is confirmed in a spatially coherent region (30 pixels) in (b) ratioed I/F and radiance data.

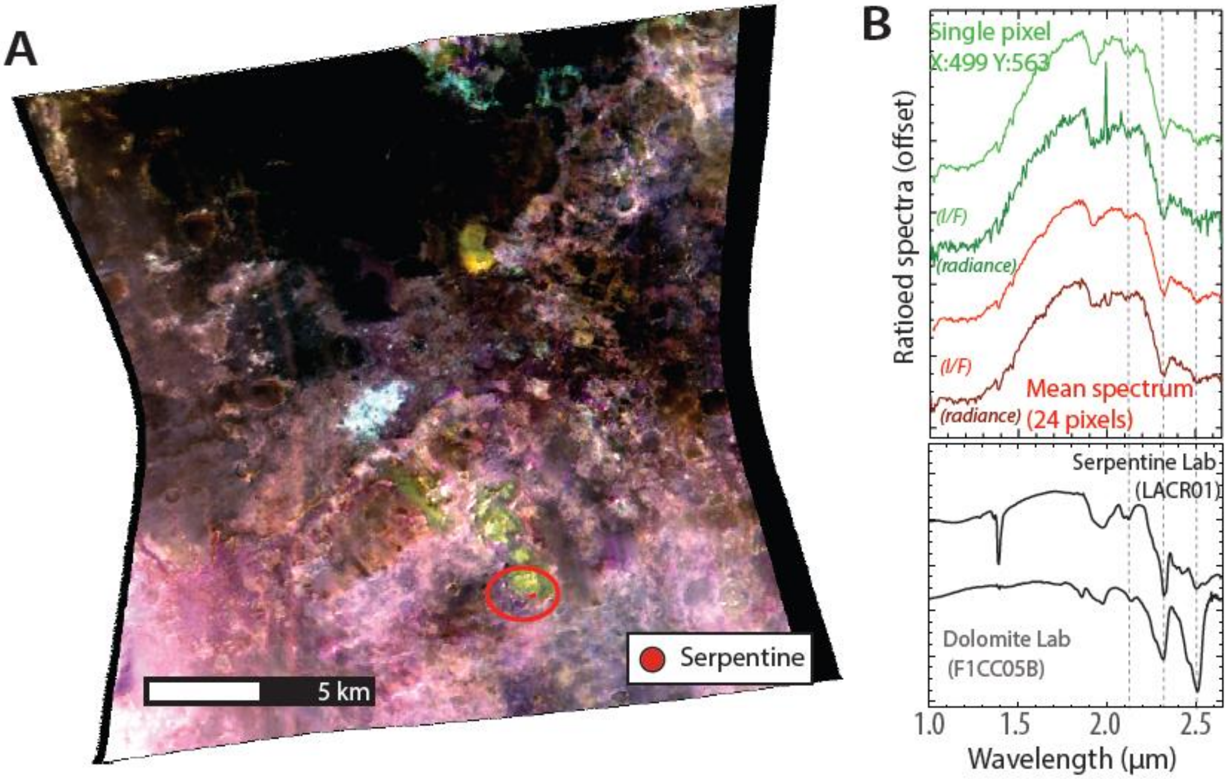

Figure S12. (a) Serpentine in Nili Fossae (FRT0000ABCB) is present in a 24-pixel contiguous area, and (b) has the 2.12-wμm absorption necessary to positively identify serpentine in both I/F and ratioed radiance data.

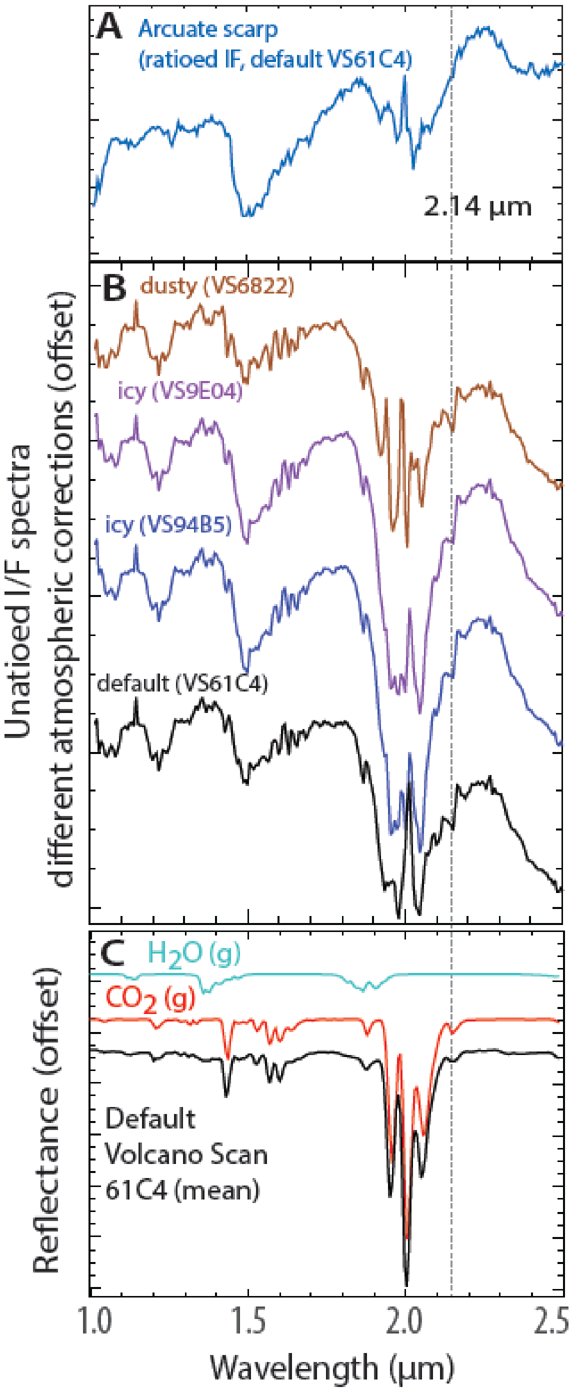

Figure S13. Testing different atmospheric corrections (using the the ‘arcuate scarp’ region from Fig. 4a-c in the main text). We present a variety of unratioed I/F spectra (b) of the same region with different atmospheric corrections applied (here, we vary the volcano scan (VS) used, using tools in CAT-ENVI). The shape of the minor 2.14 μm absorption changes with each atmospheric correction, and disappears entirely when ratioed to an in-column denominator. The absorption coincides with a minor CO2 absorption (c).

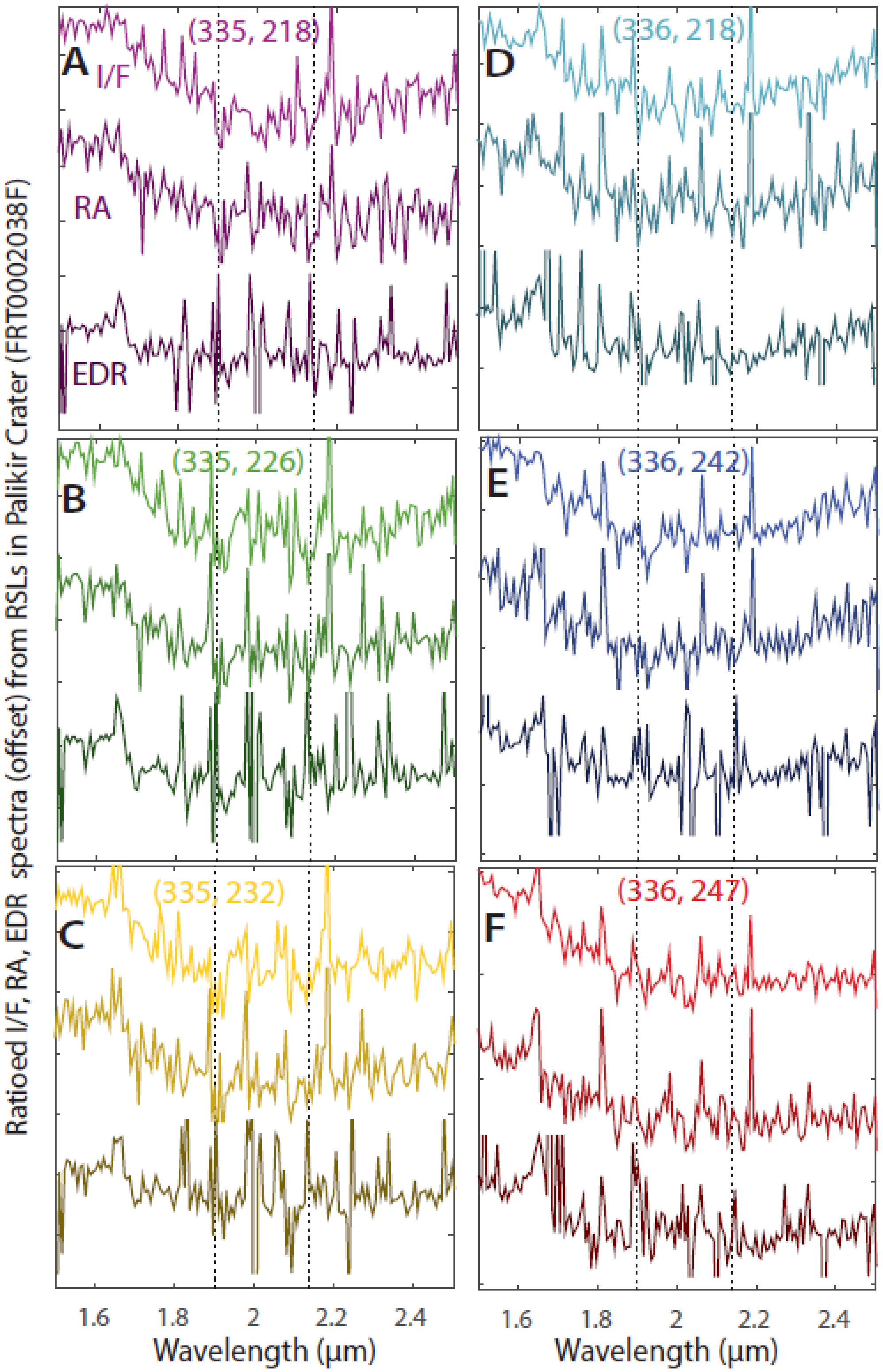

Figure S14. Potential perchlorate pixels from Palikir Crater (FRT0002038F) using coordinates provided in Ojha et al. (2015). None of these pixels have 2.14 μm absorptions that persist in ratioed radiance and raw data.

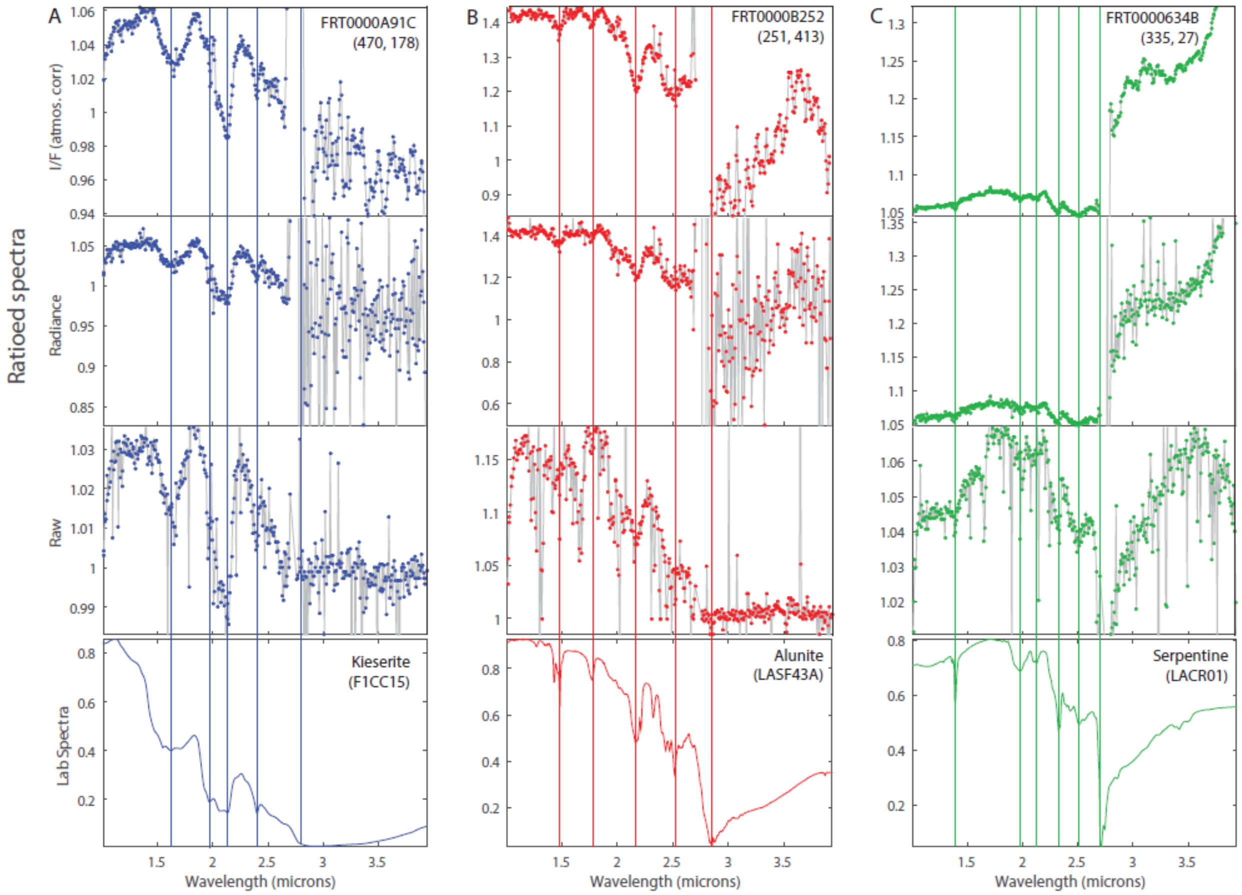

Figure S15. Single-pixel CRISM spectra (ratioed), compared to a laboratory mineral spectrum (1-4 µm). Major absorptions in the 1-2.65 µm range are evident in all forms of ratioed data, while the ~3µm absorption (present in all three laboratory spectra) is sometimes obscured by noise (especially in radiance data).

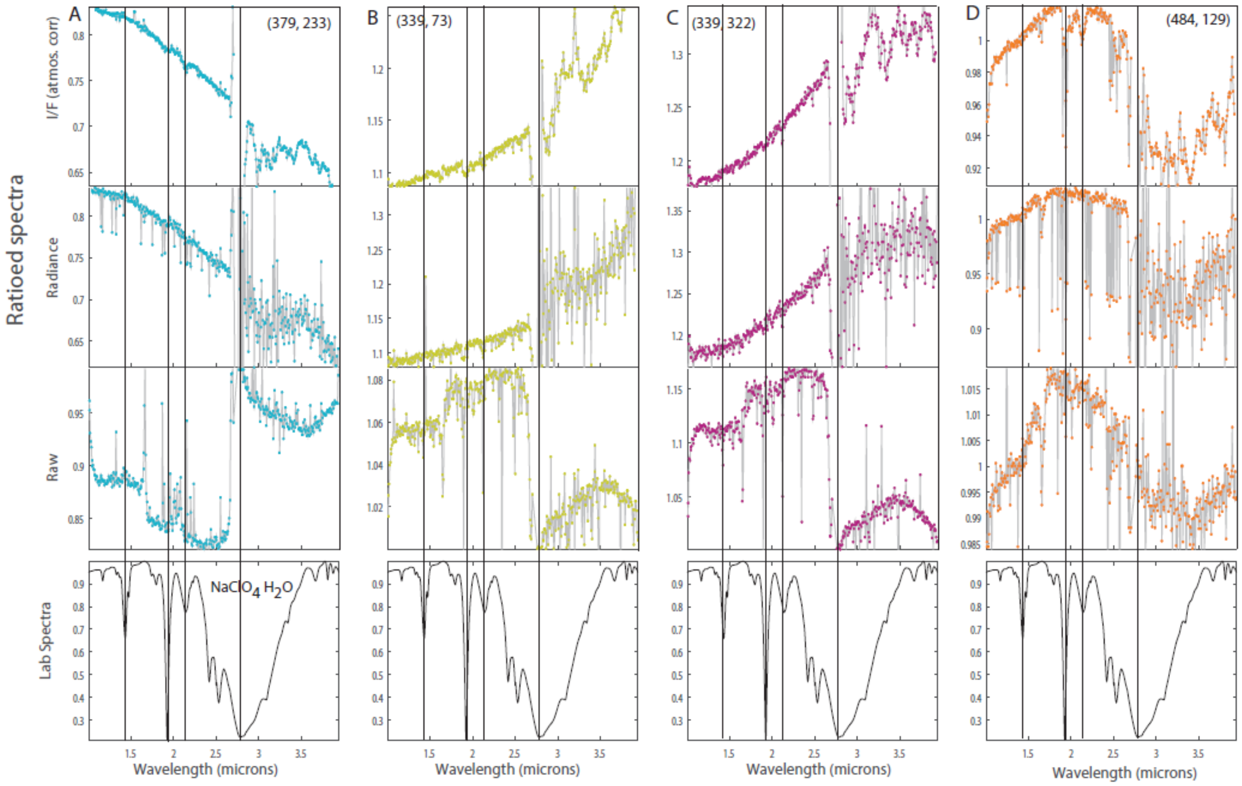

Figure S16. Single-pixel CRISM spectra from FRT00008573 (Horowitz Crater; 1-4 µm). Cyan and yellow pixels (a & b) are proposed perchlorates from Ojha et al. (2015). Two other (non-RSL) pixels are shown for comparison. Spectra in panel (c) are from the column as those in panel (b), and show a similar pattern of spikes, including those in the 1.9- and 2.1-µm regions. Panel (d) is an example of a pixel which strongly mimics several perchlorate absorptions in I/F data, but not in radiance or raw data. While all of these pixels appear to have a ~3µm absorption in ratioed I/F data, these absorptions are not clearly evident in ratioed radiance data (and are not uniquely correlated with RSL pixels). (Perchlorate spectrum shown from Hanley et al., 2015)

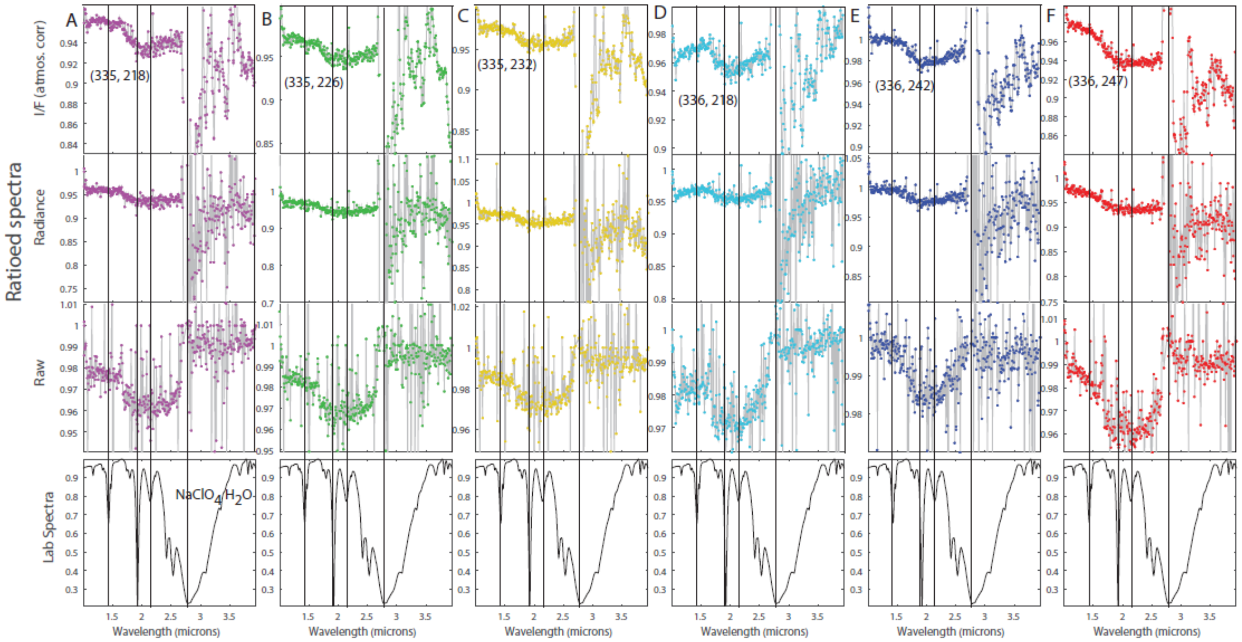

Figure S17. Single-pixel CRISM spectra from FRT0002038F (Palikir Crater; 1-4 µm), presented as possible perchlorate pixels in Ojha et al. (2015). See Fig. S14 for detail in 1-2.65 µm region. All six pixels have apparent 3-µm absorptions in ratioed I/F data, most of which appear to persist in radiance data (although noisy). However, a 3-µm absorption alone is not sufficient to identify perchlorate.

Summary Table		Number of CRISM images
Images investigated with automated algorithm		**344**
	Number of full-resolution images (Fig. 2b)	256
	Number with artifact detections	317
	Number with marginal artifact detections	6
	Number with no artifact detections	21
Images for which I/F compared to radiance at all wavelengths		**30**
	Number of icy/noisy images, excluded from summary plots (2c-d, S5, S6)	9

Table S1. Summary of the number of CRISM images analyzed and used in figures in the main and supplemental text.

Table S2. (below) List of CRISM image cubes investigated in this study, highlighting which images were used for in-depth analysis comparing radiance to I/F, and whether the automated algorithm found artifacts in that image (“Y” means yes, “N” or (blank) mean no, and “M” means marginal). The figures that incorporate data from each image are listed in column 5.

CRISM Image ID	Artifacts at 1.9 + 2.1 µm detected by algorithm?	I/F compared to radiance at all wavelengths?	Comment	Data from image included in figures:	Individual image presented in a figure
FRT00003BFB	Y	Y		2a, 2b, 2c, 2d, S1, S2, S3, S5, S6	
FRT000047A3	Y	Y		2a, 2b, 2c, 2d, S1, S2, S3, S5, S6	
HRL0000330C	Y	Y	icy (proposed perchlorate)	2a, 2c, 2d, 4a, 4b, 4c, S1, S2, S3, S5, S6, S13	*
FRT00003FB9	Y	Y		2a, 2b, 2c, 2d, S1, S2, S3, S5, S6	
HRL000040FF	Y	Y		2a, 2c, 2d, S1, S2, S3, S5, S6	
HRL000062B6	Y	Y		2a, 2c, 2d, S1, S2, S3, S5, S6	
FRT0000634B	Y	Y		2a, 2b, 2c, 2d, 3a, 3b, S1, S2, S3, S5, S6	*
HRL00005483	Y	Y		2a, 2c, 2d, S1, S2, S3, S5, S6	
FRT00008573	Y	Y	(proposed perchlorate)	2a, 2b, 2c, 2d, 4d, 4e, S1, S2, S3, S5, S6, S16	*
HRL00008565	Y	Y		2a, 2c, 2d, S1, S2, S3, S5, S6	
HRL000080CB	Y	Y		1, 2a, 2c, 2d, S1, S2, S3, S4, S5, S6	*
FRT0001BBA1	Y	Y	noisy	2a, 2b, 2c, 2d, S1, S2, S3, S5, S6	
FRT0000C518	Y	Y		2a, 2b, 2c, 2d, S1, S2, S3, S5, S6	
FRT0001663B	Y	Y	noisy	2a, 2b, 2c, 2d, S1, S2, S3, S5, S6	
FRT00009971	Y	Y		2a, 2b, 2c, 2d, S1, S2, S3, S5, S6	
FRT0000C9FB	Y	Y		2a, 2b, 2c, 2d, S1, S2, S3, S5, S6	
HRL00011D66	Y	Y	(alunite)	2a, 2c, 2d, S1, S2, S3, S5, S6, S10	*
FRT0000A09C	Y	Y		2a, 2b, 2c, 2d, S1, S2, S3, S5, S6	
FRT0000A91C	Y	Y	(kieserite)	2a, 2b, 2c, 2d, S1, S2, S3, S5, S6, S7	*
HRL000132F9	Y	Y	noisy	2a, 2c, 2d, S1, S2, S3, S5, S6	
FRT0000ABCB	Y	Y	(serpentine)	2a, 2b, 2c, 2d, S1, S2, S3, S5, S6, S12	*
FRT0000B252	Y	Y	noisy (alunite)	2a, 2b, 2c, 2d, S1, S2, S3, S5, S6, S8	*
FRT00013EEF	Y	Y	noisy (alunite)	2a, 2b, 2c, 2d, S1, S2, S3, S5, S6, S9	*
HRL0000B8C2	Y	Y	noisy (serpentine)	2a, 2c, 2d, S1, S2, S3, S5, S6, S11	*
FRT0002038F	Y	Y	noisy (proposed perchlorate)	2a, 2b, 2c, 2d, S1, S2, S3, S5, S6, S14, S17	*
FRT000042AA	M	Y	icy	2a, 2b, 2c, 2d, S1, S2, S3, S5, S6	
FRT0000A5AA	Y	Y		2b, 2c, 2d, 3c, 3d, S5, S6	*
FRT0000B072	Y	Y		2b, 2c, 2d, S5, S6	
FRT000069AF	N	Y		2b, 2c, 2d, S5, S6	
HRL000095C7	Y	Y		2c, 2d, 3e, 3f, S5, S6	*
FRT000167FA	Y			2a, 2b, S1, S2, S3	
HRL00016CFE	Y			2a, S1, S2, S3	
FRT00016D9F	Y			2a, 2b, S1, S2, S3	
FRT00016E2D	Y			2a, 2b, S1, S2, S3	
FRT00016F13	Y			2a, 2b, S1, S2, S3	
FRT00016F51	Y			2a, 2b, S1, S2, S3	
FRT00017199	Y			2a, 2b, S1, S2, S3	
FRT00017229	Y			2a, 2b, S1, S2, S3	
FRT0001735E	Y			2a, 2b, S1, S2, S3	
FRT000173F4	Y			2a, 2b, S1, S2, S3	

FRT00017412	Y			2a, 2b, S1, S2, S3	
FRT000176BD	Y			2a, 2b, S1, S2, S3	
FRT00017C55	Y			2a, 2b, S1, S2, S3	
FRT00017DBF	Y			2a, 2b, S1, S2, S3	
FRT00018146	Y			2a, 2b, S1, S2, S3	
HRL000184F8	Y			2a, S1, S2, S3	
FRT00018800	Y			2a, 2b, S1, S2, S3	
FRT00018781	Y			2a, 2b, S1, S2, S3	
FRT00019538	Y			2a, 2b, S1, S2, S3	
FRT0001957C	Y			2a, 2b, S1, S2, S3	
FRT00019DAA	Y			2a, 2b, S1, S2, S3	
FRT00019AA0	Y			2a, 2b, S1, S2, S3	
FRT00019819	Y			2a, 2b, S1, S2, S3	
FRT000027E2	Y			2a, 2b, S1, S2, S3	
HRS00002847	Y			2a, S1, S2, S3	
HRL0000285A	Y			2a, S1, S2, S3	
FRT0000454E	Y			2a, 2b, S1, S2, S3	
FRT00002879	Y			2a, 2b, S1, S2, S3	
HRL00002885	Y			2a, S1, S2, S3	
FRT0000289E	Y			2a, 2b, S1, S2, S3	
HRS0000289B	Y			2a, S1, S2, S3	
FRT000028BA	Y			2a, 2b, S1, S2, S3	
HRS00002FC5	Y			2a, S1, S2, S3	
HRL00003010	Y			2a, S1, S2, S3	
HRS0000307A	Y			2a, S1, S2, S3	
HRS000047D8	Y			2a, S1, S2, S3	
FRT00003156	Y			2a, 2b, S1, S2, S3	
FRT000048B2	Y			2a, 2b, S1, S2, S3	
FRT00003192	Y			2a, 2b, S1, S2, S3	
HRS000031C0	Y			2a, S1, S2, S3	
FRT00003E12	Y			2a, 2b, S1, S2, S3	
HRS0000326E	Y			2a, S1, S2, S3	
HRL00004A93	Y			2a, S1, S2, S3	
FRT0000334D	Y			2a, 2b, S1, S2, S3	
FRT00004AF7	Y			2a, 2b, S1, S2, S3	
FRT00004185	Y			2a, 2b, S1, S2, S3	
FRT000035D0	Y			2a, 2b, S1, S2, S3	
HRS00004259	Y			2a, S1, S2, S3	
FRT000050F2	Y			2a, 2b, S1, S2, S3	
HRL00004371	Y			2a, S1, S2, S3	
HRL000043EC	Y			2a, S1, S2, S3	
HRL00005491	Y			2a, S1, S2, S3	
FRT000063B5	Y			2a, 2b, S1, S2, S3	

HRL000063C3	Y			2a, S1, S2, S3	
FRT0000553B	Y			2a, 2b, S1, S2, S3	
FRT000064D9	Y			2a, 2b, S1, S2, S3	
FRT00005814	Y			2a, 2b, S1, S2, S3	
HRL000067F1	Y			2a, S1, S2, S3	
FRT000058A3	Y			2a, 2b, S1, S2, S3	
FRT00006841	Y			2a, 2b, S1, S2, S3	
FRT00005AA4	Y			2a, 2b, S1, S2, S3	
FRT00007431	Y			2a, 2b, S1, S2, S3	
FRT00005BB9	Y			2a, 2b, S1, S2, S3	
FRT00005C5E	Y			2a, 2b, S1, S2, S3	
FRT0000750A	Y			2a, 2b, S1, S2, S3	
FRT00006AF8	Y			2a, 2b, S1, S2, S3	
FRT00008CE1	Y			2a, 2b, S1, S2, S3	
FRT000081CF	Y			2a, 2b, S1, S2, S3	
FRT000082EE	Y			2a, 2b, S1, S2, S3	
HRL000082DA	Y			2a, S1, S2, S3	
FRT00008E5D	Y			2a, 2b, S1, S2, S3	
FRT00008F68	Y			2a, 2b, S1, S2, S3	
FRT00007BC8	Y			2a, 2b, S1, S2, S3	
HRS000084F4	Y			2a, S1, S2, S3	
FRT0000901A	Y			2a, 2b, S1, S2, S3	
FRT00007C09	Y			2a, 2b, S1, S2, S3	
FRT000085D7	Y			2a, 2b, S1, S2, S3	
HRL00007C95	Y			2a, S1, S2, S3	
FRT0000863E	Y			2a, 2b, S1, S2, S3	
HRL0000860C	Y			2a, S1, S2, S3	
FRT00007D87	Y			2a, 2b, S1, S2, S3	
FRT00007DF1	Y			2a, 2b, S1, S2, S3	
FRT000088D0	Y			2a, 2b, S1, S2, S3	
FRT00007F63	Y			2a, 2b, S1, S2, S3	
FRT0000812F	Y			2a, 2b, S1, S2, S3	
HRL0001B769	Y			2a, S1, S2, S3	
HRL0000BFF1	Y			2a, S1, S2, S3	
FRT0000929F	Y			2a, 2b, S1, S2, S3	
FRT0000C029	Y			2a, 2b, S1, S2, S3	
FRT00009312	Y			2a, 2b, S1, S2, S3	
FRT00009326	Y			2a, 2b, S1, S2, S3	
FRT00009365	Y			2a, 2b, S1, S2, S3	
FRT0000C0EF	Y			2a, 2b, S1, S2, S3	
FRT00014703	Y			2a, 2b, S1, S2, S3	
FRT000093BE	Y			2a, 2b, S1, S2, S3	
FRT0000C256	Y			2a, 2b, S1, S2, S3	

FRT0000C26C	Y			2a, 2b, S1, S2, S3	
FRT000095B8	Y			2a, 2b, S1, S2, S3	
FRT000095EE	Y			2a, 2b, S1, S2, S3	
FRT000095FE	Y			2a, 2b, S1, S2, S3	
FRT00009628	Y			2a, 2b, S1, S2, S3	
FRT0000C441	Y			2a, 2b, S1, S2, S3	
FRT0000C467	Y			2a, 2b, S1, S2, S3	
FRT0000C4BB	Y			2a, 2b, S1, S2, S3	
FRT00009786	Y			2a, 2b, S1, S2, S3	
FRT000097E2	Y			2a, 2b, S1, S2, S3	
FRT0001654F	Y			2a, 2b, S1, S2, S3	
FRT0000C620	Y			2a, 2b, S1, S2, S3	
FRT0000C67C	Y			2a, 2b, S1, S2, S3	
FRT000098B2	Y			2a, 2b, S1, S2, S3	
HRL0000C712	Y			2a, S1, S2, S3	
FRT00009A35	Y			2a, 2b, S1, S2, S3	
FRT0001C47F	Y			2a, 2b, S1, S2, S3	
HRS0001C45C	Y			2a, S1, S2, S3	
FRT0000C968	Y			2a, 2b, S1, S2, S3	
HRL0000C95A	Y			2a, S1, S2, S3	
FRT0001C558	Y			2a, 2b, S1, S2, S3	
HRL00009ABE	Y			2a, S1, S2, S3	
FRT0000C9F7	Y			2a, 2b, S1, S2, S3	
FRT0001C6A7	Y			2a, 2b, S1, S2, S3	
FRT00009B66	Y			2a, 2b, S1, S2, S3	
HRL00009B61	Y			2a, S1, S2, S3	
HRS0000CAB2	Y			2a, S1, S2, S3	
FRT0001CA91	Y			2a, 2b, S1, S2, S3	
FRT000106E4	Y			2a, 2b, S1, S2, S3	
FRT000107CA	Y			2a, 2b, S1, S2, S3	
FRT00010817	Y			2a, 2b, S1, S2, S3	
FRT00010AE2	Y			2a, 2b, S1, S2, S3	
FRT00010EC5	Y			2a, 2b, S1, S2, S3	
FRT00011188	Y			2a, 2b, S1, S2, S3	
FRT0001187B	Y			2a, 2b, S1, S2, S3	
FRT00009BD8	Y			2a, 2b, S1, S2, S3	
FRT0000CB48	Y			2a, 2b, S1, S2, S3	
FRT0000CB6F	Y			2a, 2b, S1, S2, S3	
FRT00009C03	Y			2a, 2b, S1, S2, S3	
FRT0000CBE5	Y			2a, 2b, S1, S2, S3	
HRL0000CC16	Y			2a, S1, S2, S3	
HRL00009C1F	Y			2a, S1, S2, S3	
FRT0000CC44	Y			2a, 2b, S1, S2, S3	

FRT00009CD8	Y			2a, 2b, S1, S2, S3	
FRT00009D44	Y			2a, 2b, S1, S2, S3	
FRT00009D7E	Y			2a, 2b, S1, S2, S3	
FRT00009D96	Y			2a, 2b, S1, S2, S3	
HRL00009D8A	Y			2a, S1, S2, S3	
FRT0000CDA5	Y			2a, 2b, S1, S2, S3	
FRT0001212A	Y			2a, 2b, S1, S2, S3	
FRT0000CE72	Y			2a, 2b, S1, S2, S3	
FRT00009E44	Y			2a, 2b, S1, S2, S3	
FRT00009E5D	Y			2a, 2b, S1, S2, S3	
HRL0000CEE3	Y			2a, S1, S2, S3	
FRT0000CEF7	Y			2a, 2b, S1, S2, S3	
FRT0000A053	Y			2a, 2b, S1, S2, S3	
FRT0000A102	Y			2a, 2b, S1, S2, S3	
FRT0000D23E	Y			2a, 2b, S1, S2, S3	
HRL0000D21C	Y			2a, S1, S2, S3	
FRT0000D2C9	Y			2a, 2b, S1, S2, S3	
HRL0001240E	Y			2a, S1, S2, S3	
HRL0000D349	Y			2a, S1, S2, S3	
HRL0000D364	Y			2a, S1, S2, S3	
FRT0000A253	Y			2a, 2b, S1, S2, S3	
FRT0000D4EC	Y			2a, 2b, S1, S2, S3	
FRT0000A2C2	Y			2a, 2b, S1, S2, S3	
HRL000124F2	Y			2a, S1, S2, S3	
HRS0000D616	Y			2a, S1, S2, S3	
FRT0000A348	Y			2a, 2b, S1, S2, S3	
FRT0000A377	Y			2a, 2b, S1, S2, S3	
FRT0000D74B	Y			2a, 2b, S1, S2, S3	
FRT0000A425	Y			2a, 2b, S1, S2, S3	
FRT0000A4C5	Y			2a, 2b, S1, S2, S3	
FRT0000A4FC	Y			2a, 2b, S1, S2, S3	
FRT000129D1	Y			2a, 2b, S1, S2, S3	
FRT0000A51A	Y			2a, 2b, S1, S2, S3	
FRT0001039F	Y			2a, 2b, S1, S2, S3	
FRT0000A546	Y			2a, 2b, S1, S2, S3	
FRT0000A819	Y			2a, 2b, S1, S2, S3	
FRT00012C19	Y			2a, 2b, S1, S2, S3	
FRT00012E09	Y			2a, 2b, S1, S2, S3	
FRT0000A909	Y			2a, 2b, S1, S2, S3	
FRT00012E72	Y			2a, 2b, S1, S2, S3	
FRT0000A941	Y			2a, 2b, S1, S2, S3	
FRT0000A969	Y			2a, 2b, S1, S2, S3	
FRT0000A989	Y			2a, 2b, S1, S2, S3	

HRL000132BC	Y			2a, S1, S2, S3	
FRT0000AA03	Y			2a, 2b, S1, S2, S3	
FRT0000AA7D	Y			2a, 2b, S1, S2, S3	
FRT0000AAA8	Y			2a, 2b, S1, S2, S3	
FRT0000AB32	Y			2a, 2b, S1, S2, S3	
HRL000134A3	Y			2a, S1, S2, S3	
FRT0000AB81	Y			2a, 2b, S1, S2, S3	
HRL0000ABB4	Y			2a, S1, S2, S3	
FRT000136D3	Y			2a, 2b, S1, S2, S3	
FRT00013724	Y			2a, 2b, S1, S2, S3	
FRT0000ABF2	Y			2a, 2b, S1, S2, S3	
FRT000137AD	Y			2a, 2b, S1, S2, S3	
FRT000137C2	Y			2a, 2b, S1, S2, S3	
HRS0000AC56	Y			2a, S1, S2, S3	
HRL0000AC95	Y			2a, S1, S2, S3	
FRT0000ACD7	Y			2a, 2b, S1, S2, S3	
FRT0000ACE6	Y			2a, 2b, S1, S2, S3	
FRT0000AD3D	Y			2a, 2b, S1, S2, S3	
FRT0000B092	Y			2a, 2b, S1, S2, S3	
FRT0000B0CB	Y			2a, 2b, S1, S2, S3	
FRT00013C94	Y			2a, 2b, S1, S2, S3	
FRT00013D1F	Y			2a, 2b, S1, S2, S3	
FRT00013D3B	Y			2a, 2b, S1, S2, S3	
FRT00013D4E	Y			2a, 2b, S1, S2, S3	
FRT0000B23E	Y			2a, 2b, S1, S2, S3	
FRT00013E49	Y			2a, 2b, S1, S2, S3	
FRT0000B278	Y			2a, 2b, S1, S2, S3	
HRL00013E4D	Y			2a, S1, S2, S3	
FRT0000B2A2	Y			2a, 2b, S1, S2, S3	
HRL00013EE8	Y			2a, S1, S2, S3	
FRT00013F47	Y			2a, 2b, S1, S2, S3	
HRL00013F27	Y			2a, S1, S2, S3	
FRT00013F5B	Y			2a, 2b, S1, S2, S3	
FRT0000B385	Y			2a, 2b, S1, S2, S3	
FRT0000B3E1	Y			2a, 2b, S1, S2, S3	
HRL0000B404	Y			2a, S1, S2, S3	
FRT0000B44D	Y			2a, 2b, S1, S2, S3	
FRT0000B49F	Y			2a, 2b, S1, S2, S3	
FRT0000B4B5	Y			2a, 2b, S1, S2, S3	
FRT0000B4F8	Y			2a, 2b, S1, S2, S3	
FRT0000B58A	Y			2a, 2b, S1, S2, S3	
FRT0000B59A	Y			2a, 2b, S1, S2, S3	
FRT0000B6C5	Y			2a, 2b, S1, S2, S3	

HRS0000B6A2	Y			2a, S1, S2, S3	
FRT0000B6F1	Y			2a, 2b, S1, S2, S3	
FRT0000B772	Y			2a, 2b, S1, S2, S3	
HRL0000B73D	Y			2a, S1, S2, S3	
FRT0000B80F	Y			2a, 2b, S1, S2, S3	
FRT0000B829	Y			2a, 2b, S1, S2, S3	
HRL0000B868	Y			2a, S1, S2, S3	
FRT0000BA8D	Y			2a, 2b, S1, S2, S3	
HRL0000BABA	Y			2a, S1, S2, S3	
HRL0000BADC	Y			2a, S1, S2, S3	
FRT0000BB36	Y			2a, 2b, S1, S2, S3	
FRT0000BDBE	Y			2a, 2b, S1, S2, S3	
HRS0000BDBB	Y			2a, S1, S2, S3	
FRT0000BDD9	Y			2a, 2b, S1, S2, S3	
FRT0000BE5E	Y			2a, 2b, S1, S2, S3	
FRT0000BEC0	Y			2a, 2b, S1, S2, S3	
FRT0000BEDF	Y			2a, 2b, S1, S2, S3	
HRL0000BECE	Y			2a, S1, S2, S3	
FRT0001D889	Y			2a, 2b, S1, S2, S3	
FRT0001ECAD	Y			2a, 2b, S1, S2, S3	
FRT0001EBC6	Y			2a, 2b, S1, S2, S3	
FRT0001E26E	Y			2a, 2b, S1, S2, S3	
FRT0001EC38	Y			2a, 2b, S1, S2, S3	
FRT0001E2F2	Y			2a, 2b, S1, S2, S3	
FRT00020364	Y			2a, 2b, S1, S2, S3	
FRT0002037A	Y			2a, 2b, S1, S2, S3	
FRT00020397	Y			2a, 2b, S1, S2, S3	
HRS000203B3	Y			2a, S1, S2, S3	
FRT00020C1B	Y			2a, 2b, S1, S2, S3	
FRT00020AE1	Y			2a, 2b, S1, S2, S3	
FRT00020B9D	Y			2a, 2b, S1, S2, S3	
FRT00020BF9	Y			2a, 2b, S1, S2, S3	
FRT00021B59	Y			2a, 2b, S1, S2, S3	
FRT00021C5A	Y			2a, 2b, S1, S2, S3	
FRT00021C92	Y			2a, 2b, S1, S2, S3	
FRT00021CB4	Y			2a, 2b, S1, S2, S3	
FRT00021D02	Y			2a, 2b, S1, S2, S3	
FRT00021F19	Y			2a, 2b, S1, S2, S3	
FRT00022003	Y			2a, 2b, S1, S2, S3	
FRT000233AC	Y			2a, 2b, S1, S2, S3	
FRT00023565	Y			2a, 2b, S1, S2, S3	
FRT0002362B	Y			2a, 2b, S1, S2, S3	
FRT0002376B	Y			2a, 2b, S1, S2, S3	

FRT00023898	Y			2a, 2b, S1, S2, S3	
FRT000240AC	Y			2a, 2b, S1, S2, S3	
FRT0002414F	Y			2a, 2b, S1, S2, S3	
FRT0002424C	Y			2a, 2b, S1, S2, S3	
HRL0002422E	Y			2a, S1, S2, S3	
FRT000242A3	Y			2a, 2b, S1, S2, S3	
FRT000242B1	Y			2a, 2b, S1, S2, S3	
FRT0002432F	Y			2a, 2b, S1, S2, S3	
FRT000243FF	Y			2a, 2b, S1, S2, S3	
FRT000244A8	Y			2a, 2b, S1, S2, S3	
FRT000245DD	Y			2a, 2b, S1, S2, S3	
FRT0002475A	Y			2a, 2b, S1, S2, S3	
HRL000247F2	Y			2a, S1, S2, S3	
FRT00024C1A	Y			2a, 2b, S1, S2, S3	
FRT000251C0	Y			2a, 2b, S1, S2, S3	
FRS0002749B	Y			2a, 2b, S1, S2, S3	
FRS0002BC7D	Y			2a, 2b, S1, S2, S3	
FRT0001B5F3	Y			2a, 2b, S1, S2, S3	
FRT000066A4	Y			2a, 2b, S1, S2, S3	
FRT0001E3B3	Y			2a, 2b, S1, S2, S3	
FRT00021B46	Y			2a, 2b, S1, S2, S3	
FRT00021E1D	Y			2a, 2b, S1, S2, S3	
FRT0002406A	Y			2a, 2b, S1, S2, S3	
FRT000242F0	Y			2a, 2b, S1, S2, S3	
FRT00002854	M			2a, 2b, S1, S2, S3	
FRT00005850	M			2a, 2b, S1, S2, S3	
FRT0001B8C9	M			2a, 2b, S1, S2, S3	
FRT0000C280	M			2a, 2b, S1, S2, S3	
FRT000121D0	M			2a, 2b, S1, S2, S3	
FRT00003CAB	N			2a, 2b, S1, S2, S3	
FRT000067E1	N			2a, 2b, S1, S2, S3	
HRL00006823	N			2a, S1, S2, S3	
HRL0000685F	N			2a, S1, S2, S3	
FRT00007C67	N			2a, 2b, S1, S2, S3	
FRT00007D61	N			2a, 2b, S1, S2, S3	
FRT00007E26	N			2a, 2b, S1, S2, S3	
FRT0000C101	N			2a, 2b, S1, S2, S3	
HRL0000CA5C	N			2a, S1, S2, S3	
FRT00011805	N			2a, 2b, S1, S2, S3	
FRT00011D4C	N			2a, 2b, S1, S2, S3	
FRT0000CE1D	N			2a, 2b, S1, S2, S3	
HRL0000D1A9	N			2a, S1, S2, S3	
FRT0000A650	N			2a, 2b, S1, S2, S3	

FRT00020421	N			2a, 2b, S1, S2, S3	
FRT0002459B	N			2a, 2b, S1, S2, S3	
FRS00027499	N			2a, 2b, S1, S2, S3	
FRT0001CA56	N			2a, 2b, S1, S2, S3	
FRT00021F40	N			2a, 2b, S1, S2, S3	
FRT00023284	N			2a, 2b, S1, S2, S3	
HRL000243C0	N			2a, S1, S2, S3	